ABSTRACT

Title of Document: SYSTEM IDENTIFICATION OF VEHICLE DYNAMICS AND ROAD CONDITIONS USING WIRELESS SENSORS

Noah C. Blum, Doctor of Philosophy, 2015

Directed By: Professor Yunfeng Zhang
Department of Civil and Environmental Engineering

Road quality and ride comfort are major concerns when creating and maintaining roads. Ride comfort is dependent on the interaction between the vehicle and the roughness of the road. Road roughness is currently measured by road-profiling vehicles in a quantifiable term known as the International Roughness Index (IRI). Although this method is useful for determining road surface information, it is a time consuming process, it can't be carried out every day, and it does not provide a direct indication of ride comfort. However, advancements in sensor technology provide necessary enhancements that current methods cannot address. This study aims to develop an innovative method using built-in wireless sensing and mobile computing features of smartphones to not only estimate road roughness, but to provide a direct real-time indication of ride comfort.

Estimation of road roughness based on vehicle response involves insight regarding the properties of the vehicle itself. While the vibration response of the

vehicle can be readily measured using wireless accelerometers or built-in smartphone sensors, information pertaining to the vehicle and road properties is left unknown. To address this issue, various system identification methods are evaluated for high-damped systems and applied to the vehicle. Through the application of system identification methods using vehicle response data, the unknown parameters of the vehicle can be estimated. These methods are validated through analysis of vehicle model simulation paired with standard simulated road profiles. Furthermore, these simulations create an environment to determine optimal conditions for vehicle mass prediction. With vehicle parameters identified, the dynamic response parameters of the vehicle and the input of the road surface profile can be correlated to estimate the IRI while directly providing ride comfort information. Field testing involving the use of a wireless accelerometer and GPS is also implemented to compare recorded data against the simulation findings.

This study establishes a framework that integrates wireless sensors, system identification methods, and the correlation between ride comfort and the IRI with vehicle vibration measurements. System identification methods with a focus on vehicles subjected to excitation from the road are evaluated. This involves an investigation of prediction error identification methods with the use of grey-box modeling to estimate vehicle mass under varying road conditions. With vehicle parameters known, correlation of vehicle vibration response with the IRI and ride comfort is empirically established to determine areas of road in need of maintenance along with comfortable travel routes in real-time. This study demonstrates the appeal

for including information related to road conditions and ride comfort in mobile maps for alternative travel routes.

SYSTEM IDENTIFICATION OF VEHICLE DYNAMICS AND ROAD CONDITIONS USING WIRELESS SENSORS

By

Noah C. Blum

Dissertation submitted to the Faculty of the Graduate School of the
University of Maryland, College Park, in partial fulfillment
of the requirements for the degree of
Doctor of Philosophy
2015

Advisory Committee:
Professor Yunfeng Zhang, Chair
Professor M. Sherif Aggour
Professor Amde M. Amde
Professor Chung C. Fu
Professor Sung W. Lee

Acknowledgements

I would like to express my deepest appreciation and gratitude to my advisor, Dr. Yunfeng Zhang, for the mentorship he provided me throughout my time at the University of Maryland. His knowledge and guidance continuously motivated me to explore detailed areas of research necessary to complete this dissertation. I would also like to extend my gratitude to my dissertation committee: Dr. Chung C. Fu, Dr. Amde M. Amde, Dr. Sung W. Lee, and Dr. M. Sherif Aggour.

I would also like to thank the FHWA Dwight David Eisenhower Transportation Fellowship Program for the additional funding of this research project.

Thank you to my parents, Jerrold and Arlene, and to my siblings, Joshua, and Ariel, for their continued support throughout this process. I am also thankful for the support from my friends and colleagues: Timothy K. Saad, Changjiang Zhou, and Nora Strumpf.

Table of Contents

List of Tables

List of Figures

.

Chapter 1: Introduction

1.1 Motivation

Road quality and ride comfort are two examples of what drivers expect while traveling on the road. These expected characteristics are in part attributed to road roughness. Determining the road roughness is an important part of transportation engineering and is currently evaluated through numerous methods of road profiling. The goal of this study is to create an efficient and cost effective methodology of profiling road roughness and ride comfort by using the automobile itself as a moving sensor. The profiling method can be implemented on mobile devices such as smartphones. Smartphones have already provided great advancements to the field of transportation through the use of GPS data for vehicle location and travel information. By incorporating this information, along with vibration measurements from the phone's internal accelerometer, a quick and easy profiling map can be created and the International Roughness Index (IRI) can be estimated. Once the IRI is determined, it can be used to find roads that are in need of maintenance and rehabilitation, and necessary actions can be taken to create safer driving conditions. The widespread use of smartphones by drivers facilitates large amounts of road profiling data on many U.S. roads, especially in urban areas. Therefore, real-time road profiling data poses interesting fundamental research questions to be addressed through a framework consisting of structural dynamics, system identification methods, and sensors found in smartphone devices.

Computer simulation provides a useful tool in understanding the behavior of a vehicle in motion. Creating a vehicle suspension model that can accurately react to given road profiles will be useful in determining the accuracy of the correlation between smartphone-measured vibration data and road roughness. Generating new and more accurate methods of tire-road interaction will not only be useful for this research, but can also be used for many other applications as well.

To validate computer simulations and collect smartphone vibration data, field tests must be performed. Due to the varying nature of the vehicle response, multiple tests must be completed on several different types of road profiles. This includes road surfaces ranging in roughness, and specific types of bump inputs. Data is collected through the use of a commercial off-the-shelf (COTS) accelerometer in addition to the built-in chip accelerometer found in a smartphone.

To understand the response of the moving vehicle, modal frequency identification methods will be used to determine the fundamental periods/frequencies. Due to the complexity of these calculations and the current limitations of processing power on smartphones, either an algorithm with a minimal amount of data error must be created to simplify the process or the data must be sent to a server for real-time processing via cloud computing technology. By determining the limitations of the smartphones, a simple algorithm can be made for onboard processing of modal frequencies that makes the best use of the power supplied by the phone while providing accurate data with minimal error. This application will take the sensor data collected in the

experimental runs and use the vibration response with system identification methods to estimate the vehicle mass. The application will also make use of the onboard GPS to track the location of any changes in the road conditions and vehicle speed. With this data, profile maps of road roughness and ride comfort can be created.

Technology has reached a point where detecting damages in roads can be quickly determined using information that can be given without changing our daily routines — driving with a smartphone in the car. Traffic conditions are currently updated in real-time through the use of the smartphone GPS. Recent research has also begun to take advantage of smartphone technology for collecting data, such as real-time pothole detection (Mednis, et al., 2011) and earthquake detection for early warning (Zambrano, et al., 2014). Through the use of a smartphone and a properly constructed algorithm, information about the road roughness can be collected and calculated on-the-spot for fast evaluation in a way that has never been done before. This study will not only be able to be used for detecting the roughness index, but will also provide a direct measure of ride comfort using smartphone technology to determine and offer drivers with the most comfortable driving routes.

1.2 Research Objective

The main objective in this study is to establish the fundamental technologies that support the viable use of wireless sensors or smartphones in everyday vehicles to create a ubiquitous sensor network. This network can be used to develop a real-time picture of road roughness and ride comfort from the perspective of users with different needs. This involves using system identification techniques to determine

vehicle parameters to relate the response to the input statistics of the road itself. Many specific contributions are made while accomplishing the main goal of this study:

- Evaluate system identification methods for use of parameter identification of highly-damped systems, specifically used for estimation of vehicle mass. This involves performing system identification methods with the use of acceleration data collected with a single wireless sensor.
- Road profiling does not represent the user experience. The comfort of a ride is dependent on the type of vehicle combined with the weight of the passengers and cargo. Road profilers are used to determine the changing elevation of the road and relate it to roughness. Although useful, determining the roughness of the road does not provide a direct indication of the users' sense of ride comfort. This research not only examines various methods of determining the roughness of roads, but also relates the unevenness of the road to the comfort of the user.
- Create road profile maps relating the vehicle response to user perception and road roughness information. These maps, based on vertical acceleration of the vehicle, directly relate the output to both the roughness of the road profile and the comfort of the user, which varies based on vehicle type.
- Take advantage of new mobile sensing and computing technology, such as smartphones, to enable real-time updating of road conditions, which current profiling methods are ill-equipped to do.

1.3 Dissertation Outline

Chapter 2 compiles a review of current methods of road profiling, classification of roads, calculation of road roughness, and quantification of ride comfort. This review is necessary for a complete understanding of the inputs and outputs of the vehicle.

Chapter 3 investigates various system identification methods for high-damped systems typical of a vehicle, including algorithms such as ERA, ARMAX, N4SID, and PEM. These processes are evaluated to determine which identification techniques are best suited for identification of vehicle parameters using system response data with an estimated input.

Chapter 4 includes numerical simulation of system identification of the vehicle parameters and statistical properties of the road profile. To perform system identification, simulation of road profiles and vehicle dynamic responses is first studied to create a system with similar real world input and output. Relations between profile roughness to acceleration response and ride comfort are found with Monte Carlo simulation methods.

Chapter 5 demonstrates the effectiveness of the application of system identification methods through field testing. These tests include the vertical acceleration vibrations affected by vehicle speed, road roughness, and various bumps in the road through the use of wireless sensor data collection.

Chapter 6 consists of analysis of the data gathered during the field tests. This analysis includes the use of estimated road inputs to predict the vehicle mass. With vehicle parameters known, a relation correlating the vertical acceleration response to the IRI is determined. This relation, in addition to the direct measure of comfort, is used to create two profile maps; one to display areas of roughness, and one to show ride comfort.

Chapter 2: Vehicle Input / Output

2.1 Viewing the Vehicle as a System

Before the parameters of a vehicle can be analyzed, an understanding of the various vehicle inputs and outputs must be understood. As seen in Figure 2.1, the vehicle can be viewed as a system:

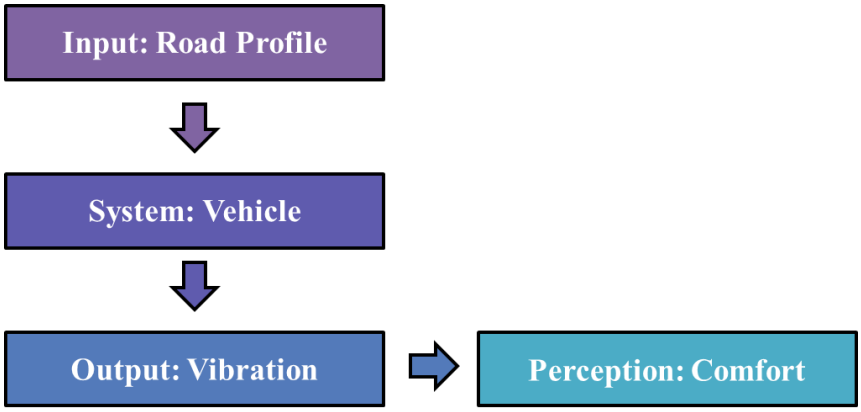

Figure 2.1: Vehicle as a System

This system has both an input and an output. In the case of the vehicle, the input is the changing road profile elevation, while the output is viewed as the vibrational response. This vibration, felt by the user of the vehicle, correlates to the perceived comfort. This comfort is an important factor in determining whether a road meets the standards set by the FHWA or whether maintenance is required. The following sections of this chapter examine the classification of road profiles determined by the amount of surface roughness. The level of roughness is then calculated through the International Roughness Index (IRI), which is used to determine the quality of the road. In regards to system output, the vibration response and its relation to human comfort is considered.

2.2 Road Profiling

Road smoothness is a major factor concerning both ride comfort and driver safety. Determination of the smoothness of a road surface is completed through the process of road profiling. A road profile can be taken laterally and longitudinally as seen in Figure 2.2. Lateral profiles show the superelevation and crown of the road, while longitudinal profiles are used to describe the design grade, roughness, and texture of the road (Sayers, et al., 1998).

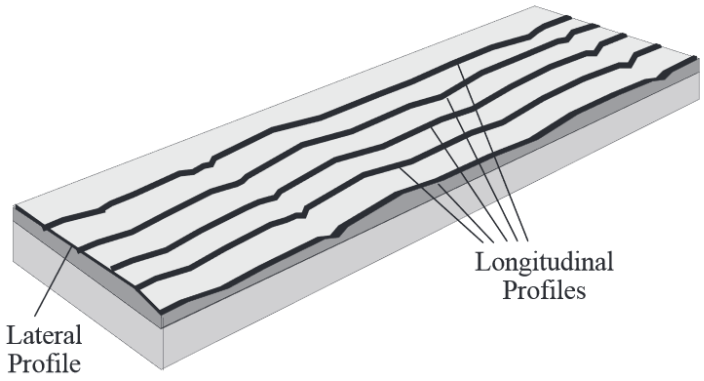

Figure 2.2: Road Profile Orientation (Sayers, et al., 1998)

Road profiling has become a necessary tool used to monitor conditions of existing road networks, evaluate the quality of newly constructed or repaired road sections, and examine specific segments of roads for rehabilitation or research (Sayers, et al., 1998).

Road profilers are currently used in a majority of the United States for evaluation of existing road networks and newly paved or recently rehabilitated road surfaces. In addition to this, at least ten states also use profilers for construction quality control for individual projects (Wang, et al., 2009). Many different profilers exist, such as the rod and level, which uses a static reference point while measuring the surrounding elevation of the area, and walking profilers used to measure the height relative to a moving reference point. Although effective, these types of profilers are slow and are not ideal for determining the profiles of an entire network of roads. To overcome this weakness, General Motors Research Laboratories developed the inertial profiler (Sayers, et al., 1998). Introduced in the 1960s, the inertial profiler made high-speed profiling possible through the use of a moving vehicle. As visualized in Figure 2.3, this profiler makes use of an accelerometer in conjunction with devices such as laser transducers, and infrared and ultrasonic sensors to measure the height of the ground beneath the vehicle. The accelerometer is used to measure the vertical acceleration as an inertial reference point for the relative height to the ground.

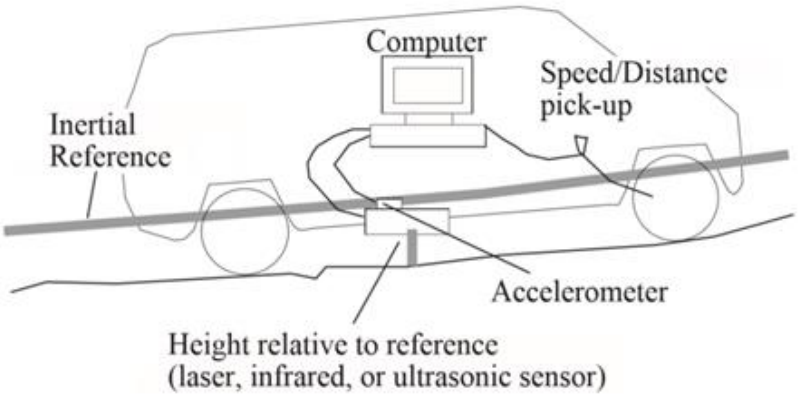

Figure 2.3: High-Speed Profiler (Sayers, et al., 1998)

Beginning in 1996, the entire National Highway System has been profiled annually with these high-speed profilers (PennDOT, 2015). Each road profiler is equipped with an on-board computer used to interface with the accelerometers and lasers attached to the vehicle. Two persons are needed to perform profiling, one to operate the computer and one to drive the vehicle. Testing is typically limited to the months of March through November due to weather conditions.

Figure 2.4: Operator Control Unit for High-Speed Profiler (PennDOT, 2015)

Although improvements have been made since the development of high-speed profilers, the current profiling process is very costly and time consuming. A 2003 survey conducted by the National Cooperative Highway Research Program has shown that out of the 52 agencies surveyed, all of them monitor road roughness, but the minimum time between updating the profile is limited to a single year. Table 2.1 shows the survey results containing the frequency of profiling in years along with the application for the data.

Table 2.1: Summary of Automated Monitoring Frequencies Employed (McGhee, 2004)

Frequency, Years	Cracking	Smoothness / Roughness	Rut Depth	Joint Faulting
1	9	26	24	10
2	18	20	20	13
3	2	4	4	0
Other	1	2	2	0
Total	30	52	50	23

Cost is also major concern when it comes to profiling an entire network of roads. Collection and processing data through road profiling averages more than $30 per lane-km ($50 per lane-mi) and can reach up to $125 per lane-km ($200 per lane-mi) in urban or high traffic areas (McGhee, 2004).

Technological advancements have been made since the introduction of the high-speed inertial profiler that current profiler vehicles are not taking advantage of. Current road profilers take the road profile roughness into account, but do not investigate the impact the surface has on the user. Through the use of smartphone technology, not only can roughness be estimated, but the ride comfort can be directly measured as further shown in this study.

2.2.1 ISO Classification

The International Organization for Standardization (ISO) has specifications for reporting longitudinal road profile data which uses the calculated PSD of the vertical displacement profile. The use of PSD to describe road irregularities was first introduced by Dodds and Robson by viewing the road surface profile as a homogeneous and isotropic two-dimensional Gaussian random process (Dodds, et al., 1973). The procedure in which roads are classified uses this description and is detailed in *ISO 8608: Mechanical Vibration - Road Surface Profiles - Reporting of Measured Data*. This procedure is used for the reporting of road profiles such as streets, highways, and off-road terrain areas. Each profile is given a class based on its roughness, which range from classes A to H. Paved roads are generally classified as A to D, with A being a very good profile (smooth), and D being poor (rough). A class A or B profile may consist of newer roads or extremely smooth pavement, such as airport runways. Class C profiles can typically be viewed as older roadways which are not maintained. Classifications of D or E are rough profiles which may be due to highly deteriorated pavement or a layer consisting of a material such as cobblestone (Tyan, et al., 2009).

Due to its random nature, functions of road profiles are described in terms of probability statements instead of defined equations. Power spectral density (PSD) is the limiting mean-square value of a signal per unit frequency bandwidth. Since the surface roughness is a spatial disturbance rather than a disturbance in time, the PSD is represented in spatial frequency, cycle/m, in place of the commonly used frequency

units of cycle/s (Xu, et al., 1992). When determining the road roughness, certain frequencies can be filtered out when looking at the road profile. Road surface qualities can be split into three categories: topography, road roughness, and road texture. Topography consists of the vertical changes of the road due to the varying landscape. These changes due to landscape have large wavelengths above 100 m, providing frequencies below 0.01 cycle/m, and do not affect the vehicle dynamics. High variability components, known as road texture, have small wavelengths, below 10 cm, and frequencies above 10 cycle/m. These components also don't affect the dynamics of the vehicle because they are filtered out by the tire. The area of interest, road roughness, ranges between these two limits (Johannesson, et al., 2012).

When reporting road profiles using the procedures established in ISO 8608, the profile can be described in terms of either displacement or acceleration PSD. This method of characterization of road profiles in PSD form is useful because it can be used to describe roughness as a single term (Dodds, et al., 1973). Equations 2.1 and 2.2 represent the displacement PSD as described with spatial frequency with units of cycle/m, n, and angular spatial frequency, rad/m, Ω.

$$G_d(n) = G_d(n_0)\left(\frac{n}{n_0}\right)^{-w} \quad \textbf{(2.1)}$$

$$G_d(\Omega) = G_d(\Omega_0)\left(\frac{\Omega}{\Omega_0}\right)^{-w} \quad \textbf{(2.2)}$$

These equations are sometimes split into two parts with a change in the roughness exponent, w, depending on whether the spatial frequency, n, is greater or than the discontinuity frequency, n_0. To simplify the road surface roughness, the roughness

exponent, *w*, also known as the *waviness* is typically assumed to be 2 regardless of the wave number (Sukhvarsh, et al., 2008). The degree of roughness, $G_d(n_0)$, can be estimated by looking at the displacement PSD at the reference spatial frequency. This reference is taken as $n_0 = 0.1$ cycles/m. This degree of roughness is used to give the profile a letter classification as previously mentioned. Table 2.2 provides the upper and lower bounds for the degree of roughness for the classifications ranging from A to H (ISO 8608, 1995). Figure 2.5 shows the bounds of each classification as represented on the PSD plot, with a spatial frequency range corresponding to the road roughness range of interest.

Table 2.2: Road Classification, Spatial Frequency Units

Road Class	Degree of Roughness: $G_d(n_0)$, 10^{-6} m^2(cycle/m)		
	Lower Limit	Geometric Mean	Upper Limit
A	-	16	32
B	32	64	128
C	128	256	512
D	512	1,024	2,048
E	2,048	4,096	8,192
F	8,192	16,384	32,768
G	32,768	65,536	131,072
H	131,072	262,144	-
n_0 = 0.1 cycle/m			

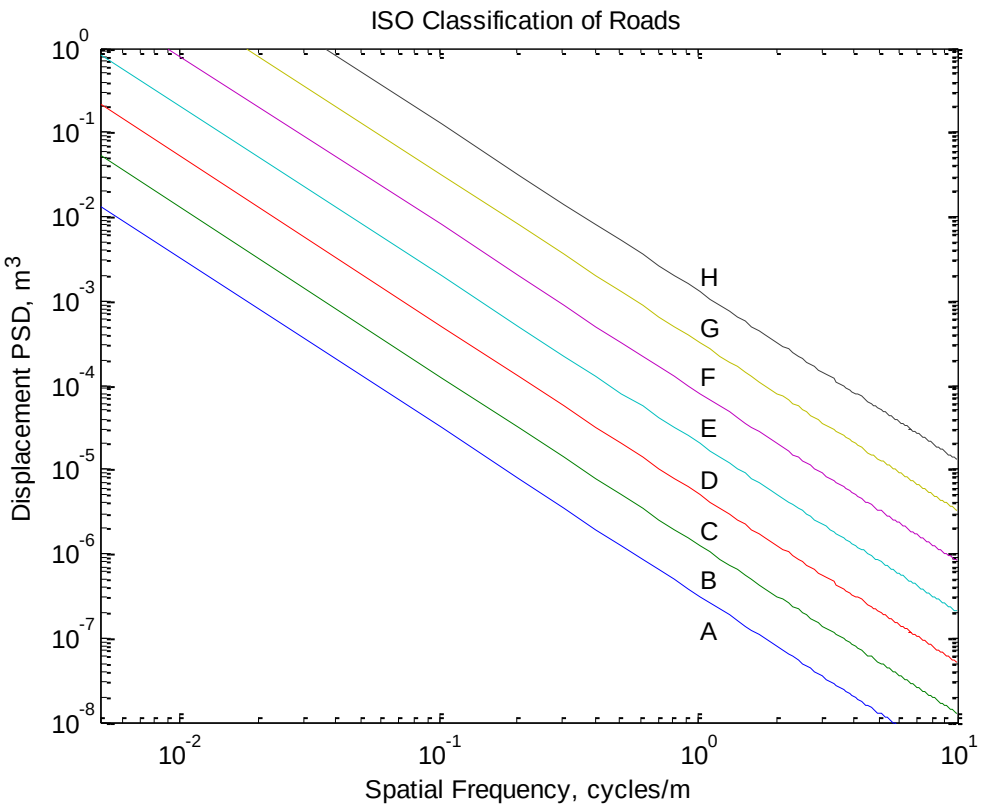

Figure 2.5: Road Classification (ISO 8608)

The relationship between the displacement PSD and acceleration PSD can be seen in Equation 2.3.

$$G_a(n) = (2\pi n)^4 \cdot G_d(n) \tag{2.3}$$

To provide a sense for a typical profile PSD plot, examples of simulated profiles with different roughness are shown in Figure 2.6 and Figure 2.8 with their corresponding displacement PSD's plotted in Figure 2.7 and Figure 2.9. Observing the differences in the PSD plots, it can be seen that low wave numbers have higher amplitudes when compared to the high wave numbers with lower amplitudes (Sayers, et al., 1996). It can also been seen that the displacement PSD amplitude is shifted upward for all wave numbers for road profiles with increased roughness.

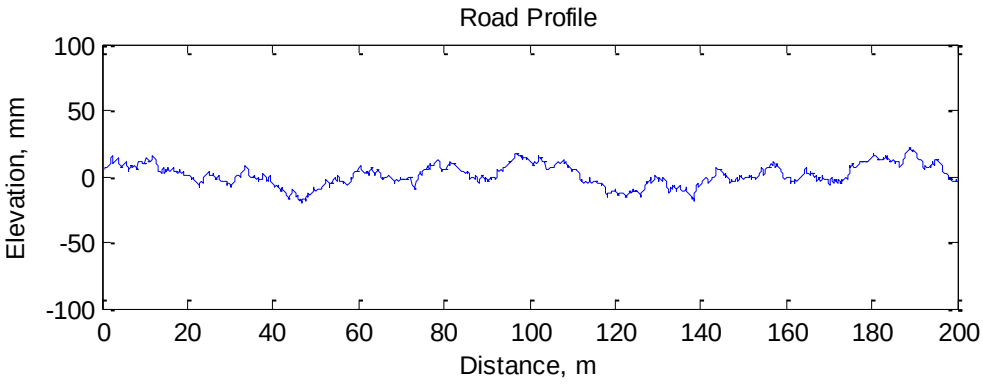

Figure 2.6: Simulated Smooth Road Profile

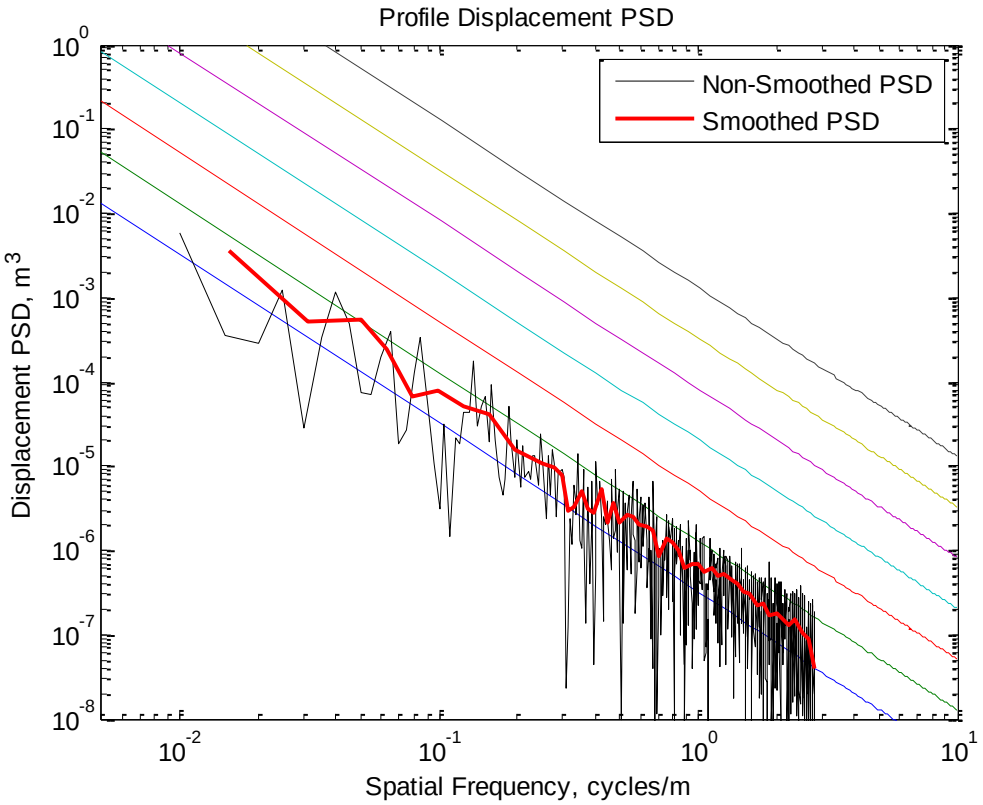

Figure 2.7: PSD Plot of Simulated Class B Profile

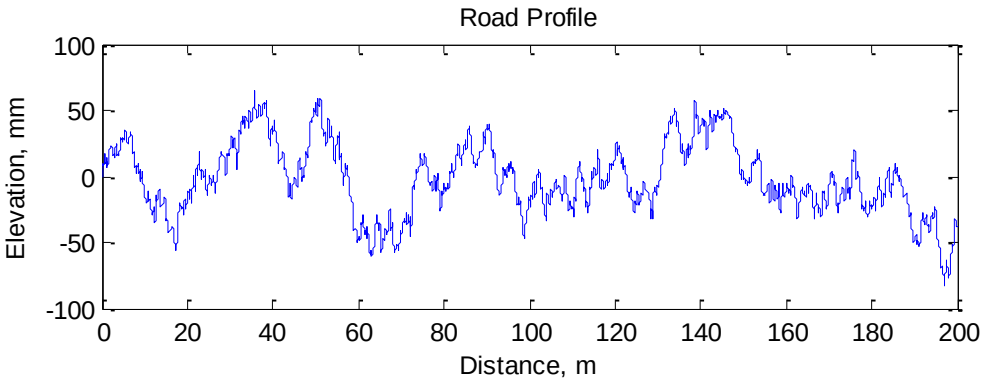

Figure 2.8: Simulated Rough Road Profile

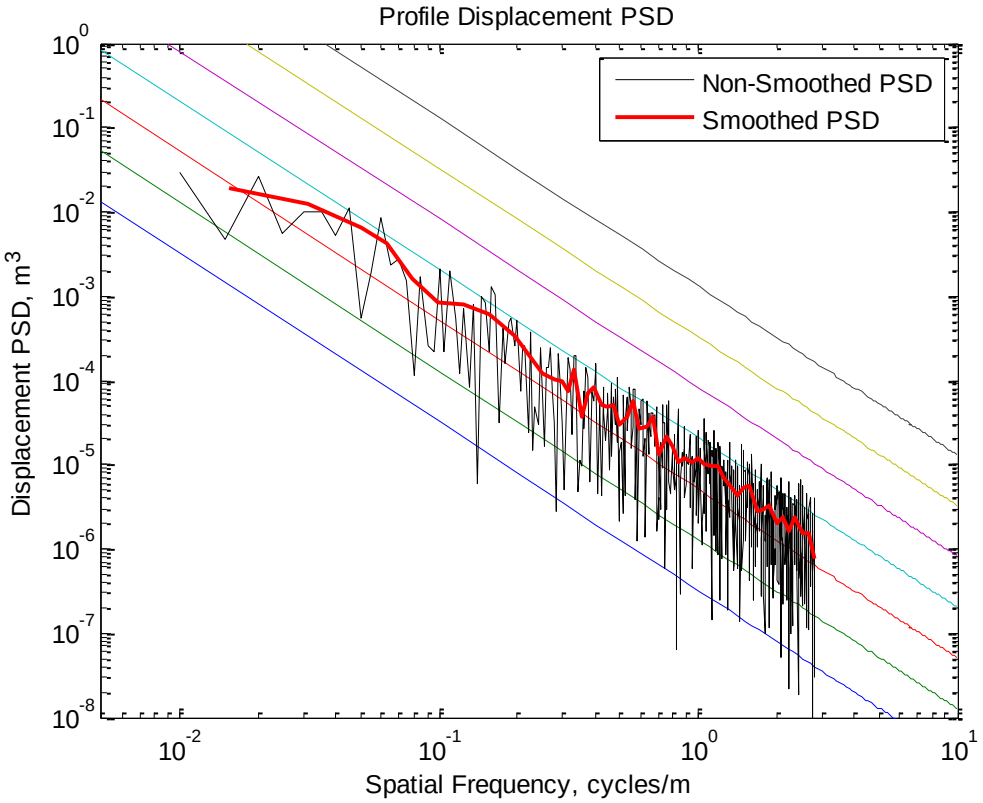

Figure 2.9: PSD Plot of Simulated Class D Profile

Since the PSD's for road profiles are calculated with a constant bandwidth, there is an appearance of high fluctuation caused by the statistical noise. To account for this, a smoothing process is implemented as per ISO 8608. This smoothing process is completed by dividing the PSD into different octave bands and using the root mean square values. This process is outlined is Equations 2.4, 2.5, and 2.6, where $G_s(i)$ represents the smoothed PSD in smoothing band *i*, and B_e is the frequency resolution given in cycles/m. The upper and lower cut-off frequencies are included in the equations as n_h and n_l. A list of the specific cut-off values used for each bandwidth can be found in ISO 2631-1.

$$G_s(i) = \frac{[(n_L + 0.5) \cdot B_e - n_l(i)] \cdot G(n_L)}{n_h(i) - n_l(i)} + \frac{\sum_{j=n_L+1}^{n_H-1} G(j) \cdot B_e}{n_h(i) - n_l(i)} + \frac{[n_h(i) - (n_H - 0.5) \cdot B_e] \cdot G(n_H)}{n_h(i) - n_l(i)} \quad \textbf{(2.4)}$$

$$n_H = INT\left(\frac{n_h(i)}{B_e} + 0.5\right) \quad \textbf{(2.5)}$$

$$n_L = INT\left(\frac{n_l(i)}{B_e} + 0.5\right) \quad \textbf{(2.6)}$$

As seen in Figure 2.7 and Figure 2.9, classification of the road profiles becomes easier once the PSD representation has been smoothed.

2.2.2 International Roughness Index

Since the introduction of gas-powered vehicles, the need for smooth roads has been present. Determination of roughness has been a major factor in the maintenance and preservation of smooth roads. Due to the varying response from early roughness measuring devices, such as the rolling straightedge, Profilograph, and Roughometer, the necessity of a single standard became apparent (Gillespie, 1992). Objectives of creating a new standard include the relation to vibration response of the vehicle rather than vehicle performance, a scale that is stable with time, measureable with a range of different types of hardware, and the ability to be consistently replicated for tests around the world. This need for a new standard led to the introduction of the standard scale known as the International Roughness Index (IRI). Rather than directly using hardware to measure roughness of a road profile, the IRI is calculated by using an algorithm that simulates a vehicle driven over a measured profile. This algorithm acts as a replacement for a roadmeter and eliminates the possible difference in vehicle dynamics and the need for calibration by creating a standard set of parameters to be used in all IRI calculations. This change from roughness measurement hardware to software became a major advantage of the use of the IRI as the standard, as it could be used in conjunction with different types of road profilers and remains consistent over time (Sayers, et al., 1986). Consistency of the IRI values through the use of different types of profiles has been verified by the Road Profiler User Group and the Federal Highway Administration (Sayers, et al., 1998).

The IRI is a calculated statistic that quantitatively expresses the quality of road conditions based on the recorded road profile. The IRI can be viewed as a mathematical transform of a measured road profile (Prem, et al., 2005). It is calculated by observing the simulated relative displacement response of a quarter car's sprung and unsprung mass while traveling along the profile of interest. The quarter car system is chosen to show a similar response to that of a passenger car as displayed in Figure 2.10 (Toyota, 2015).

Figure 2.10: Quarter Car Representation

Since the adoption of the IRI as the standard measure of roughness, the FHWA has started programs, such as the *Pavement Smoothness Initiative*, which are established to ensure smooth pavements by setting a target limit IRI (FHWA, 2014). To calculate the IRI, the FHWA uses ProVAL, an engineering software application capable of analyzing measured road profiles. Beginning with its introduction in 2001, ProVAL has been a trusted source for pavement analysis and has been used by State Departments of Transportation in the study of pavement smoothness following construction (FHWA, 2003). A sample of a recorded road profile can be seen in Figure 2.11 with its calculated IRI in Figure 2.12.

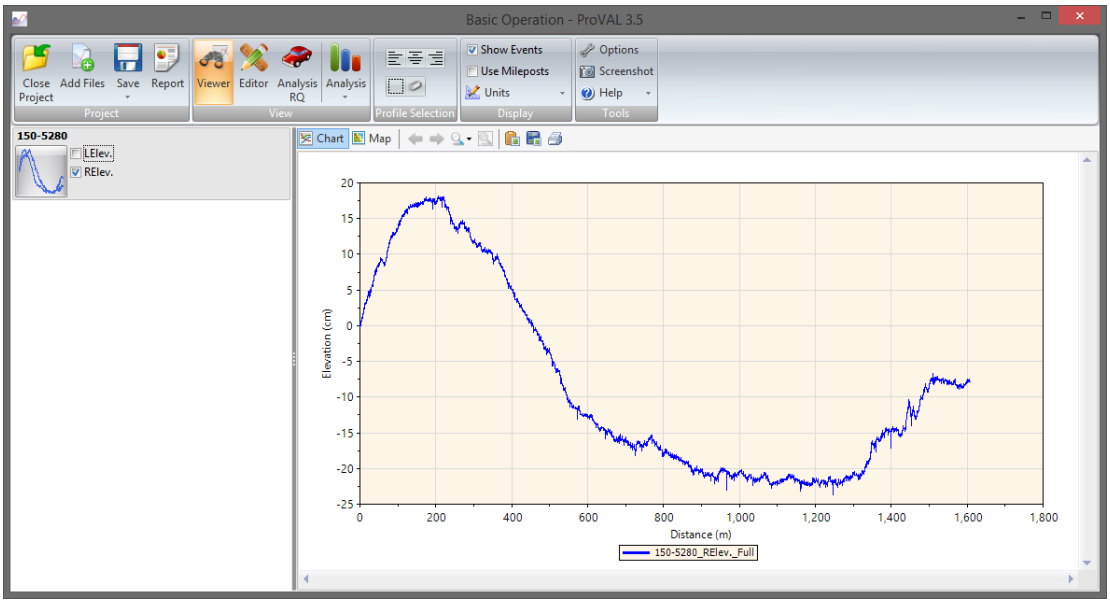

Figure 2.11: ProVAL – Road Profile

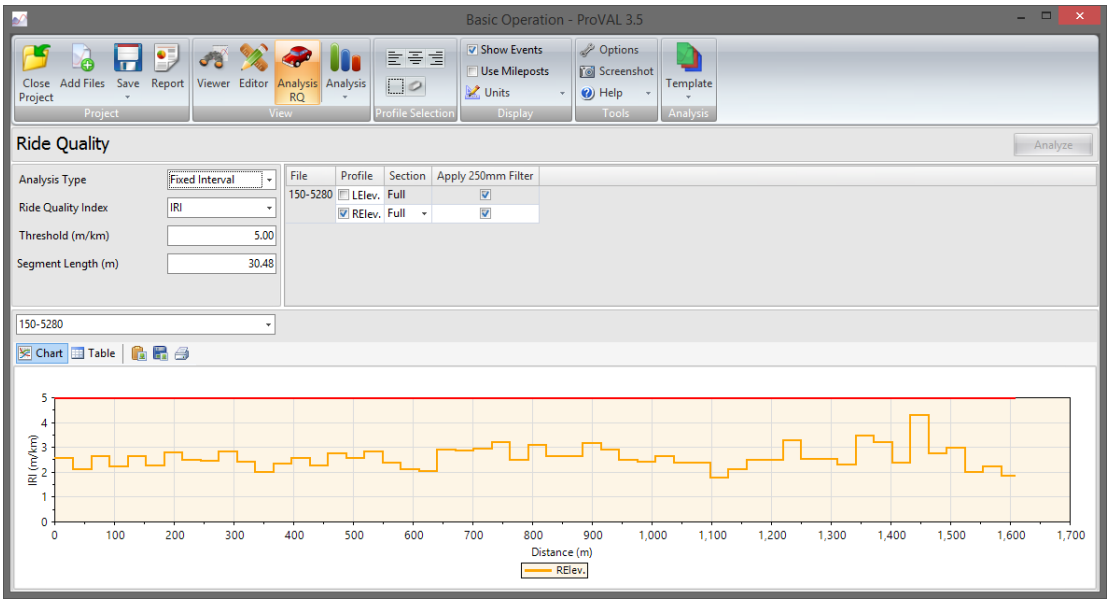

Figure 2.12: ProVAL – International Roughness Index

2.2.2.1 IRI Sensitivity

One reason the IRI is chosen to characterize road roughness is due to its ability to describe the profile roughness that causes vehicle vibrations. The parameters of the simulated quarter car model in the calculation of the IRI were specifically chosen by the United States National Cooperative Highway Research Program (NCHRP) to provide a model that offers similar results as a majority of passenger vehicles (Gillespie, et al., 1980). The quarter car with these parameters, given as ratios as shown below, is known as *The Golden Car*.

$$\frac{k_s}{m_s} = 63.3 \qquad \frac{k_t}{m_s} = 653 \qquad \frac{c_s}{m_s} = 6 \qquad \frac{m_u}{m_s} = 0.15$$

These ratios relate the suspension stiffness, tire stiffness, suspension damping, and unsprung damping to the sprung mass. *The Golden Car* was developed in an attempt to create a uniform calibration system that has a high correlation with the vehicles that were used to measure the road elevation when profiling. These parameters, used to maximize the output of the system, are similar to highway vehicles, with the exception of an increased amount of damping. This additional damping prevents the simulated vehicle from "tuning in" to certain wavelengths that a majority of vehicles are not sensitive to (Sayers, et al., 1998). Sensitivity of the IRI is significant as it relates to the resonant frequency of typical highway vehicles. The IRI gain slope represents the ratio of the output IRI to the amplitude of the input sinusoids. Figure 2.13 shows the calculated IRI values for sinusoids with wavelengths varying from 0.1 to 100 m. This figure shows the maximum sensitivity of the IRI at two specific points; the first peak at a wave number of 0.065 cycles/m and the second peak at a

wave number of 0.42 cycles/m. These two points correspond to wheel hop and body bounce of the vehicle, respectively. Evaluating these wave numbers with an 80 k/hr quarter car model, the resonant frequencies are calculated as 1.44 and 9.33 Hz. These two frequencies are important because they are approximately equal to the frequencies designed for vehicles to minimize transmission of road inputs (Sayers, et al., 1998). The sensitivity of the IRI to these frequencies is the basis for the usefulness for calculating road roughness. The resonance seen in the IRI gain slope provides dominant results when using suspension deflection as the measured response (Gillespie, 1992).

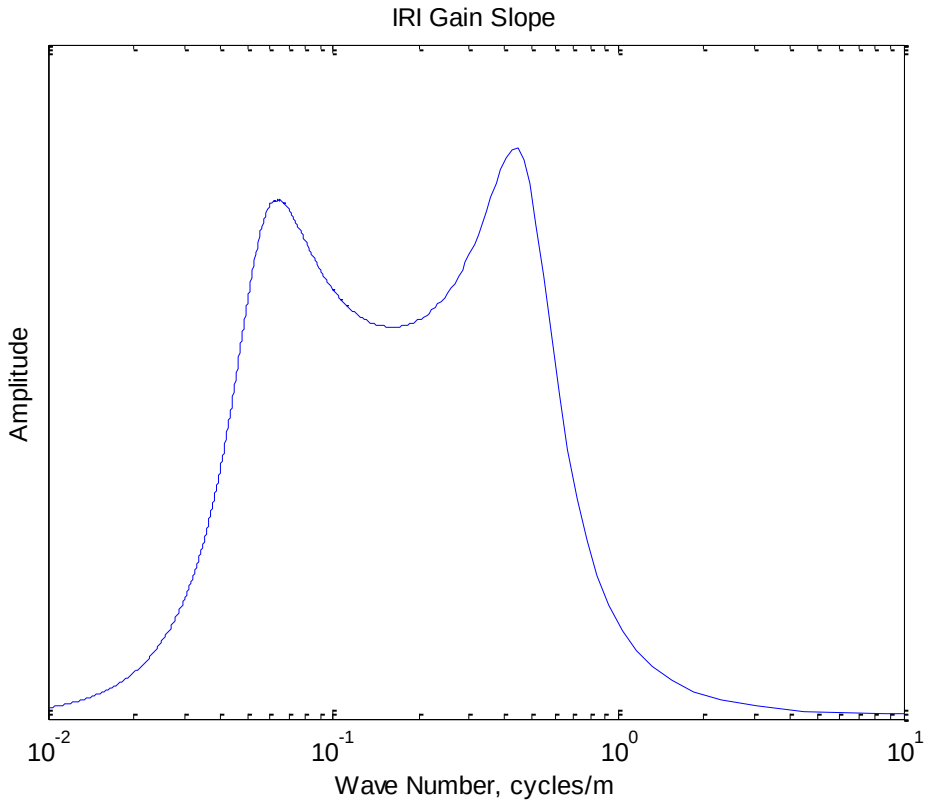

Figure 2.13: IRI Sensitivity to a Range of Wavelengths

2.2.2.2 Calculation of the International Roughness Index

To calculate the IRI of a longitudinal profile, two filters are applied; a moving average and a quarter car filter. As seen in Figure 2.5, when a tire makes contact with the road, the tire covers an area rather than a single point. This area is known as the contact patch and is taken into consideration when performing vehicle simulation. During simulation, the road is typically viewed as an input to the system as a series of points. Using point inputs may over-emphasis small dips and bumps in the road that might not affect the tire or the output of the system. To account for the contact patch and its interaction with the road profile, a moving average is used on the profile data. This moving average as seen in Equation 2.7 (Sayers, et al., 1998) acts as a low pass filter to the road profile data.

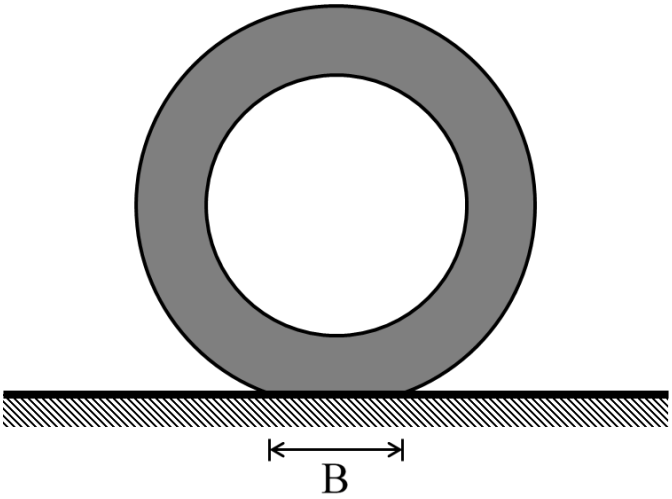

Figure 2.14: Tire Contact Patch

$$p_{fL}(i) = \frac{1}{N} \sum_{j=i+\frac{B}{2\Delta X}}^{i+\frac{B}{2\Delta X}} p(j) \qquad \textbf{(2.7)}$$

In this equation, the original road profile, p, sampled with a ΔX interval is split into segments summed over the base length, B, and divided by the number of samples, N, included in the summation. The base length (contact patch length) is dependent on tire size and tire pressure, but is typically taken as a value of 250 mm for this smoothing process (Sayers, et al., 1996). The effect of this smoothing process on a sample longitudinal profile is shown in Figure 2.15.

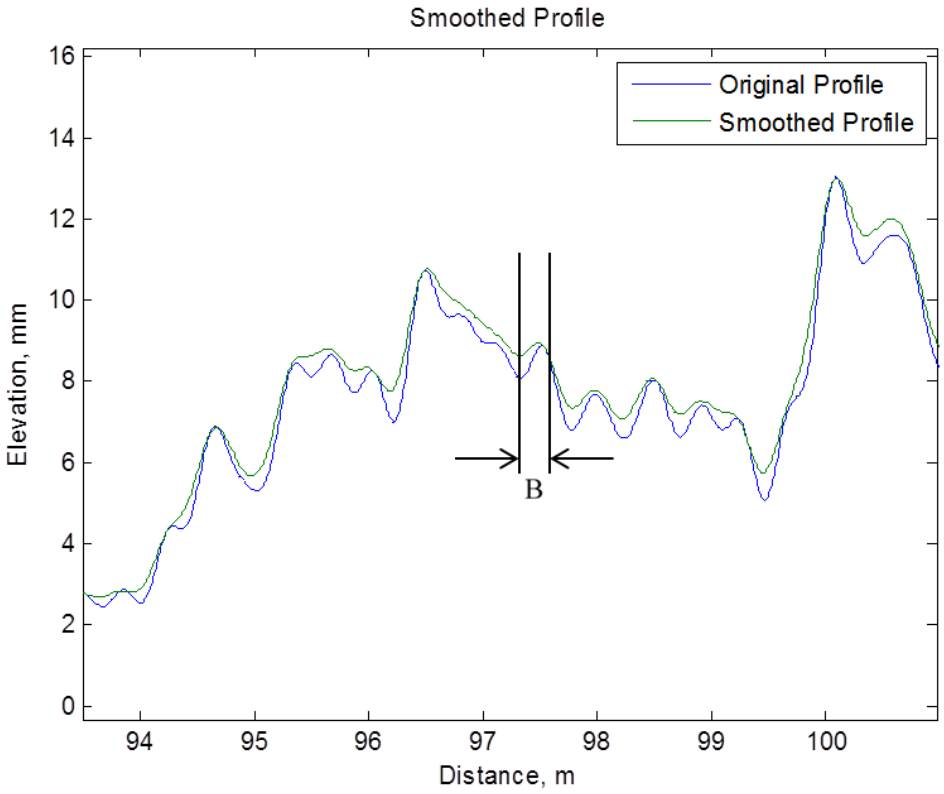

Figure 2.15: Smoothed Profile due to Contact Patch

The second filter applied to the profile in the calculation of the IRI is the quarter car filter. This consists of the simulation of an 80 k/hr quarter car model along the smoothed profile. The quarter car model uses the Golden Car parameters as previously discussed. This simulation is completed to calculate the vertical displacement response of the sprung and unsprung masses, typically calculated

through state space methods. The IRI represents the average rectified slope, which is the accumulated suspension motion divided by the distance traveled.

$$IRI = \frac{1}{n-k}\sum_{i=1}^{n-k}\left|s_{s,i} - s_{u,i}\right| \quad \textbf{(2.8)}$$

In this equation s_s and s_u are defined by the derivatives of the vertical displacement of the sprung and unsprung masses with respect to distance, providing units of m/km or inches/mile. These slopes are summed and divided by the total number of samples subtracted by the number of samples enveloped by the contact patch length, expressed as *n-k* in the equation.

2.2.2.3 IRI Scale

To give a sense for the meaning behind the values of the IRI, Figure 2.16 and Table 2.3 provide approximate ranges of roughness for defining certain road types (Sayers, et al., 1998). An airport runway will likely have an IRI of below 1.75 m/km to ensure smoothness for flight takeoff, while an IRI of 8.00 m/km or above would most likely be a rough unpaved road. Additional road quality descriptions relating to IRI can be found in Table 2.4. The aforementioned FHWA *Pavement Smoothness Initiative*, originally used 2.68 m/km (170 inches/mile) as a target IRI for highways when beginning in 2002. In 2006, the target performance goal was reduced to 1.50 m/km (95 inches/mile) in an effort to further improve the nation's highways (FHWA, 2014).

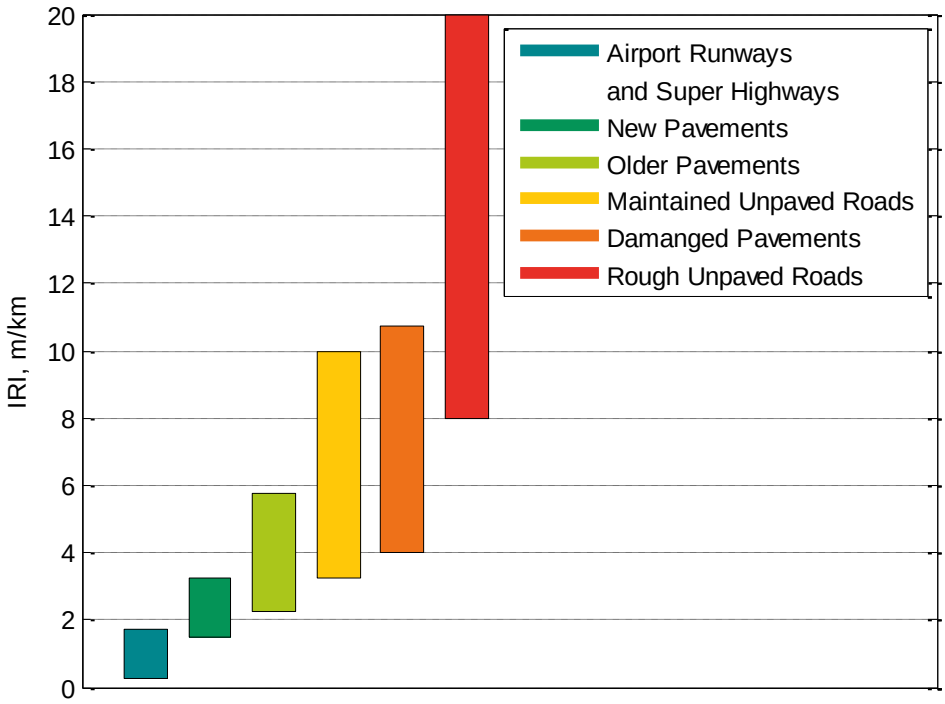

Figure 2.16: International Roughness Index for Roads Classes (Sayers, et al., 1998)

Table 2.3: Approximate IRI Road Class Ranges

International Roughness Index: Approximate Road Class Ranges	Lower Bound (m/km)	Upper Bound (m/km)
Airport Runways and Super Highways	0.25	1.75
New Pavements	1.50	3.25
Older Pavements	2.25	5.75
Maintained Unpaved Roads	3.25	10.00
Damaged Pavements	4.00	10.75
Rough Unpaved Roads	8.00	20.00

Table 2.4: Road Roughness Estimation Scale for Paved Roads (ASTM E1926 - 08, 2013)

IRI (m/km)	Road Quality Description
0	
1	Ride comfortable over 120 km/h. Undulation barely perceptible at 80 km/h in range 1.3 to 1.8. No depressions, potholes or corrugations are noticeable; depressions < 2mm/3m. Typical high quality asphalt 1.4 to 2.3, high quality surface treatment 2.0 to 3.0.
2	
3	Ride comfortable up to 100-120 km/h. At 80 km/h, moderately perceptible movements or large undulations may be felt. Defective surface; occasional depressions, patches or potholes (e.g. 5-15mm/3m or 10-20mm/5m with frequency 2-1 per 50m), or many shallow potholes (e.g. on surface treatment showing extensive raveling). Surface without defects; moderate corrugations or large undulations.
4	
5	Ride comfortable up to 70-90 km/h, strongly perceptible movements and swaying. Usually associated with defects; frequent moderate and uneven depressions or patches (e.g. 15-20mm/3m or 20-40mm/5m with frequency 5-3 per 50m), or occasional potholes (e.g. 3-1 per 50m). Surface without defects; strong undulations or corrugations.
6	
7	Ride comfortable up to 50-60 km/h, frequent sharp movements or swaying. Associated with severe defects; frequent deep and uneven depressions and patches (e.g. 20-40mm/3m or 40-80mm/5m with frequency 5-3 per 5m), or frequent potholes (e.g. 4-6 per 50m).
8	
9	Necessary to reduce velocity below 50 km/h. Many deep depressions, potholes and severe disintegration (e.g. 40-80mm deep with frequency 8-16 per 50m).
10	
11	
12	

2.3 Ride Comfort

Early studies of roads focused on road profiling, which was later extended to take the vehicle motion into account (Liu, et al., 1999). Traditional roughness measurement systems only provide information about the road profile quality, but lack a direct measure of ride comfort experienced by the vehicle occupants (Prem, et al., 2005). Profile roughness is only indirectly related to ride quality due to the wide range of vehicle models. Although the IRI provides a good understanding in regards to the roughness of the road, it is based on the response between the vibrations of the vehicle axle and body. This quantity is fundamentally different than ride vibrations felt by the passenger and cannot always indicate the ride quality.

Although other factors concerning comfort while driving exist, such as noise, small vehicle vibrations, and temperature, the focus of ride discomfort is produced by the vibration response of the vehicle suspension from the input of a road profile (Dahlberg, 1978). Ride comfort is therefore based on the vertical acceleration response cause by the excitation of the road profile. Vehicle simulation studies have shown the main factors of ride comfort controlled by vehicle dynamics are the suspension stiffness and damping, tire pressure, and speed of the moving vehicle (Gao, et al., 2011). The vibration response is filtered through the passenger's seat and weighted in the frequency range of human sensitivity. Whole-body vibration influences comfort, performance, and long-term health effects of the subject (Nahvi, et al., 2009). To understand the ride quality and comfort of the occupants of a vehicle, the dynamics of the entire vehicle and the limits of human tolerance to whole-body vibration must be recognized.

2.3.1 Effect of Vibration on the Human Body

The human body can be viewed as a linear passive mechanical system for small amplitude vibrations. Vibrations up to 12 Hz affect all of the human organs, while local effects occur at higher frequencies (Hostens, et al., 2003). For subjects exposed to vibrations in the vertical direction, resonance changes depending on body position. For a seated person, the first resonance occurs between 4 and 6 Hz, while for a standing person, resonance occurs at both 6 and 12 Hz (Piersol, et al., 2009). For a seated person, vibrations occurring at resonant frequency have effects on organs in the abdominal cavity and the lower spine. Muscle fatigue that may lead to back injury can occur just after one hour of seated vibration if vibrating at the resonant frequency of 4-6 Hz (Nahvi, et al., 2009). Larger vibration frequencies, such as 20-30 Hz and 60-Hz, affect the head and eyeball respectively.

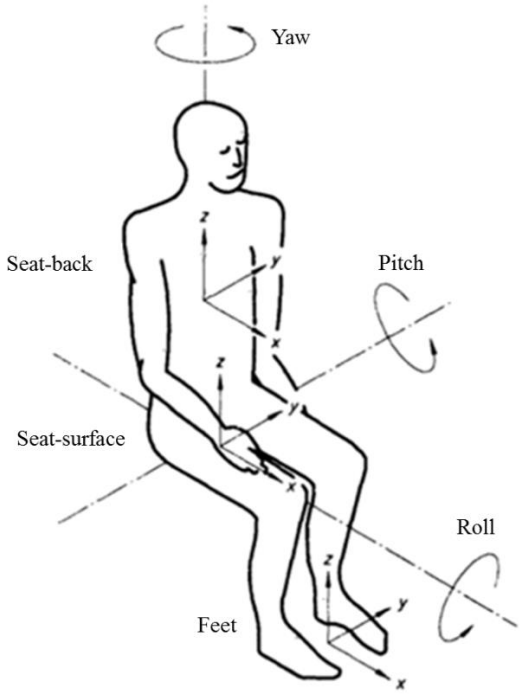

Figure 2.17: Axes for Vibration of Seated Person (ISO 2631-1, 1997)

2.3.2 Vibration Standards

Guidelines for human vibration can be found in International Standard ISO 2631: Evaluation of Human Exposure to Vibration and Shock – Evaluation of Human Exposure to Whole-Body Vibration. Additionally, the British Standard for vibration can be found in BS 6427: Guide to Evaluation of Human Exposure to Vibration in Buildings. Both standards contain very similar methods and philosophies concerning evaluation of vibration after the revision of ISO 2631 in 1997 (Griffin, 1998). These standards outline the transfer of vibration to the human response through frequency weightings and include methods for evaluating the effect of whole-body motions. The equations summarized in ISO 2631 will be used to quantify ride comfort through use of the recorded vertical acceleration data.

2.3.3 Forms of Discomfort

Due to the laws of physical systems, humans do not sense displacement and velocity if they are not changing (Liu, et al., 1999). Ride discomfort stems from sensitivity due to vertical acceleration and large sudden changes in acceleration, known as jerk. Jerk is defined as the rate of change in acceleration and expressed in meters per second cubed. Large magnitudes of acceleration can cause discomfort, but even on roads where vibration magnitudes are low, jerk can still be sensed due to bumps and potholes.

2.3.4 Quantifying Comfort

Although ride quality can be viewed as a perception of comfort, in many ways it can be quantified based on the reaction of the human body to specific frequency ranges. Vibration is evaluated through a weighted root mean square of the recorded acceleration. This acceleration value as seen in Equation 2.9 is weighted based on specified frequency domains which are dependent on position of the subject and direction of vibration (ISO 2631-1, 1997).

$$a_w = \left[\frac{1}{T}\int_0^T a_w^2(t)dt\right]^{1/2} \quad \textbf{(2.9)}$$

Typical ranges of this frequency weighted acceleration and its relations to comfort can be found in Table 2.5, where values of a_w less than 0.315 m/s^2 may be comfortable for a seated person, while an a_w value larger than 2.0 m/s^2 corresponds to extreme discomfort of the subject. Fifty percent of sitting or standing healthy people can detect frequency weighted accelerations in the range of 0.01 to 0.02 m/s^2 with a median of 0.015 m/s^2. This range considers the variation in the ability to perceive vibration between individuals.

Table 2.5: Comfort Based on Vibration Level

a_w (m/s^2)	Reaction
< 0.315	not uncomfortable
0.315 - 0.63	a little uncomfortable
0.5 - 1.0	fairly uncomfortable
0.8 - 1.6	uncomfortable
1.25 - 2.5	very uncomfortable
> 2.0	extremely uncomfortable

Due to shock and transient vibrations, another method of comfort evaluation that takes these short term accelerations into account is used. Known as the running root mean square acceleration method, presented in Equation 2.10, this method includes a time variable, τ, to represent the integration time for the running average. This time variable is recommended to be set as one second to only envelope the short duration response. The maximum absolute value of $a_w(t_0)$ is known as the *maximum transient vibration value* (Equation 2.11).

$$a_w(t_0) = \left[\frac{1}{\tau}\int_{(t_0-\tau)}^{t_0} a_w^2(t)dt\right]^{1/2} \quad \textbf{(2.10)}$$

$$\text{MTVV} = \max|a_w(t_0)| \quad \textbf{(2.11)}$$

Furthermore, the *vibration dose value*, defined in Equation 2.12, is similar to frequency weighted acceleration in terms of equation, but instead uses the fourth power, giving a value that is more sensitive to peaks in the weighted acceleration data. The units of VDV are calculated as $m/s^{1.75}$.

$$VDV = \left[\int_0^T [a_w(t)]^4 dt\right]^{1/4} \quad \textbf{(2.12)}$$

To determine which equation provides the best estimation of acceleration related to comfort, a *crest factor* is used. The crest factor is defined as the ratio of the maximum instantaneous peak value of the frequency weighted acceleration to its RMS value. For crest values below or equal to 9, the basic frequency weight acceleration value from Equation 2.9 is considered to be adequate. Furthermore, MTVV or VDV should be used in addition to the root mean square of the weighted acceleration if $\text{MTVV} > 1.5a_w$ or $\text{VDV} > 1.75a_wT^{1/4}$ (Piersol, et al., 2009).

2.3.4.1 Calculation of Frequency Weightings

Frequency weightings are provided in ISO 2631-1 for human vibrations in the 0.5 to 80 Hz range. Weighting functions relate the human sensitivity to vibration as a function of frequency and are weighted based on the sensitivity at given frequencies (Smith, et al., 1976). These weights act as low and high-pass filters to isolate the significant frequency range based on location and vibration axis. Table 2.6 provides a listing of all six different frequency weightings and their applicability to directional vibration effects on health and comfort (Piersol, et al., 2009). The principle weightings, W_k, W_d, and W_f, are used to assess the effects of vibration on health, comfort, and perception during whole body vibration. Weighting W_k is used for vibration in the z-direction, excluding the head, while W_d is the weighting for x and y directions of vibration. W_f is a frequency weighting included specifically for the assessment of motion sickness caused by low-frequency vibrations. Additional weightings, W_c, W_e, and W_j, are provided for special cases including seat-back vibrations, rotational body vibrations, and head motion of a reclining person, respectively. For the purpose of understanding ride comfort in a forward moving passenger car, W_k is used as the weighting function. Although seat-back vibration and vibrations in other directions exist, the vertical seat surface vibrations are dominant when compared to the others.

Table 2.6: Directions for Whole-Body Vibration Frequency Weightings

Frequency Weighting	Health	Comfort	Perception	Motion Sickness
$\mathbf{W_k}$	Z	Z-seat X, Y, Z-feet Z-standing X-lying	Z	
$\mathbf{W_d}$	X-seat Y-seat	X-seat Y-seat X, Y-standing Y, Z-lying Y, Z-back	X, Y	
$\mathbf{W_f}$				Z
$\mathbf{W_c}$	X-seat back	X-seat back		
$\mathbf{W_e}$		θ_x, θ_y, θ_z		
$\mathbf{W_j}$		X-lying (head)		

The frequency weightings are expressed mathematically by a combination of transfer functions that are made up of various frequencies, *f*, and resonance quality factors, *Q*. These values are given in Table 2.7 and Table 2.8. The overall transfer function includes a band limiting two-pole filter, an acceleration-velocity transition, and an upward step. Equations 2.13 and 2.14 make up the high and low pass filters with Butterworth characteristics. These filters reduce the amount of unwanted frequencies that lie outside the bounds of the effective frequency acceleration range for human comfort. Accelerations at low frequencies are transferred through Equation 2.15, while Equation 2.16 takes accelerations due to jerk into consideration. Combining these four functions through multiplication (Equation 2.17), a single transfer function for each of the different frequency weightings is provided. Plots of the weights in terms of frequency against amplitude can be seen in Figure 2.18 for principle weightings and Figure 2.19 for additional weightings.

Table 2.7: Principle Frequency Weighting Transfer Function Parameters (ISO 2631-1, 1997)

Weighting	Band-Limiting		Acceleration-Velocity Transition			Upward Step			
	f_1 (Hz)	f_2 (Hz)	f_3 (Hz)	f_4 (Hz)	Q_4	f_5 (Hz)	Q_5	f_6 (Hz)	Q_6
W_k	0.4	100	12.5	12.5	0.63	2.37	0.91	3.35	0.91
W_d	0.4	100	2.0	2.0	0.63	∞	—	∞	—
W_f	0.08	0.63	∞	0.25	0.86	0.0625	0.80	0.1	0.80

Table 2.8: Additional Frequency Weighting Transfer Function Parameters (ISO 2631-1, 1997)

Weighting	Band-Limiting		Acceleration-Velocity Transition			Upward Step			
	f_1 (Hz)	f_2 (Hz)	f_3 (Hz)	f_4 (Hz)	Q_4	f_5 (Hz)	Q_5	f_6 (Hz)	Q_6
W_c	0.4	100	8.0	8.0	0.63	∞	—	∞	—
W_e	0.4	100	1.0	1.0	0.63	∞	—	∞	—
W_j	0.4	100	∞	∞	—	3.75	0.91	5.32	0.91

$$|H_h(p)| = \left|\frac{1}{1+\sqrt{2}\omega_1/p+(\omega_1/p)^2}\right| = \sqrt{\frac{f^4}{f^4+f_1^4}} \tag{2.13}$$

$$|H_l(p)| = \left|\frac{1}{1+\sqrt{2}p/\omega_2+(p/\omega_2)^2}\right| = \sqrt{\frac{f_2^4}{f^4+f_2^4}} \tag{2.14}$$

$$|H_t(p)| = \left|\frac{1+p/\omega_3}{1+p/(Q_4\omega_4)+(p/\omega_4)^2}\right| = \sqrt{\frac{f^2+f_3^2}{f_3^2}}\cdot\sqrt{\frac{f_4^4\cdot Q_4^2}{f^4\cdot Q_4^2+f^2\cdot f_4^2(1-2Q_4^2)+f_4^4\cdot Q_4^2}} \tag{2.15}$$

$$|H_s(p)| = \left|\frac{1+p/(Q_5\omega_5)+(p/\omega_5)^2}{1+p/(Q_5\omega_6)+(p/\omega_6)^2}\cdot\left(\frac{\omega_5}{\omega_6}\right)^2\right| = \frac{Q_6}{Q_5}\sqrt{\frac{f^4\cdot Q_5^2+f^2\cdot f_5^2(1-2Q_5^2)+f_5^4\cdot Q_5^2}{f^4\cdot Q_5^2+f^2\cdot f_5^2(1-2Q_5^2)+f_6^4\cdot Q_6^2}} \tag{2.16}$$

$$H(p) = H_h(p)\cdot H_l(p)\cdot H_t(p)\cdot H_s(p) \tag{2.17}$$

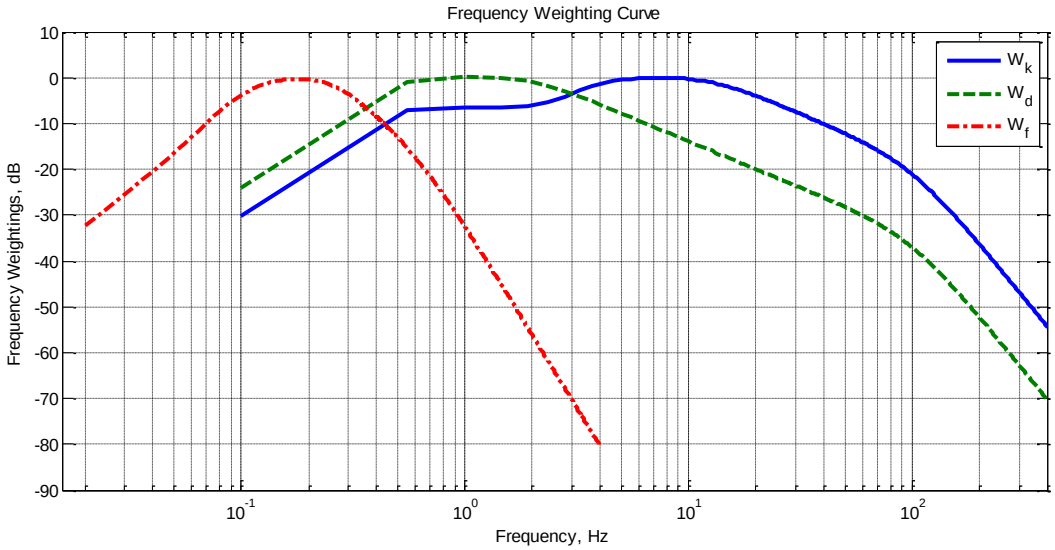

Figure 2.18: Frequency Weighting Curves for Principle Weightings

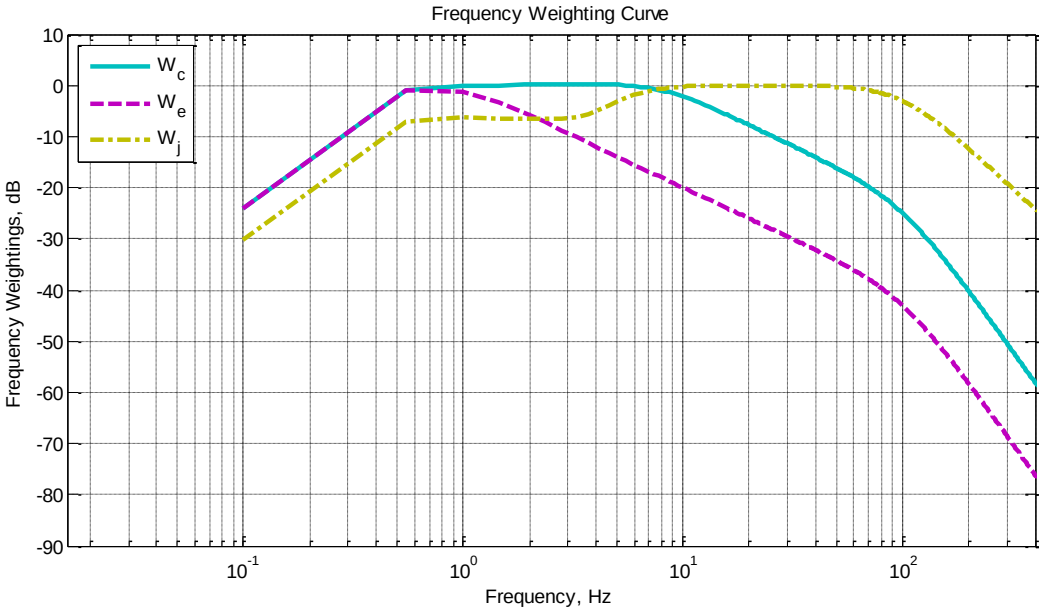

Figure 2.19: Frequency Weighting Curves for Additional Weightings

2.3.5 Human Tolerance Criteria

Vibration not only affects short term ride comfort, but can also pose possible long term health concerns. These concerns include possible risks affecting the lower spine and the connected nervous system for seated persons (ISO 2631-1, 1997). The effect of duration follows a power law relationship that assumes responses are related to equivalent energy given as

$$\phi^n t = \text{constant} \tag{2.18}$$

where t is the duration of exposure and n is index and is equal to either 2 or 4 depending on the study (Piersol, et al., 2009). Guidance for health concerns due to whole body vibrations are outlined in ISO2631-1 and shown in Figure 2.20.

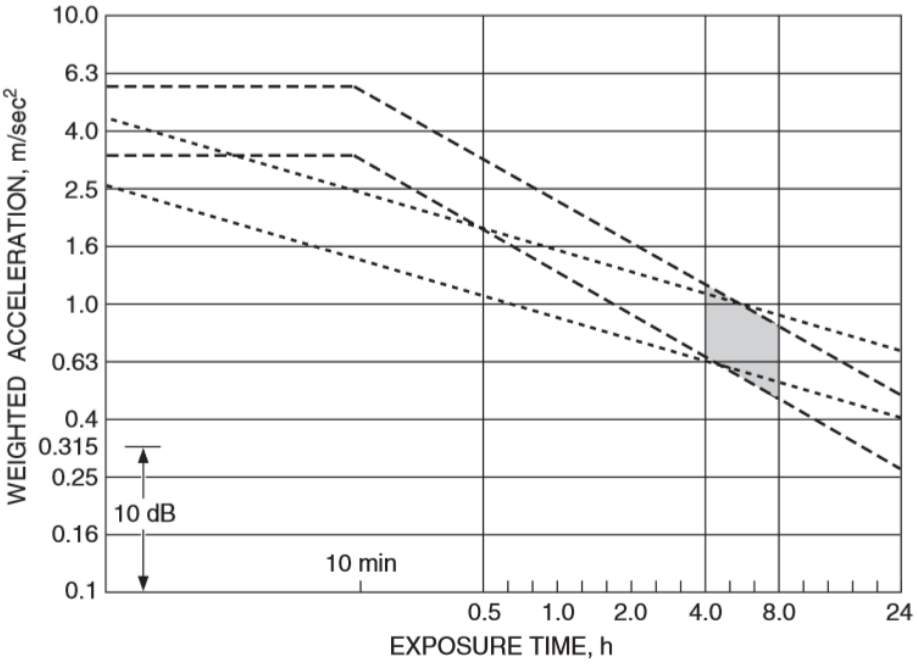

Figure 2.20: Health Guidance Caution Zone (Piersol, et al., 2009)

The upper and lower lines correspond to VDV values of 8.5 and 17 respectively. The dashed lines represent an index of $n = 2$, while the dotted lines represent $n = 4$. The shaded area existing between 4 and 8 hour daily exposure duration shows where there is an increase for potential health effects. Below this shaded area, health effects have not been observed, but are expected for exposure above the shaded zone.

Preventative measures are taken into consideration to avoid daily exposure to intense vibrations by reducing the amount of transmission of vibration from the vehicle by using a seat cushion. The seat cushion acts as an isolating spring to reduce the amount of vibration felt by the user. Aside from comfort, the goal of using the seat cushion is to isolate the frequencies felt between 2 and 5 Hz. This range is avoided because it envelopes the resonance of a seated person. Effectively, the seat cushion should have a natural frequency that is small when compared to the forcing frequency, such as 1 Hz (Piersol, et al., 2009).

Chapter 3: System Identification

Mathematical models are used to describe the dynamic behavior of a system as a function of time. These models can be used for simulation when a real system is shown to be either too expensive or complicated to test. Creating an exact model is not always necessary as it may be more useful to create a system that shows potential application rather than creating a complex design at the start. Although there is a trade-off for complexity and accuracy, using simplified models has been proven to be very useful in demonstrating the overall performance of the system (Van Overschee, et al., 1996).

A key step in creating the initial model involves the use of system identification techniques, including stochastic methods used in prediction error. Although different than physical models, as they may provide no physical meaning, system identification models are easily attainable and diverse enough to create systems comparable to the physical models. State-space models provide a useful and simple way of relating a mathematical model to a physical model though a system defined by its equations of motion. By creating a state-space model, the input and output of a system have a mathematical relationship with physical meaning that relates to the real model parameters. Depending on the structure, these models can include physical parameters, such as mass, damping, and stiffness that are to be identified using experimental dynamic data (De Angelis, et al., 2002).

3.1 State-Space Introduction

A state-space model is used to relate the input and output of a physical system by using a mathematical model to rewrite second order differential equations as two first order matrix equations. This simplified state-space form can be seen in Equations 3.1 and 3.2.

$$\dot{x} = Ax + Bu \tag{3.1}$$

$$y = Cx + Du \tag{3.2}$$

In this form, the physical model is represented in matrix form as the state matrix, *A*. The transfer of the input into the system is described in matrix *B*. State vector, *x*, describes the location of the input to the system, while input vector, *u*, contains the actual input data. The second state-space equation describes the output of the system, where *y* is the output vector, and *C* is the output matrix constructed based on the desired output of the system.

For the case of a moving vehicle, state vector, *x*, represents the displacement and velocity of the sprung and unsprung masses of the vehicle. The input vector is the elevation of the road profile in which the vehicle is traveling. The output vector provides the displacement, velocity, or acceleration of the vehicle masses depending on the configuration of the output matrix.

State-space is used because it provides a method in which the physical parameters can be extracted directly from the matrices based on the dynamic system properties. The state-space matrices can be determined from the input/output data using system

identification methods. These methods provide a means of obtaining a state-space model by fitting it to the given input/output data. This method is purely mathematic, which is why it must work in conjunction with the equations of motions obtained from the physical properties of the system.

3.2 Parameter Identification Techniques

Parameter identification begins with the representation of the second order differential equations of motion of the dynamic system in state-space form. The state-spaces equations described in Equations 3.1 and 3.2 characterize the system in continuous-time, which can be evaluated at any instance in time. Because experimental data is discrete in nature due to sampling, the continuous-time state-space model must be represented in a discrete-time form for analysis (Ren, et al., 2004):

$$x_{k+1} = Ax_k + Bu_k \tag{3.3}$$

$$y_k = Cx_k + Du_k \tag{3.4}$$

Process noise and measurement noise is also considered when describing the system due to uncertainties in the model. Process noise, w_k, is caused by disturbances and model inaccuracies, while measurement noise, v_k, is due to sensor inaccuracies (Ren, et al., 2004). If these stochastic components are considered, the state-space model becomes:

$$x_{k+1} = Ax_k + Bu_k + w_k \tag{3.5}$$

$$y_k = Cx_k + Du_k + v_k \tag{3.6}$$

Due to the difficulty of precisely determining the process and measurement noise characteristics, it is assumed they are each zero mean, stationary, white noise vector sequences (Van Overschee, et al., 1996). As shown in Equation 3.7, the two noise terms are assumed to be statically independent of each other.

$$E\left[\begin{pmatrix} w_p \\ v_p \end{pmatrix}\begin{pmatrix} w_q^T & v_q^T \end{pmatrix}\right] = \begin{pmatrix} Q & S \\ S^T & R \end{pmatrix}\delta_{pq} \tag{3.7}$$

In this next section of the study, various algorithms that use this state-space form are examined to determine the proper system identification techniques best suited for vehicle parameter identification.

3.2.1 ERA

Through the use of an impulse force, the Eigensystem Realization Algorithm (ERA) excludes the input and feedthrough matrices in the state-space model for modal identification. The Natural Excitation technique is used with ERA to simulate this impulse response due to excitation from a white noise input load (Chang, et al., 2012). This method has been found to be accurate, but requires impulse for free response data under noiseless conditions (Petsounis, et al., 2001). Additional steps and data may need to be taken to account for the distortion due to noise.

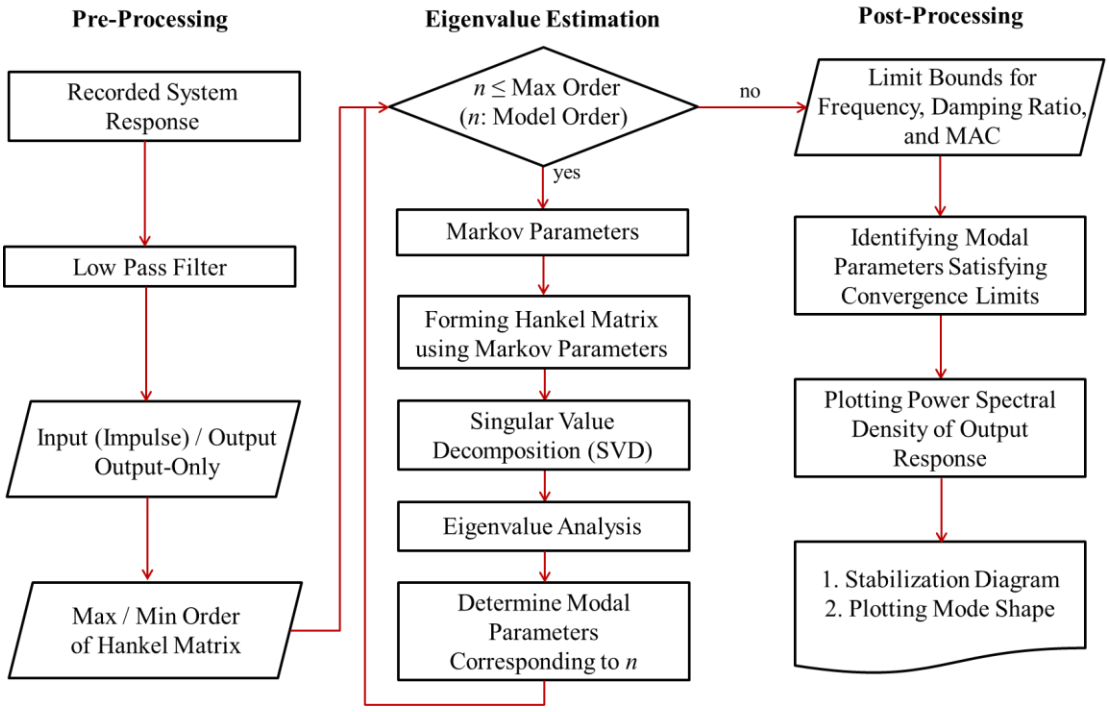

Figure 3.1: ERA Process (Chang, et al., 2012)

3.2.2 N4SID

Numerical algorithms for subspace state space system identification, known as N4SID, compare projections of future output against recorded output data (Van Overschee, et al., 1993). The predicted state-space model is found once the projection of the future output and recorded output has been minimized. This process of parameter identification through eigenvalue estimation is shown in in Figure 3.2 (Chang, et al., 2012).

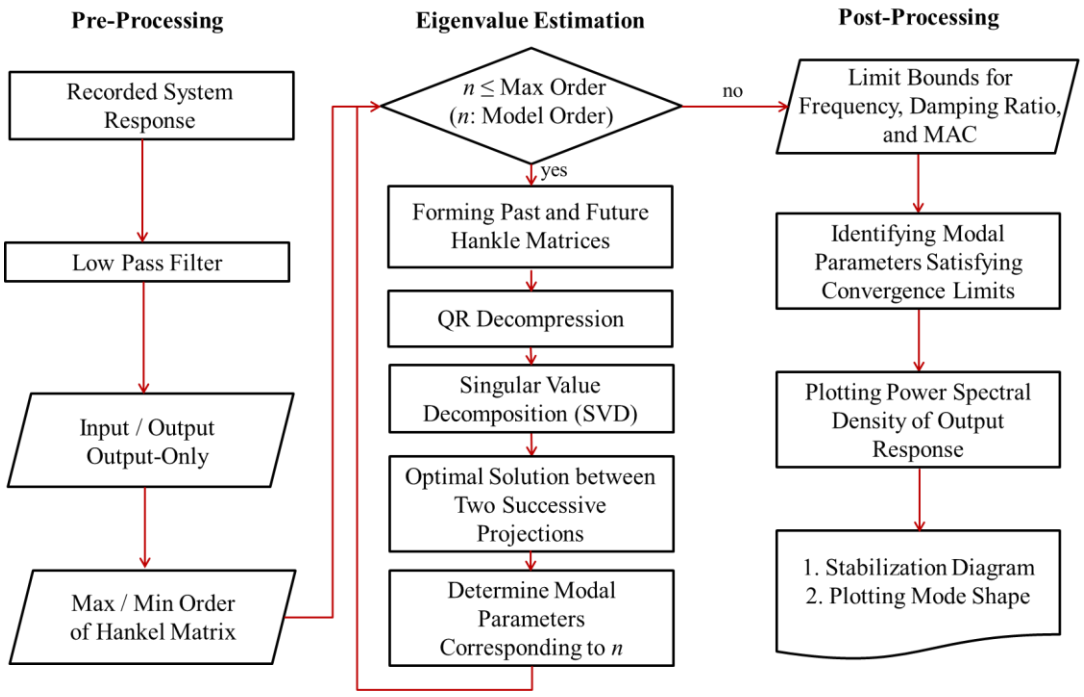

Figure 3.2: N4SID Process (Chang, et al., 2012)

3.2.3 ARMAX (ARX /AR)

Other popular linear models include the AutoRegressive Moving Average (ARMA) model and AutoRegressive Moving Average with eXogenous excitation (ARMAX) model. These methods use past values in the time series to predict future behavior of the response. Described respectively, in Equations 3.8 and 3.9 (Li, et al., 2006), these models express the output in terms of the current input in addition to the previous step of input/output (Chang, et al., 2012).

$$y_k = \sum_{i=1}^{p} \alpha_i y_{k-i} + \sum_{i=0}^{q} \beta_i u_{k-i} + \sum_{i=0}^{r} \gamma_i e_{k-i} \quad \textbf{(3.8)}$$

$$y_k = \sum_{i=1}^{p} \alpha_i y_{k-i} + \sum_{i=0}^{r} \gamma_i e_{k-i} \quad \textbf{(3.9)}$$

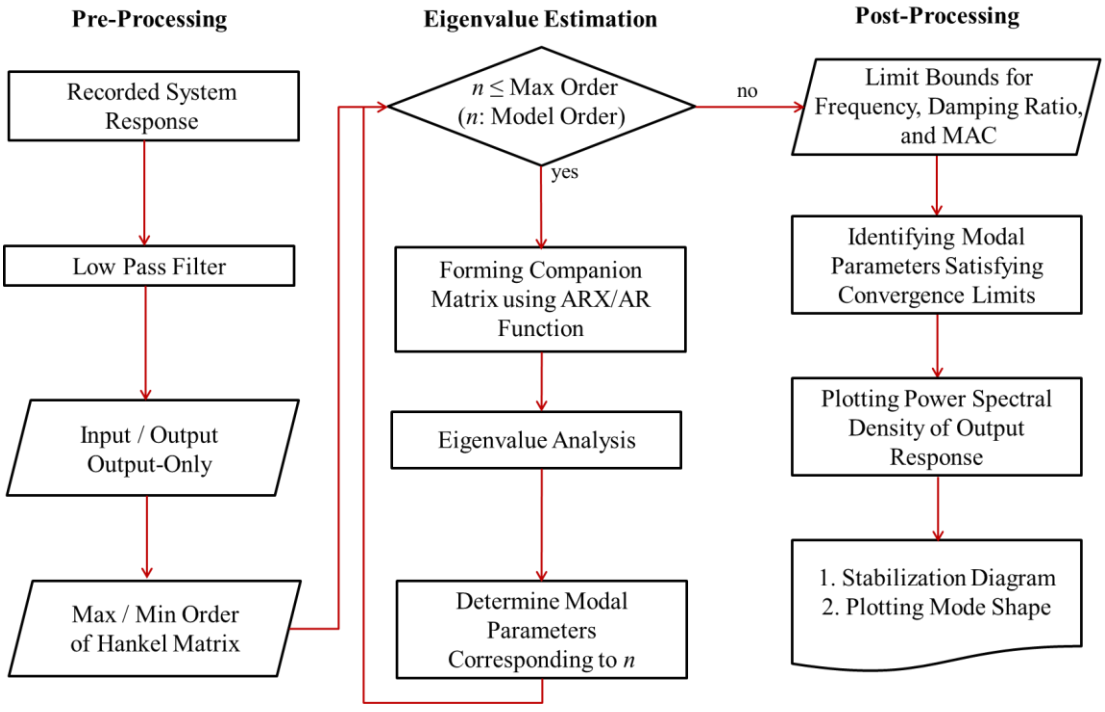

Figure 3.3: ARX/AR Process (Chang, et al., 2012)

3.2.4 PEM

The previously mentioned algorithms are useful for identification of first order system parameters, such as natural frequencies, damping ratios, and modes of the structure. Additional methods are needed for further prediction of second order parameters consisting of system mass, stiffness, and damping. Known as the *prediction-error identification method* (PEM), this method provides the additional steps necessary for parameter estimation (Ljung, 1987). The prediction error method begins by describing the model as a predictor of future output based on past data (Ljung, 2002):

$$\hat{y}_m(t|t-1) = f(Z^{t-1}) \tag{3.10}$$

The left-hand side of Equation 3.10 represents the predicted output, while f is an arbitrary function of past data and Z^n is the observed data. This predictor can be parameterized as shown in Equation 3.11.

$$\hat{y}(t|\theta) = f(Z^{t-1}, \theta) \tag{3.11}$$

Here, θ, represents a finite-dimensional parameter vector. Through the minimization of distance between the predicted output, $\hat{y}(t|\theta),\ldots,\hat{y}(N|\theta)$, and measured output, $y(1),\ldots,y(N)$, a suitable estimate of the parameter vector can be made. This estimation is completed through the following minimization technique:

$$\hat{\theta}_N = \arg\min V_N(\theta) \tag{3.12}$$

$$V_N(\theta) = \sum_{t=1}^{N} l\big(y(t) - f(Z^{t-1}, \theta)\big) \tag{3.13}$$

where l is chosen based on an acceptable distance limit, $l(\varepsilon) = \|\varepsilon\|^2$.

The state-space model with known and unknown physical parameters can be written as:

$$\dot{x}(t) = A(\theta)x(t) + B(\theta)u(t) \quad \textbf{(3.14)}$$

$$y(t) = Cx(t) + Du \quad \textbf{(3.15)}$$

Here it can be seen that the state and input matrices are both functions of the unknown parameters.

Several types of methods can be used to form the system when either no model data or partial data is available. If a system cannot be modeled, whether the construction is unknown or the physical interactions are too complicated, a standard model can be used. This standard model is capable of handling a range of various system dynamic problems (Ljung, 2002). This method is known as black-box modeling and involves the use of the ARMAX model. This technique creates a model based on the input/output or output-only measured response of the system. For the case of a known system with partially unknown parameters, grey-box modeling can be used. When available, the use of the grey-box model is advantageous as more information is available for the use of PEM.

3.3 Output-Only Parameter Identification

Within a laboratory setting, excitation can be applied to a structure through means such as impact loading, forced vibration, or applying vibration via shake table. These controlled experiments all have known applied forces which can be used to help identify the unknown parameters of the system when combined with the response. Unlike testing in the laboratory, controlled tests of real world structures through applied forces can either be impractical or costly. In cases such as this, output-only identification techniques are required to determine the unknown parameters of the system (Peeters, et al., 1999).

In the case of output-only identification, the input term of the state-space model, u_k, is not known. For ambient vibration testing, it becomes impossible to distinguish this input term from noise terms w_k and v_k (Li, et al., 2006). By modeling the input term as noise terms, the system becomes purely stochastic:

$$x_{k+1} = Ax_k + w_k \tag{3.16}$$

$$y_k = Cx_k + v_k \tag{3.17}$$

While the input is now described by the noise terms, the white noise assumptions cannot be omitted. If the input of the system contains dominant frequency components combined with the white noise, these components cannot be separated from the eigenfrequencies of the system (Ren, et al., 2004). Violation of this white noise assumption largely affects the poles of the state matrix, *A*. The goal of this form of output-only analysis is to determine the mathematical

description of the structure as represented by the state matrix. Once the state matrix is predicted, the modal parameters, including natural frequencies, damping ratios, and mode shapes can be calculated through eigenvalue decomposition.

Output-only identification methods have been used on civil structures for parameter estimation involving structural health monitoring. Due to the inability to apply specific loading for excitation of in-use civil structures, the natural ambient vibrations provided by wind, traffic, and human activity are examined (Ren, et al., 2004). Stochastic subspace identification methods involving these natural vibrations have been used to determine the modal parameters of bridges for post-earthquake structural integrity investigations (Londono, et al., 2004). Furthermore, these methods have been used for structural damage detection involving the prediction of strength and stiffness deterioration (Nagarajaiah, et al., 2009).

3.4 Vehicle Parameter Studies

Recent studies have been completed for vehicle mass estimation using various system identification methods. Research on recursive least squares for off-road vehicles has shown its effectiveness in sprung mass estimation involving the use of acceleration signals from both the sprung and unsprung masses (Pence, et al., 2009). The added measurement of the unsprung mass response creates a technique in which the estimation of the ground input can be avoided. A further study shows that regression methods, such as recursive least squares and recursive total least squares, are not suitable for the output-only estimation of the sprung mass because of their sensitivity to tuning parameters (Pence, et al., 2011). Another study includes the use of multiple accelerometers on heavy duty vehicles for measurement of the longitudinal response. Recursive least squares with multiple forgetting factors is used for the simultaneous estimation of vehicle mass and road grade (Vahidi, et al., 2005).

3.5 Summary of System Identification Algorithms

This chapter presents various algorithms currently used for identification of input/output and output-only systems. This review shows that methods such as ERA, N4SID, and ARMAX are capable of solving first order parameters, such as natural frequencies, damping ratios, and modes of a system. However, these methods are purely based on mathematical models and lack any physical meaning necessary to describe the second order parameters, including mass, stiffness, and damping. For the case of a typical passenger vehicle, which includes known physical component interactions, the system can be represented in state-space form for the use of grey-box modeling with PEM for estimation of the unknown parameters.

Chapter 4: Numerical Simulation

4.1 Simulation Overview

Computer modeling is performed for a full understanding of the requirements for system identification of the vehicle parameters. Modeling includes road profile generation and vehicle simulation. Simulation of a traveling vehicle is accomplished through the use of state-space analysis. State-space representation of the vehicle creates a method in which the response of the vehicle can be determined by providing an input to the system. In this case, the input is the elevation of the generated road profile. State-space representation is also useful for grey-box model estimation for parameter identification of the vehicle used in system identification algorithms.

The simulated vehicle is excited through input of generated road profiles that include various bumps. Analysis is performed to determine how much excitation is needed to provide a response sufficient enough for system identification. Once the vehicle parameters are determined, an index can be created, which relates the roughness of the road to the vertical vehicle acceleration.

4.2 Road Profile Simulation

Comprehension of the dynamic response of a vehicle driven over a road begins with an understanding of the input, which in this case is the road profile. Through the use of inertial profilers to determine profile elevation, studies have found that typical road surfaces are made up of random excitation with a Gaussian distribution (Dodds, et al., 1973). Furthermore, statistical research performed concerning road profiles has determined that profiles can be viewed as a summation of a series of sinusoids (Sayers, et al., 1996). Figure 4.1 shows a series of sinusoids with random wavelengths, amplitudes, and phases. Although in reality road profiles do not contain identifiable sinusoids, a good approximation can be made by adding a series of sinusoids together to create a simulated profile, as observed in Figure 4.2.

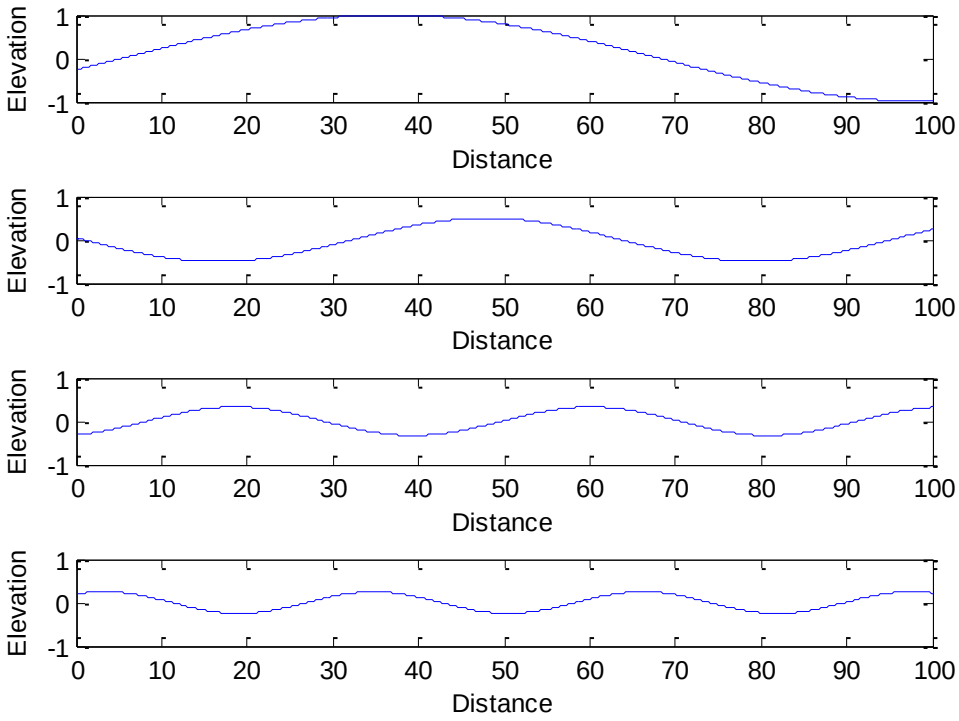

Figure 4.1: Series of Sinusoids with Varying Wavelengths, Amplitudes and Phases

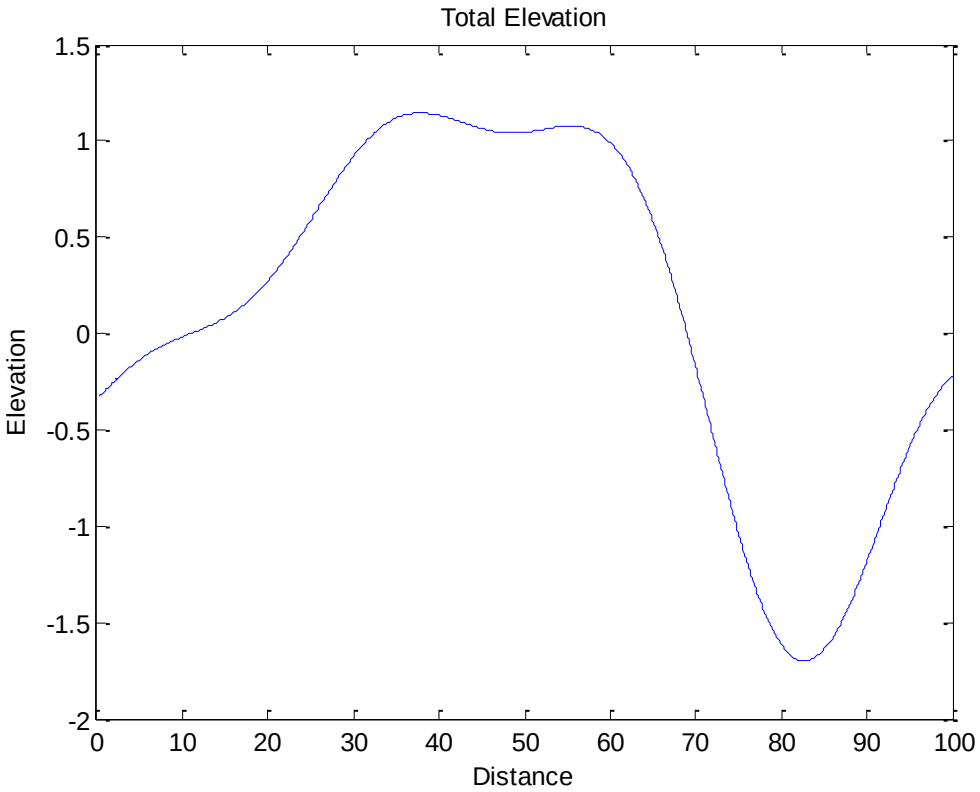

Figure 4.2: Example Profile Consisting of a Summation of Random Sinusoids

4.2.1 Generated Road Profile

Generating road profile elevations in the time domain follows the notion of a combination of a series of harmonics related to the power spectral density interpretation of profiles presented in Equation 2.1. This summation of harmonics is expressed in Equation 4.1 as a function of distance (Da Silva, 2004).

$$r(x) = \sum_{i=1}^{N} A_i cos(n_i x - \varphi_i) \quad \textbf{(4.1)}$$

Variation of spatial frequency and phase angle is defined by n and φ, respectively. Spatial frequency, n, ranges from 0.011 to 2.83 cycles/m, which corresponds to the frequency range defined in ISO 8608 for classification of road profiles (Johannesson, et al., 2012). These frequencies are linearly distributed between this range for *N* interpolations. The range of spatial frequency can also be shown as $n_i = n_{\min} + \Delta n(i-1)$ where the increment is calculated as $\Delta n = (n_{\max} - n_{\min})/N$ (Da Silva, 2004). The phase angle in Equation 4.1 is randomly normally distributed over the range of 0 and 2π. As shown in Equation 4.2, the amplitude of the harmonic is proportional to the roughness of the power spectral density function, $G_d(n_i)$.

$$A_i = \sqrt{2\Delta n G_d(n_i)} \quad \textbf{(4.2)}$$

For a profile consisting of *N* harmonics, a mathematical approximation can be made consisting of *N*/2 sinusoids (Sayers, et al., 1996). In addition to this generated profile, if large local irregularities such as bumps and potholes exist, they must be added separately because the roughness of the PSD function does not take them into account (Cebon, 2000).

4.2.2 Road Profile Verification

Road profile elevation is typically expressed in terms of millimeters over a distance of meters. The choice of units can make the profile elevation appear to be greatly exaggerated as the unit of elevation is three orders of magnitude smaller than the units of distance. Two example profiles, generated using Equation 4.1 are shown below. Figure 4.3 shows a road profile consisting of "very good" pavement quality with a degree of roughness value, $G_d(n_0)$, equal to 16 cm^3. Figure 4.4 shows a generated profile with a degree of roughness of 256 cm^3, categorizing the profile as a road of "poor" quality, according to ISO 8606.

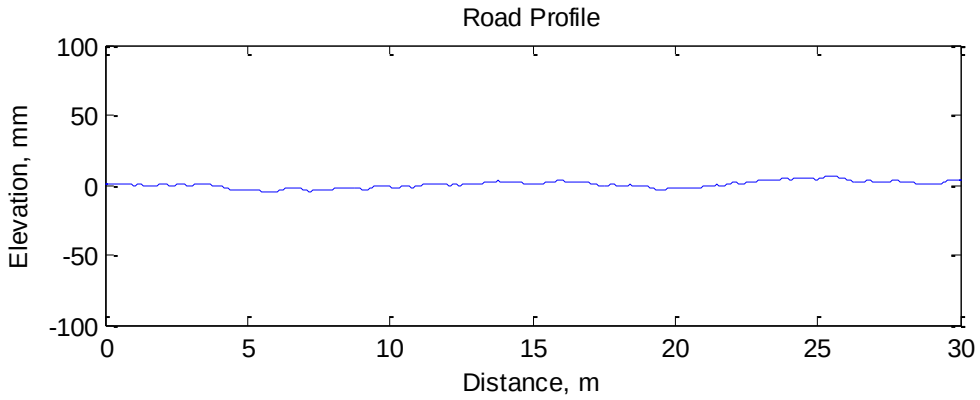

Figure 4.3: Road Profile - Very Good Pavement Quality

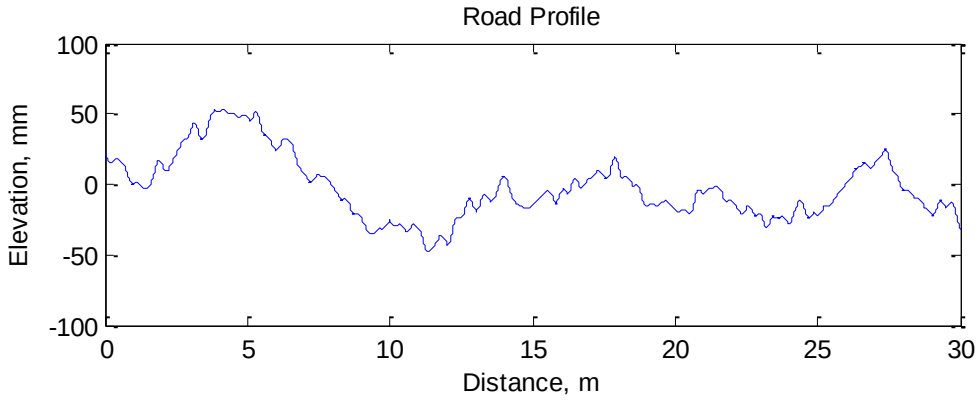

Figure 4.4: Road Profile - Poor Pavement Quality

These generated profiles are verified by calculating the root mean square of the profile elevations and comparing them to previous road profile studies. A plot of the range of elevation based on degrees of roughness ranging from 1 to 1024 cm^3 can be seen in Figure 4.5.

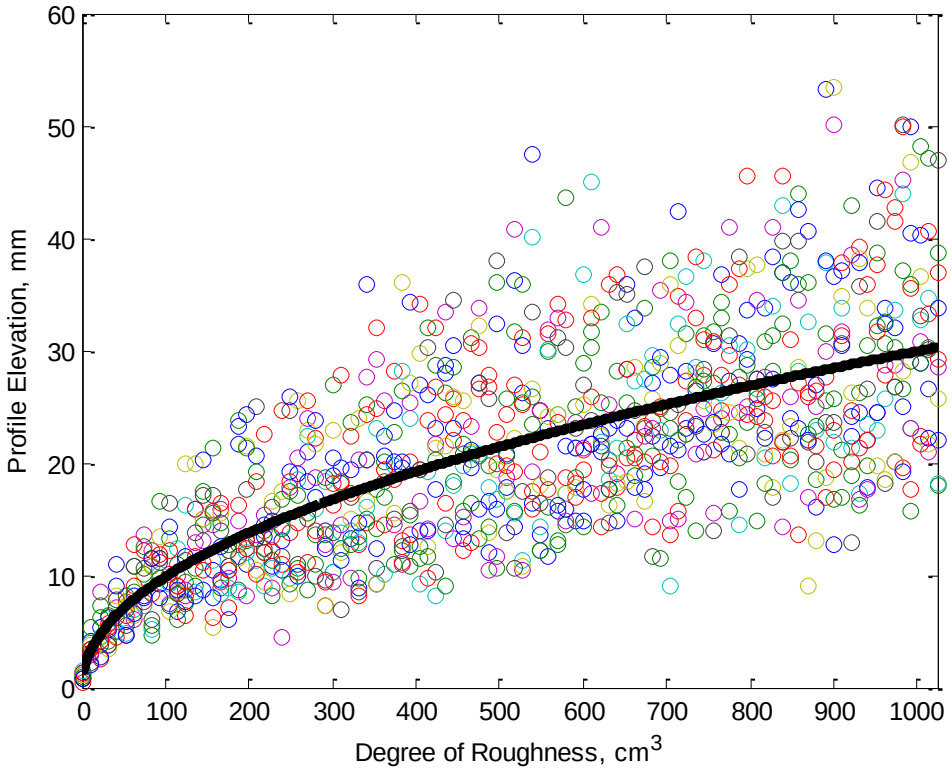

Figure 4.5: Profile Elevation with Varying Degree of Roughness

Although there is a large standard deviation of elevation in the generated profiles, the mean of the samples show results similar to elevations found in previous work (Da Silva, 2004).

4.3 Vehicle Model

Two types of vehicle models are used in this study; a quarter car and a half car model. The quarter car model is used to calculate the IRI of simulated and recorded road elevation profiles as per FHWA standards, while the half car model is used to compare recorded acceleration response of the actual vehicle against the simulated vehicle. The decision to use the half car model stems from the need to include the road surface input of both the front and rear tires and the combined interaction they provide to the vehicle body. This interaction cannot be properly simulated through the use of a quarter car model. Although a full car model would provide the necessary response, it is not needed because these simulations focus on the roughness of the longitudinal profiles while small lateral effects can be neglected.

These models take the basic fundamentals of the vehicle system and break them into the necessary pieces that represent the dynamics of the vehicle in a mathematical model. The models are made up of masses, suspension stiffness, suspension damping, and tire stiffness. The contact patch where the tire surface meets the road is taken into account by using a 250 mm moving average low-pass filter.

4.3.1 Quarter Car Model

The quarter car model is a two degree-of-freedom linear system that is widely used by the automotive industry for predicting dynamic response, parameter identification, and system optimization of ground vehicles (Verros, et al., 2005). Although highly simplified, the quarter car model provides considerable insight into the dynamic response of a vehicle without over-complicating the analysis (Turkay, et al., 2005). The quarter car model represents one fourth of a typical four-tired vehicle as shown in Figure 4.6. The two masses used in the quarter car model consist of the sprung and unsprung masses. The sprung mass is the mass supported above the vehicle's suspension system, which is ¼ the mass of the body of the vehicle. The unsprung includes the mass of one of the wheels and the suspension system connected to it.

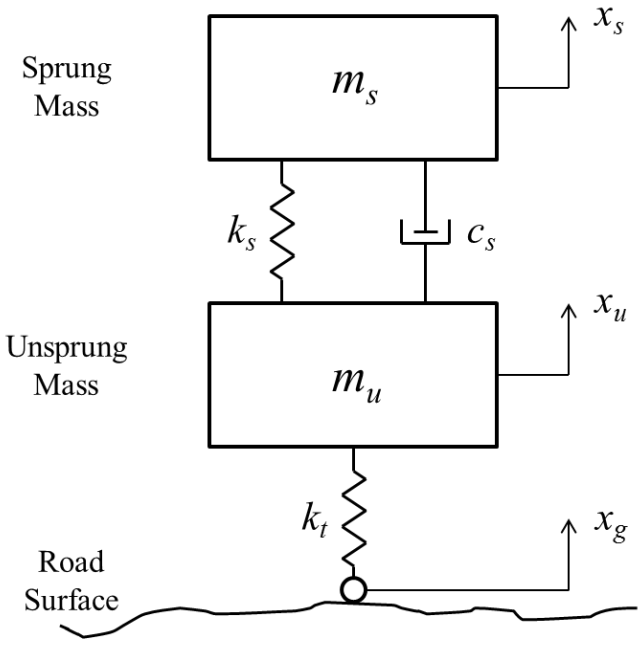

Figure 4.6: Quarter Car Model

The main suspension system is made up of a spring for stiffness and a viscous damping shock absorber. This suspension system supports the sprung mass of the vehicle, while the unsprung mass is in direct contact with the ground through the stiffness of the tire. The tires are sometimes modeled with a damping value in addition to stiffness. Due to the small value of tire damping compared to the damping of the suspension system, it can be neglected (Jazar, 2008). It is assumed that the tire is always in contact with the ground for the quarter car model. This assumption holds true at low frequency vibrations, while the tire may not stay in contact when exposed to high frequencies.

The quarter car model is limited in that it does not provide the geometric effects of longitudinal and lateral connections that are included in full and half car models. Although the quarter car model does not include these interactions, it still gives a good dynamic representation of the vehicle response due to road unevenness without over-complicating the system (Turkay, et al., 2005).

4.3.1.1 Diagram and Equations

The calculation of the IRI is based on the relative displacement of the sprung and unsprung masses of the quarter car model induced by the unevenness of the road profile. The goal of simulating this quarter car model is to calculate the displacements of the two masses based on an input displacement profile.

The equation of motion for the quarter car model is shown in Equation 4.3. This equation is set equal to zero due to the fact that the model will assume profile elevation as the input rather than an applied force.

$$M\ddot{x} + C\dot{x} + Kx = 0 \tag{4.3}$$

The two degrees of freedom in this model are the vertical displacements of the sprung and unsprung masses. The mass, damping, and stiffness matrices, as shown below, account for the vehicle mass and spring and damping coefficients that represent the suspension system and tire.

$$M = \begin{bmatrix} m_s & 0 \\ 0 & m_u \end{bmatrix} \qquad C = \begin{bmatrix} c_s & -c_s \\ -c_s & c_s \end{bmatrix} \qquad K = \begin{bmatrix} k_s & -k_s \\ -k_s & k_s + k_t \end{bmatrix}$$

These three matrices used in the equation of motion represent the entire quarter car model as a system that includes interactions between the degrees of freedom with the input profile.

Determining the displacement response of the quarter car model involves the conversion of the equation of motion into state-space form. State-space representation replaces nth order differential equations with first order matrix differential equations, given as a system of two equations. For the quarter car model, this system of equations is given in Equations 4.4 and 4.5.

$$\begin{bmatrix} \dot{x_s} \\ \dot{x_u} \\ \ddot{x_s} \\ \ddot{x_u} \end{bmatrix} = A \begin{bmatrix} x_s \\ x_u \\ \dot{x}_s \\ \dot{x}_u \end{bmatrix} + B[x_g] \tag{4.4}$$

$$\begin{bmatrix} x_s \\ x_u \end{bmatrix} = C \begin{bmatrix} x_s \\ x_u \\ \dot{x}_s \\ \dot{x}_u \end{bmatrix} + D[x_g] \tag{4.5}$$

Equation 4.4 is know as the state equation. This equation is made up of the state matrix, *A*, input matrix, *B*, the state vector $\begin{bmatrix} x_s \\ x_u \\ \dot{x}_s \\ \dot{x}_u \end{bmatrix}$, and input vector $[x_g]$. The state equation includes the first order derivative of the state vector on the left hand side. The output equation, Equation 4.5, includes the output matrix, *C*, and the feedthrough matrix, *D*. Output matrix, *C*, is formed to provide the desired kinematic quantity, whether it be displacement, velocity, or acceleration.

Formation of the state matrix, *A*, is determined by relating the system input and output through the system itself using equations of motion for each degree of freedom. The free body diagram for the sprung mass, seen in Figure 4.7, shows the connection of the vehicle body mass to the suspension system. The suspension stiffness, k_s, is multiplied by the difference in displacements between the sprung and unsprung masses, while the damping coefficient, c_s, is multiplied by the difference in velocity. The output is labeled as x_s, representing the displacement of the sprung mass relative to the ground.

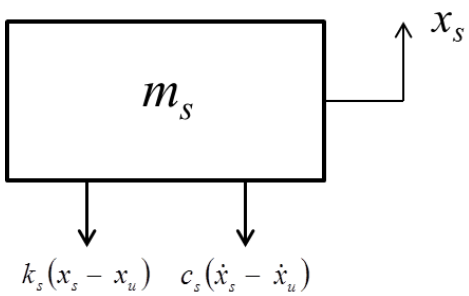

Figure 4.7: Quarter Car Model – Sprung Mass Free Body Diagram

Application of Newton's second law of motion and summation of each component leads to Equation 4.6.

$$m_s\ddot{x}_s + c_s(\dot{x}_s - \dot{x}_u) + k_s(x_s - x_u) = 0 \quad \textbf{(4.6)}$$

This equation is rearranged to isolate the acceleration of the mass on the left hand side to determine the components used in the state matrix:

$$\ddot{x}_s = -\frac{k_s}{m_s}x_s + \frac{k_s}{m_s}x_u - \frac{c_s}{m_s}\dot{x}_s + \frac{c_s}{m_s}\dot{x}_u \quad \textbf{(4.7)}$$

Similarly, a free body diagram is presented for the unsprung mass. The unsprung mass, which represents the mass of the suspension system and tire, provides the necessary connections to relate the vehicle body to the road itself. The displacement elevation of the road is denoted on the diagram as x_g.

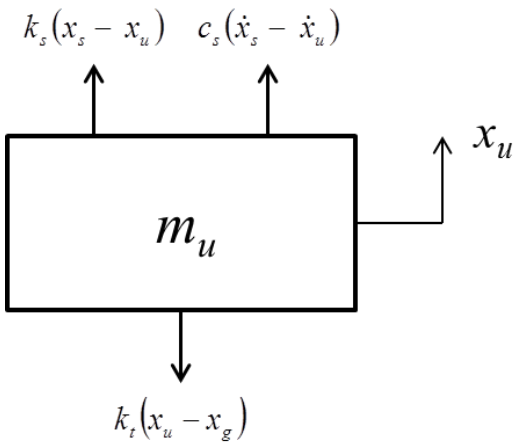

Figure 4.8: Quarter Car Model – Unsprung Mass Free Body Diagram

$$m_u\ddot{x}_u - c_s(\dot{x}_s - \dot{x}_u) - k_s(x_s - x_u) + k_t(x_u - x_g) = 0 \qquad \textbf{(4.8)}$$

Again, the acceleration of the mass is isolated on the left hand side to develop the state matrix. Unlike the equation of motion for the sprung mass, Equation 4.9 has an additional term for the inclusion of the profile input, x_g. The coefficient multiplied by this input, $\frac{k_t}{m_u}$, is used in the construction of the input matrix.

$$\ddot{x}_u = \frac{k_s}{m_u}x_s - \frac{(k_s + k_t)}{m_u}x_u + \frac{c_s}{m_u}\dot{x}_s - \frac{c_s}{m_u}\dot{x}_u + \frac{k_t}{m_u}x_g \qquad \textbf{(4.9)}$$

The state and input matrices are developed by transforming Equations 4.7 and 4.9 into matrix form. Arrangement of the coefficients found in these two equations leads to space matrix, *A*, and input matrix, *B*. In the case of the quarter car model, the input matrix is a vector because the system has only a single input.

$$A = \begin{bmatrix} 0 & 0 & 1 & 0 \\ 0 & 0 & 0 & 1 \\ -\frac{k_s}{m_s} & \frac{k_s}{m_s} & -\frac{c_s}{m_s} & \frac{c_s}{m_s} \\ \frac{k_s}{m_u} & -\frac{(k_s + k_t)}{m_u} & \frac{c_s}{m_u} & -\frac{c_s}{m_u} \end{bmatrix} \qquad B = \begin{bmatrix} 0 \\ 0 \\ 0 \\ \frac{k_t}{m_u} \end{bmatrix}$$

Output matrix, *C*, is constructed based on the desired output. For the case of this quarter car model, the desired output is displacement for both the sprung and unsprung masses. The output matrix seen below is selected to relate the state vector, $\begin{bmatrix} x_s \\ x_u \\ \dot{x}_s \\ \dot{x}_u \end{bmatrix}$, to an output of $\begin{bmatrix} x_s \\ x_u \end{bmatrix}$, through multiplication as seen in the second state-space equation for the quarter car model, Equation 4.5. For the case of relative displacement of the system, the feedthrough constant, *D*, is equal to 0.

$$C = \begin{bmatrix} 1 & 0 & 0 & 0 \\ 0 & 1 & 0 & 0 \end{bmatrix} \qquad D = 0$$

State-space matrices, *A*, *B*, *C*, and *D*, make up the state-space model used to simulate the time response of the dynamic system.

4.3.2 Half Car Model

A half car model is used for a more accurate assessment of relating the acceleration response of the vehicle to the elevation of the road profile. This two-axle vehicle, shown in Figure 4.9, is modeled as a four degree-of-freedom system. Unlike the quarter car model, the half car model includes both the front and rear suspension systems, which interact through the connection and rotation of the vehicle body. The degrees of freedom include the vertical motions of the front and rear suspension systems, and the vertical motion and rotation of the vehicle body itself. The assumption of small rotation of the vehicle body is made to retain vertical movement of the end points (Wakeham, et al., 2011). This assumption maintains the linearity of the model.

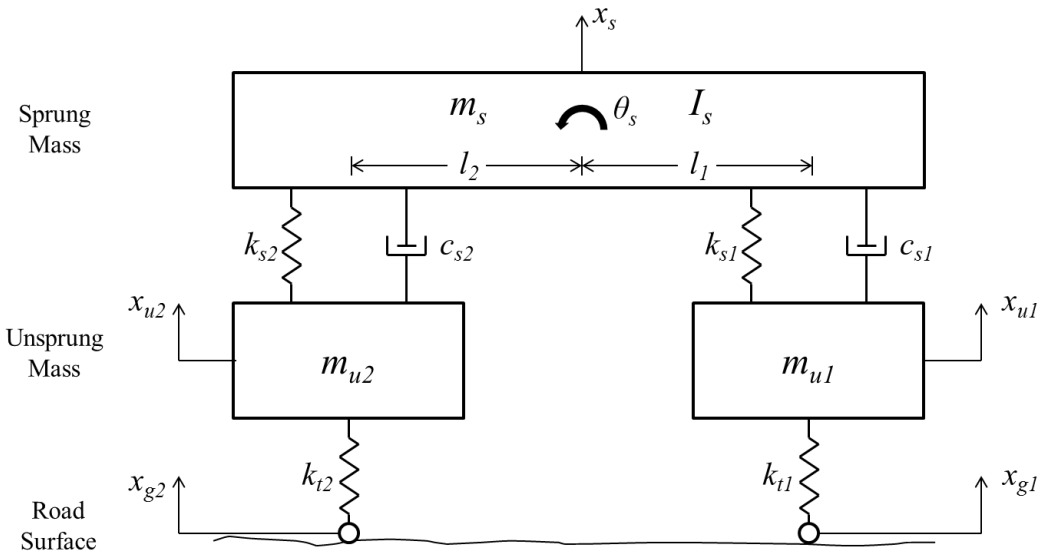

Figure 4.9: Half Car Model

For the half car model, road uneveness is input into the system at both the front and rear tires, represented as x_{g1} and x_{g2} in Figure 4.9. The input of road elevation to the front and rear tires is separated by a time delay:

$$x_{g2}(t) = x_{g1}(t - \tau) \tag{4.10}$$

This time delay, τ, is a function of the distance between the front and rear tires and the vehicle forward moving velocity:

$$\tau = \frac{(l_1 + l_2)}{v} \tag{4.11}$$

A visualization of the road elevation input for the half car model is shown in Figure 4.10.

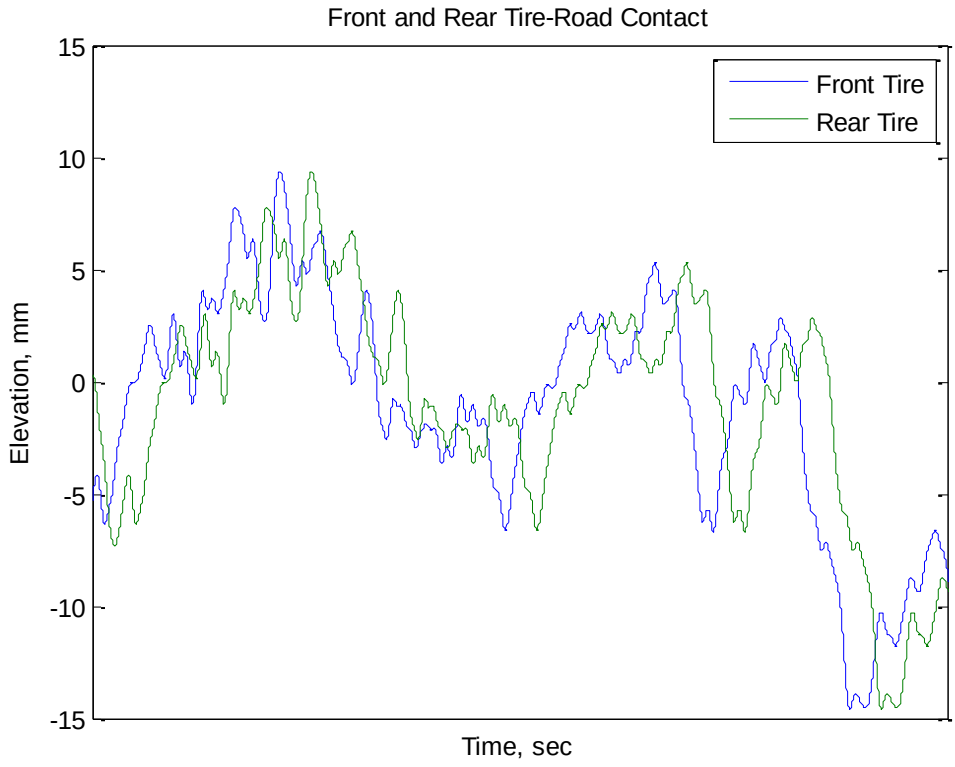

Figure 4.10: Front and Rear Tire-Road Contact

4.3.2.1 Diagram and Equations

Similar to the quarter car model, the equation of motion is set equal to zero in Equation 4.12.

$$M\ddot{x} + C\dot{x} + Kx = 0 \tag{4.12}$$

The mass, damping, and stiffness matrices now include the effect of the moment of inertia for rotation, and interaction of the front and rear suspension systems based on the distance between them.

$$M = \begin{bmatrix} m_s & 0 & 0 & 0 \\ 0 & I_s & 0 & 0 \\ 0 & 0 & m_{u1} & 0 \\ 0 & 0 & 0 & m_{u2} \end{bmatrix}$$

$$C = \begin{bmatrix} c_{s1} + c_{s2} & c_{s1}l_1 - c_{s2}l_2 & -c_{s1} & -c_{s2} \\ c_{s1}l_1 - c_{s2}l_2 & c_{s1}l_1^2 + c_{s2}l_2^2 & -c_{s1}l_1 & c_{s2}l_2 \\ -c_{s1} & -c_{s1}l_1 & c_{s1} & 0 \\ -c_{s2} & c_{s2}l_2 & 0 & c_{s2} \end{bmatrix}$$

$$K = \begin{bmatrix} k_{s1} + k_{s2} & k_{s1}l_1 - k_{s2}l_2 & -k_{s1} & -k_{s2} \\ k_{s1}l_1 - k_{s2}l_2 & k_{s1}l_1^2 + k_{s2}l_2^2 & -k_{s1}l_1 & k_{s2}l_2 \\ -k_{s1} & -k_{s1}l_1 & k_{s1} + k_{t1} & 0 \\ -k_{s2} & k_{s2}l_2 & 0 & k_{s2} + k_{t2} \end{bmatrix}$$

A free body diagram for the vehicle body is shown in Figure 4.11. This diagram includes the rotation and end point motions of the sprung mass.

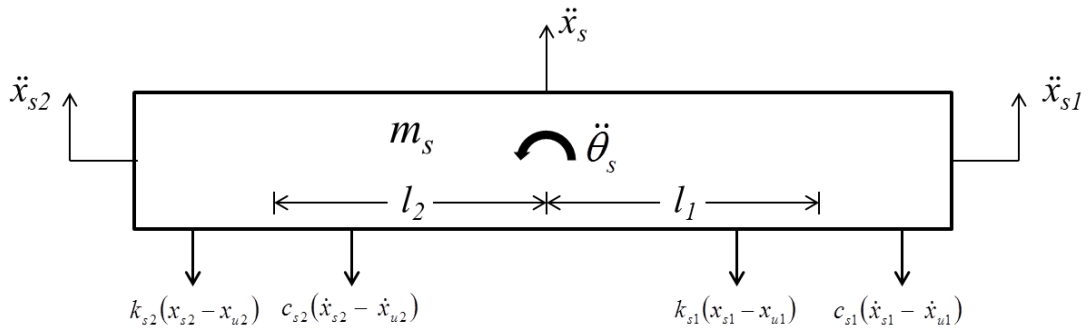

Figure 4.11: Half Car Model – Sprung Mass Free Body Diagram

Because this study is based on a single acceleration response of the vehicle, it is necessary to relate the two end point motions to a singular motion at the center of gravity of the vehicle body. The relations of these motions are detailed in Equations 4.13 through 4.16:

$$x_s = \theta_s l_2 + x_{s2} = \frac{x_{s1} - x_{s2}}{l_1 + l_2} l_2 + x_{s2} \tag{4.13}$$

$$\theta_s = \frac{x_{s1} - x_{s2}}{l_1 + l_2} \tag{4.14}$$

$$x_{s1} = x_s + \theta_s l_1 \tag{4.15}$$

$$x_{s2} = x_s - \theta_s l_2 \tag{4.16}$$

State-space formulation of the half car model is represented to relate the road elevation to the vertical acceleration of the vehicle body at its center of gravity. Equation 4.17 characterizes the equation of motion for the sprung mass based on equilibrium. Rearranging the terms to provide a formula for the vertical sprung mass acceleration leads to Equation 4.18. Substituting Equations 4.15 and 4.16 into Equation 4.18, replaces the end point accelerations with terms based on rotation and the location of the center of gravity of the vehicle body. This substitution is done to create a state matrix that directly relates the road profile to vehicle acceleration response.

$$m_s\ddot{x}_s + k_{s1}(x_{s1} - x_{u1}) + c_{s1}(\dot{x}_{s1} - \dot{x}_{u1}) + k_{s2}(x_{s2} - x_{u2}) + c_{s2}(\dot{x}_{s2} - \dot{x}_{u2}) = 0 \quad \textbf{(4.17)}$$

$$\ddot{x}_s = -\frac{k_{s1}}{m_s}x_{s1} - \frac{k_{s2}}{m_s}x_{s2} + \frac{k_{s1}}{m_s}x_{u1} + \frac{k_{s2}}{m_s}x_{u2} - \frac{c_{s1}}{m_s}\dot{x}_{s1} - \frac{c_{s2}}{m_s}\dot{x}_{s2} + \frac{c_{s1}}{m_s}\dot{x}_{u1} + \frac{c_{s2}}{m_s}\dot{x}_{u2} \quad \textbf{(4.18)}$$

$$\begin{aligned}\ddot{x}_s = &-\frac{k_{s1}}{m_s}(x_s + \theta_s l_1) - \frac{k_{s2}}{m_s}(x_s - \theta_s l_2) + \frac{k_{s1}}{m_s}x_{u1} + \frac{k_{s2}}{m_s}x_{u2} - \frac{c_{s1}}{m_s}\left(\dot{x}_s + \dot{\theta}_s l_1\right) \\ &- \frac{c_{s2}}{m_s}\left(\dot{x}_s - \dot{\theta}_s l_2\right) + \frac{c_{s1}}{m_s}\dot{x}_{u1} + \frac{c_{s2}}{m_s}\dot{x}_{u2}\end{aligned} \quad \textbf{(4.19)}$$

$$\begin{aligned}\ddot{x}_s = &-\frac{k_{s1} + k_{s2}}{m_s}x_s - \frac{k_{s1}l_1 - k_{s2}l_2}{m_s}\theta_s + \frac{k_{s1}}{m_s}x_{u1} + \frac{k_{s2}}{m_s}x_{u2} - \frac{c_{s1} + c_{s2}}{m_s}\dot{x}_s \\ &- \frac{c_{s1}l_1 - c_{s2}l_2}{m_s}\dot{\theta}_s + \frac{c_{s1}}{m_s}\dot{x}_{u1} + \frac{c_{s2}}{m_s}\dot{x}_{u2}\end{aligned} \quad \textbf{(4.20)}$$

Following a similar approach to the formation of Equation 4.20, Equations 4.21 through 4.25 provide the necessary steps in creating relation for the rotational acceleration of the vehicle body.

$$I_s\ddot{\theta}_s + k_{s1}(x_{s1} - x_{u1})l_1 + c_{s1}(\dot{x}_{s1} - \dot{x}_{u1})l_1 - k_{s2}(x_{s2} - x_{u2})l_2 - c_{s2}(\dot{x}_{s2} - \dot{x}_{u2})l_2 = 0 \quad \textbf{(4.21)}$$

$$I_s\ddot{\theta}_s = -(k_{s1}l_1x_{s1} - k_{s1}l_1x_{u1}) - (c_{s1}l_1\dot{x}_{s1} - c_{s1}l_1\dot{x}_{u1}) + (k_{s2}l_2x_{s2} - k_{s2}l_2x_{u2}) + (c_{s2}l_2\dot{x}_{s2} - c_{s2}l_2\dot{x}_{u2}) \quad \textbf{(4.22)}$$

$$\ddot{\theta}_s = -\frac{k_{s1}l_1}{I_s}x_{s1} + \frac{k_{s2}l_2}{I_s}x_{s2} - \frac{k_{s1}l_1}{I_s}x_{u1} + \frac{k_{s2}l_2}{I_s}x_{u2} - \frac{c_{s1}l_1}{I_s}\dot{x}_{s1} + \frac{c_{s2}l_2}{I_s}\dot{x}_{s2} + \frac{c_{s1}l_1}{I_s}\dot{x}_{u1} - \frac{c_{s2}l_2}{I_s}\dot{x}_{u2} \quad \textbf{(4.23)}$$

$$\ddot{\theta}_s = -\frac{k_{s1}l_1}{I_s}(x_s + \theta_s l_1) + \frac{k_{s2}l_2}{I_s}(x_s - \theta_s l_2) - \frac{k_{s1}l_1}{I_s}x_{u1} + \frac{k_{s2}l_2}{I_s}x_{u2} - \frac{c_{s1}l_1}{I_s}(\dot{x}_s + \dot{\theta}_s l_1) + \frac{c_{s2}l_2}{I_s}(\dot{x}_s - \dot{\theta}_s l_2) + \frac{c_{s1}l_1}{I_s}\dot{x}_{u1} - \frac{c_{s2}l_2}{I_s}\dot{x}_{u2} \quad \textbf{(4.24)}$$

$$\ddot{\theta}_s = -\frac{k_{s1}l_1 - k_{s2}l_2}{I_s}x_s - \frac{k_{s1}l_1^2 + k_{s2}l_2^2}{I_s}\theta_s - \frac{k_{s1}l_1}{I_s}x_{u1} + \frac{k_{s2}l_2}{I_s}x_{u2} - \frac{c_{s1}l_1 - c_{s2}l_2}{I_s}\dot{x}_s - \frac{c_{s1}l_1^2 + c_{s2}l_1^2}{I_s}\dot{\theta}_s + \frac{c_{s1}l_1}{I_s}\dot{x}_{u1} - \frac{c_{s2}l_2}{I_s}\dot{x}_{u2} \quad \textbf{(4.25)}$$

Equilibrium equations of the front unsprung mass are shown below, followed by the equations for the rear unsprung mass on the next page.

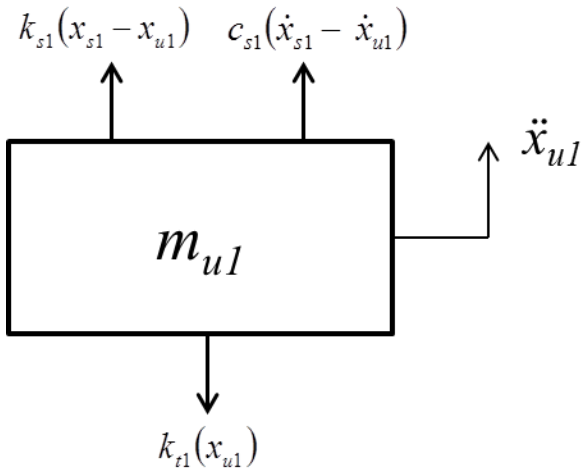

Figure 4.12: Half Car Model – Front Unsprung Mass Free Body Diagram

$$m_{u1}\ddot{x}_{u1} - k_{s1}\,(x_{s1} - x_{u1}) - c_{s1}(\dot{x}_{s1} - \dot{x}_{u1}) + k_{t1}(x_{u1} - x_{g1}) = 0 \qquad \textbf{(4.26)}$$

$$\ddot{x}_{u1} = \frac{k_{s1}}{m_{u1}}x_{s1} - \frac{k_{s1}}{m_{u1}}x_{u1} + \frac{c_{s1}}{m_{u1}}\dot{x}_{s1} - \frac{c_{s1}}{m_{u1}}\dot{x}_{u1} - \frac{k_{t1}}{m_{u1}}x_{u1} + \frac{k_{t1}}{m_{u1}}x_{g1} \qquad \textbf{(4.27)}$$

$$\ddot{x}_{u1} = \frac{k_{s1}}{m_{u1}}(x_s + \theta_s l_1) - \frac{k_{s1}}{m_{u1}}x_{u1} + \frac{c_{s1}}{m_{u1}}(\dot{x}_s + \dot{\theta}_s l_1) - \frac{c_{s1}}{m_{u1}}\dot{x}_{u1} - \frac{k_{t1}}{m_{u1}}x_{u1} + \frac{k_{t1}}{m_{u1}}x_{g1} \qquad \textbf{(4.28)}$$

$$\ddot{x}_{u1} = \frac{k_{s1}}{m_{u1}}x_s + \frac{k_{s1}l_1}{m_{u1}}\theta_s - \frac{k_{s1}+k_{t1}}{m_{u1}}x_{u1} + \frac{c_{s1}}{m_{u1}}\dot{x}_s + \frac{c_{s1}l_1}{m_{u1}}\dot{\theta}_s - \frac{c_{s1}}{m_{u1}}\dot{x}_{u1} + \frac{k_{t1}}{m_{u1}}x_{g1} \qquad \textbf{(4.29)}$$

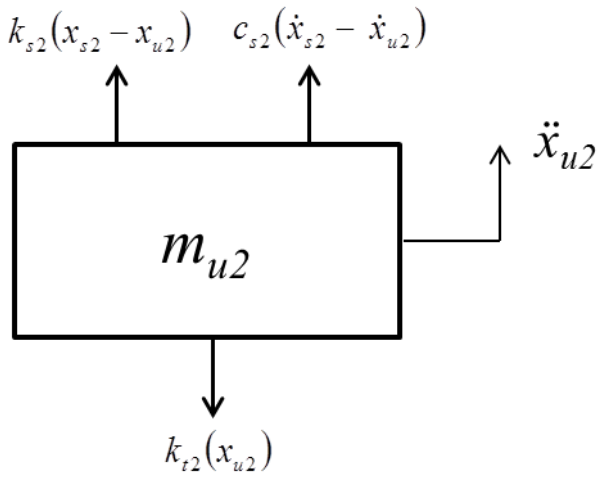

Figure 4.13: Half Car Model – Rear Unsprung Mass Free Body Diagram

$$m_{u2}\ddot{x}_{u2} - k_{s2}(x_{s2} - x_{u2}) - c_{s2}(\dot{x}_{s2} - \dot{x}_{u2}) + k_{t2}(x_{u2} - x_{g2}) = 0 \quad \textbf{(4.30)}$$

$$\ddot{x}_{u2} = \frac{k_{s2}}{m_{u2}}x_{s2} - \frac{k_{s2}}{m_{u2}}x_{u2} + \frac{c_{s2}}{m_{u2}}\dot{x}_{s2} - \frac{c_{s2}}{m_{u2}}\dot{x}_{u2} - \frac{k_{t2}}{m_{u2}}x_{u2} + \frac{k_{t2}}{m_{u2}}x_{g2} \quad \textbf{(4.31)}$$

$$\ddot{x}_{u2} = \frac{k_{s2}}{m_{u2}}(x_s - \theta_s l_2) - \frac{k_{s2}}{m_{u2}}x_{u2} + \frac{c_{s2}}{m_{u2}}(\dot{x}_s - \dot{\theta}_s l_2) - \frac{c_{s2}}{m_{u2}}\dot{x}_{u2} - \frac{k_{t2}}{m_{u2}}x_{u2} + \frac{k_{t2}}{m_{u2}}x_{g2} \quad \textbf{(4.32)}$$

$$\ddot{x}_{u2} = \frac{k_{s2}}{m_{u2}}x_s - \frac{k_{s2}l_2}{m_{u2}}\theta_s - \frac{k_{s2}+k_{t2}}{m_{u2}}x_{u2} + \frac{c_{s2}}{m_{u2}}\dot{x}_s - \frac{c_{s2}l_2}{m_{u2}}\dot{\theta}_s - \frac{c_{s2}}{m_{u2}}\dot{x}_{u2} + \frac{k_{t2}}{m_{u2}}x_{g2} \quad \textbf{(4.33)}$$

The state-space equations are formed in a way to provide road elevation displacement, $\begin{bmatrix} x_{g1} \\ x_{g2} \end{bmatrix}$, as an input and vehicle acceleration response, $\begin{bmatrix} \ddot{x}_s \\ \ddot{\theta}_s \\ \ddot{x}_{u1} \\ \ddot{x}_{u2} \end{bmatrix}$, as the output:

$$\begin{bmatrix} \dot{x}_s \\ \dot{\theta}_s \\ \dot{x}_{u1} \\ \dot{x}_{u2} \\ \ddot{x}_s \\ \ddot{\theta}_s \\ \ddot{x}_{u1} \\ \ddot{x}_{u2} \end{bmatrix} = A \begin{bmatrix} x_s \\ \theta_s \\ x_{u1} \\ x_{u2} \\ \dot{x}_s \\ \dot{\theta}_s \\ \dot{x}_{u1} \\ \dot{x}_{u2} \end{bmatrix} + B \begin{bmatrix} x_{g1} \\ x_{g2} \end{bmatrix} \tag{4.34}$$

$$\begin{bmatrix} \ddot{x}_s \\ \ddot{\theta}_s \\ \ddot{x}_{u1} \\ \ddot{x}_{u2} \end{bmatrix} = C \begin{bmatrix} x_s \\ \theta_s \\ x_{u1} \\ x_{u2} \\ \dot{x}_s \\ \dot{\theta}_s \\ \dot{x}_{u1} \\ \dot{x}_{u2} \end{bmatrix} + D \begin{bmatrix} x_{g1} \\ x_{g2} \end{bmatrix} \tag{4.35}$$

The state-space matrices used to relate the input and output of the system can be found on the following page. Matrices *A* and *B* are formed based on the acceleration response of each of the four degrees of freedom as found in Equations 4.20, 4.25, 4.29, and 4.33. Matrices *C* and *D* are made up of the constants that relate the road elevation to the acceleration response based on the state vector multiplied by *C*, as seen in Equation 4.35.

$$A = \begin{bmatrix} 0 & 0 & 0 & 0 & 1 & 0 & 0 & 0 \\ 0 & 0 & 0 & 0 & 0 & 1 & 0 & 0 \\ 0 & 0 & 0 & 0 & 0 & 0 & 1 & 0 \\ 0 & 0 & 0 & 0 & 0 & 0 & 0 & 1 \\ -\frac{k_{s1}+k_{s2}}{m_s} & -\frac{k_{s1}l_1-k_{s2}l_2}{m_s} & \frac{k_{s1}}{m_s} & \frac{k_{s2}}{m_s} & -\frac{c_{s1}+c_{s2}}{m_s} & -\frac{c_{s1}l_1-c_{s2}l_2}{m_s} & \frac{c_{s1}}{m_s} & \frac{c_{s2}}{m_s} \\ -\frac{k_{s1}l_1-k_{s2}l_2}{I_s} & -\frac{k_{s1}l_1^2+k_{s2}l_2^2}{I_s} & \frac{k_{s1}l_1}{I_s} & -\frac{k_{s2}l_2}{I_s} & -\frac{c_{s1}l_1-c_{s2}l_2}{I_s} & -\frac{c_{s1}l_1^2+c_{s2}l_2^2}{I_s} & \frac{c_{s1}l_1}{I_s} & -\frac{c_{s2}l_2}{I_s} \\ \frac{k_{s1}}{m_{u1}} & \frac{k_{s1}l_1}{m_{u1}} & -\frac{k_{s1}+k_{t1}}{m_{u1}} & 0 & \frac{c_{s1}}{m_{u1}} & \frac{c_{s1}l_1}{m_{u1}} & -\frac{c_{s1}}{m_{u1}} & 0 \\ \frac{k_{s2}}{m_{u2}} & -\frac{k_{s2}l_2}{m_{u2}} & 0 & -\frac{k_{s2}+k_{t2}}{m_{u2}} & \frac{c_{s2}}{m_{u2}} & -\frac{c_{s2}l_2}{m_{u2}} & 0 & -\frac{c_{s2}}{m_{u2}} \end{bmatrix}$$

$$B = \begin{bmatrix} 0 & 0 \\ 0 & 0 \\ 0 & 0 \\ 0 & 0 \\ 0 & 0 \\ 0 & 0 \\ \frac{k_{t1}}{m_{u1}} & 0 \\ 0 & \frac{k_{t2}}{m_{u2}} \end{bmatrix}$$

$$C = \begin{bmatrix} -\frac{k_{s1}+k_{s2}}{m_s} & -\frac{k_{s1}l_1-k_{s2}l_2}{m_s} & \frac{k_{s1}}{m_s} & \frac{k_{s2}}{m_s} & -\frac{c_{s1}+c_{s2}}{m_s} & -\frac{c_{s1}l_1-c_{s2}l_2}{m_s} & \frac{c_{s1}}{m_s} & \frac{c_{s2}}{m_s} \\ -\frac{k_{s1}l_1-k_{s2}l_2}{I_s} & -\frac{k_{s1}l_1^2+k_{s2}l_2^2}{I_s} & \frac{k_{s1}l_1}{I_s} & -\frac{k_{s2}l_2}{I_s} & -\frac{c_{s1}l_1-c_{s2}l_2}{I_s} & -\frac{c_{s1}l_1^2+c_{s2}l_2^2}{I_s} & \frac{c_{s1}l_1}{I_s} & -\frac{c_{s2}l_2}{I_s} \\ \frac{k_{s1}}{m_{u1}} & \frac{k_{s1}l_1}{m_{u1}} & -\frac{k_{s1}+k_{t1}}{m_{u1}} & 0 & \frac{c_{s1}}{m_{u1}} & \frac{c_{s1}l_1}{m_{u1}} & -\frac{c_{s1}}{m_{u1}} & 0 \\ \frac{k_{s2}}{m_{u2}} & -\frac{k_{s2}l_2}{m_{u2}} & 0 & -\frac{k_{s2}+k_{t2}}{m_{u2}} & \frac{c_{s2}}{m_{u2}} & -\frac{c_{s2}l_2}{m_{u2}} & 0 & -\frac{c_{s2}}{m_{u2}} \end{bmatrix}$$

$$D = \begin{bmatrix} 0 & 0 \\ 0 & 0 \\ \frac{k_{t1}}{m_{u1}} & 0 \\ 0 & \frac{k_{t2}}{m_{u2}} \end{bmatrix}$$

4.3.3 Model Vehicle Parameters

Natural frequencies for a typical passenger car are around 1 and 10 Hz (Jazar, 2008). The lower frequency is due to the bounce of the sprung mass, while the higher frequency has to do with the response of the unsprung mass. The sprung mass is excited by bumps which have wavelengths greater than the distance of the front and rear tire while driving at average speeds. These bumps cause bounce motions of the sprung mass. At a higher speed, bumps will have shorter wavelengths, and act as an impulse to the system. This impulse causes the wheels to oscillate at the natural frequency of the unsprung mass. Due to the different natural frequencies of the sprung and unsprung masses, the excitation of 10 Hz of the unsprung mass is isolated through the suspension system to prevent any discomfort of the vehicle user. Although high frequencies can be isolated from the vehicle body, low frequency vibration of 5 Hz or less can cause resonance of the mass.

The amount of damping provided to a vehicle is chosen as a tradeoff between ride comfort and vehicle handling. Due to this compromise between comfort and handling, the damping ratio is selected based on the goal of the specific vehicle. Typical passenger cars will have a damping ratio close to 0.3, which provides a comfortable ride through the inclusion of soft dampers, but lessens the overall control of the vehicle. This is in contrast to a vehicle such as a racecar, which is designed for handling and includes a much higher ideal damping ratio of 1.0 (Dixon, 2007).

Parameters of the simulated models are chosen to accurately describe the behavior of a typical passenger vehicle. Because the quarter car model will only be used to calculate the IRI, the parameters are selected to represent *The Golden Car*. These parameters are based on sprung mass ratios used to maximize the output of the vehicle. Damping of *The Golden Car* is larger than what would be found in a typical vehicle to avoid sensitivity to certain wavelengths (Sayers, et al., 1998). The sprung mass is set equal to 1.00 with the units of the parameters omitted because they are all based on ratios to the sprung mass. Since the IRI is calculated based on the relative motion between the sprung and unsprung mass, the amplitude of the masses is not a factor.

Table 4.1: Quarter Car Model Parameters

Quarter Car Parameters	
m_s	1.00
m_u	0.15
k_s	63.3
c_s	6.00
k_t	653

Performing eigenvalue analysis to determine the natural frequencies of the model with these parameters leads to frequencies of 1.2 and 11 Hz, which is within the range of natural frequencies for passenger vehicles. The damping ratio is calculated to be 0.40, which is the target amount of damping for this model.

The half car parameters are selected to represent the vehicle used for testing in this study. The testing vehicle, as shown in Figure 4.14, is the 2009 Toyota RAV4, a compact sports utility vehicle.

Figure 4.14: 2009 Toyota RAV4 (Toyota, 2015)

The curb weight of the vehicle, which is the total weight when not loaded with passengers or cargo is 3360 lbs or 1524.07 kg (Edmunds, 2015). Ratios similar to the ones used in calculation of *The Golden Car* will be used to estimate parameters of the vehicle. Assuming the unsprung mass is 15% of the sprung mass, the total mass can be shown as the sum of the two masses as seen in Equation 4.36.

$$m_t = m_s + 0.15m_s \tag{4.36}$$

With this assumption, the sprung mass can be calculated as $m_s = \frac{m_t}{1.15}$ with the addition of mass for each passenger, in this case taken as 72.57 kg (160 lbs). Due to the increased damping of the quarter car model, the damping is lowered to provide a damping ratio of 0.30 for the vehicle. The lengths from the front of the rear tire to the center of gravity of the vehicle were both measure to be 1.47 m. The full list of parameters used for the half car model is shown in Table 4.2.

Table 4.2: Half Car Model Parameters

Half Car Parameters			
m_s (kg)	875	k_{s1} (N/m)	23088
I (kg/m^2)	1100	k_{s2} (N/m)	23088
m_{u1} (kg)	55	c_{s1} (N·s/m)	1776
m_{u2} (kg)	55	c_{s2} (N·s/m)	1776
l_1 (m)	1.47	k_{t1} (N/m)	238180
l_2 (m)	1.47	k_{t2} (N/m)	238180

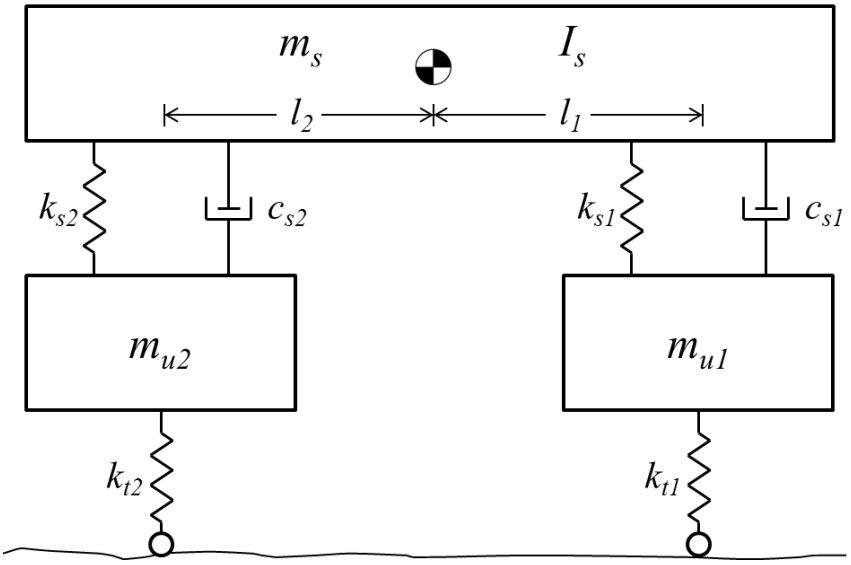

Figure 4.15: Half Car Model

Similar to typical passenger vehicles, these parameters provide natural frequencies of 1.1 and 11 Hz, with a damping ratio of 0.30.

4.3.4 Correlation of Roughness Index and IRI

To simulate road profiles at specific IRI values, it is necessary to directly relate the IRI to the roughness coefficient, $G_d(n_0)$, used for ISO classification (Equation 2.1) and profile simulation (Equation 4.1). A direct relation between the values of the roughness coefficient and the IRI is found empirically through simulation. Four sets of 100 generated road profiles are simulated from roughness coefficients ranging from 2 to 4096 cm^3. This range is chosen based on the ISO Classification of roads within Road Classes A through D. Because the IRI is calculated based on a quarter car model with a forward moving velocity of 80 km/h, varying vehicle speeds do not need to be taken into consideration. IRI is calculated for each generated road profile. The effect of profile roughness on the value of the IRI is shown in Figure 4.16. Based on the relation of the two parameters in the log-log scale in Figure 4.17, it can be seen that the use of a nonlinear regression power model to determine the correlation is appropriate (Seber, et al., 2003).

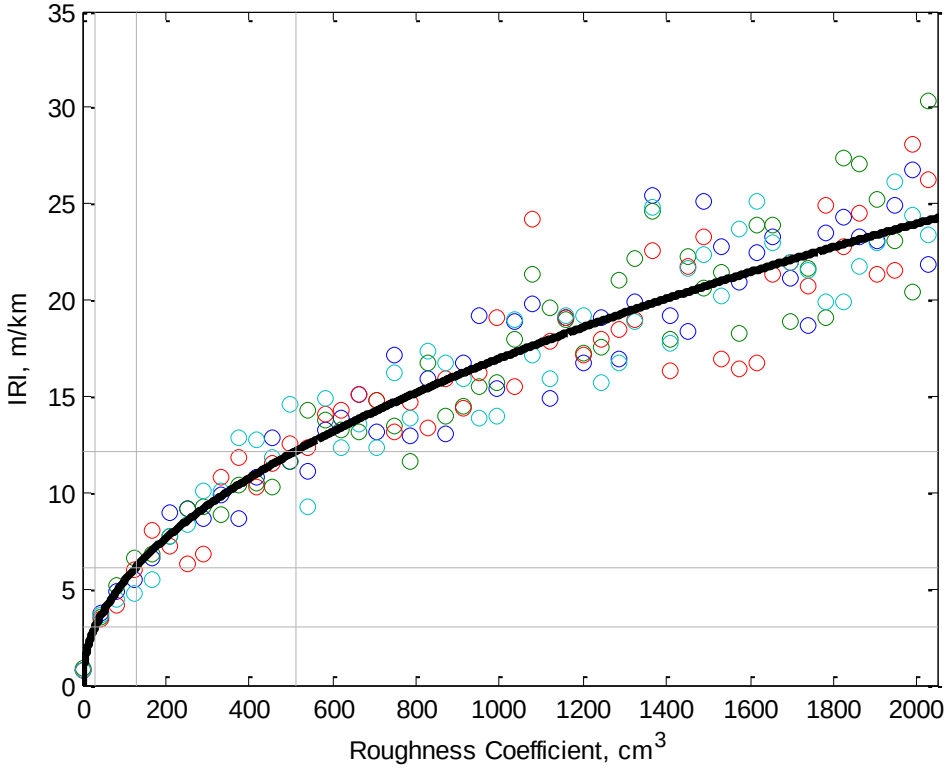

Figure 4.16: Degree of Roughness vs. IRI

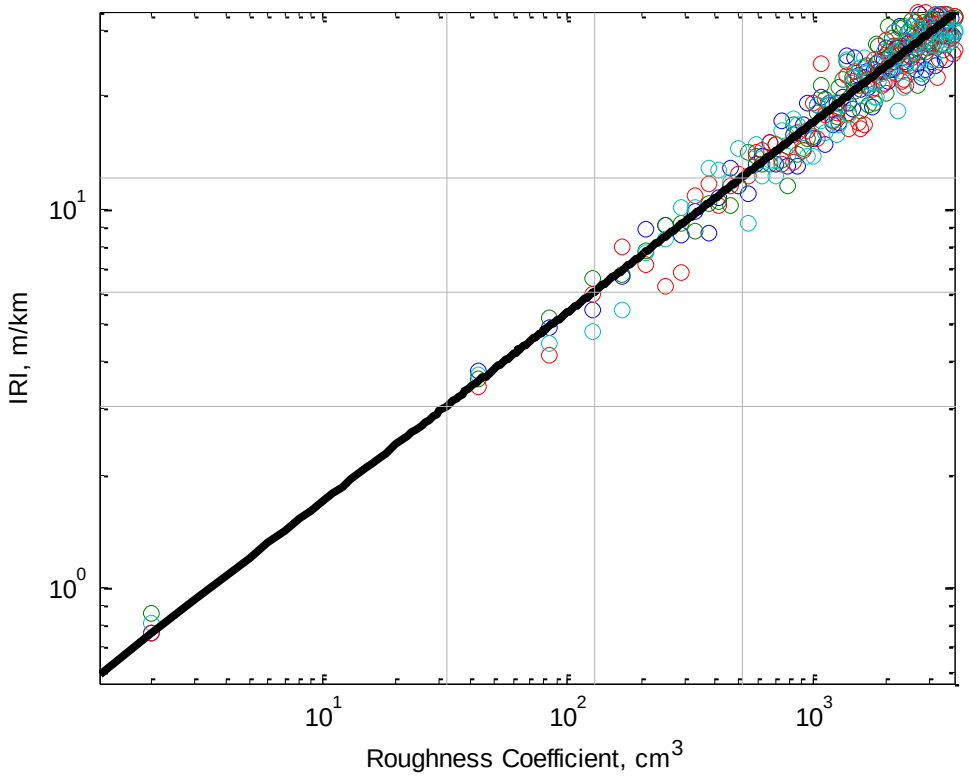

Figure 4.17: Degree of Roughness vs. IRI (Log-Log)

A power model is used to linearize the data and create a simple power-law relationship as $y = cx^b$. Linearization leads to the following form, $ln(y) = ln(c) + b * ln(x)$, where coefficients *b* and *c* are computed using Equation 4.37. Based on the simulated data, computation of these coefficients results in a power model relating the IRI to the roughness coefficient as shown in Equation 4.39. The trendline formed by this nonlinear regression is shown in both Figure 4.16 and Figure 4.17.

$$\begin{bmatrix} ln(c) \\ b \end{bmatrix} = \frac{ln(y)}{[1 \quad ln(x)]} \tag{4.37}$$

$$\begin{bmatrix} ln(c) \\ b \end{bmatrix} = \frac{ln(IRI)}{\begin{bmatrix} 1 \\ \vdots \quad ln\left(G_d(n_0)\right) \\ 1 \end{bmatrix}} \tag{4.38}$$

$$IRI = 0.5386 \cdot G_d(n_0)^{0.5} \tag{4.39}$$

$$G_d(n_0) = \left(\frac{IRI}{0.5386}\right)^2 \tag{4.40}$$

The inverse of this relation is presented in Equation 4.40. The inverse relation is used to determine the roughness coefficients for generating road profiles with specific IRI values.

This relation is validated by comparing the correlated roughness coefficients and IRI values with their respective physical meaning as defined in Chapter 2. A road with an IRI value of 3.05 m/km or below is considered a newly paved road, airport runway, or superhighway, which correlates to the Road Class A ISO classification as shown in Table 4.3. A road with an IRI value ranging between 12.19 and 24.37 m/km would most likely be damaged pavements or rough unpaved roads, relating to Road Class D, or a poor quality road profile.

Table 4.3: Comparison of Roughness Coefficient and IRI Values

Road Class	Roughness Coefficient: $G_d(n_0)$, cm^3		IRI (m/km)	
	Lower Limit	Upper Limit	Lower Limit	Upper Limit
A	-	32	-	3.05
B	32	128	3.05	6.09
C	128	512	6.09	12.19
D	512	2,048	12.19	24.37

The results are validated further by creating generated profiles with IRI values ranging from 1 to 20. These profiles are processed through ProVAL for calculation of the exact IRI values. The results are shown in Figure 4.18. Due to the random nature of the generated profiles, two sets of data were used for validation. Based on the results and their highly linear correlation, this method for generating random road profiles based on selected IRI values is valid.

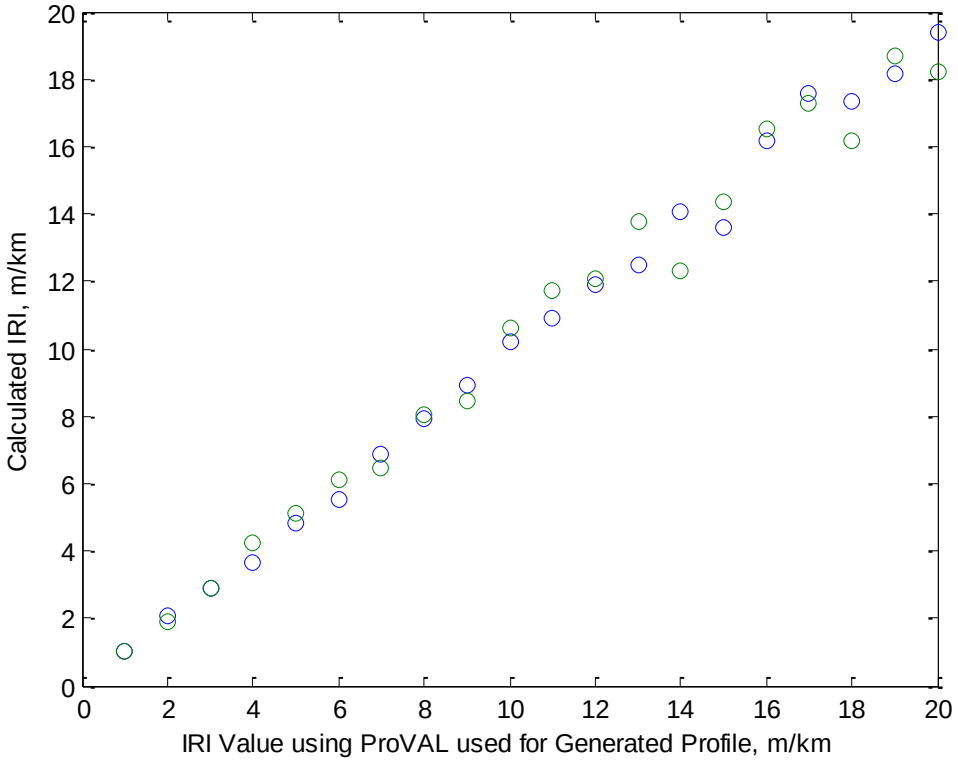

Figure 4.18: Validation of Generated Profiles using ProVAL

4.4 System Identification Study Based on Simulated Data

Simulation of the half car model traveling along various road types is conducted to show the effectiveness of system identification used for determining unknown vehicle parameters. Parameter identification is performed through prediction error estimation using a linear grey-box model. This grey-box model is constructed with the state-space matrices which represent the vehicle, omitting the variables selected as unknowns. For the prediction of the unknown vehicle mass, only the sprung mass is defined as the unknown, while all other parameters are defined. In addition to predicting unknown parameters of the half car model, simulation is also performed to show how varying road irregularities cause discomfort to the user of the vehicle.

Simulation consists of two main sources of excitation: speed bumps and bridge bumps. Speed bumps are chosen because they provide a well-defined vehicle response. Bridge bumps are used to determine whether or not the response provides a signal-to-noise ratio strong enough to perform system identification. A study on the discomfort caused by bridge bumps is also performed.

4.4.1 System Identification: Known Input

PEM is performed for a system with a known input to determine the process's effectiveness.. For this case, a vehicle represented as a half car model is simulated traveling on a road surface with a single bump. This bump is required to excite the vertical acceleration of the system and provide a response for analysis. The first known input-output test analyzes the effect of the time window for system identification. This shows how the prediction of the parameters is affected by the range that is being analyzed. The second test shows the effects of the initial parameter estimation to determine the importance of the initial guess for convergence of the exact mass.

4.4.1.1 Effect of Time Window

Figure 4.19 and Figure 4.20 show the effect of a bump on the vertical acceleration of the vehicle. The input is shown for both the front and rear tires as a function of time. The output of the system is simulated based on a road with existing roughness, while the input is replaced with a profile that lacks the added noise from the unevenness of the road. This is done because the added effects of the road roughness typically remain unknown. In this case, the road profile is given an IRI of 5 m/km. Each of the two figures are shown to represent different time windows used for analysis. Figure 4.19 covers a 15 m range, while Figure 4.20 includes the profile for a length of 100 m.

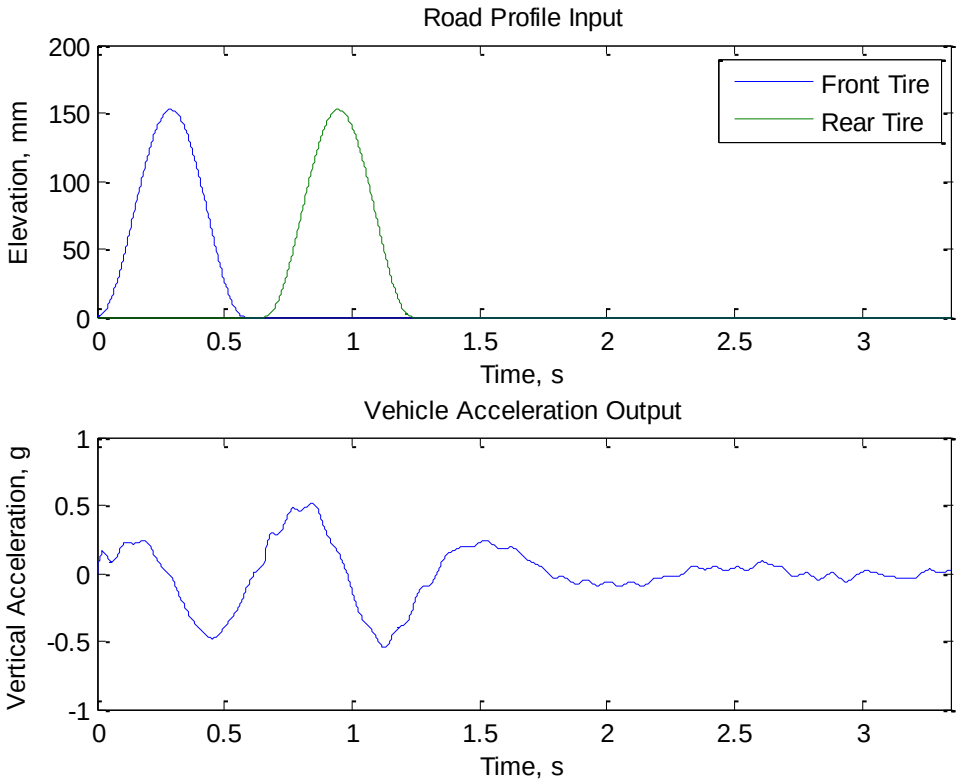

Figure 4.19: System ID Window – 15 m

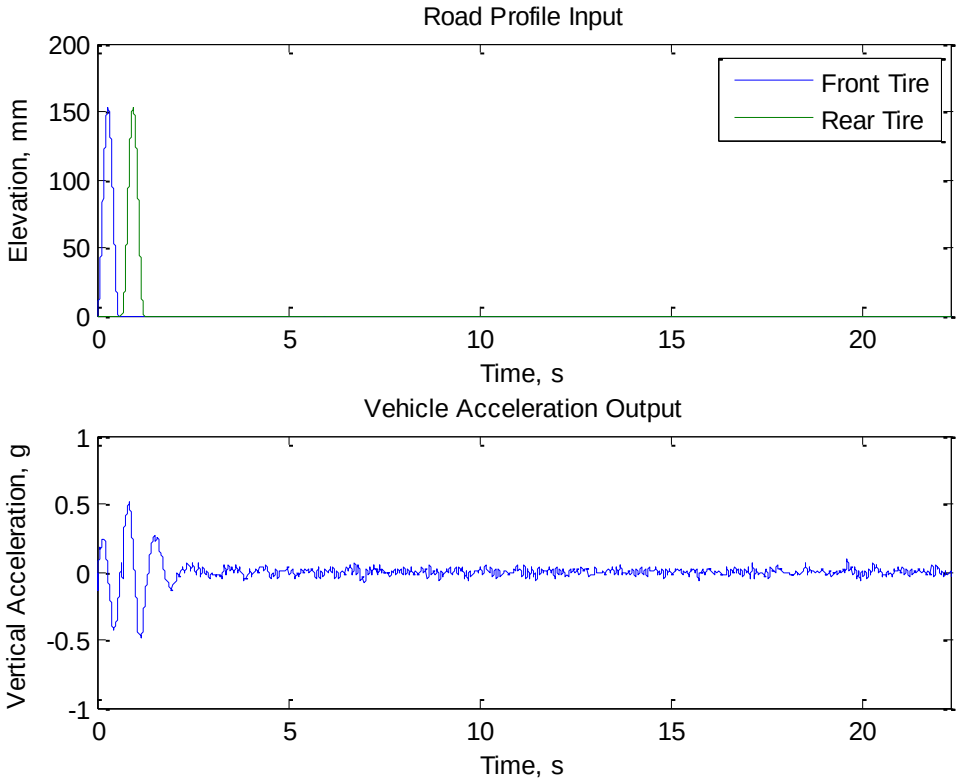

Figure 4.20: System ID Window – 100 m

Parameter identification of the unknown vehicle mass is performed for time windows ranging from 5 to 100 m in 5 m increments, as shown in Figure 4.21. This figure shows the accuracy of the system identification process for the varying time window. Even with the added noise to the output response due to the roughness of the road, the predicted mass of the half car model is shown to be very close to the exact 875 kg for each case. These results show that with strong signal-to-noise ratio consistent road roughness, the size of the window has little effect on the prediction of the mass.

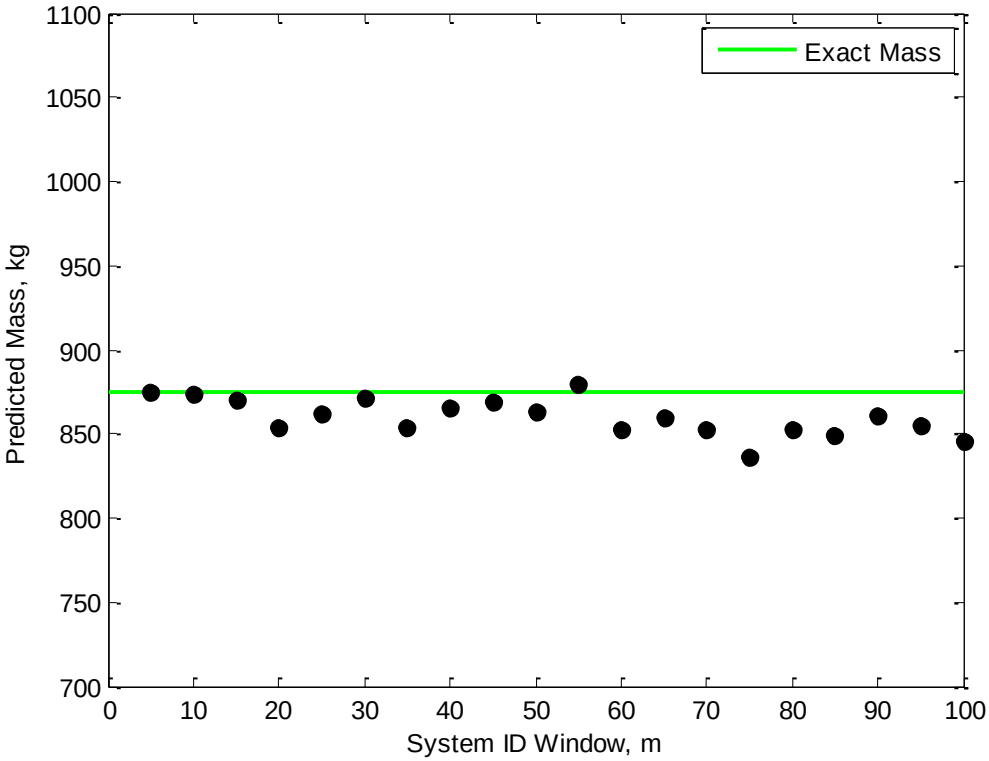

Figure 4.21: Effect of System ID Window

4.4.1.2 Effect of Mass Estimation

This next case examines the initial guess of the estimated mass and its effect on the predicted mass using PEM. Twenty estimates are made, linearly ranging from 700 to 1100 kg for the half car. This range is selected to properly reflect the mass range of typical passenger cars with varying passengers and cargo loads. Similar to the previous case, the input is taken to be a bump as shown in Figure 4.19. The predicted masses are shown in Figure 4.22. These results demonstrate the effectiveness of the system identification process for systems with known inputs. All predicated masses are within 6% of the actual 875 kg mass.

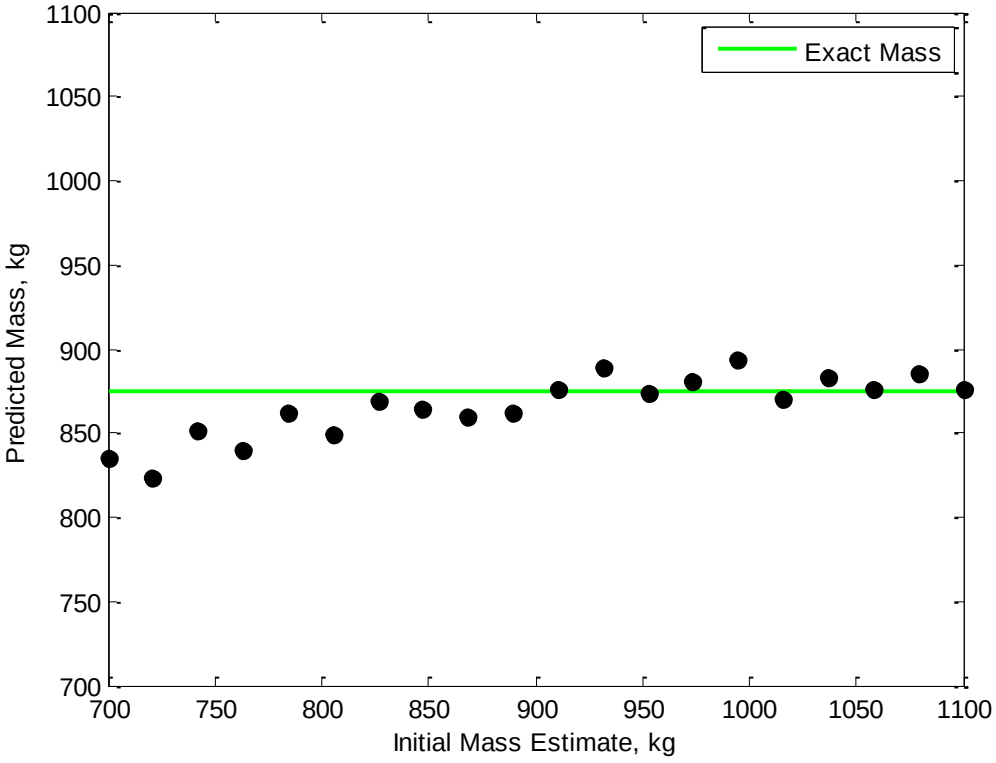

Figure 4.22: Effect of Initial Mass Estimation

4.4.2 Varying Bump Height, Width, Time

To perform parameter identification, an input needs to be provided to the vehicle to excite a response from the system. A speed bump is used to obtain an acceleration response with a strong signal-to-noise ratio. Typical speed bumps can be modeled as a cosine function, as seen in Figure 4.23 (Kropac, et al., 2008).

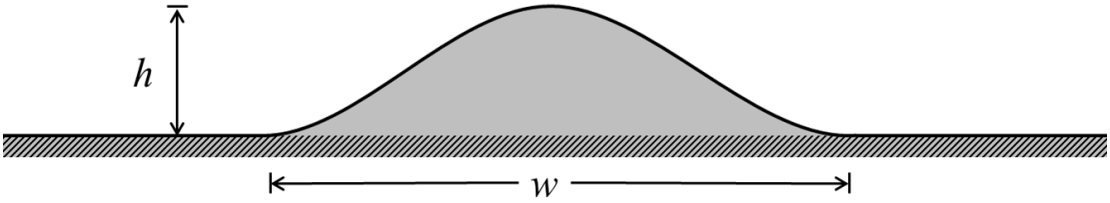

Figure 4.23: Half-Cycle Cosine Function Speed Bump Simulation

This bump is modeled using Equations 4.41 and 4.42, where h is the height and t_d is the time is takes for a single tire of the vehicle to pass over the bump. This time variable is dependent on bump width, w, and vehicle velocity, v.

$$b(t) = -\frac{h}{2} cos(2\pi\, t_i / t_d) + \frac{h}{2} \tag{4.41}$$

$$t_d = \frac{w}{v} \tag{4.42}$$

The size of the bump, which is represented as height and width, determines the amplitude of the vehicle response. This information is necessary to provide the vehicle with enough of a response to produce a signal-to-noise ratio strong enough for the parameter identification.

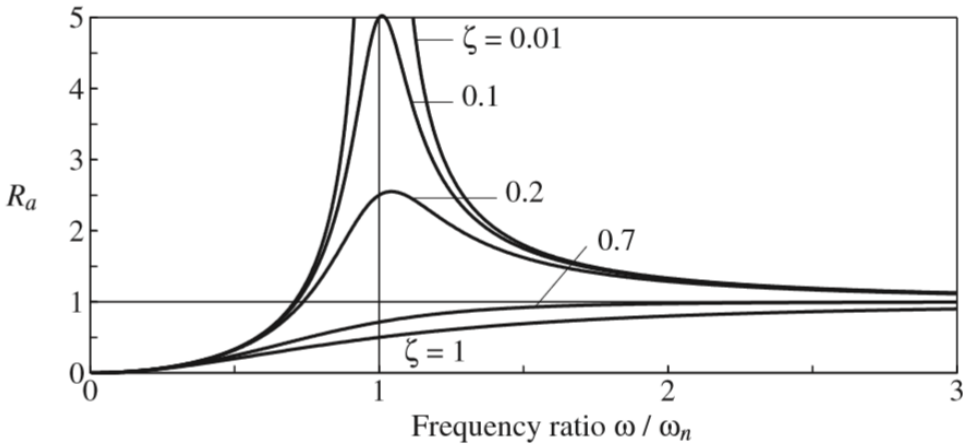

Figure 4.24: Acceleration Response for a Damped System Excited by Harmonic Force (Chopra, 2007)

As shown in Figure 4.24, the acceleration response of a damped system excited by a harmonic force is dependent on the ratio of the frequency of the input to the natural frequency of the system (Chopra, 2007). Other factors that affect the response include the amplitude of the input force and the damping ratio of the system. For passenger cars, the damping ratio is typically 0.3. Calculation of the input frequency is shown in Equation 4.43. Equation 4.44 shows the ratio of frequencies is based on bump width, vehicle velocity, and vehicle natural frequency.

$$\omega = \frac{1}{2t_d} = \frac{v}{2w} \tag{4.43}$$

$$\frac{\omega}{\omega_n} = \frac{v}{2w \cdot \omega_n} \tag{4.44}$$

For the case of constant velocity and constant natural frequency, the only factor for acceleration response is the width of the bump. For this study on the effect of speed bumps for system response, both the velocity and vehicle parameters will remain constant.

The vehicle velocity is limited to 16.1 kph (10 mph) to prevent any wheel hop caused by the bump. The natural frequency of the vehicle is taken as 1.2 Hz. The peak acceleration response of the half car model based on bumps with varying height and width is shown in Figure 4.25. The height of the bump varies from 101.6 to 203.2 mm (4 to 8 in.), with a width varying from 1.83 to 3.35 m (6 to 11 ft). The results shown in Figure 4.25 are expected; the larger the height, the larger the peak acceleration response, and the larger the width, the smaller the peak response. Although seemingly trivial, this information is necessary for estimation of the input of the system when only the vehicle response is provided.

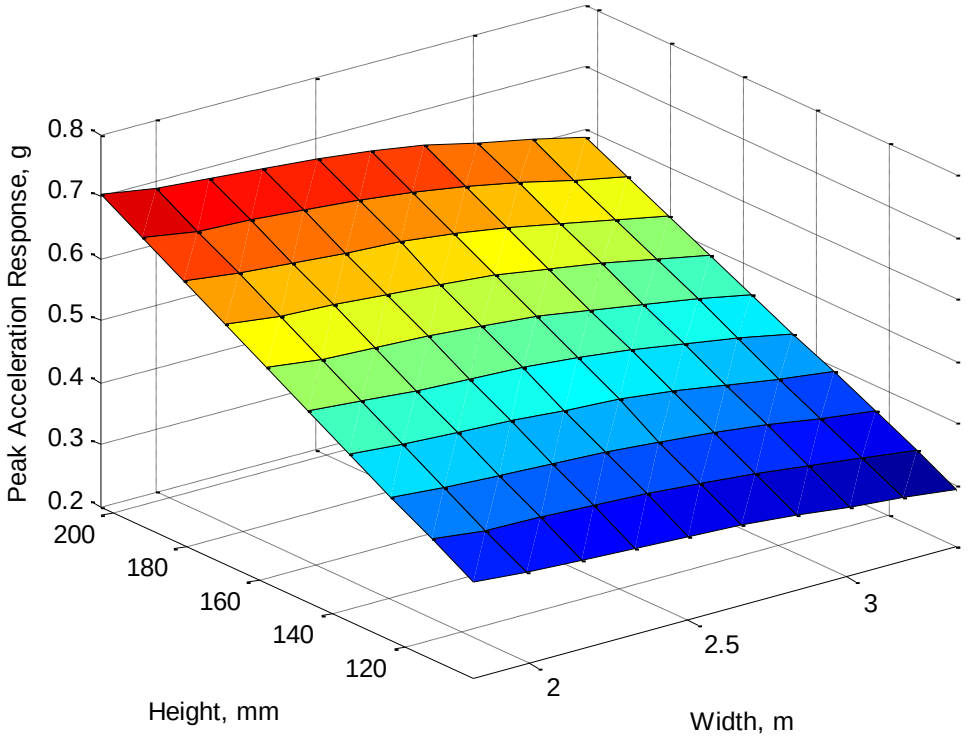

Figure 4.25: Peak Acceleration Response Based on Variation of Input Bump Width and Height

4.4.3 Estimation of Input

It is necessary to provide an input estimate of the road for detection of changes in vehicle parameters with the use of PEM. For a vehicle at a known velocity with known system parameters, it may be possible to estimate input properties based on the acceleration response.

Simulation is conducted to determine the sensitivity of the PEM algorithm for predicated mass with varying estimated bump input. The estimation of the bump is based on height and width. The vehicle response is simulated with a bump height and width of 150 mm and 2.60 m, respectively. For the estimated input, the height varies from 72.2 to 228.6 mm (3 to 9 in.), while the width ranges from 1.82 to 3.35 m (6 to 11 ft). The results for percent error based on the variation of estimation height and mass input is shown in Figure 4.26. The range of percent error is limited to 50% to exclude any extreme values. This plot clearly shows a region where the estimation produces accurate results. Upon further inspection of the data in Figure 4.27, it can be seen that it is possible to get a correct prediction of vehicle mass with height and width estimation that are different than the exact values. This angled dark blue region is due to the variance of the width and height combining to provide similar vehicle response to those found through the actual simulation. Returning to Figure 4.24, it is seen that the amplitude of acceleration response is based on the ratio of input frequency to the natural frequency of the system. Typically, for a larger width, the response is lessened. To compensate, the height of the bump has to be increased as seen in Figure 4.27.

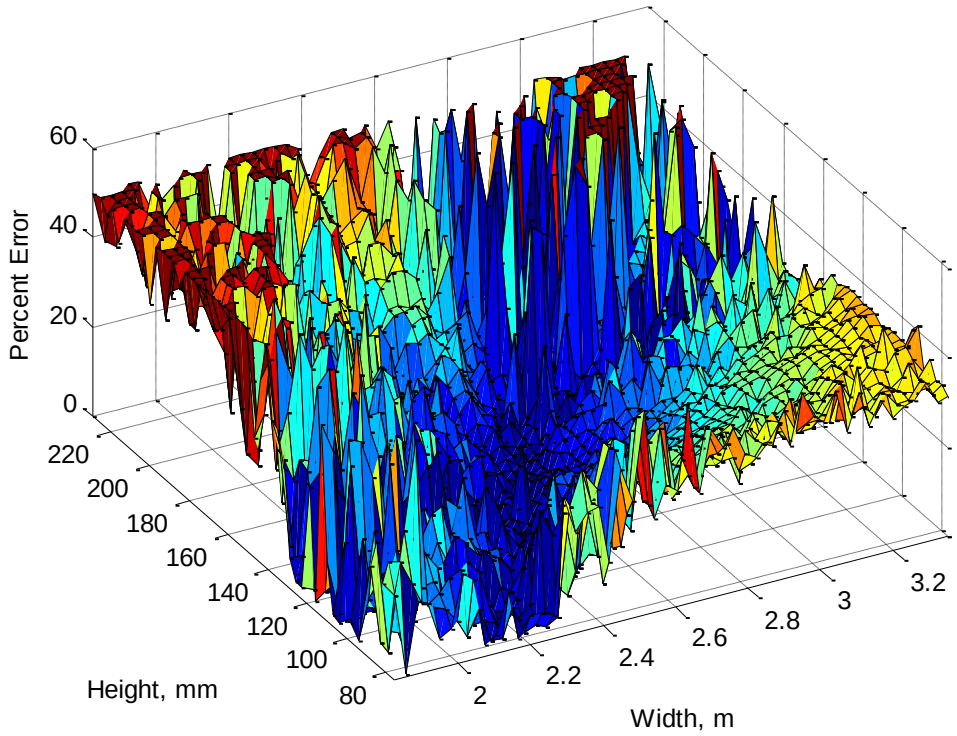

Figure 4.26: Percent Error Due to Variation in Estimated Bump Width and Height

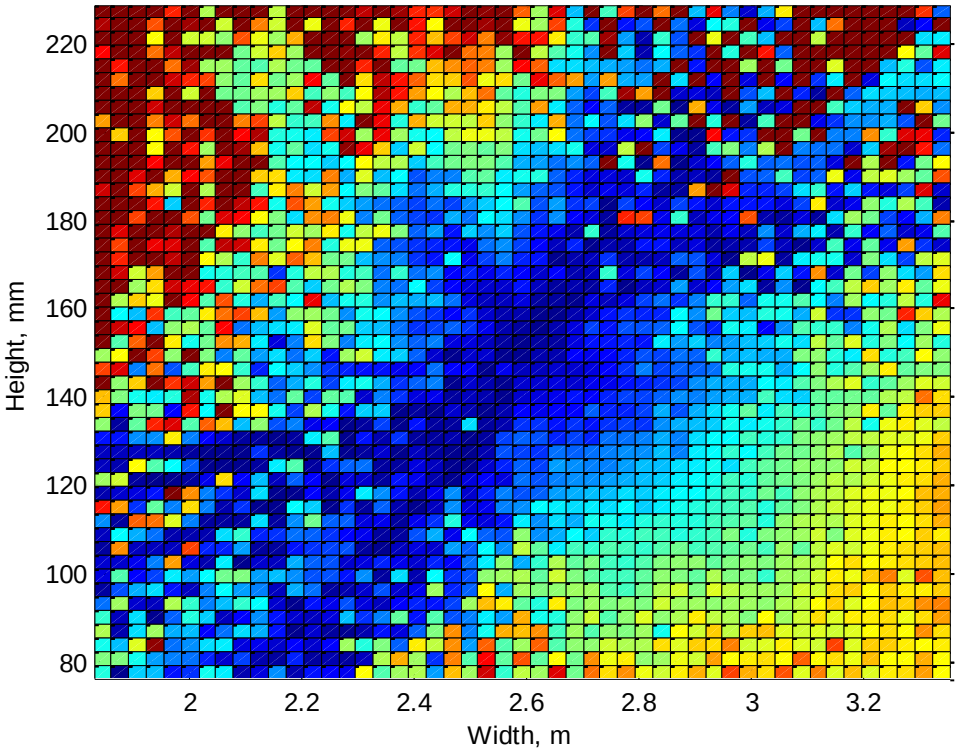

Figure 4.27: Percent Error Due to Variation in Estimated Bump Width and Height

4.4.4 Simultaneous Identification of Mass and Stiffness

This next simulation assumes not only the mass of the vehicle is unknown, but the suspension stiffness as well. To perform this analysis, estimated masses and suspension stiffness are made for a known input/output system. Estimation of mass varies from 700 to 1100 kg, with an exact value of 875 kg. Suspension stiffness for both the front and rear suspension systems is estimated at equal values with a range of 20,000 to 25,000 kg.

The percent error for the predicted vehicle body mass and the suspension stiffness for both the front and rear suspension systems is shown in Table 4.4 through Table 4.6. According to the results, each predicted value falls within 3% of the exact value. This data shows that not only can the use of PEM provide accurate results for a single unknown parameter, but that it can also be used to determine the unknown mass and stiffness simultaneously for systems with known input/output. Information concerning changing stiffness of a system can be used to assess damage to a system, assuming there is no change in mass (Bighamian, et al., 2013).

Table 4.4: Mass Prediction Error for System with Unknown Mass & Stiffness

Predicted Mass Percent Error		Estimated Stiffness, N/m				
		20000	21250	22500	23750	25000
Estimated Mass, kg	700	0.96	2.04	1.96	1.95	1.91
	800	1.43	1.20	1.12	1.45	0.94
	900	1.05	0.68	0.18	0.54	0.67
	1000	1.11	1.14	1.05	1.07	0.84
	1100	1.93	1.92	2.19	1.98	2.40

Table 4.5: Front Suspension Stiffness Prediction Error for System with Unknown Mass & Stiffness

Predicted Stiffness (Front Suspension) Percent Error		Estimated Stiffness, N/m				
		20000	21250	22500	23750	25000
Estimated Mass, kg	700	0.50	1.29	1.04	0.78	0.51
	800	1.29	1.10	0.82	0.84	0.50
	900	0.78	0.83	0.23	0.24	0.24
	1000	0.86	0.89	0.54	0.41	0.65
	1100	0.87	0.38	0.85	0.15	0.18

Table 4.6: Rear Suspension Stiffness Prediction Error for System with Unknown Mass & Stiffness

Predicted Stiffness (Rear Suspension) Percent Error		Estimated Stiffness, N/m				
		20000	21250	22500	23750	25000
Estimated Mass, kg	700	1.66	1.67	1.44	1.16	0.90
	800	1.93	1.83	1.41	1.15	1.16
	900	1.68	2.56	1.74	0.41	0.38
	1000	1.14	1.15	0.89	0.93	1.09
	1100	0.80	0.39	0.69	0.21	0.33

4.4.5 Bridge Bump Identification

As of 1995, of the 600,000 bridges located in the United States, 150,000 of them had bumps formed at the ends (Briaud, et al., 1997). Simply put, these bumps at the ends of the bridges are caused by a differential in settlement at the joint connecting the bridge approach and the bridge deck, as shown in Figure 4.28. Major causes of the bump include compression of the fill material, settlement of the soil beneath the embankment, design and construction errors, high traffic loads, and poor drainage. Additional causes of bump formation are shown in Figure 4.29. Some sources state that at a height differential of 12.7 mm (0.5 in.) between the bridge deck and road pavement, the bridge requires maintenance (Dupont, et al., 2002). A 1995 survey conducted in Illinois showed that more than 27% of bridges had bumps larger than 50.8 mm (2 in.) (Stark, et al., 1995).

One concern surrounding the bumps involves the discomfort they cause on drivers. If the segment of road containing a bridge bump has an IRI of less than 4.0 m/km, it is considered as good quality, while an IRI of 10 m/km for the end of the bridge is considered to be poor quality (Islam, 2010). This next section of the study investigates the use of bridge bumps as a source of vehicle excitation for use with PEM for mass identification.

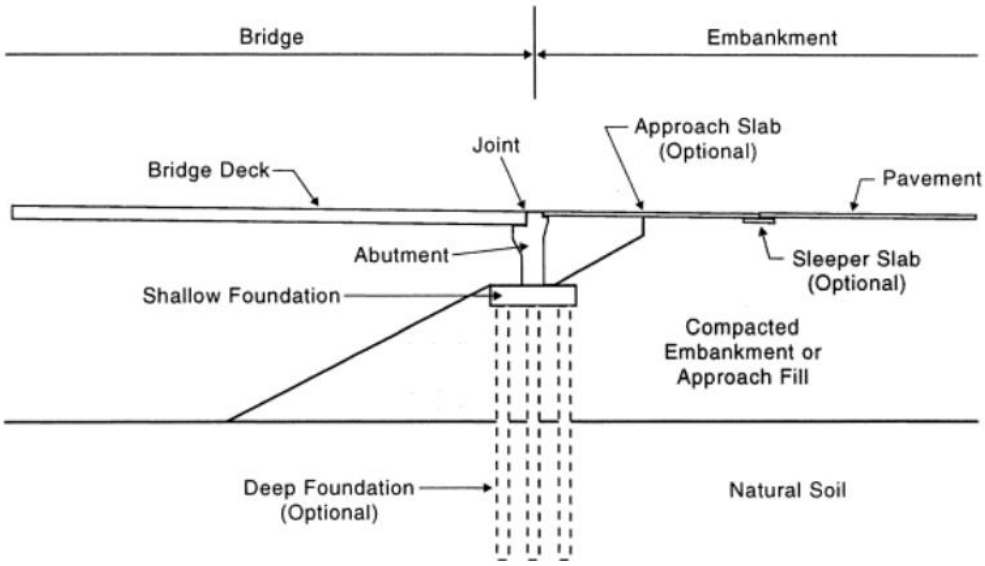

Figure 4.28: Bridge Approach Diagram (Briaud, et al., 1997)

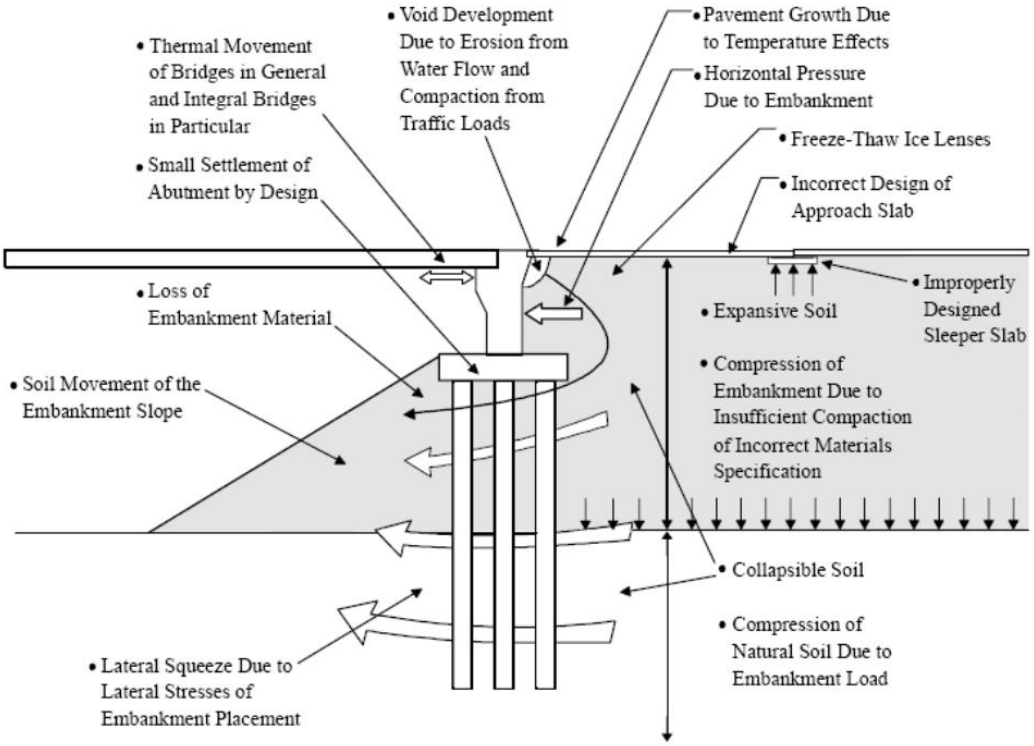

Figure 4.29: Causes of Bridge Bumps (Briaud, et al., 1997)

The use of bridge bumps as an input for system identification is advantageous because the input of the system can be easily located based on the vehicle response. Assuming there is no approach slab, the bump can be modeled as a step (Dupont, et al., 2002). Because the bump is modeled as a step function, the only unknown variable is the height of the step. A simulated response to a bridge bump is shown in Figure 4.30.

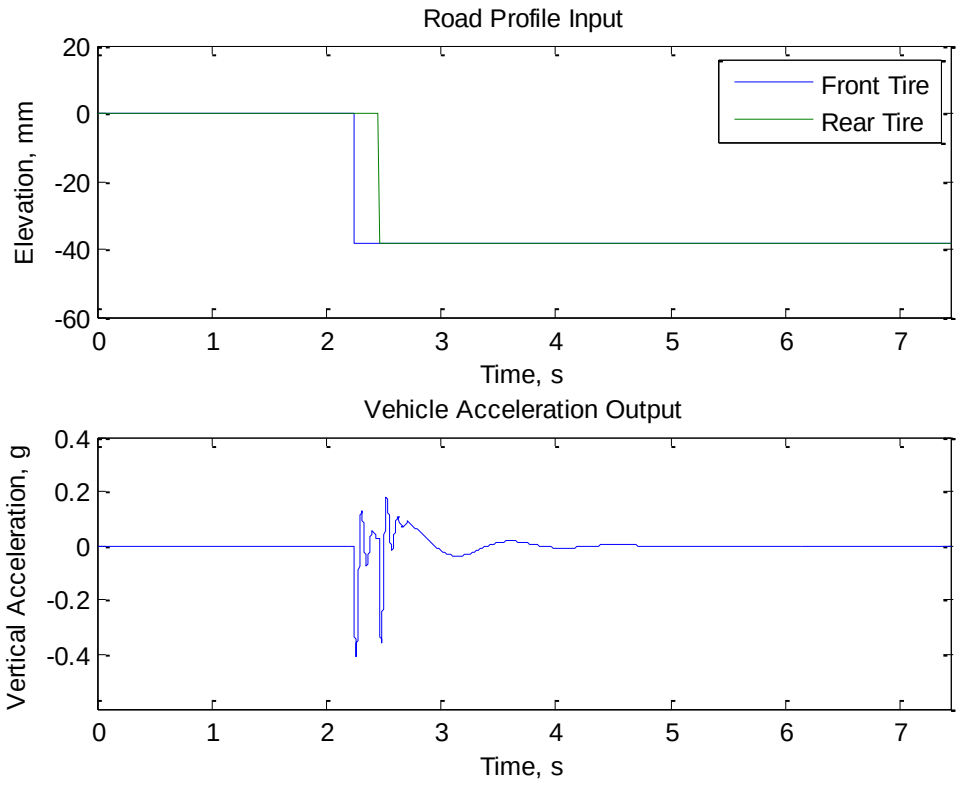

Figure 4.30: Input/Output Response of Bridge Bump

This next analysis is performed using the response of the vehicle model traveling at 48.3 m/s (30 mph) over a 38.1 mm (1.5 in.) step. Mass prediction is performed using estimated step inputs varying from heights of 25.4 to 50.8 mm (1.0 to 2.0 in.). The results are shown in Figure 4.31.

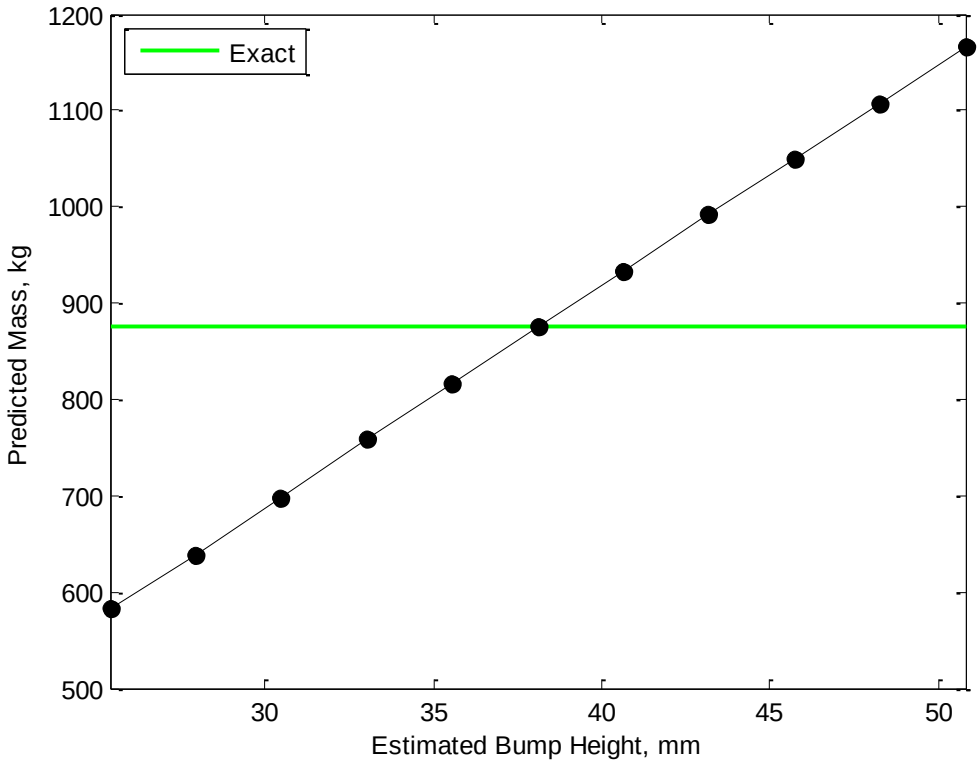

Figure 4.31: Predicted Mass based on Estimated Step Height

These results show that with the amplitude of the step unknown, the system identification analysis provides large amounts of error. It can be seen that the mass is linearly proportion to the estimated height. Although the mass cannot be predicted without knowing the actual step amplitude, these results still have potential application for estimating the input. For a vehicle with a known mass, the step height can be calculated from the amount of error found in the calculation of the predicted mass. This essentially turns the vehicle into a sensor for estimating bridge bump size, which can determine areas in need of maintenance.

4.4.6 Bridge Bump Discomfort

Bridge bumps are an area of great concern because of the amount of discomfort they cause to the vehicle user when travelling over them. This next case demonstrates the amount of discomfort caused by bridge bumps through an investigation of the acceleration response they provide. As shown in Figure 4.32, a bridge bump is modeled as a step on a smooth road with an IRI of 2 m/km. This downward step is given a height of 38.1 mm (1.5 in.). The response of the half car model traveling over the bump at 48.3 (30 mph) is displayed in Figure 4.33. This response clearly shows the effect of the bump to the motion of vehicle when compared to the other sections of the road surface.

To understand how much discomfort this bump causes, the frequency weighted acceleration is calculated based on the response of the vehicle. These values are shown for segments of 1 and 10 m in Figure 4.34 and Figure 4.35, respectively. These frequency weighted acceleration values, based on human comfort criteria, reach up to values close to 1.5 m/s^2. Following the values provided for levels of comfort provided in ISO 2631 and shown in Table 2.5, this amount of vibration would be considered as "uncomfortable" to "very uncomfortable." Even at 10 m segments, it is still clear that this bump causes a discomfort.

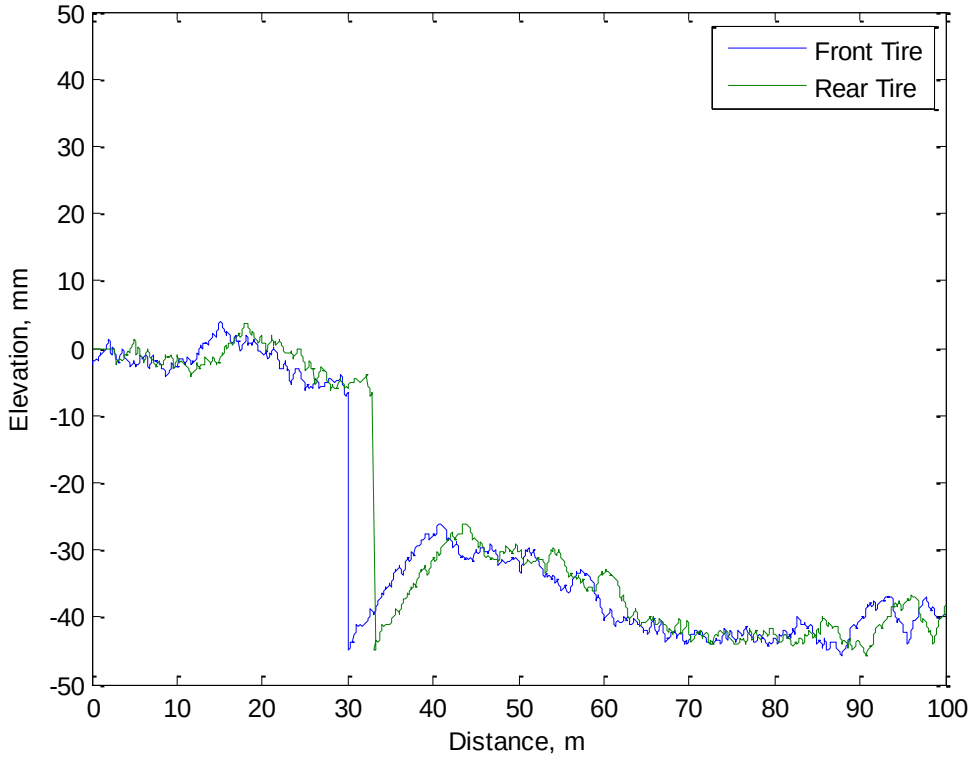

Figure 4.32: Generated Bridge Bump on Smooth Road

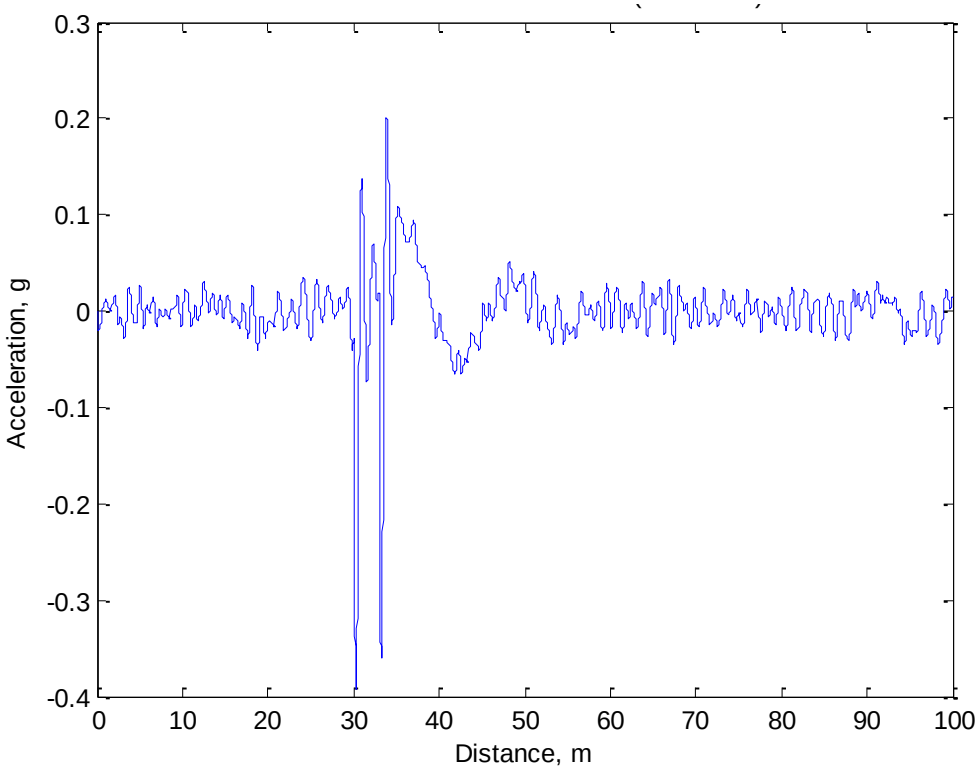

Figure 4.33: Acceleration Response to Bridge Bump

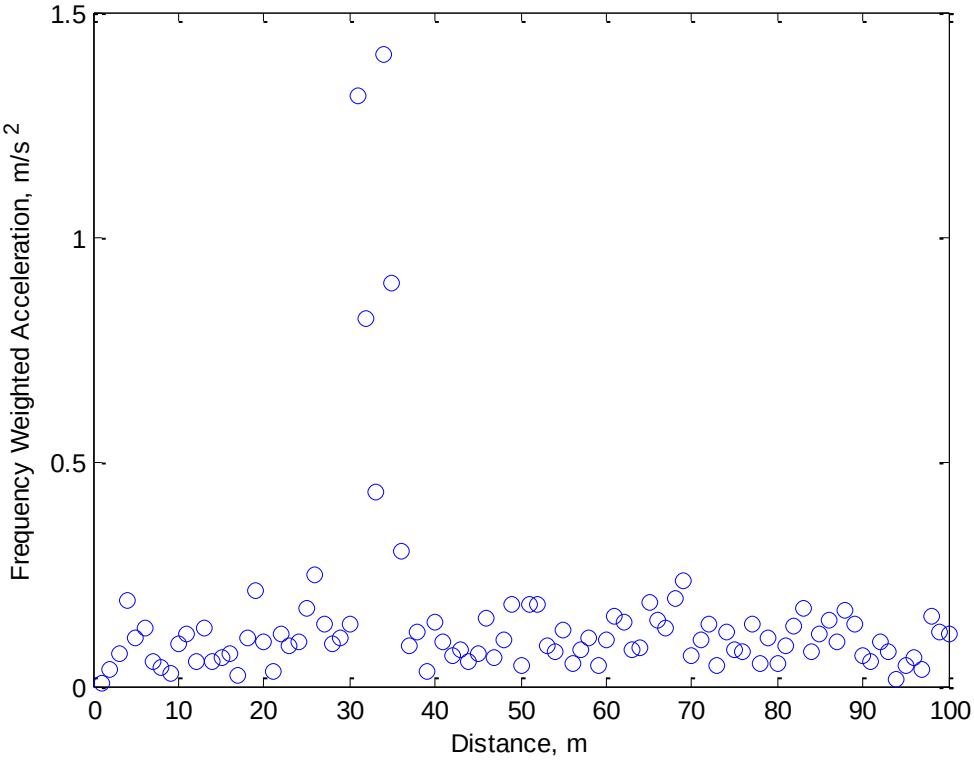

Figure 4.34: Effect of Bridge Bump on Comfort – 1 m Interval

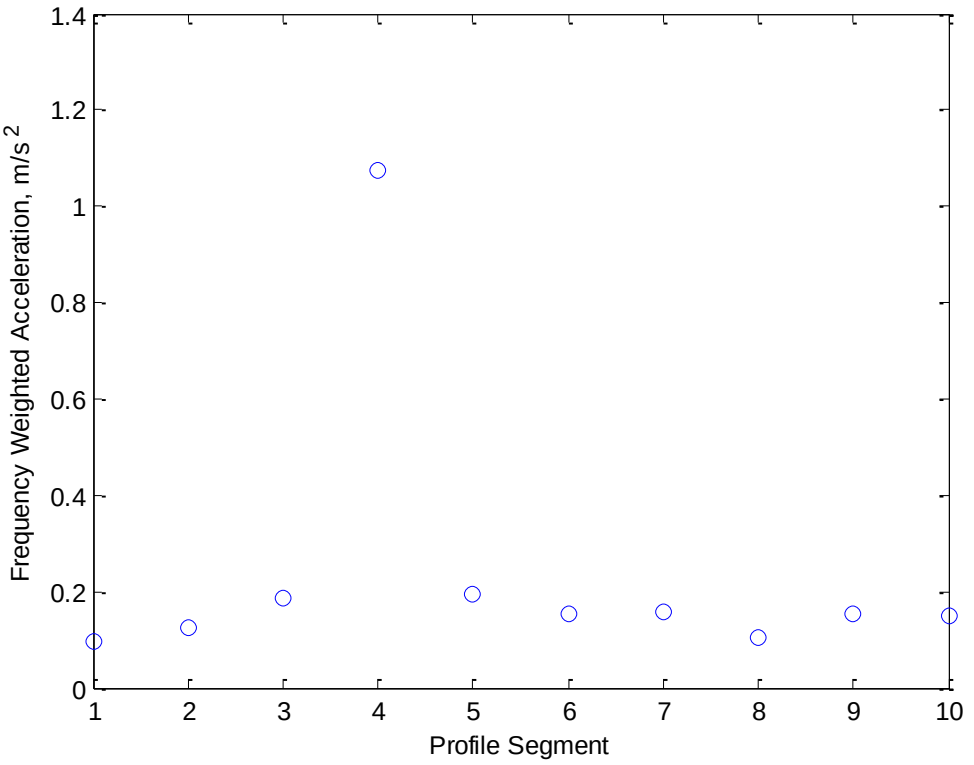

Figure 4.35: Effect of Bridge Bump on Comfort – 10 m Interval

Further simulation is completed to express the range of discomfort based on both a change in bump height and vehicle speed. These points represent the peak frequency weighted acceleration for a vehicle traveling along a road with no roughness aside from the step representing a bridge bump. This is done to isolate the effect of the bump without any additional effects from other sources of roughness. The results displayed in Figure 4.36 are split to show varying ranges of comfort. Points below the lower horizontal green line show a comfortable ride, the section between the two horizontal lines may provide some discomfort, while anything above the red line causes noticeable discomfort.

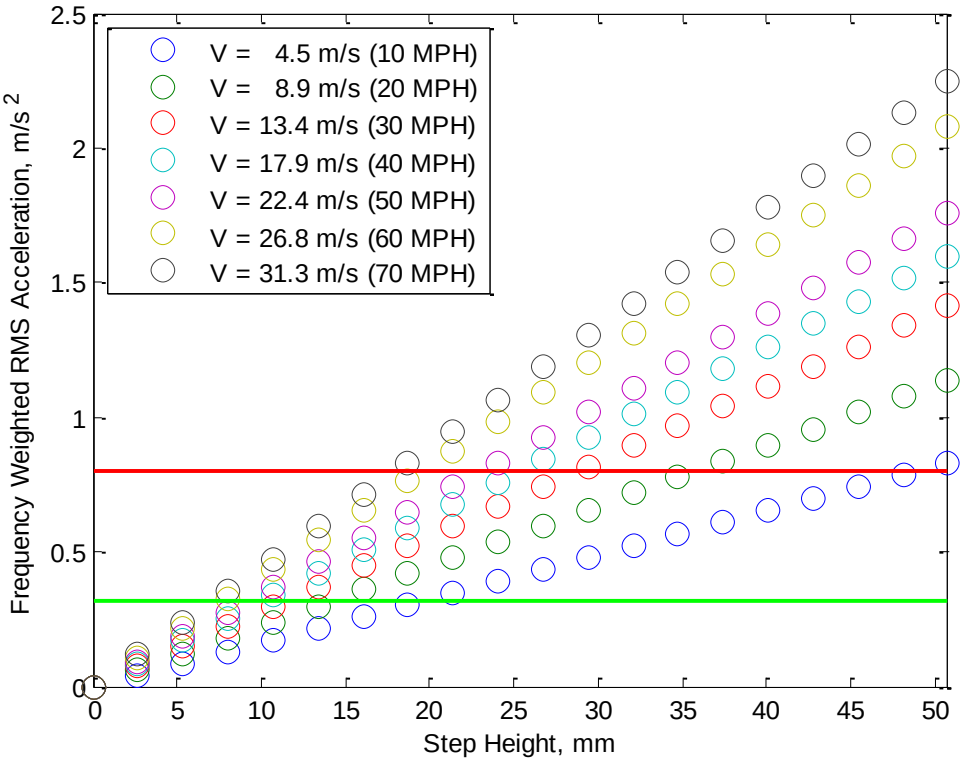

Figure 4.36: Discomfort Due to Bridge Bumps

4.5 Summary of Simulation Results

Simulation of vehicle-road interaction shows the effectiveness of grey-box modeling combined with PEM for vehicle parameter identification. Simulation shows that vehicle mass can be accurately predicted for known input profiles regardless of initial mass estimation even with the inclusion of noise due to road roughness. Sensitivity studies also show the effect of input estimation involving speed bumps. This study shows that the mass can be predicted assuming the estimated input, even if different than the actual input, and can produce a similar response to that of the actual vehicle response. Further studies show that mass and stiffness can simultaneously be predicted for known or accurately estimated input.

In addition to the effect of speed bumps, bridge bumps are also analyzed with assumed step inputs for mass prediction and ride comfort. Performing PEM with varying estimated step amplitude results in a linear correlation between mass prediction and input height estimation under ideal conditions. This proves to be useful for prediction of input height for known vehicle mass based on the deviation of the prediction to the actual mass. Step amplitude and vehicle speed are related to ride comfort to show the effect from the user perspective.

Chapter 5: Field Testing

5.1 Overview of Testing Process

Determining the effectiveness of system identification for unknown vehicle mass is accomplished by collecting the vertical acceleration response through wireless sensing and processing the data with PEM analysis. Testing is performed on a variety of surfaces for this study to understand the behavior of the vehicle based on the input. This includes road surfaces ranging from smooth to rough and damaged pavements. In addition to these surfaces, known inputs are also used, such as speed bumps, bumps at the ends of bridges, and an extension cable used to simulate a pneumatic road tube. For the speed bump, the input is known, while the mass of the vehicle is assumed as unknown.

Figure 5.1: Testing Process for Known Input

For the case of the bumps located at the ends of the bridge, the vehicle parameters are considered to be known and used to estimate the input based on the error in the prediction of the mass.

Figure 5.2: Testing Process for Estimated Input

5.2 Wireless Accelerometer

The iPhone 5S contains many sensors, including an accelerometer, ambient light sensor, proximity sensor, three-axis gyro sensor, and a digital compass. The accelerometer is the Bosch Sensortec BMA220 low-power high performance three axis MEMS sensor. This sensor is capable of recording acceleration from 0.5 Hz to 1 kHz with a range of ±16. The footprint of the sensor is 2 x 2 mm with a height of 0.98 mm (Bosch Sensortec, 2011).

Figure 5.3: iPhone 5S Accelerometer – BMA220 (Bosch Sensortec, 2011)

The acceleration response can be recorded directly on the smartphone using apps for data collection, such as SPARKvue®, shown in Figure 5.4.

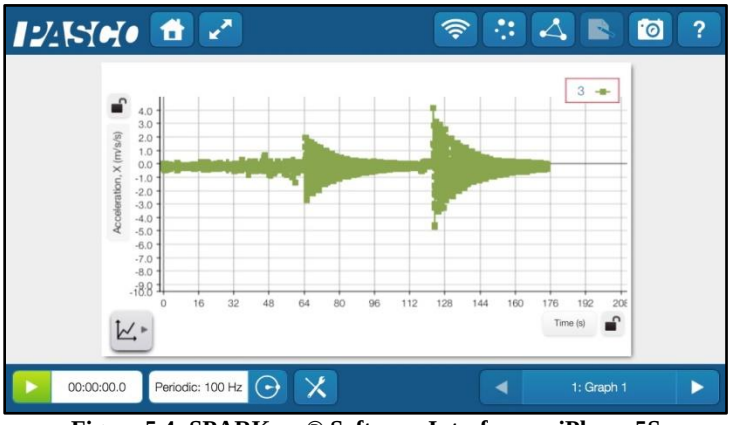

Figure 5.4: SPARKvue® Software Interface on iPhone 5S

Although smartphones are capable of recording acceleration data at large sample rates, the sensor used for testing in this study is the PASCO PS-2119. Shown in Figure 5.5, this three axis acceleration sensor has a range of ±10 g with a resolution of 0.010 g (PASCO, 2015). For wireless communication, this sensor is paired with the AirLink$_2$. The AirLink$_2$ is an interface for the sensors that wirelessly connects to devices for data collection through Bluetooth^{TM}. It has a wireless range of 10 m with a sampling rate up to 1 kHz (PASCO, 2015).

Figure 5.5: PS-2199 3-Axis Accelerometer / PASPORT AirLink$_2$

The reason this sensor is used for testing rather the smartphone is due to its reliability. The PASCO PS-2119 is a commercial grade, factory calibrated sensor. Due to its reliability, this sensor provides a high level of confidence when recording acceleration data used for system identification analysis.

5.3 Model Analysis

To ensure the PS-2119 and iPhone 5S are comparable accelerometers, they are simultaneously used to record the free vibration response of a model structure. This test is also performed to ensure the sensors are properly calibrated by comparing the experimental results with calculated analytical results.

The testing model is a five-story shear frame building made of aluminum floors and polycarbonate siding as shown in Figure 5.6. Each aluminum floor has a plan size of 152.4 mm by 101.6 mm (6 by 4 in.) and a height of 152.4 mm (6 in.) for each story. The side columns consist of a 1.6 mm (1/16 in.) thick polycarbonate sheet. Both accelerometers are tightly clamped side by side to the top of the model using C-clamps. A closer view of this configuration is shown in Figure 5.7.

Figure 5.6: Five-Story Test Model

Figure 5.7: Accelerometer Configuration

Acceleration is recorded for a free vibration response based on an applied displacement of the top floor of the model. The data is recorded with a frequency of 100 Hz. The acceleration response of both sensors is shown in Figure 5.8. Through observation, it is clear that both sensors provide very comparable results based on similar acceleration peaks and matching phase angles. This observation is further verified by comparing the root mean square of each set of data.

Table 5.1: Model Structure Acceleration Response RMS Values

Sensor	RMS (m/s^2)
PS-2119	0.0458
iPhone	0.0445

$$\frac{|(iPhone)_{RMS} - (PS-2119)_{RMS}|}{(\text{PS-2119})_{\text{RMS}}} \times 100\% = \frac{|0.0445 - 0.0458|}{0.0458} \times 100\% = 2.85\% \quad \textbf{(5.1)}$$

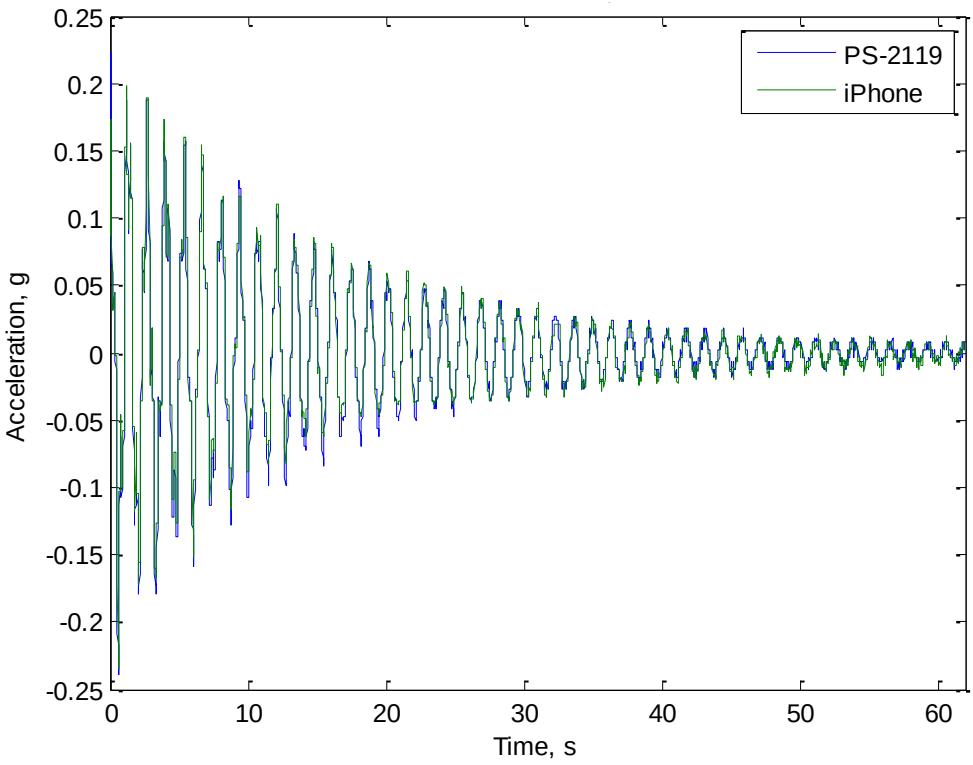

Figure 5.8: Accelerometer Comparison

Analysis of the modal frequencies and a further investigation of the similarities between the two sensors are completed by comparing the FFT in Figure 5.9. The peaks in the FFT represent the modal frequencies of the model structure. The values for the first three modal frequencies are displayed in Table 5.2.

Table 5.2: Model Structure Modal Frequencies

Mode	Frequency, Hz	
	PS-2119	iPhone
1	0.074	0.074
2	2.548	2.548
3	4.226	4.226

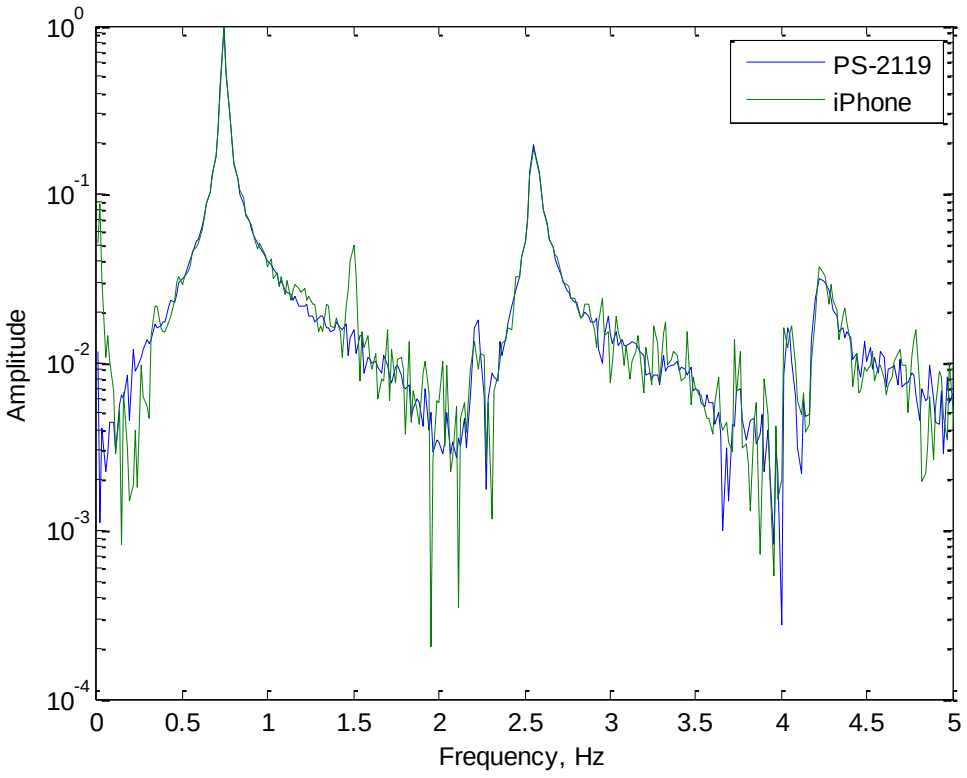

Figure 5.9: Fast Fourier Transform of Recorded Acceleration

An analytical solution is found to confirm the experimental results. The structure can be idealized as a simplified lumped mass structure with five degrees of freedom, one for each floor as displayed in Figure 5.10 (Chopra, 2007). For this idealization, it is assumed that the floors are rigid in flexure and axial deformation is neglected.

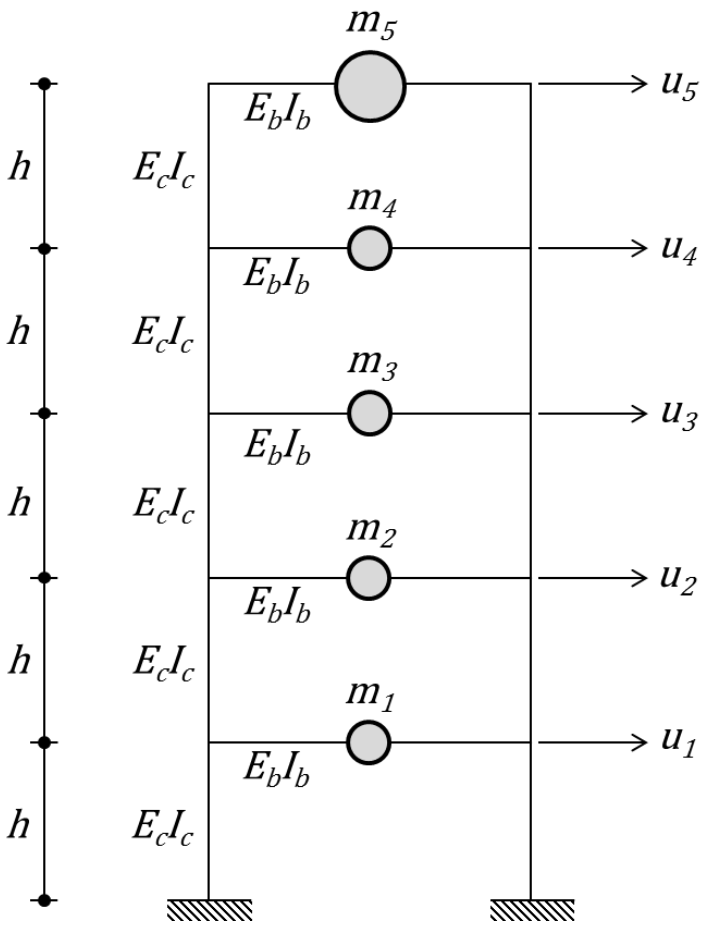

Figure 5.10: Simplified Representation of Test Model

Each of the five degrees of freedom is represented by *u*, which consists of the horizontal movements of each floor of the structure. The mass matrix, shown below, is made up of the mass floor of the structure.

$$M = \begin{bmatrix} m_1 & 0 & 0 & 0 & 0 \\ 0 & m_2 & 0 & 0 & 0 \\ 0 & 0 & m_3 & 0 & 0 \\ 0 & 0 & 0 & m_4 & 0 \\ 0 & 0 & 0 & 0 & m_5 \end{bmatrix}$$

The masses of all the floors are equal except for the top floor, which takes into consideration the additional mass of the sensors and C-clamps. The mass of each component is detailed in Table 5.3.

Table 5.3: Mass of Model Components

Component	Mass, g
Aluminum Block	346
iPhone 5S	112
PS-2119	48
AirLink2	78
C-Clamp	358.34

$$m_1 = m_2 = m_3 = m_4 = 346\ g$$

$$m_5 = 346 + 2 \cdot (358.34) + 112 + (48 + 78) = 1300.7\ g$$

The boundary conditions for the columns can be viewed as torsional spring, meaning they are somewhere between pinned and fixed-end connections. To account for this, the stiffness value is taken between the two terms shown below.

Fixed-Fixed: $k = \frac{3EI}{h^3}$ Fixed-Free: $k = \frac{12EI}{h^3}$

For the polycarbonate siding, $E = 2.2$ GPa, $I = 33.873$ mm^4, and $h = 142.875$ mm

$$K = k\begin{bmatrix} 2 & -1 & 0 & 0 & 0 \\ -1 & 2 & -1 & 0 & 0 \\ 0 & -1 & 2 & -1 & 0 \\ 0 & 0 & -1 & 2 & -1 \\ 0 & 0 & 0 & -1 & 1 \end{bmatrix}$$

The amount of damping must be determined experimentally because it is impossible to be determined analytically (Chopra, 2007). The damping ratio is based on the change in amplitude per cycle of the response of the structure. For lightly damped structures, this value can be obtained using Equation 5.2 with the recorded acceleration data displayed in Figure 5.8.

$$\zeta = \frac{1}{2\pi j} ln \frac{\ddot{u}_i}{\ddot{u}_{i+j}} \quad (5.2)$$

Peak	Time, sec	Acceleration, m/s^2
1	1.19	0.1978
11	14.83	0.8545

$$\zeta = \frac{1}{2\pi(10)} ln \frac{0.198\text{ g}}{0.085\text{ g}} = 0.0134 \text{ or } 1.34\% \quad (5.3)$$

Application of differential equation solutions for the equation of motion for a non-damped structure leads to Equation 5.4, which is used to solve for the natural frequencies as seen in Equation 5.5 (Chopra, 2007).

$$[K - \omega_n^2 M]\phi_n = 0 \tag{5.4}$$

$$det[K - \omega_n^2 M] = 0 \tag{5.5}$$

Performing an eigenvalue analysis of the idealized non-damped system leads to the modal frequencies in Table 5.4.

Table 5.4: Model Structure Modal Frequencies, Experimental vs. Analytical

Mode	Frequency, Hz		Percent Error
	Experimental	Analytical	
1	0.7419	0.7453	0.46%
2	2.548	2.500	1.88%
3	4.226	4.534	7.29%

The experimental and analytical modal frequencies show very similar results. Small analytical error is most likely only due to the simplification of the model for analysis.

The use of this model has not only shown that the iPhone accelerometer can produce results that match expected analytical outcomes, but that its results are extremely similar to that of a commercial grade sensor.

5.4 Testing Setup

All testing in this study is performed using a 2009 Toyota RAV4. For data collection, the PASCO PS-2119 acceleration sensor is firmly attached to the vehicle's center console using Velcro straps as seen in Figure 5.11. In addition to the use of straps, the sensor is pushed down by hand to prevent additional vibration. The sensor is attached to the center console rather than one of the seats due to consistency of data results. Because the seat cushion acts as spring, attaching the sensor to the cushion would add an unknown as to how firmly the cushion is being pressed in and the value of the stiffness constant.

Figure 5.11: Wireless Sensor Setup

Acceleration response is recorded at a fixed sampling rate of 100 Hz. This sampling rate is chosen to ensure all components of vehicle vibrations are properly reported.

Some assumptions are made regarding the vehicle during data collection concerning vehicle speed and dynamics. For all recordings, it is assumed that the vehicle has reached its intended forward moving velocity and remains constant throughout the data collection process. It is also assumed that the vehicle stays in contact with the ground at all times and that the mass is evenly split between the left and right side of the vehicle.

5.5 Testing Results

Test results are shown for the vertical acceleration response for each of the varying inputs. All tests are performed using the 2009 Toyota RAV4 with the PASCO PS-2119 acceleration attached to the center console. The recorded acceleration responses are compared to the simulated results of the half car model found in Chapter 4. If the responses are found to be suitable, they are then used to predict the vehicle mass using system identification methods in Chapter 6.

5.5.1 Road Surfaces

To begin the testing, the acceleration response of the vehicle is recorded while traveling on pavements with varying surface roughness. As shown on the pages 120-123, the road surfaces include a newly paved road, a rough road, a road with damaged pavement, and a parking lot with a row of speed bumps. As previously mentioned, the combination of the size of the input and speed of the vehicle excite different modes of the vehicle. Large bumps at average speeds will excite the sprung mass of the vehicle at 1 Hz, while smaller inputs at high speeds tend to excite unsprung mass used to isolate the vibration from the vehicle body at 10 Hz (Jazar, 2008). The effect of the

road surface on the vehicle resonance can be seen by looking at the response in the frequency domain. For an accurate estimate of the response in the frequency domain, the Fast Fourier transform is implemented on even segments of the acceleration response, which is then summed. This process removed unwanted noise from the frequency domain representation. The effects of each of the tested surfaces on the vehicle response are detailed in Table 5.5. For comparison, the natural frequencies of the half car model used for simulation were found to be 1.1 and 11 Hz.

Table 5.5: Vehicle Response due to Varying Surface Roughness

Surface Type	Vehicle Speed, kph	Max Response, g	f_1, Hz	f_2, Hz
Newly Paved Road	40.2 (25 mph)	0.2017	2.51	13.57
Rough Road	40.2 (25 mph)	0.8899	1.01	12.82
Damaged Pavement	32.2 (20 mph)	0.8437	2.01	12.06
Speed Bumps	16.1 (10 mph)	0.8703	1.51	12.56

Although the newly paved road is fairly smooth, small bumps in the surface excite the response of the vehicle. Due to the small amplitude of the bumps, they are shown to have little effect on the overall resonance of vehicle. As seen in Figure 5.15, due to the consistent unevenness of the surface, the vehicle suspension system vibrate at their natural frequencies. This resonance is also seen for the damaged pavement at a lower vehicle speed.

The speed bumps provide the clearest response for prediction of the vehicle natural frequencies. Due to the first large initial input and following vibration, the frequency domain shows the vehicle to have natural frequencies of 1.51 and 12.56 Hz, which are similar to those calculated using the half car model.

Figure 5.12: Newly Paved Road

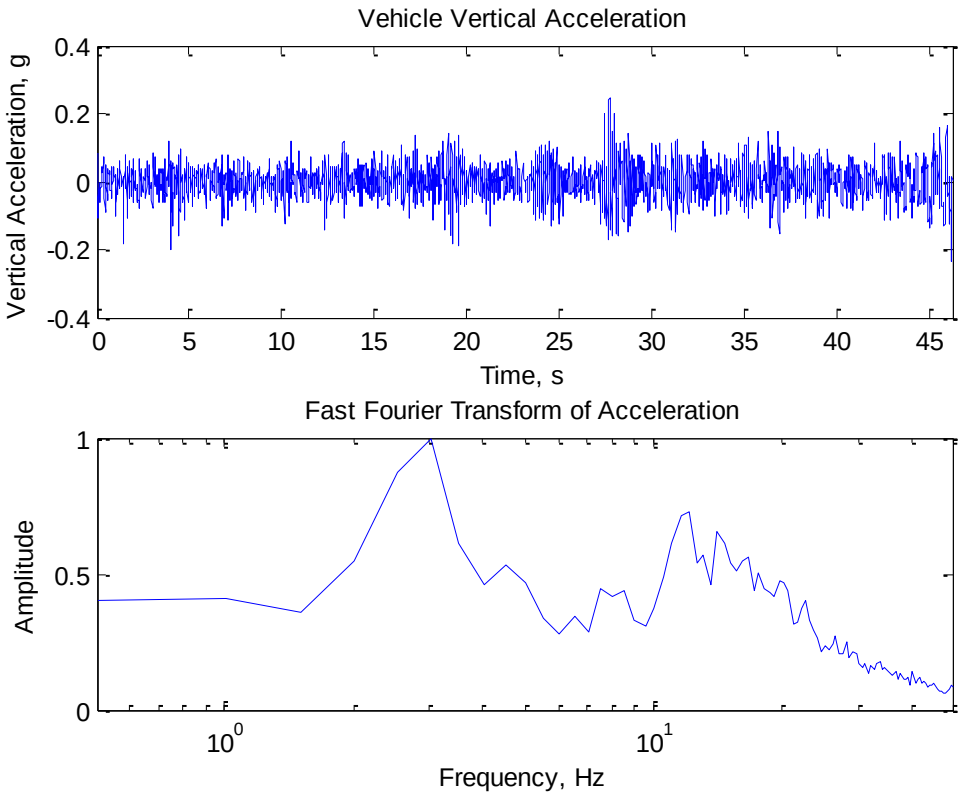

Figure 5.13: Acceleration Response due to Newly Paved Road

Figure 5.14: Rough Road

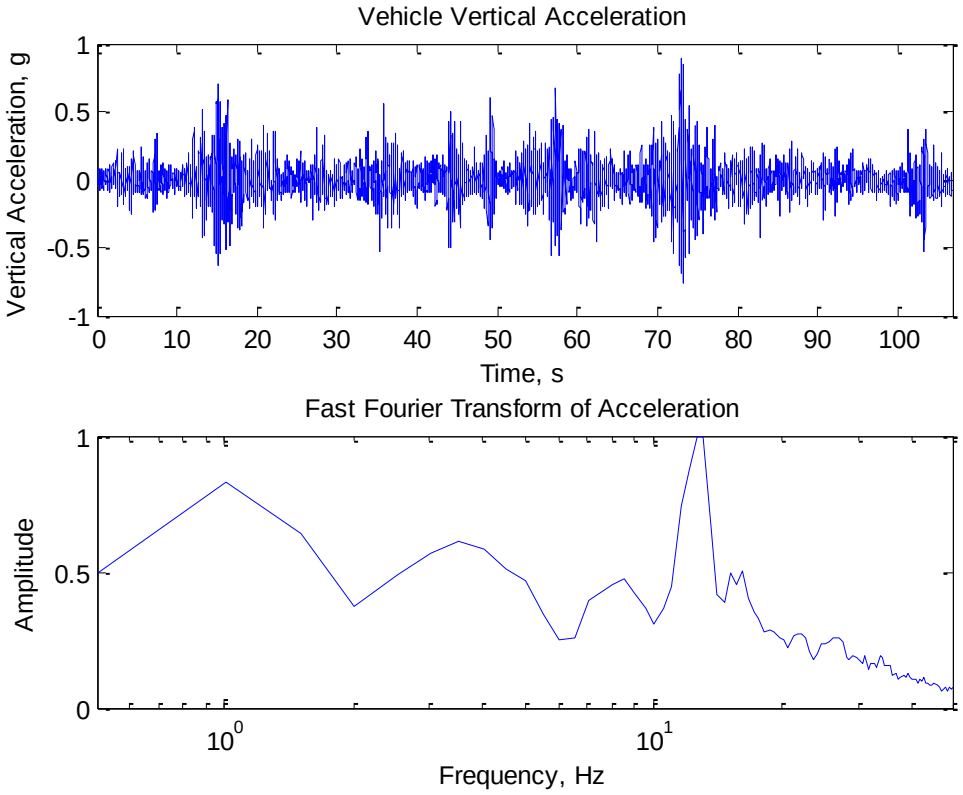

Figure 5.15: Acceleration Response due to Rough Road

Figure 5.16: Damaged Pavement

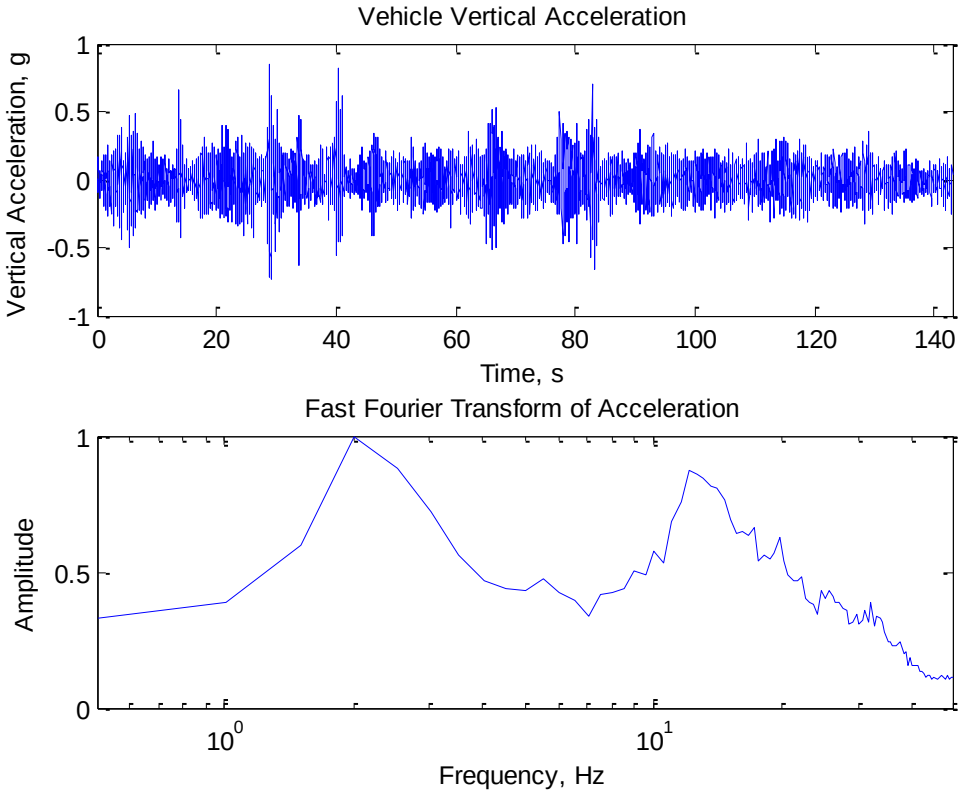

Figure 5.17: Acceleration Response due to Damaged Pavement

Figure 5.18: Speed Bumps

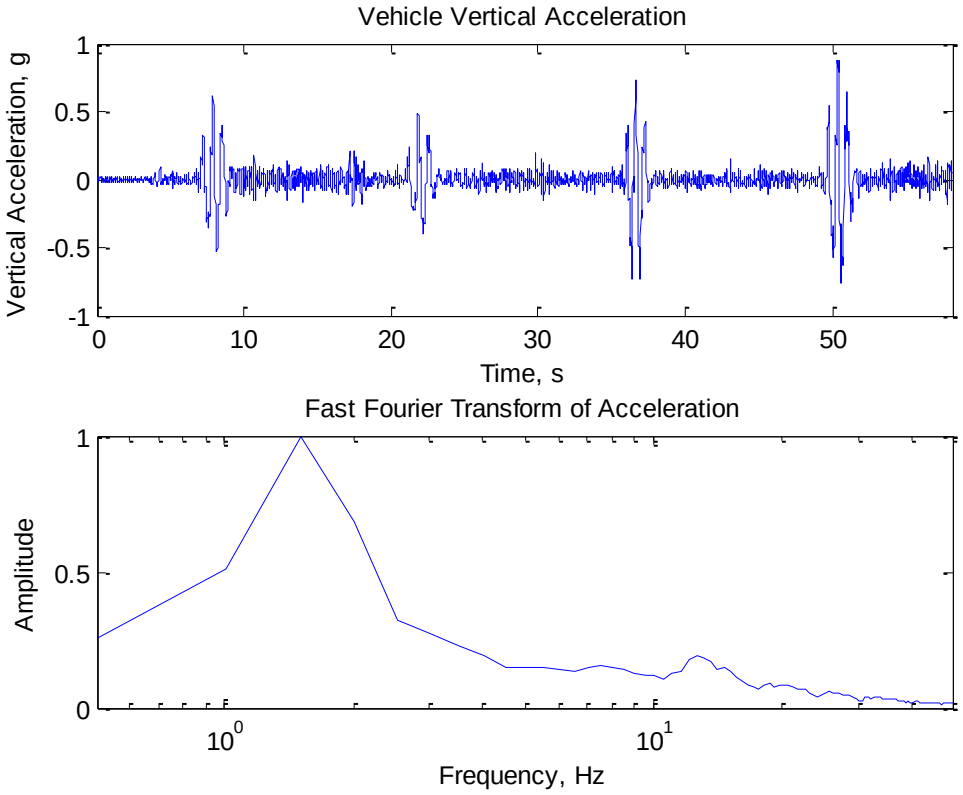

Figure 5.19: Acceleration Response due to Speed Bumps

5.5.2 Speed Bumps

Speed bumps are used as a system input because they provide a large system response and are easy to measure. A set of four similar speed bumps are driven over at 16.1 kph (10 mph). Each speed bump is measured to have a width of 2.60 (8.5 ft) and height of 150 mm (6 in.) as shown in Figure 5.21.

Figure 5.20: Speed Bump

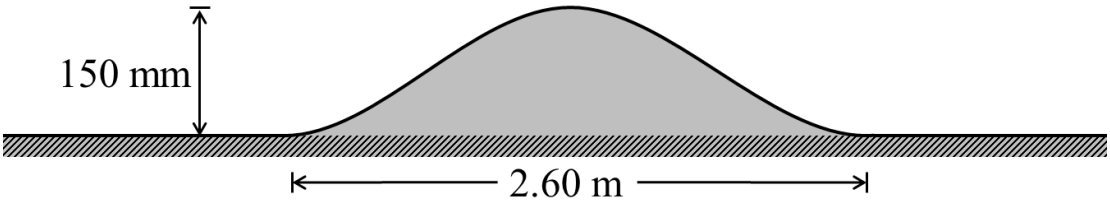

Figure 5.21: Speed Bump used for Testing

As seen in Figure 5.22, the recorded vertical acceleration of the vehicle is very similar to the simulated response of the half car model. Although there is added noise from the roughness of the road itself, the response due to the size of the bump provides a strong signal-to-noise ratio, making the use of this data ideal for performing system identification for mass estimation.

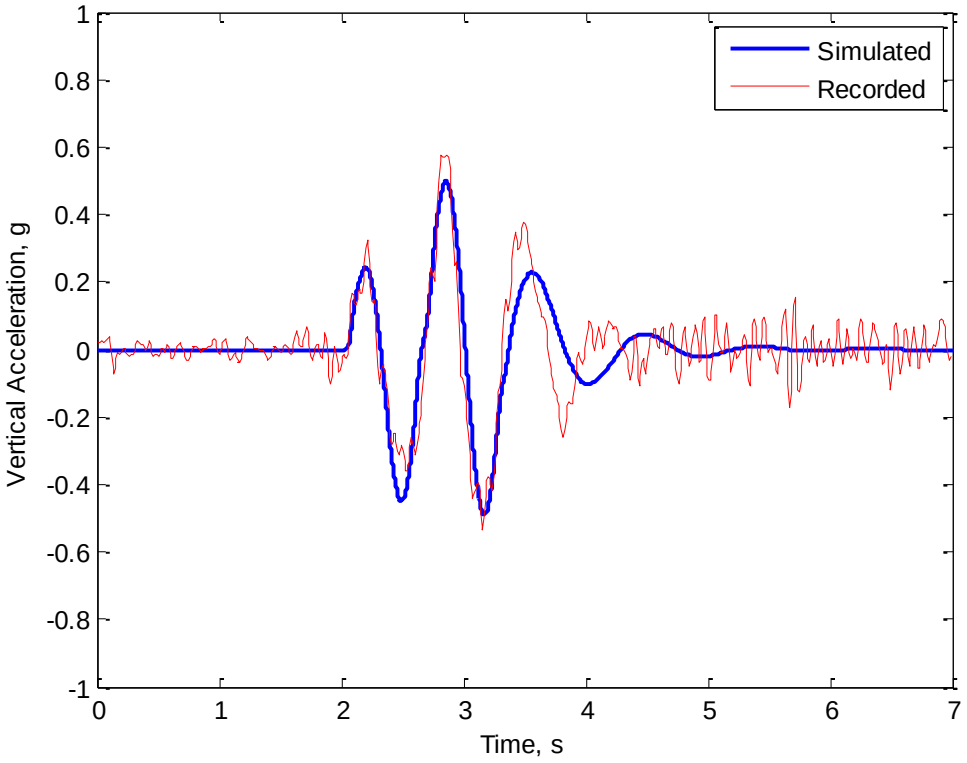

Figure 5.22: Simulated and Recorded Speed Bump Acceleration Response

Data is collected for two sets of the four speed bumps to determine the consistency with the predicted parameter results.

5.5.3 Bridge Bumps

Bumps at the ends of bridges provide a possible source of excitation for the use with system identification methods. The bridge shown in Figure 5.23 is used to test this hypothesis and used to compare the vehicle acceleration response with the simulated response found in Chapter 4. Seen in Figure 5.24, there is a distinct joint where the pavement meets the bridge slab. It is the differential in settlement between these two segments of road that meet at the joint that create the bump felt by the vehicle.

To perform this next test, the vertical acceleration response is recorded while travelling at a speed of 48.2 kph (30 mph). Data is collected at both ends of the bridge to account for possible positive and negative differentials in the step found at the joint. The acceleration response from one of the bridge ends can be seen in Figure 5.25, with a closer look of the response at the bump in Figure 5.26. This data shows how similar the actual response is to the simulated response when assuming a step input. It can clearly be seen when each of the front and rear tires interact with the step input with two large spikes in vertical acceleration when compared to the rest of the vehicle response.

Figure 5.23: Bridge

Figure 5.24: Bridge-End Bump

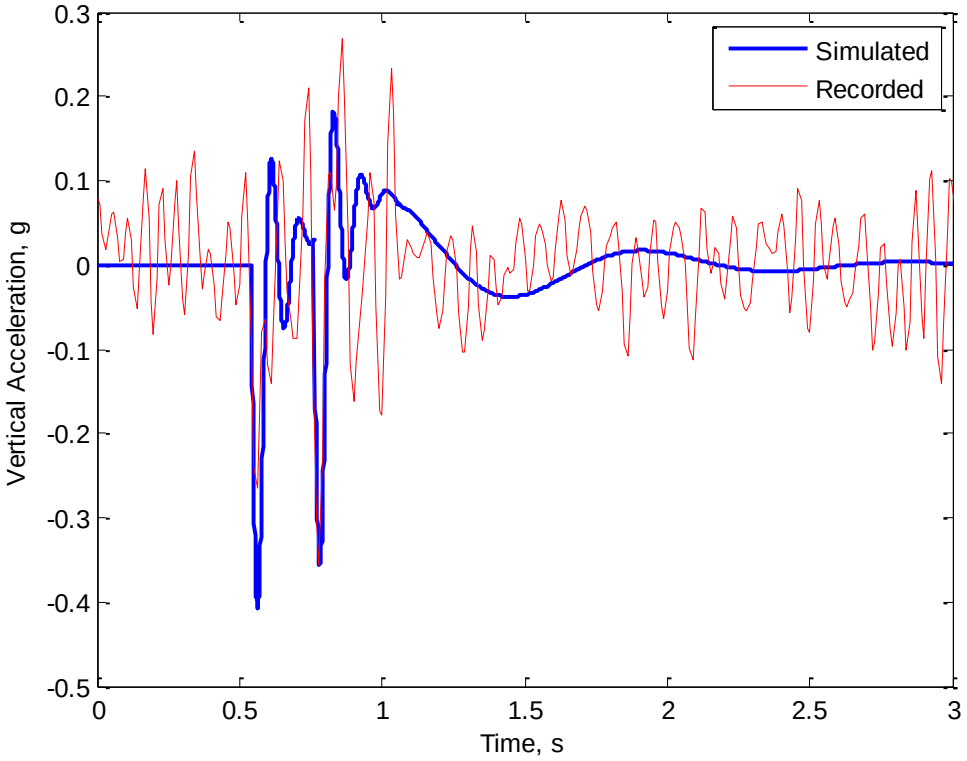

Figure 5.25: Simulated and Recorded Bridge Bump Acceleration Response

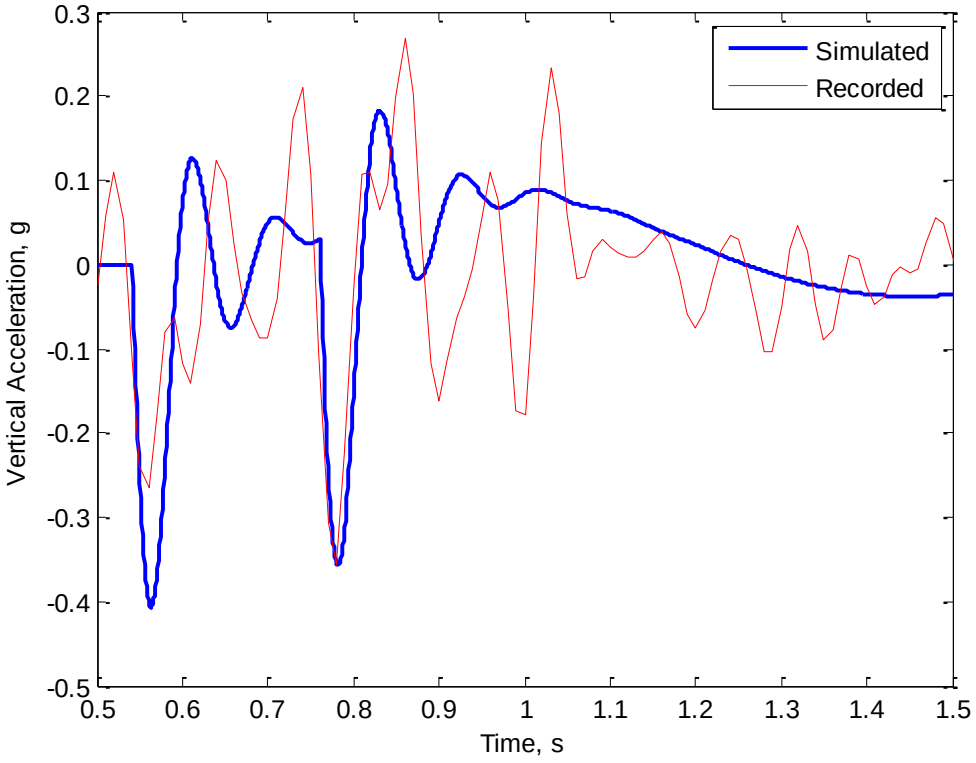

Figure 5.26: Simulated and Recorded Bridge Bump Acceleration Response (Enhanced View)

5.5.4 Effects of Pneumatic Road Tube

Commonly seen across roads in the United States, pneumatic road tubes are used for collecting traffic volume and vehicle speed (McGowen, et al., 2011). The use of rubber tubes creates a means of data collection that is non-obstructive to the driver while traveling over them. The goal of this next test is to determine whether these road tubes can cause enough excitation to the passing vehicle for system identification or if the response is isolated from the motion of the vehicle body.

Performing this test is accomplished through the use of a 6.35 mm (0.25 inch) diameter extension cable in place of a standard pneumatic road tube as shown in Figure 5.27. The cable is firmly stretched and taped in the center and on each end to prevent movement while the vehicle passes. This test is performed in a parking lot to prevent additional road roughness from interfering with the input of the cable.

Figure 5.27: Extension Cord used for Testing

Acceleration response when driven at 16.1 kph (10 mph) is shown in Figure 5.28. The two arrows show the points at which the front and rear tires hit, respectively. Although visible in this test, the response of the signal is not much greater than the response due to the natural uneveness of the road even on a smooth road profile.

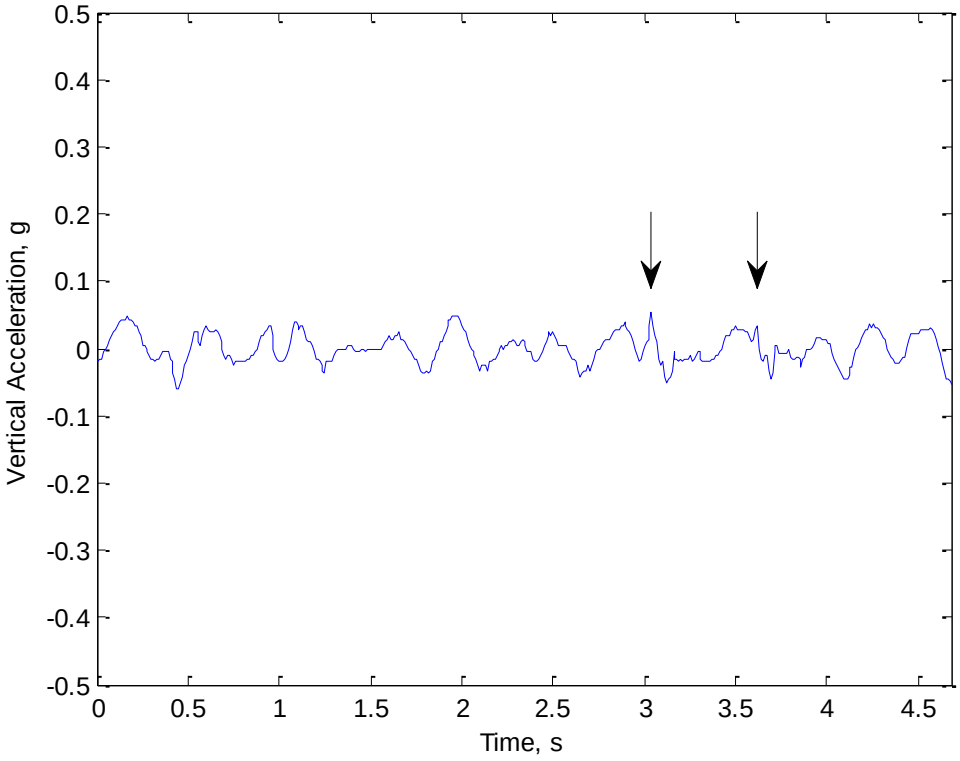

Figure 5.28: Pneumatic Road Tube, 16.1 kph (10 mph)

Tested again at a higher vehicle speed, the location of the excitation due to the cable cannot even be determined due to the overall amount of vibration cause by roughness of the parking lot pavement itself.

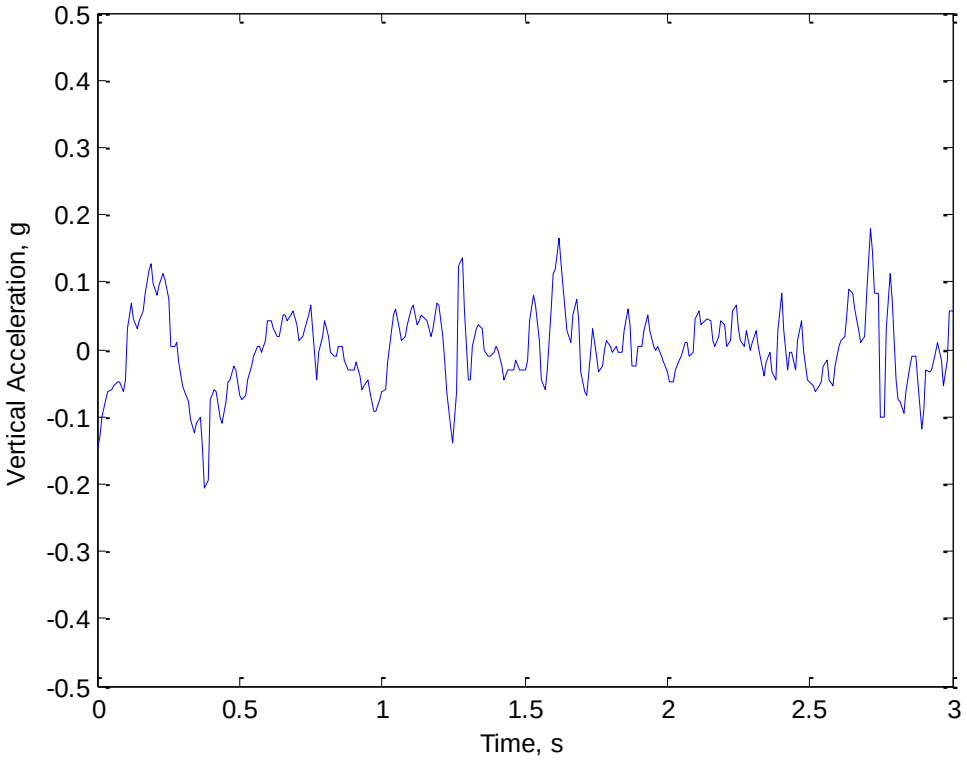

Figure 5.29: Pneumatic Road Tube, 32.2 kph (20 mph)

This pilot shows that the use of road tubes do not provide much excitation in this specific situation. Due to the small vehicle response compared to the noise from the pavement itself, it can be seen that a larger source of excitation is needed to perform system identification analysis. This test only accounts for a specific scenario at low vehicle speeds. Additional testing is needed to further evaluate the practicality of pneumatic road tubes for use with parameter identification techniques.

Chapter 6: Data Processing

6.1 Data Processing Overview

This chapter presents the processed data collected throughout the field tests. This includes the acceleration response from sources of excitation including speed bumps, bridge bumps, and various roads in the surrounding area. Analysis is performed using parameter identification methods for mass and input estimation. Acceleration response is correlated to road roughness for a road profile map based on IRI values. A second map shows the comfort perceived by the user of the vehicle.

6.2 Parameter Identification

Data collected through field testing is analyzed through the use of parameter identification with PEM and grey-box modeling. Speed bumps and bridge bumps are both analyzed as sources of input excitation, while the simulated pneumatic road tube is omitted due to the small response in this study. Each test is recorded twice to determine the consistency with the results. For each trial, the initial mass is estimated at 875 kg.

6.2.1 System Identification: Speed Bumps

For parameter identification using speed bumps, the size of the input either has to be known or estimated. In this case, the input is known to have a width of 2.60 (8.5 ft) and a height of 150 mm (6 in.). The generated input bump is related to the recorded acceleration output for parameter estimation through the use of grey-box modeling. Shown in Figure 6.1, the bump is estimated and modeled using a cosine function. This estimated input is used with the response shown below to determine the actual mass of the system. A 20 Hz low pass filter is applied to the recorded data to remove any noise due to vehicle vibrations caused by anything other than the expected input.

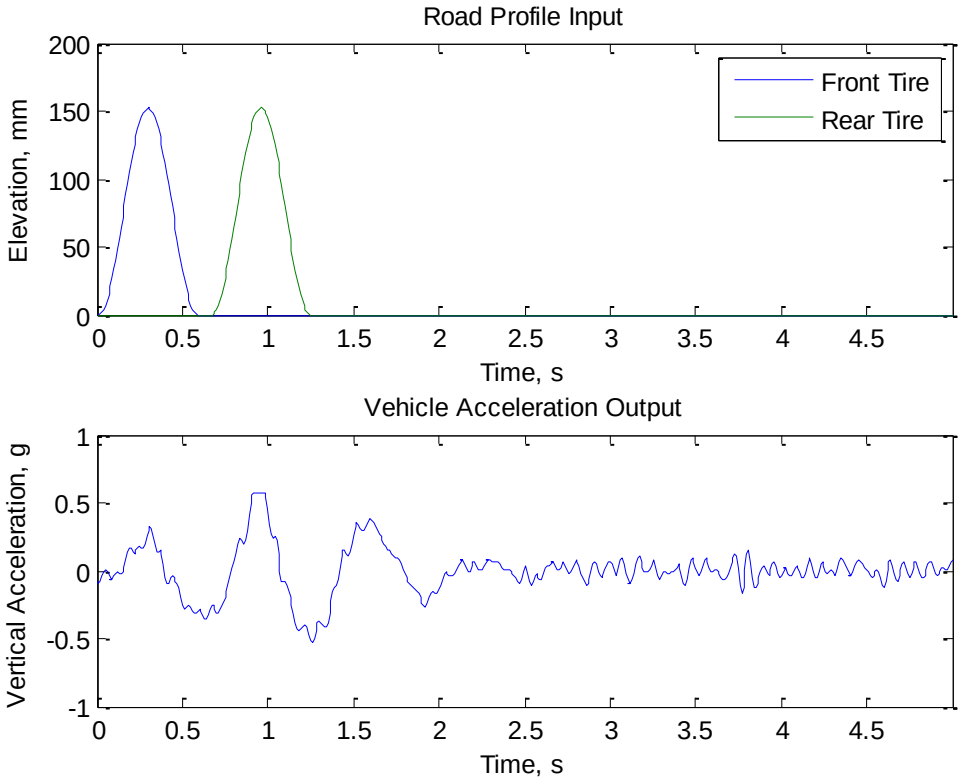

Figure 6.1: Speed Bump Response used for Mass Estimation

The mass is predicted for two sets of four bumps to ensure consistency. The results for the both trials are shown in Table 6.1 and Table 6.2.

Table 6.1: Predicted Mass - Speed Bumps, Trial 1

Bump	Predicted Mass, kg	Percent Error
1	870.658	0.50%
2	927.464	6.00%
3	519.555	40.62%
4	672.677	23.12%

Table 6.2: Predicted Mass - Speed Bumps, Trial 2

Bump	Predicted Mass, kg	Percent Error
1	844.053	3.54%
2	911.141	4.13%
3	660.512	24.51%
4	817.204	6.61%

While adequate results are found for the first two bumps, bumps three and four include error. Possible sources of error include discrepancy of actual bump width and height, changes in vehicle speed, and additional vehicle excitation from the surrounding area. The full set of estimated inputs and recorded response can be found in Appendix B.

6.2.2 System Identification: Bridge Bump

Theoretical system identification methods applied to ideal bridge bump step input excitation show that the predicted vehicle mass is proportional to the step amplitude estimation. Although this information cannot be used to predict unknown vehicle mass, it can be used to determine the step amplitude if the mass is already known. As seen in Figure 6.2, the bridge selected for this study does provide a noticeable excitation to the vehicle where the pavement meets the bridge deck, but does not provide a strong signal-to-noise ratio necessary to accommodate accurate performance of system identification methods.

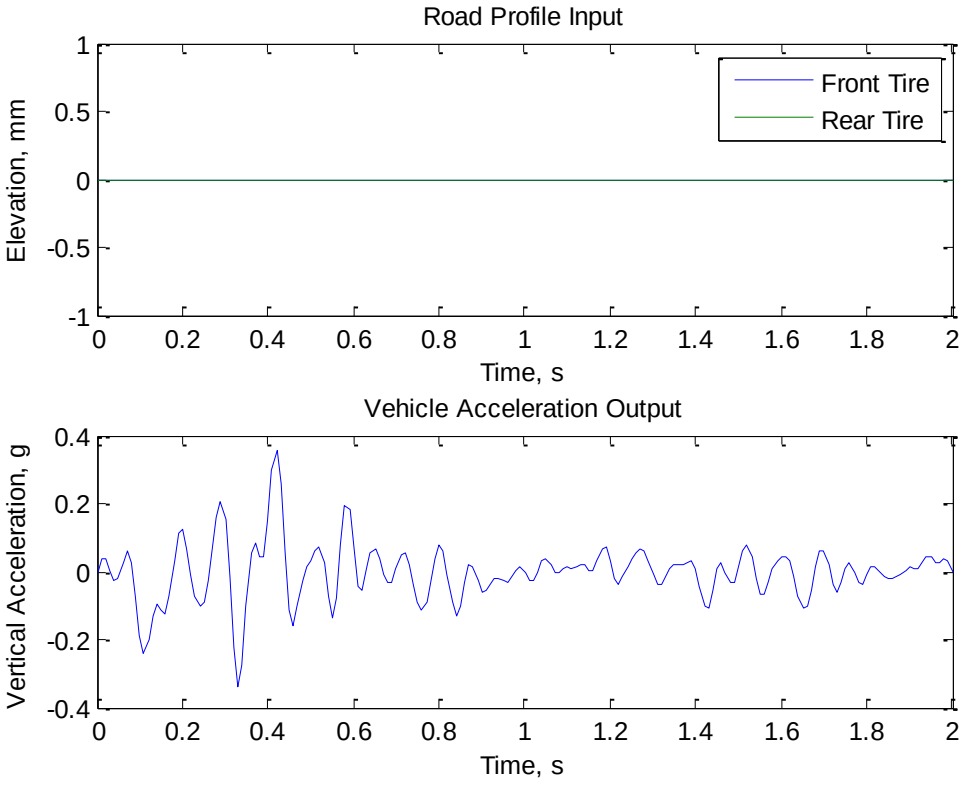

Figure 6.2: Bridge Bump Response used for Mass Estimation

It is found that performing parameter identification through the use of PEM offers meaningless results estimating any step amplitude other than zero for this case. Because of this, the input is modeled as a flat surface.

Table 6.3: Predicted Mass - Bridge Bump, Trial 1

Bump	Predicted Mass, kg	Percent Error
1-1	700.528	19.94%
1-2	596.911	31.78%
2-1	576.042	34.17%
2-2	416.843	52.36%

Table 6.4: Predicted Mass - Bridge Bump, Trial 2

Bump	Predicted Mass, kg	Percent Error
1-1	1398.92	59.88%
1-2	983.834	12.44%
2-1	460.687	47.35%
2-2	496.564	43.25%

The results presented in Table 6.3 and Table 6.4 show inconsistencies between each trial. This error may be caused by the weak signal-to-noise ratio in addition to the sources of excitation surrounding the bridge bump. Although testing on this bridge does not provide beneficial results for the use of system identification methods, statistical analysis can be performed across many different bridges to draw further conclusions concerning the viability of bridge bumps as a source of excitation for parameter identification.

6.3 Road Profile Identification

Once the vehicle parameters are known, either through system identification or previously known properties, the relation of the acceleration response can be directly related to the roughness of the profile. The relation between the vehicle output response and the IRI is shown in Figure 6.3.

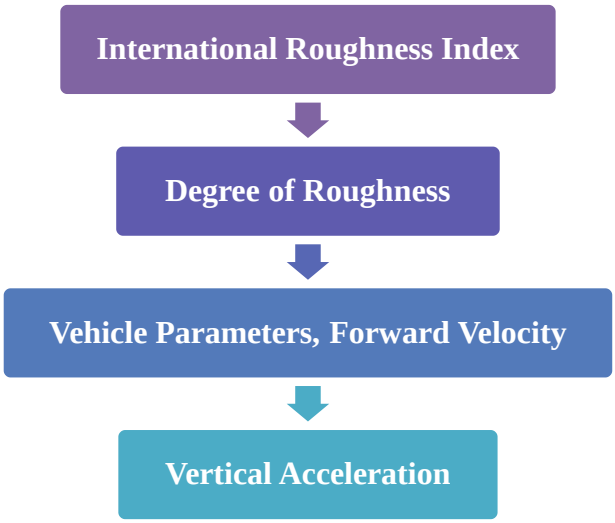

Figure 6.3: Relation of Vertical Acceleration to the International Roughness Index

The vehicle response varies based on a combination of the vehicle forward moving speed and the roughness of the road surface. To determine this relationship, simulation of a moving vehicle is performed on generated road profiles ranging in roughness. With this relationship defined, a correlation can be used to approximate the IRI based on the acceleration response of the vehicle.

This correlation is determined using 100 m simulated road profiles with varying degrees of roughness, ranging from G_d = 2 cm^3 to G_d = 4096 cm^3. This range is chosen to include smooth roads and extremely rough roads in the simulation. For each

profile, the half car model with known parameters is simulated at speeds of 4.5 m/s (10 mph) to 31.3 m/s (70 mph) to observe the variance in vehicle response. Results are found empirically and are shown in Figure 6.4. Power trendlines are used to show the relation between the RMS of the acceleration and the IRI based on the nonlinear relationship. The relation is shown again using a log-log scale in Figure 6.5. This relation shows that roads with larger amounts of roughness produce larger acceleration response at higher speeds. To determine consistency of these results, simulation is performed a second time with a shorter road length. The output proves to be independent of segment length for this analysis as each profile simulates a specific roughness to avoid any change in response over time.

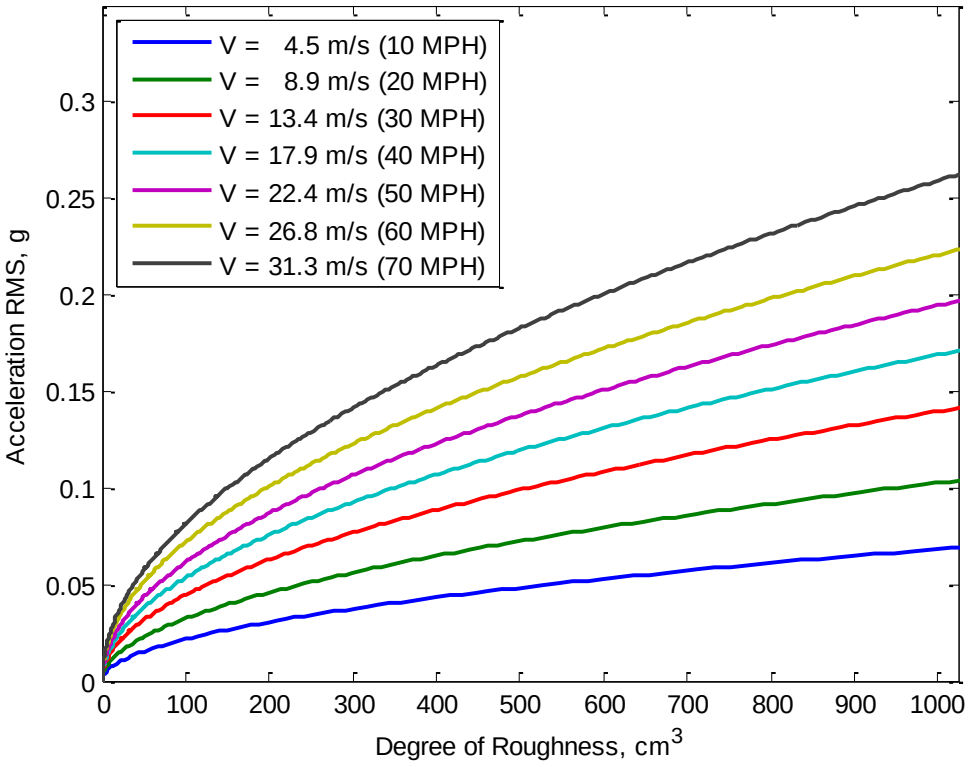

Figure 6.4: Relation of Degree of Roughness and Vertical Acceleration

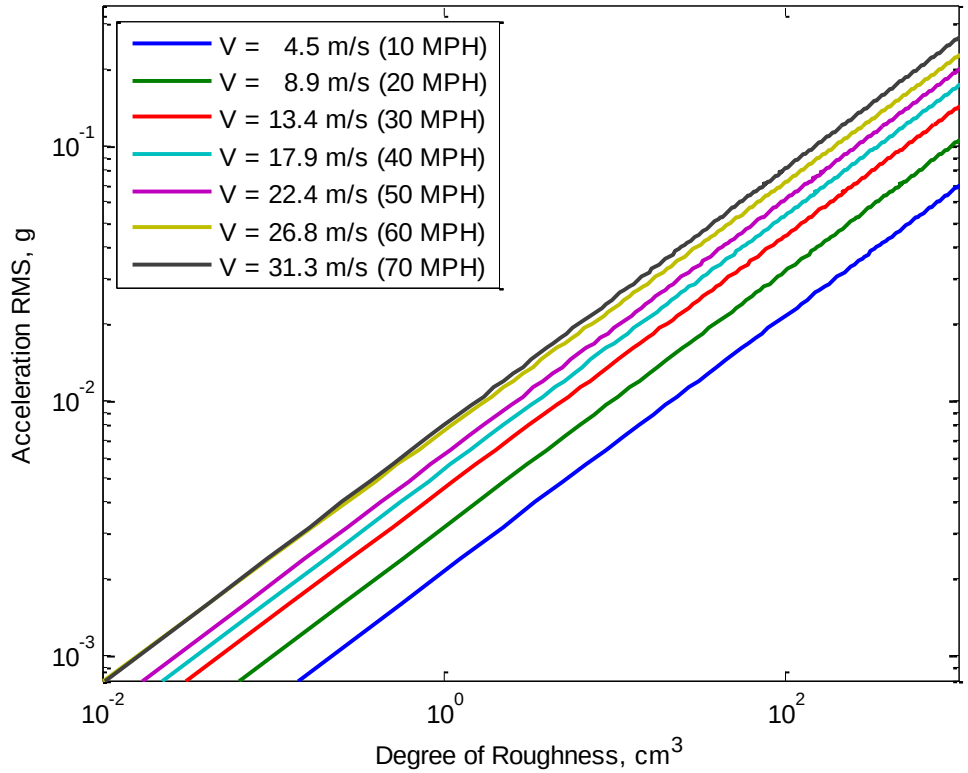

Figure 6.5: Relation of Degree of Roughness and Vertical Acceleration (Log-Log)

To further analysis this correlation, the root mean square of the acceleration response is directly related to the IRI using the relation found in Equation 4.39, relating the IRI to the roughness coefficient. Applying this conversion gives a direct linear relation between the IRI and acceleration response, as shown in Figure 6.6.

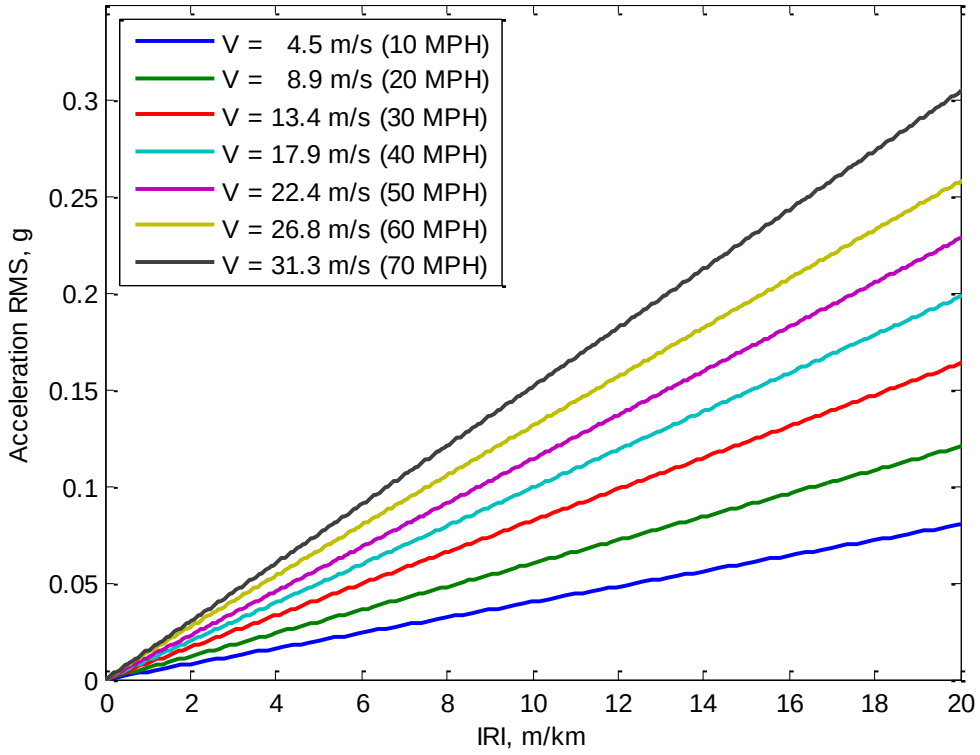

Figure 6.6: Relation between Vertical Acceleration Response and IRI

This relationship is valuable because it essentially turns every vehicle into a high-speed road profiler through the use of wireless sensing. This relation can be pre-calculated for a large variety of vehicles with varying parameters and is used to determine the roughness of the roads being traversed. Normally, the IRI is reported annually for national highway systems and up to every two years for all other roads (FHWA, 2014). Through the use of wireless sensors, the roughness of the road can be continuously monitored and areas of concern can be immediately discovered.

The effect of changing vehicle parameters is analyzed by adding mass to the vehicle and evaluating a change in the correlation between the IRI and acceleration response. The updated correlation is shown in Figure 6.7 for the addition of two passengers to the vehicle. Comparing this updated correlation with the added mass against the original relationship, it can be seen that the addition of mass to the vehicle decreases the acceleration response regardless of road roughness or vehicle speed. An exaggerated case, doubling the original mass of the vehicle, is shown in Figure 6.8.

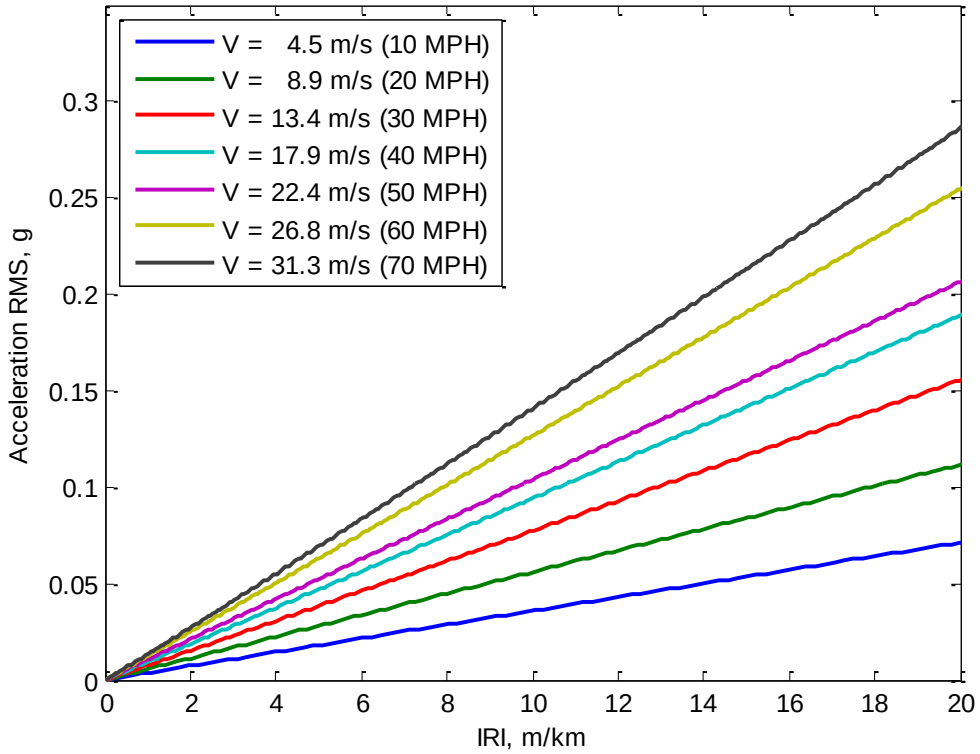

Figure 6.7: Relation between Vertical Acceleration Response and IRI - Two Additional Passengers

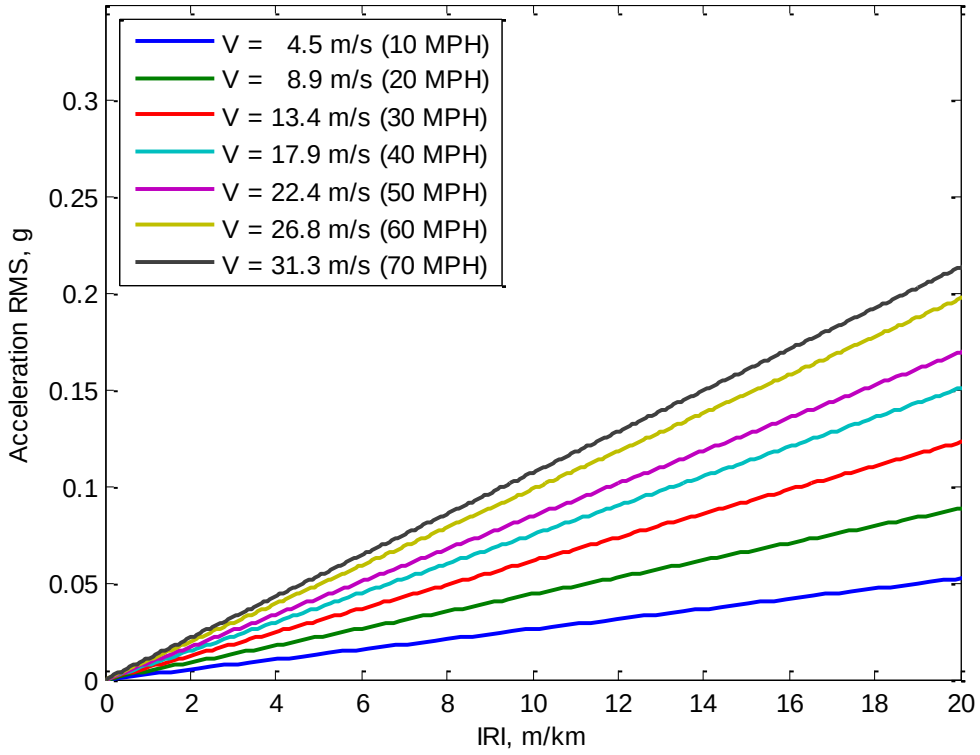

Figure 6.8: Relation between Vertical Acceleration Response and IRI - Double Vehicle Body Mass

6.3.1 Verification of Acceleration to IRI Relationship

To verify the relationship of the acceleration response to the IRI found in Figure 6.6, a sample road profile recorded with a high-speed road profiler is used (ProVAL, 2015). This profile, shown in Figure 6.9, is used to compare the exact IRI using ProVAL against the approximated values found using the acceleration response relation.

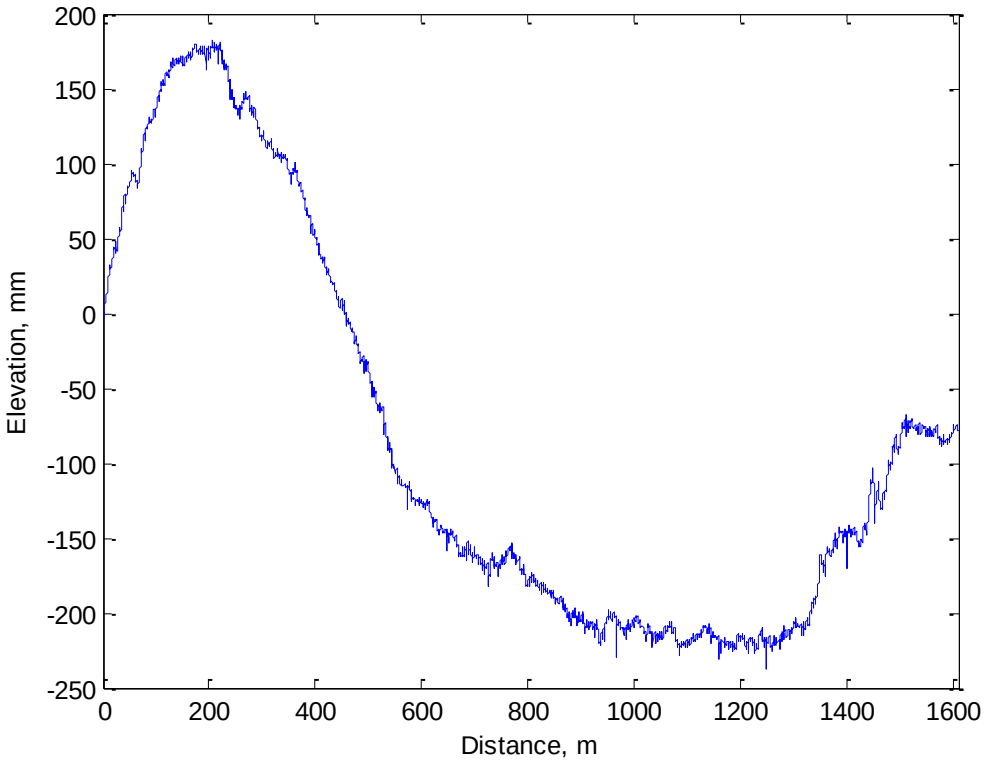

Figure 6.9: Measured Profile

The half car model is used to simulate the vertical acceleration response used to estimate the IRI. This response is shown in Figure 6.10.

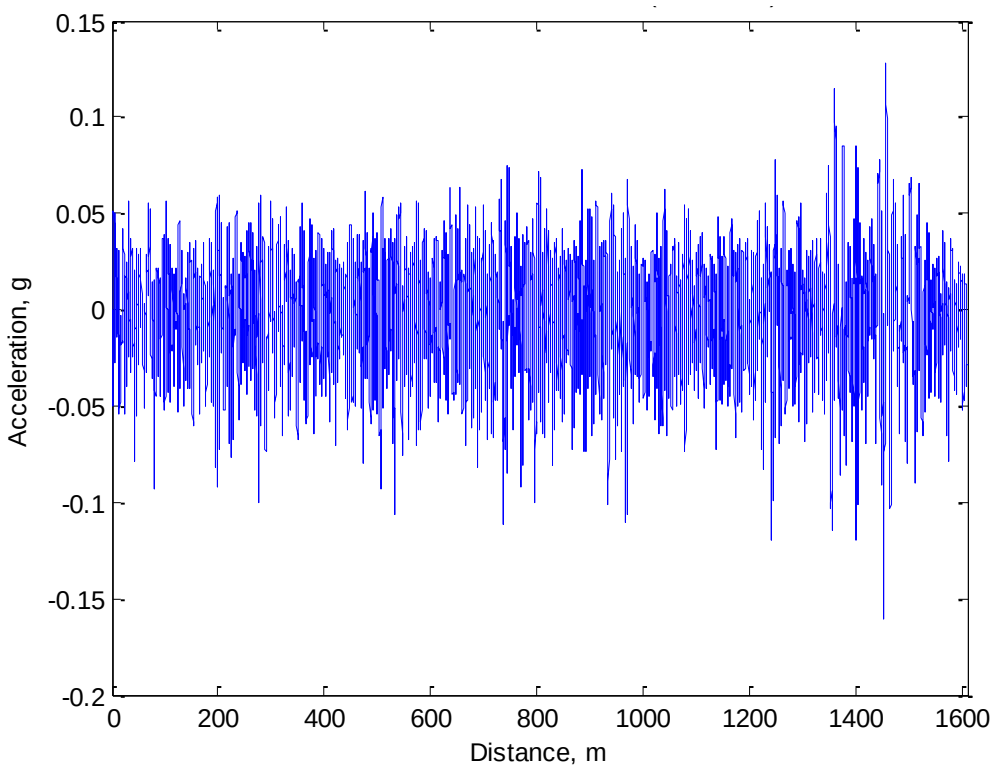

Figure 6.10: Simulated Acceleration Response

The relation between the acceleration response and the IRI found in Figure 6.6 is dependent on the speed of the vehicle. Ideally, the estimated IRI should remain the same regardless of vehicle speed because the road profile is fixed, whereas the response differs depending on the vehicle velocity. The effect of vehicle velocity for the approximation of the IRI is shown in Figure 6.11. This plot shows the approximation of IRI is higher at low travel velocities 16.1 kph (10 mph) when compared to the approximation made at high vehicle speeds 112.7 kph (70 mph).

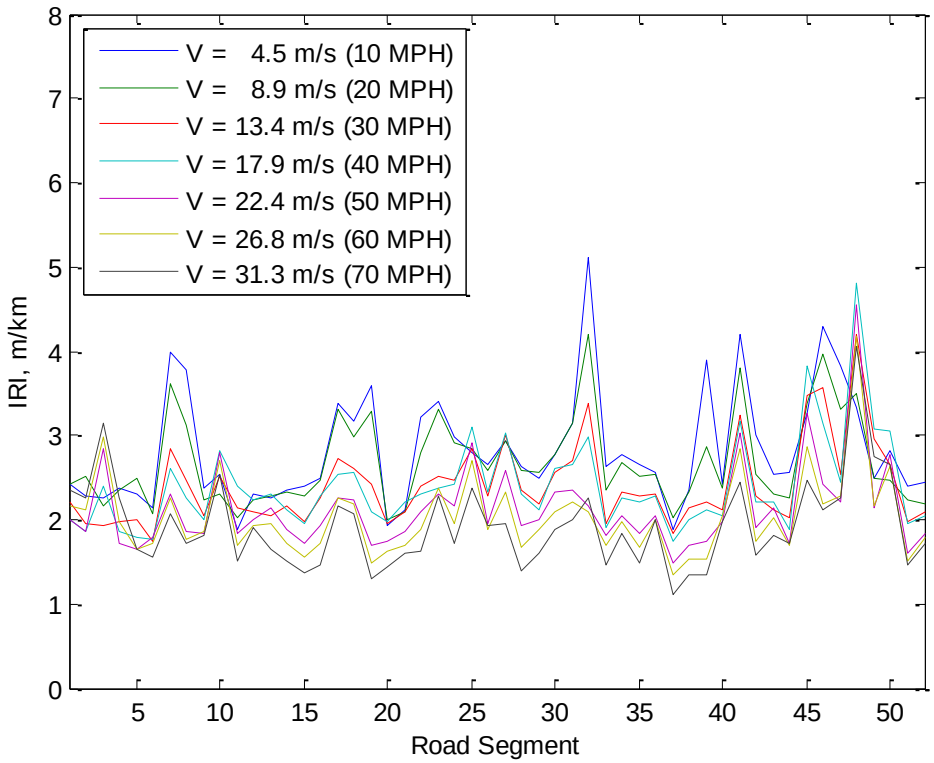

Figure 6.11: Estimated IRI from Acceleration Response at Varying Speeds

ProVAL is used to calculate the exact IRI values for this profile. These values are compared with the estimated results based on the response acceleration at 17.9 m/s (40 mph) using the correlation in Figure 6.6. Comparisons for results taken at 30.48 m (100 ft) and 7.62 m (25 ft) profile segments are shown in Figure 6.13 and Figure 6.15, respectively. These results show the accuracy of the use of acceleration output for IRI estimation at 17.9 m/s (40 mph). It can be determined that lower vehicle speeds overestimate the IRI values, while high speeds underestimate the IRI from the results found in Figure 6.11.

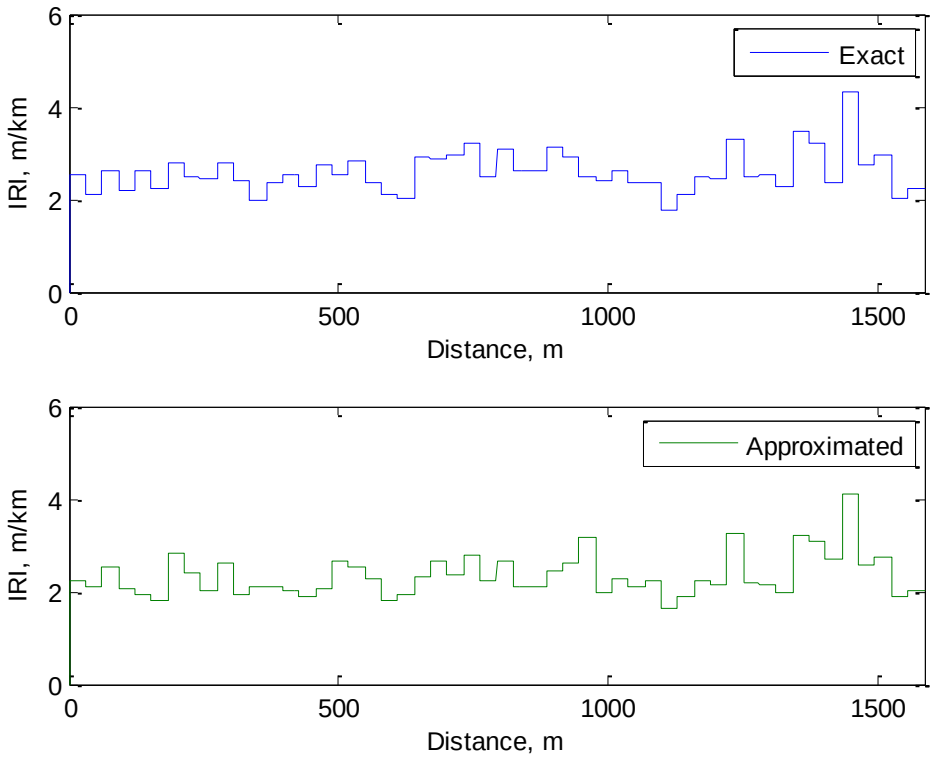

Figure 6.12: Comparison of Exact and Approximated IRI Values, 30.48 m (100 ft) Interval

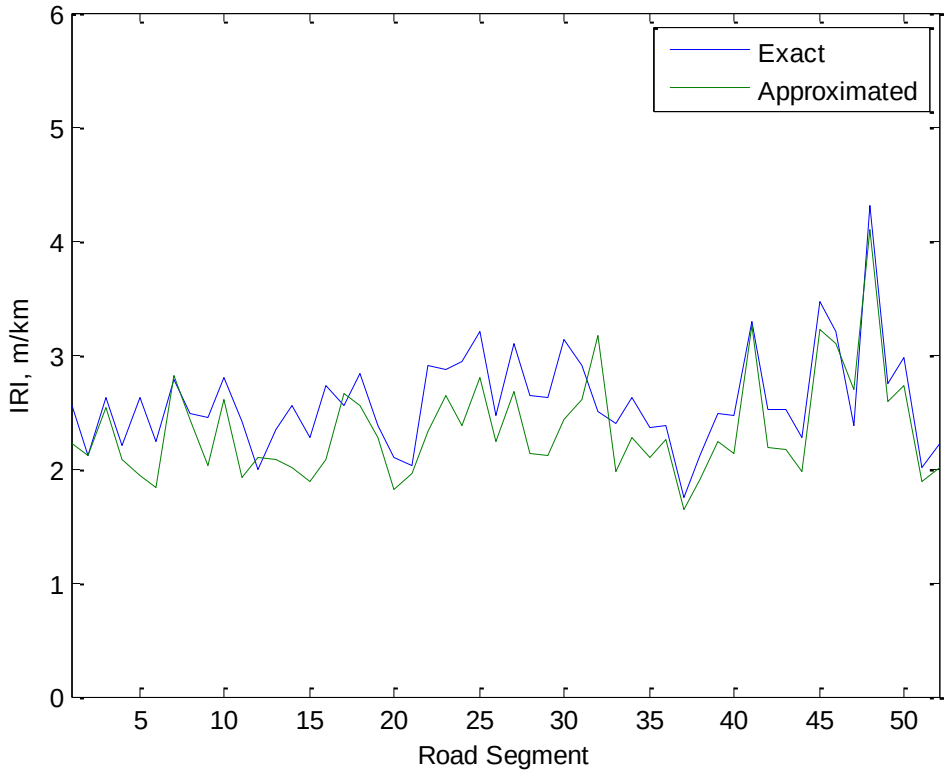

Figure 6.13: Comparison of Exact and Approximated IRI Values per 30.48 m (100 ft) Segment

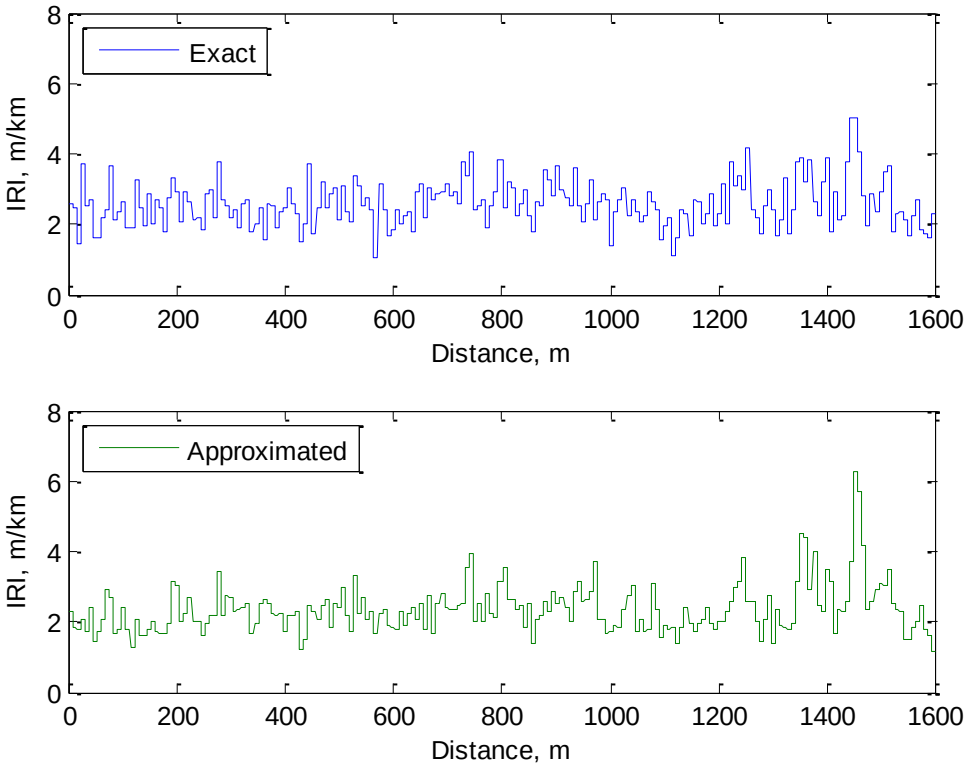

Figure 6.14: Comparison of Exact and Approximated IRI Values, 7.62 m (25 ft) Interval

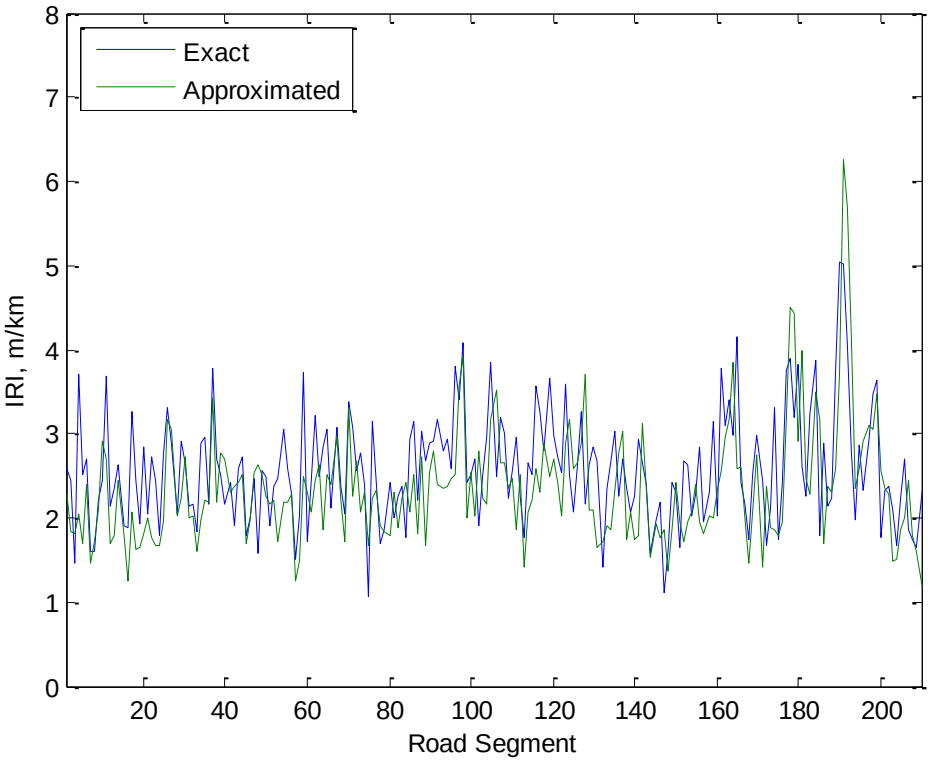

Figure 6.15: Comparison of Exact and Approximated IRI Values Per 7.62 m (25 ft) Segment

6.4 Ride Comfort

A major objective in this study is to determine the direct relation between the road roughness and the ride comfort. While high-speed road profilers manage to capture the elevation and roughness of the road surface, they do not relate this information to the perception of the user. The main source of ride discomfort stems from the vibrations of the vehicle in the vertical direction. These vibrations are based on the dynamic properties of the vehicle, meaning the perception of comfort may vary from user to user based on the vehicle properties.

The goal of this next simulation is to relate the frequency weighted acceleration response to the road profile. This is done to determine the effects of road roughness, vehicle speed, and vehicle parameters on ride comfort. This is completed by generating road profiles with IRI values ranging from 1 to 10 m/km, and simulating a half car model traveling along them. The frequency weighted acceleration, which is used to quantify comfort based on vertical vibrations, is calculated for profile at speeds ranging from 4.5 m/s (10 mph) to 31.3 m/s (70 mph). Results are shown in Figure 6.16 and Figure 6.17.

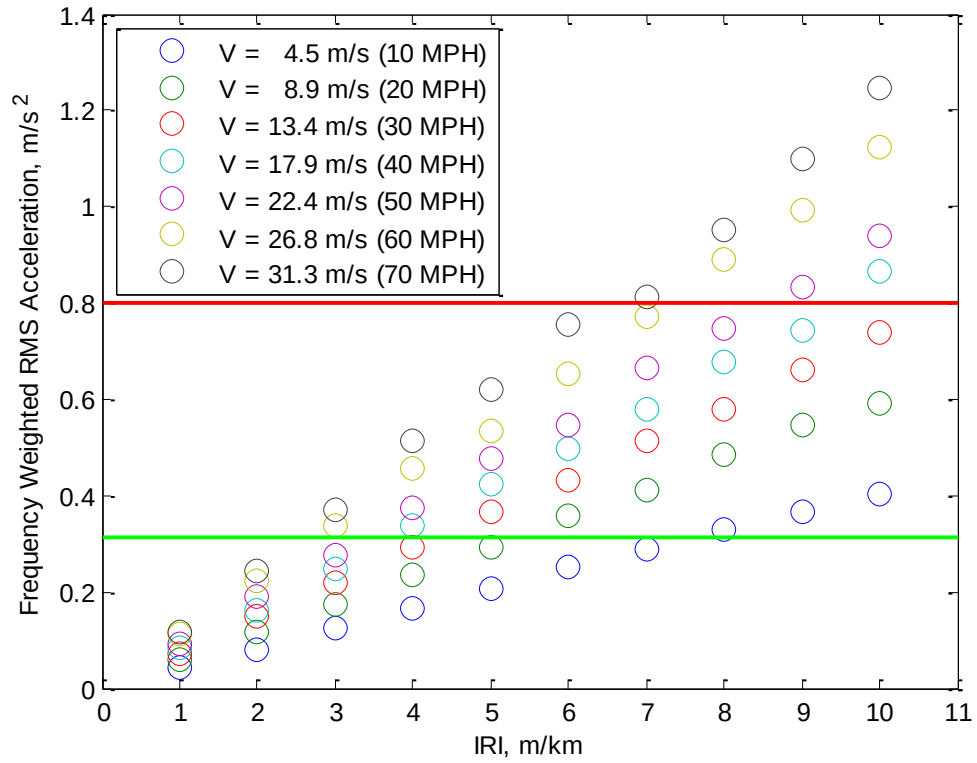

Figure 6.16: Effect of Road Roughness and Vehicle Velocity on Ride Comfort

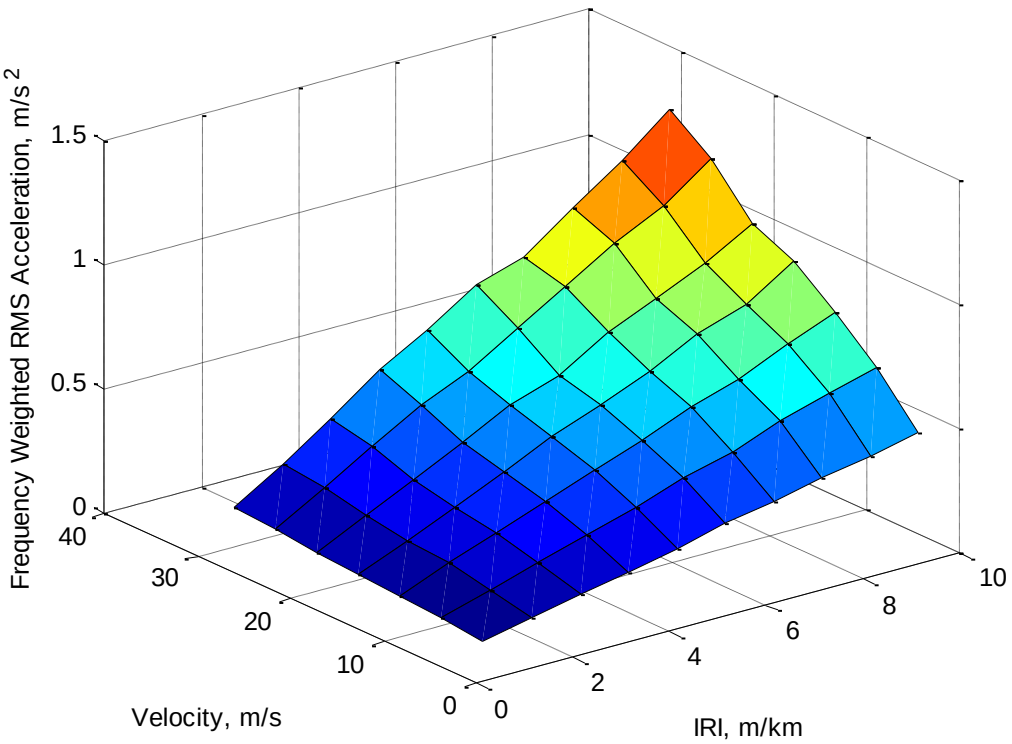

Figure 6.17: 3D Plot of Level of Comfort Based on IRI and Velocity of Vehicle

6.5 Profile Maps

Application of the correlation of acceleration response to road roughness and comfort is presented in this section. Two maps are generated using recorded vehicle vibrations: one map based on the correlation to the acceleration response to the IRI and a second map directly relating the response to the comfort of the user of the vehicle. These maps are created by recording vehicle vertical acceleration along the roads through and around the University of Maryland, College Park campus. The use of IRI and comfort scales each have different applications. A map displaying road roughness based on the IRI values can be used by the Department of Transportation to determine sections of roads in need of maintenance and rehabilitation. The second map, consisting of comfort level, can be used by the drivers themselves. Using real-time vehicle acceleration response in combination with vehicle location determined by the smartphone's GPS, these profile maps can be continuously updated.

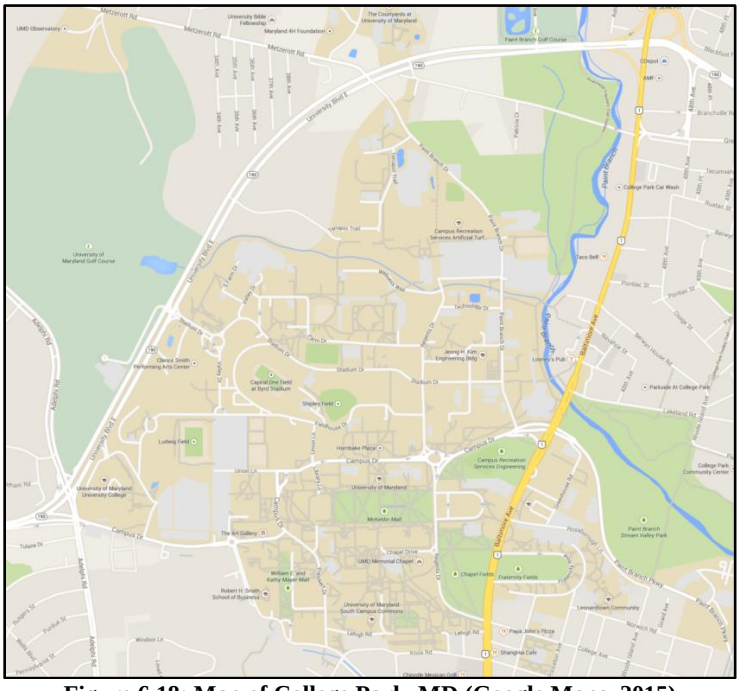

Figure 6.18: Map of College Park, MD (Google Maps, 2015)

To create these profile maps, 37 sections of roads are traveled along to gather data. These sections of roads are shown in Figure 6.19. For each segment, only a single lane is tested. It is assumed that the profile roughness is similar for the left and right tires. It is also assumed that the vehicle remains at a constant velocity throughout each segment. A 15 Hz low pass filter is used to remove the high frequency vibrations caused by the vehicle console where the sensor is attached.

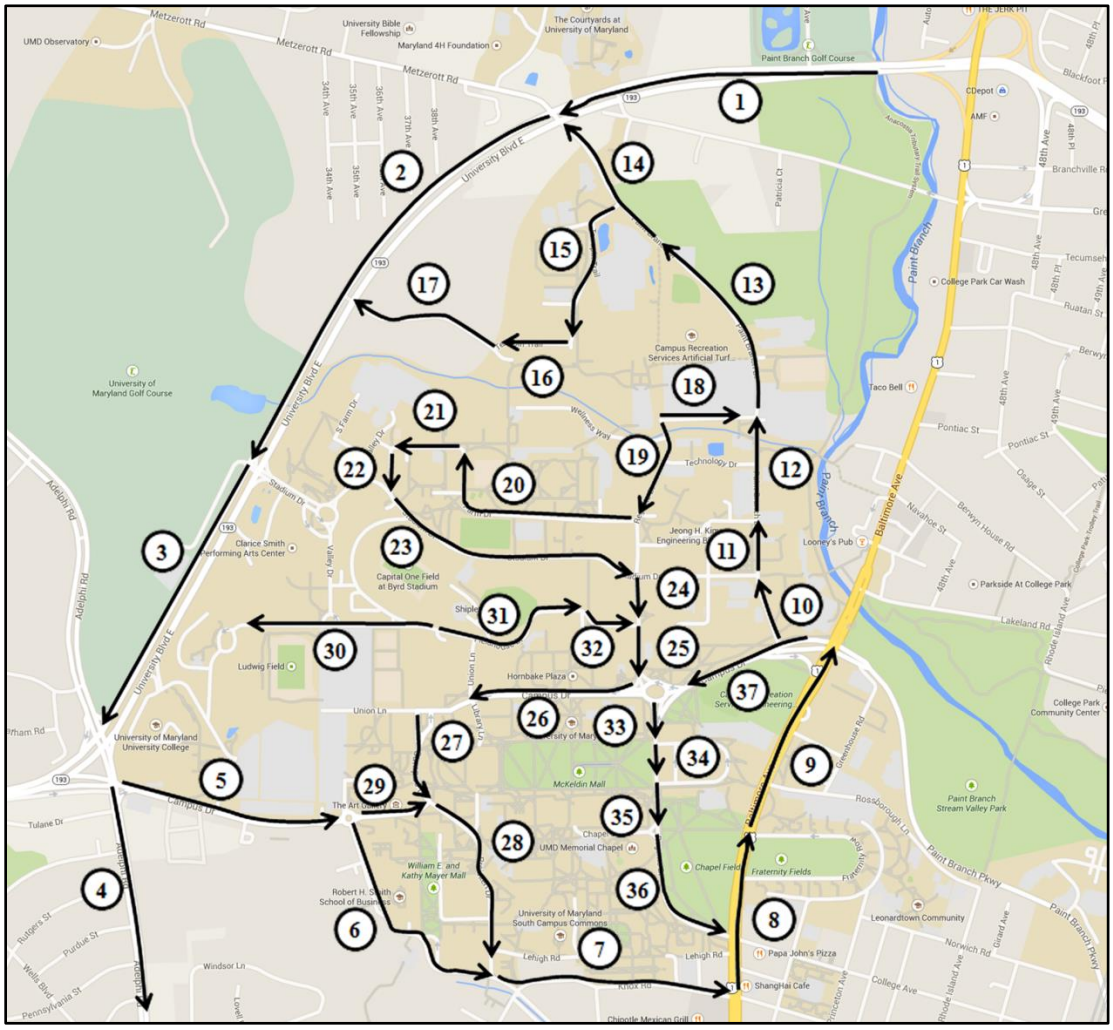

Figure 6.19: Location of Road Segments

A color scale is created to visualize the IRI and comfort levels on the profile map. Two individual scales are established that relate to the IRI roughness descriptions and the comfort described by the frequency weighted accelerations. The selection of IRI values is based on an approximate IRI for various road classes shown in Figure 2.16. As for the level of comfort, the values are based on vertical vibration response described in ISO 2631-1. Further description of this range can be found in Table 2.5.

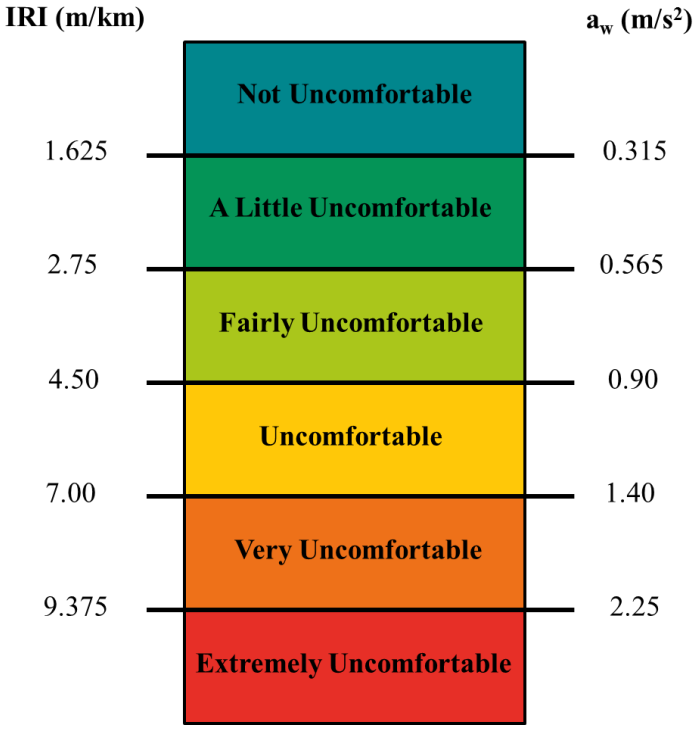

Figure 6.20: IRI / Comfort Scale

Maryland SHA standards state the IRI is reported every 25 ft (Maryland SHA, 2012). Following this standard, the IRI and level of comfort are approximated every 25 ft for this study. An example of this approximation using the created color scale is shown in Figure 6.21for the IRI and Figure 6.22 for the level of comfort. As seen from the two figures, the use of coloring makes it very clear to see where there are areas of roughness and sections of road that may cause discomfort.

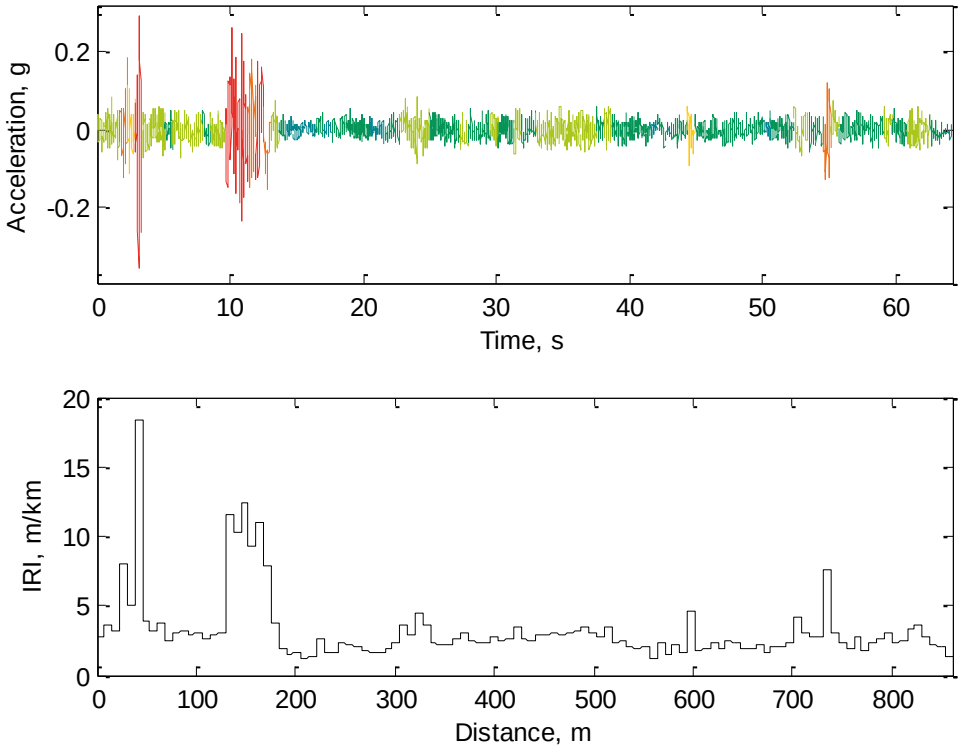

Figure 6.21: Approximation of IRI Based on Acceleration Response

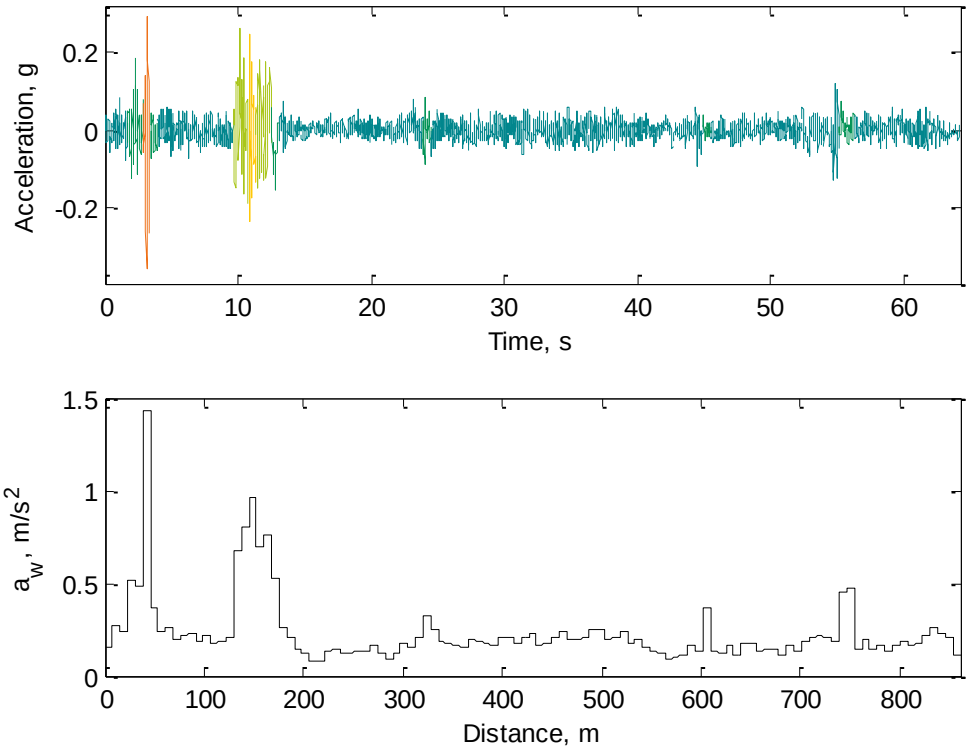

Figure 6.22: Approximation of Comfort Based on Frequency Weighted Acceleration

6.5.1 Profile Map: Road Roughness

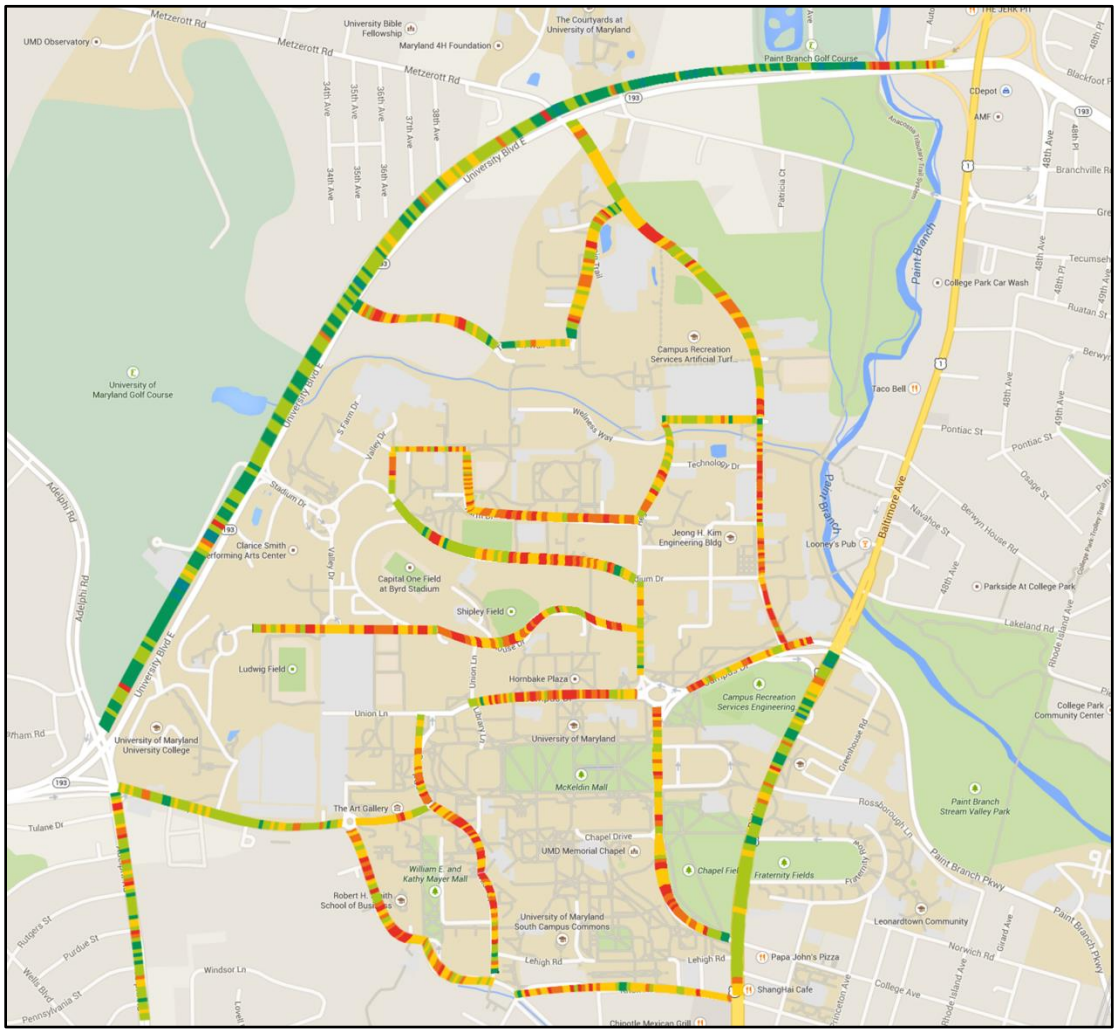

Figure 6.23: Road Roughness Map

The profile map displaying the road roughness is shown Figure 6.23 for the tested area. While IRI approximation provides reasonable results for roads traveled at high speeds, IRI values found at the center of the campus map, driving at speed below 32.2 kph (20 mph), appear to be overestimated.

6.5.2 Profile Map: Level of Comfort

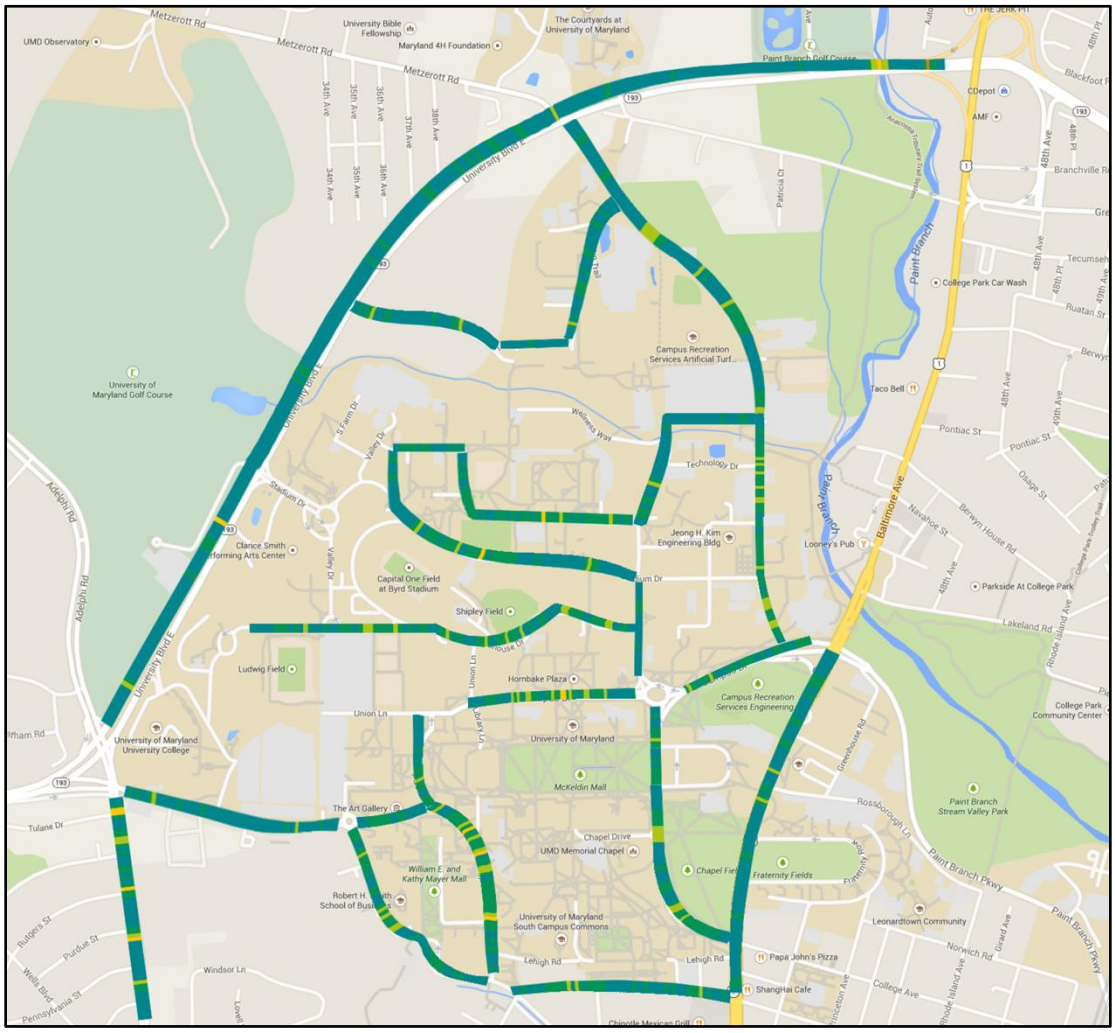

Figure 6.24: Ride Comfort Map

As shown in Figure 6.24, ride comfort is directly measured through the acceleration response, and is applied to profile mapping for additional information. This map shows which road sections provide more comfort over others. Overall, a majority of the roads are comfortable in this area and additional testing should be conducted in other areas to show additional effects of road roughness on ride comfort.

6.5.3 Revisiting Areas of Interest

Selected areas of interest are revisited to demonstrate the effectiveness of the comfort profile map. These areas are selected based on the level of discomfort they provide according to the color scale used on the map. Three areas, displayed on pages 157 through 159, are chosen with varying levels of discomfort. The first area, found on road segment 5, shows a slight discomfort. This discomfort is due to the intersection of a newly paved section of road with the existing road. Road segment 6 shows that a manhole located in the road provides reasonable discomfort. Lastly, an uncomfortable section of road is found on road segment 23. This area shows the discomfort is caused by damaged pavement. These three revisited areas are summarized in the following table:

Table 6.5: Areas of Interest Based on Comfort Level

Location	Road Segment	Perception	Reason for Discomfort
1	5	A Little Uncomfortable	Intersection of new and old pavement
2	6	Fairly Uncomfortable	Manhole
3	23	Uncomfortable	Damaged pavement

Figure 6.25: Location of Interest #1

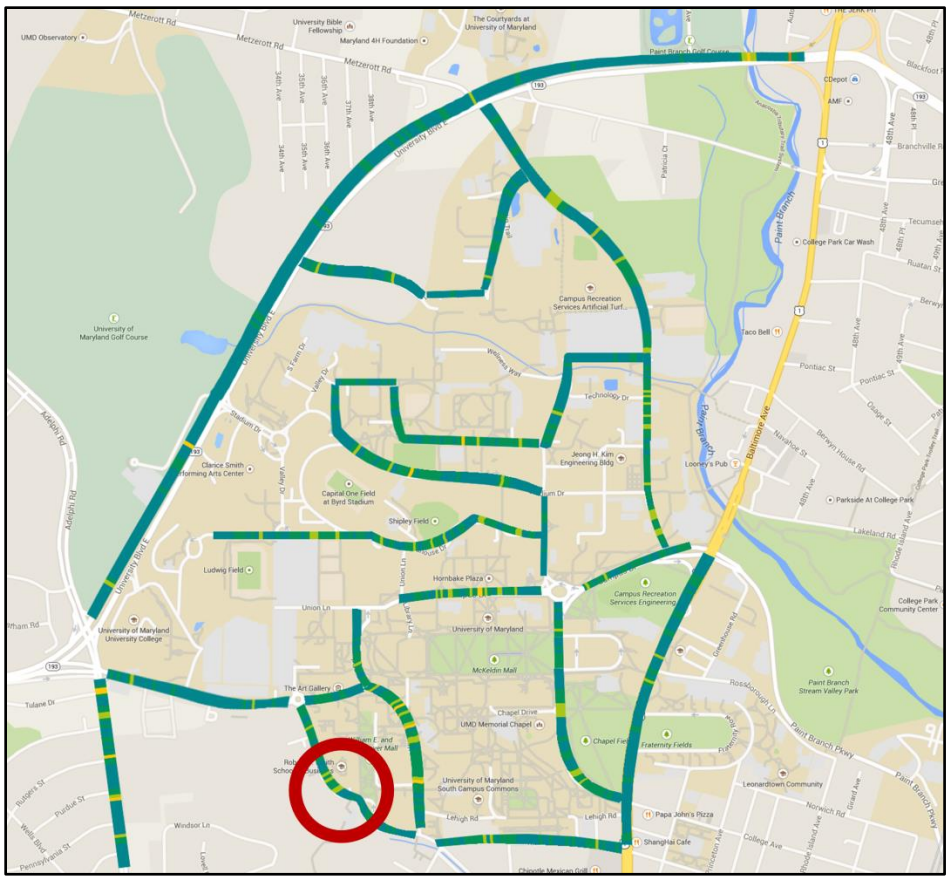

Figure 6.26: Location of Interest #2

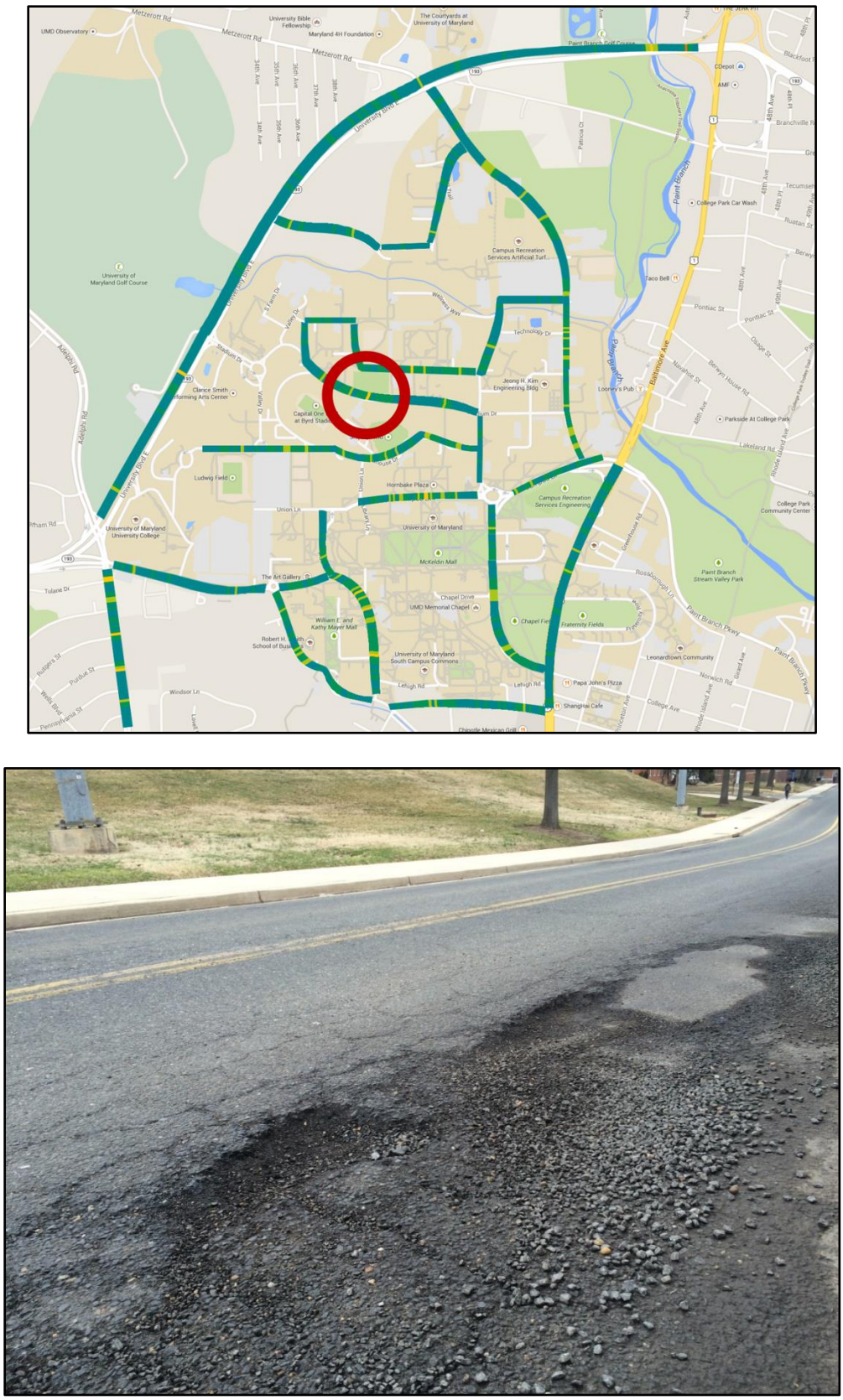

Figure 6.27: Location of Interest #3

6.6 Summary of Analysis

This chapter evaluates the accuracy of PEM for mass estimation for acceleration response recorded on actual roads. It is found that the selected speed bumps provide accurate results assuming the input is properly estimated. The bridge bumps used in this study were found to have a weak signal-to-noise ratio, providing inconsistent results using system identification methods. Additional testing is required to determine the overall effectiveness for the use of bridge bumps as a source of vehicle excitation for use with PEM.

The correlation between IRI and vehicle response is found to be linear and dependent on vehicle speed. This correlation varies depending on vehicle mass. Additionally, the comfort of the driver and passengers can be determined; the vertical acceleration response can be directly related to comfort through a weighting function provided in ISO 2631-1. These correlations provide additional information concerning road roughness and comfort that are used to create two road profile maps — an IRI profile map and a comfort level profile map. The ability to obtain this information in real-time using smartphone acceleration and GPS sensors is advantageous because it provides necessary data that can be used to determine the most comfortable travel routes and roads in need of maintenance, which is currently unavailable.

Chapter 7: Conclusions

7.1 Research Conclusions

High-speed road profilers are currently used to measure the elevation of road surfaces to calculate road roughness, but do not provide a direct measure of ride comfort of the user. Due to technological advancements, mobile sensing has become a viable tool for measuring vibrations, which can be applied to the analysis of road conditions and ride comfort. It addition to providing another layer of information by including ride comfort, key road information can be updated in real-time through the use of mobile sensing, whereas current profiles are updated between every one to two years.

The research completed in this dissertation demonstrates the viability of estimating road roughness and directly measuring ride comfort through wireless sensing. Due to the variation in vehicle properties, this study focuses on parameter identification of high-damped systems. This includes the evaluation of system identification methods and the necessary requirements to obtain an accurate prediction of the vehicle mass by applying these methods. Knowledge of the vehicle parameters is essential in determining a correlation between the vehicle vibration response and the road surface roughness. Through simulation and experimental testing using mobile sensors, system identification of vehicle dynamics and road conditions is performed to show the effectiveness in creating this correlation. Major findings of this study are summarized as follows:

- Through the evaluation of various system identification techniques, a combination of PEM with the use of grey-box modeling proves to be an effective method for parameter identification of high-damped systems with known input, specifically when used for vehicle mass identification. Due to the similarities in structure between typical passenger cars, grey-box modeling provides an effective way of relating the input and output while partial system parameters are left unknown. Application of PEM is used to predict these unknowns. With both simulated studies and field testing, this method proves to be effective in the prediction of vehicle mass, providing little to no error when provided with information concerning the system input.
- Vehicle mass can be accurately predicted using the PEM algorithm over a range of realistic initial guesses for mass estimation assuming known input excitation and measured output response. The mass of the half car model used in this study is 875 kg with the inclusion of two passengers. The range of initial mass estimates is selected to vary from 700 to 1100 kg to envelope the empty vehicle mass through the mass of the vehicle at full capacity.
- Based on research through vehicle simulation, it is found that unknown input gives poor identification results due to sinusoidal response waveform. Because of this, an input either needs to be known or estimated to provide accurate results for vehicle parameter prediction. If the input is known, the prediction is significantly improved.
- Comparison of the BMA220 accelerometer found in the iPhone 5S and the PASCO PS-2119, shows that the iPhone 5S provides similar acceleration data

quality to that of a COTS wireless accelerometer. This is found through simultaneously recording the acceleration response of a model structure with each sensor.

- With a careful selection of an input bump height and width combined with speed of the vehicle, response data with a strong signal-to-noise ratio can be provided for use with system identification methods. In the case of the bump, it is assumed that the vehicle remains in contact with the ground at all times.
- Although bridge bumps provide a response viable for use with system identification methods under theoretical ideal situations, the bridge investigated in field testing provides a weak signal-to-noise ratio and inconsistent results. The bumps at the ends of bridges differ from bridge to bridge, and due to many varying factors, one bridge does not provide enough data. More tests are required to show similarities between simulated and recorded responses.
- A pilot test using an extension cable to simulate pneumatic road tubes shows small vehicle response at low speeds of 16.1 to 32.2 kph (10 to 20 mph). The measured test data shows low signal-to-noise ratio, which greatly decreases the accuracy of system identification techniques. Further conclusions concerning the use of pneumatic road tubes as a source of vehicle excitation requires additional testing.
- By simulating vehicle response while traveling on roads with varying roughness, the relation between the IRI and vertical acceleration response is determined empirically. This correlation shows that the IRI of the road profile

and the vertical acceleration response is linearly proportional at constant speeds. Assuming the profile is static, the estimated IRI should remain constant regardless of vehicle speed. The correlation appears to provide overestimated IRI values at low vehicle speeds (16.1 kph / 10 mph) and underestimated values at high speeds (112.65 kph / 70 mph). This is realized by analyzing the differences between the estimated IRI values found through the acceleration correlation and the exact values calculating using ProVAL.

7.2 Recommendations for Future Work

- This study presents the necessity of accurately estimating the input of the vehicle when applying system identification methods for prediction of vehicle parameters. Further research can be conducted to estimate the profile input based additional information, such as natural frequencies and damping ratio of the vehicle found in the output acceleration response.
- Although the half car model provides a worthwhile representation of the vehicle for parameter identification studies, it can be further extended to a full car model to account for lateral effects due to road unevenness and mass position of passengers and cargo.
- For this study, the sensor is assumed to be located at the center of gravity of the vehicle to negate effects of vertical vibration due to vehicle pitch (rotation). A further look into the influence of sensor location can demonstrate the effect of vehicle pitch on the recorded response.
- Field testing in this study is limited to the response of a single vehicle model with road inputs from the surrounding area. Testing vehicles of different sizes

with user-created inputs in an open test area could provide additional information concerning the effect of input size and vehicle response due to varying vehicle parameters. This also includes further testing of various bridge bumps and pneumatic road tubes at higher vehicle speeds.

- The correlation established between the vehicle vertical acceleration response and the road surface roughness in this study shows an overestimation of the IRI at low vehicle speeds and an underestimation at higher speeds. In actuality, the IRI, which is based on a static road profile, should remain constant regardless of vehicle speed. A further study on the effects of vehicle speed on measured response with a single accelerometer is necessary to create an improved correlation needed for IRI estimation.

Appendices

Appendix A: MATLAB Code

A.1 Road Profile

```
function [x, h] = profile_sim(Gdn0,L,dx)

%% Road Profile Simulation
% Input
%   Gdn0, roughness coefficient, m^3
%   L, profile length, m
%   dx, length interval, m
% Output
%   x, profile distance, m
%   h, profile elevation, mm

x = (0:dx:L)';     % length of profile, m

N = round(length(x)/2);       % number of waves
n_min = 0.011;  % minimum spatial frequency, cycle/m
n_max = 2.83;   % maximum spatial frequency, cycle/m
n0 = 0.1;       % reference spatial frequency, cycle/m
w = 2;          % exponent of fitted PSD calculated on Gd

n = linspace(n_min,n_max,N)';   % spatial frequency range, cycle/m

Gd = Gdn0*(n/n0).^-w;

A = sqrt(2*dn*Gd);      % amplitude of harmonic waves

% random phase angles, [0 2pi]
phi_min = 0;    phi_max = 2*pi;
phi = phi_min + (phi_max-phi_min).*rand(N,1);

% initialize profile
h = zeros(length(x),1); hi = zeros(N,1);

for i = 1:length(x)
    for j = 1:N
        hi(j) = A(j)*cos(2*pi*n(j)*x(i)-phi(j));
    end
    h(i,1) = sum(hi)*1000;  % m to mm
end
```

A.2 Half Car Model Simulation

```
% Mass Matrix
M1 = diag([ms Is mu1 mu2]);

% Stiffness Matrix
K1 = [   ks1+ks2       ks1*l1-ks2*l2     -ks1       -ks2
      ks1*l1-ks2*l2  ks1*l1^2+ks2*l2^2  -ks1*l1    ks2*l2
          -ks1            -ks1*l1        ks1+kt1      0
          -ks2             ks2*l2          0       ks2+kt2];

% Damping Matrix
C1 = [   cs1+cs2       cs1*l1-cs2*l2     -cs1       -cs2
      cs1*l1-cs2*l2  cs1*l1^2+cs2*l2^2  -cs1*l1    cs2*l2
          -cs1            -cs1*l1         cs1         0
          -cs2             cs2*l2          0         cs2];

ndof = size(M1,1);

A = [zeros(ndof) eye(ndof); -inv(M1)*K1 -inv(M1)*C1];
B = [zeros(ndof,2); 0 0; 0 0; kt1/mu1 0; 0 kt2/mu2];
C = [-inv(M1)*K1 -inv(M1)*C1];
D = [0 0; 0 0; kt1/mu1 0; 0 kt2/mu2];

msmd = ss(A,B,C,D);
acc = lsim(msmd,[h1 h2],t); % use road profile elevation input

acc_o = acc(:,1)/9.81; % sprung mass acceleration response, g
```

Appendix B: Speed Bumps

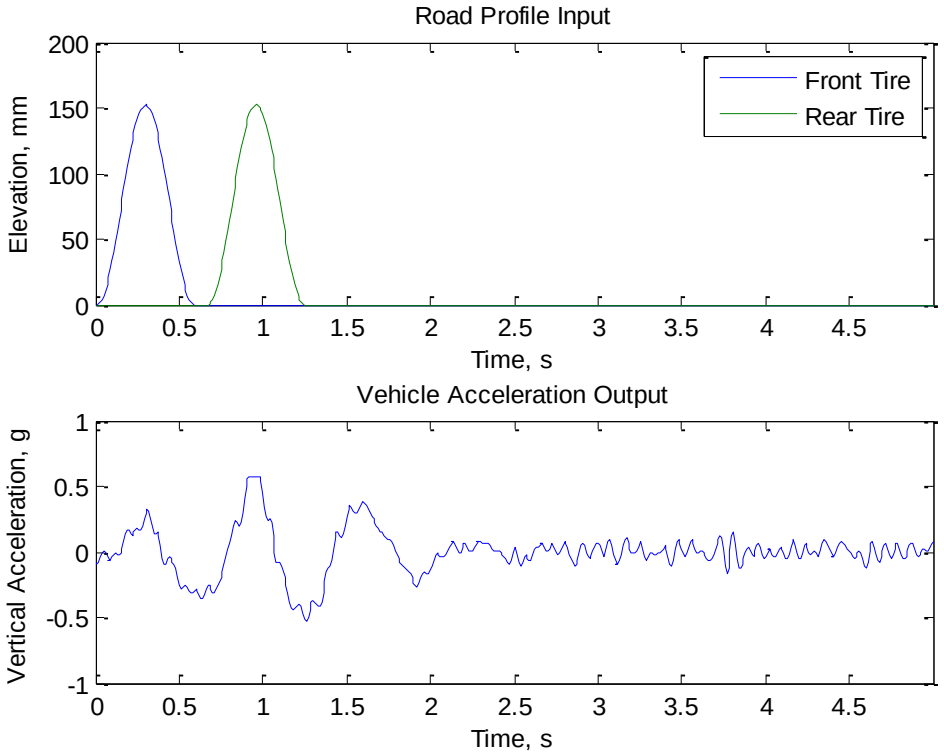

Figure B.1: Estimated Input / Recorded Response — Speed Bump 1, Trial 1

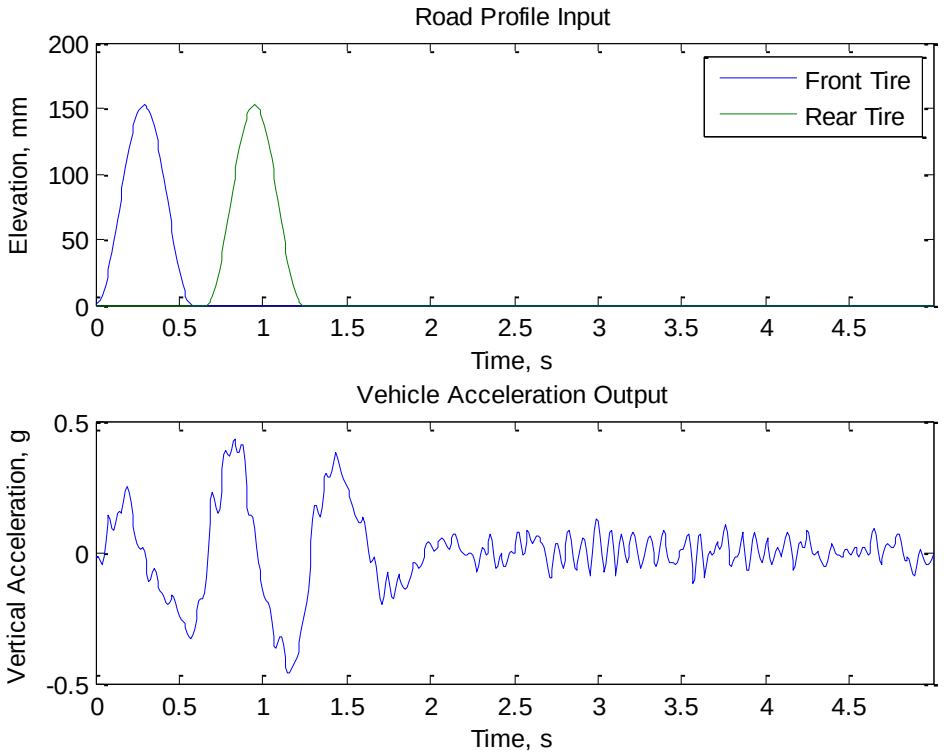

Figure B.2: Estimated Input / Recorded Response — Speed Bump 1, Trial 2

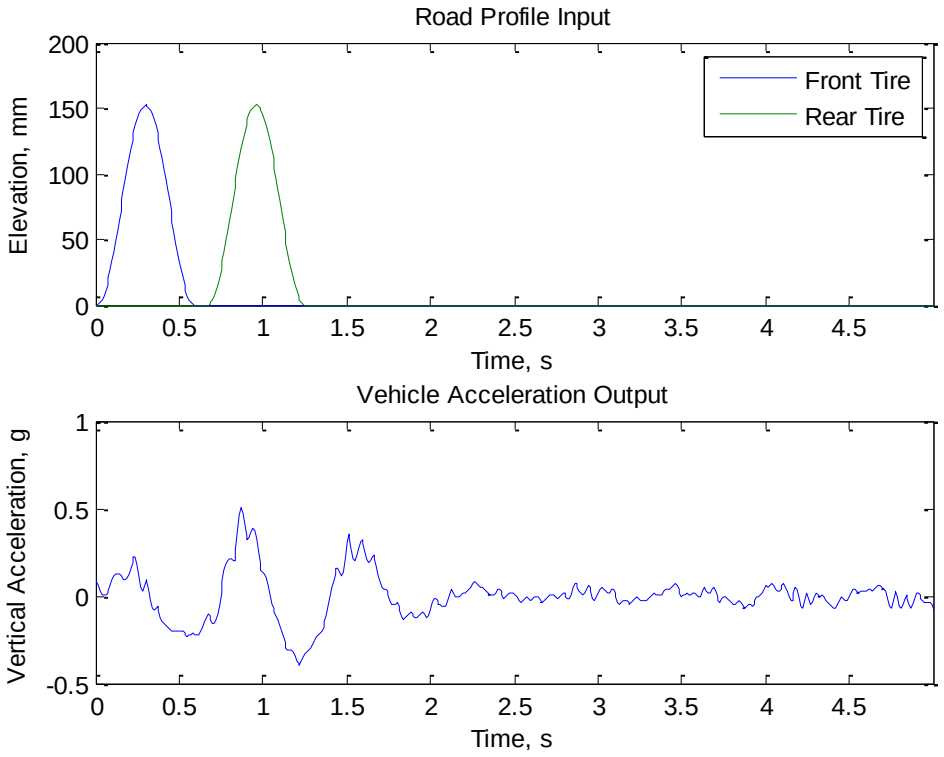

Figure B.3: Estimated Input / Recorded Response — Speed Bump 2, Trial 1

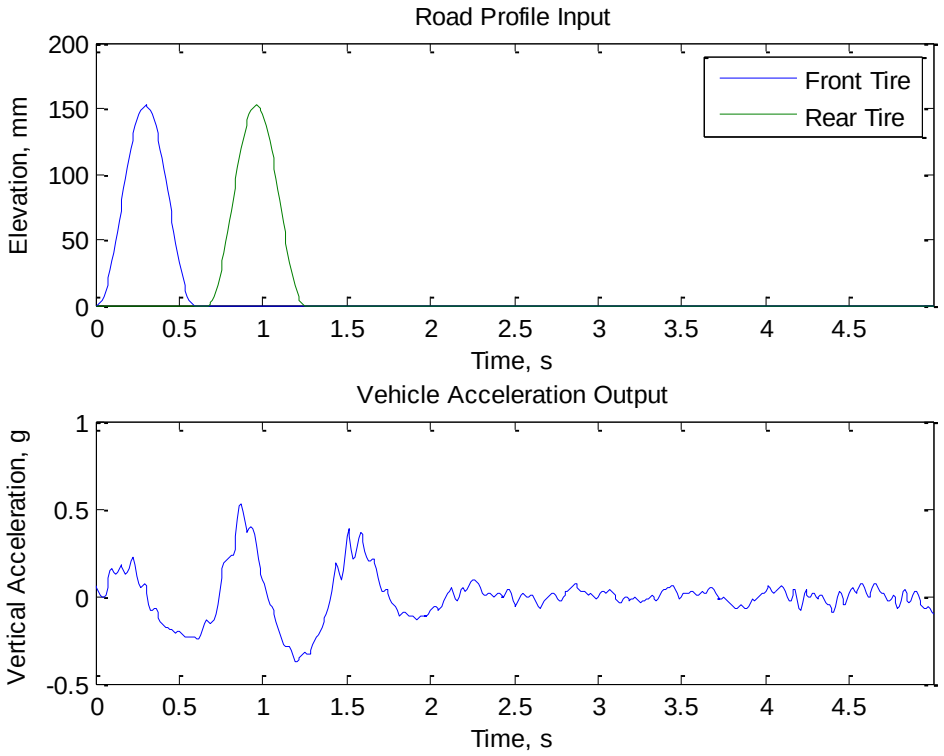

Figure B.4: Estimated Input / Recorded Response — Speed Bump 2, Trial 2

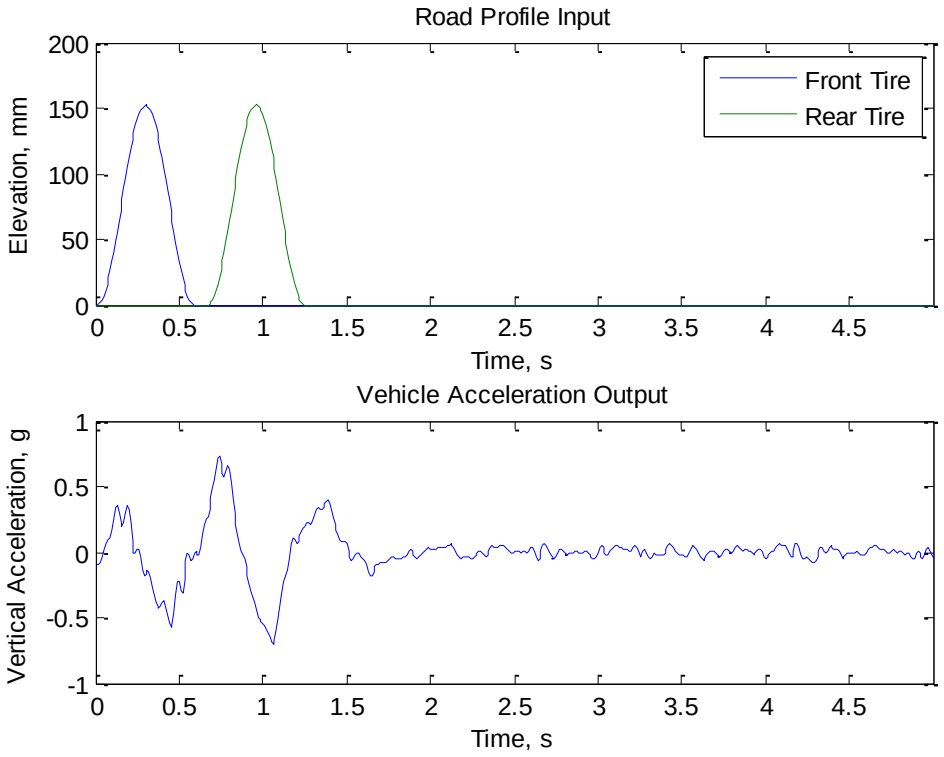

Figure B.5: Estimated Input / Recorded Response — Speed Bump 3, Trial 1

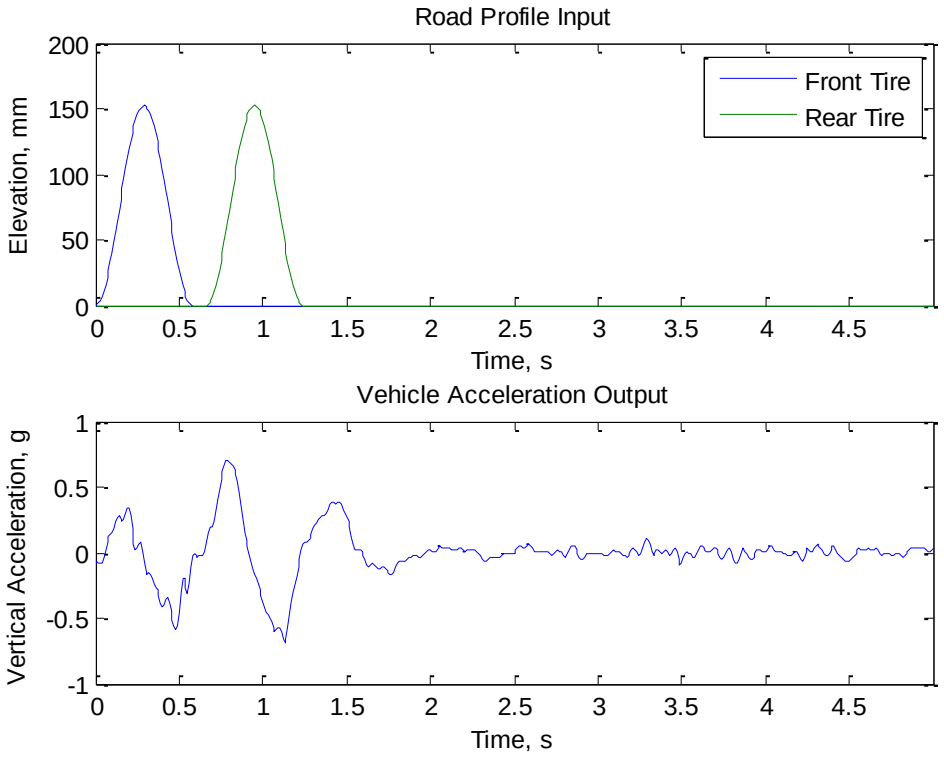

Figure B.6: Estimated Input / Recorded Response — Speed Bump 3, Trial 2

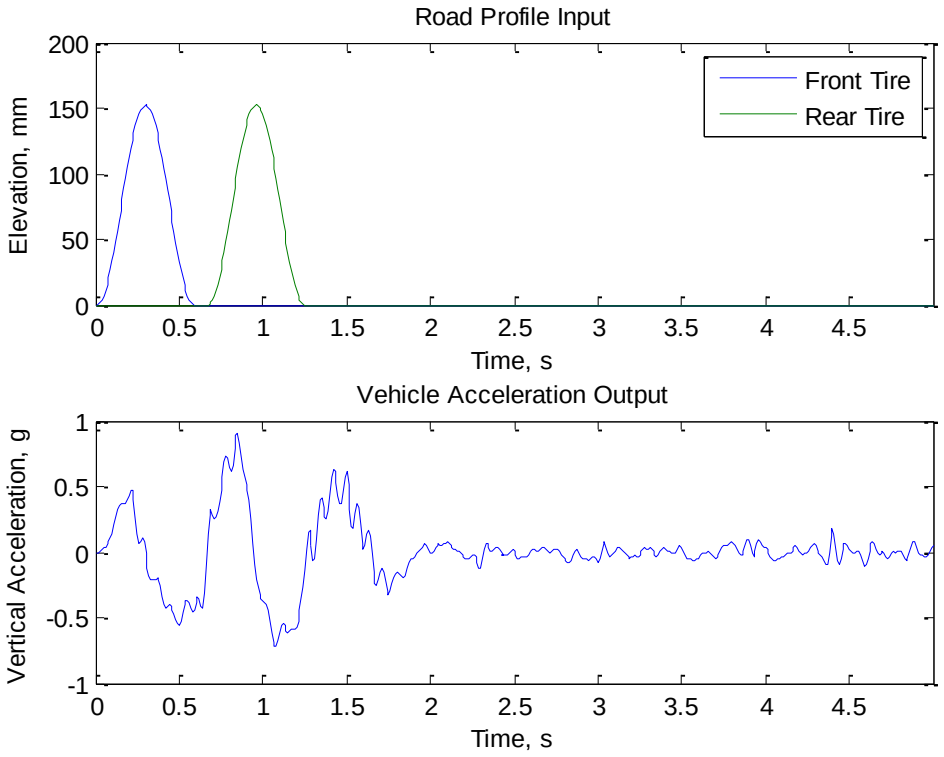

Figure B.7: Estimated Input / Recorded Response — Speed Bump 4, Trial 1

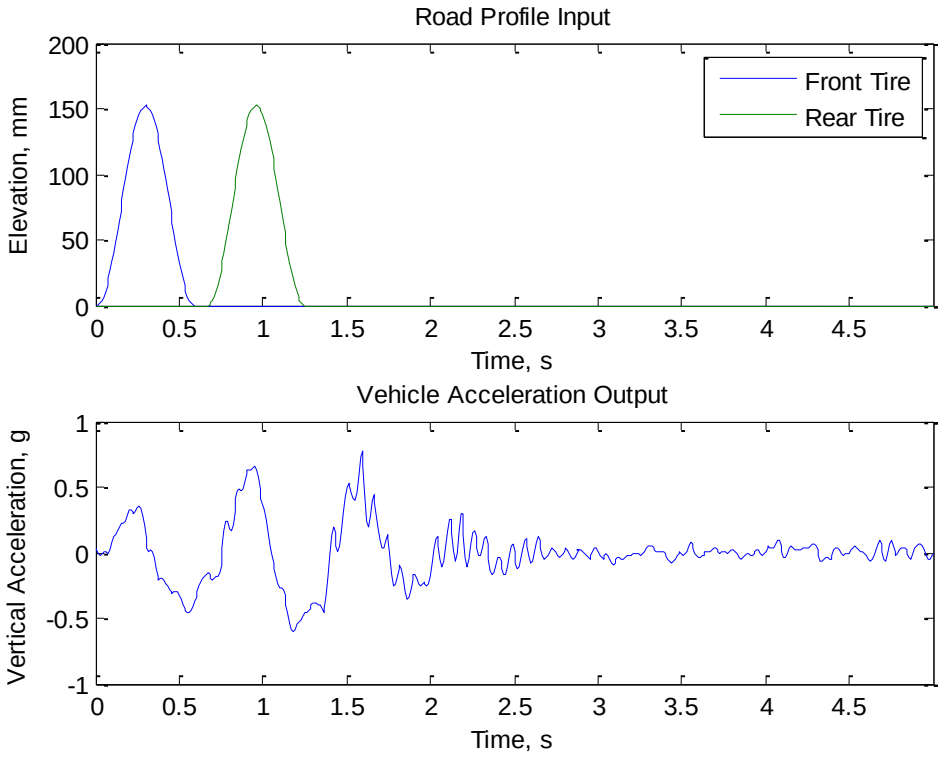

Figure B.8: Estimated Input / Recorded Response — Speed Bump 4, Trial 2

Appendix C: Bridge Bumps

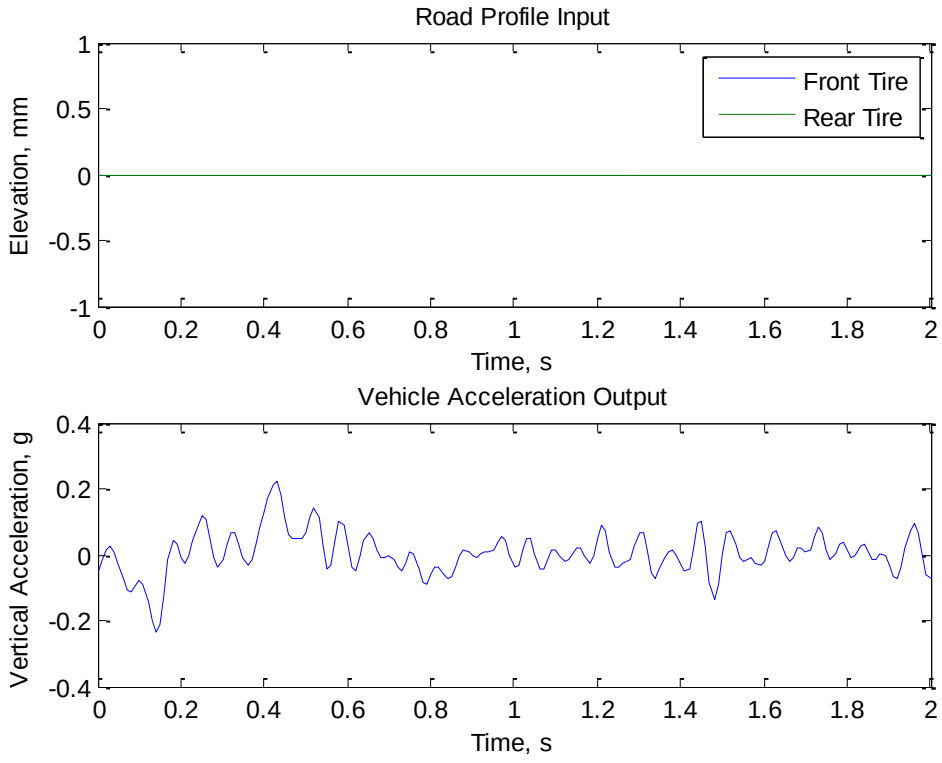

Figure C.1: Estimated Input / Recorded Response — Bridge Bump 1, Trial 1

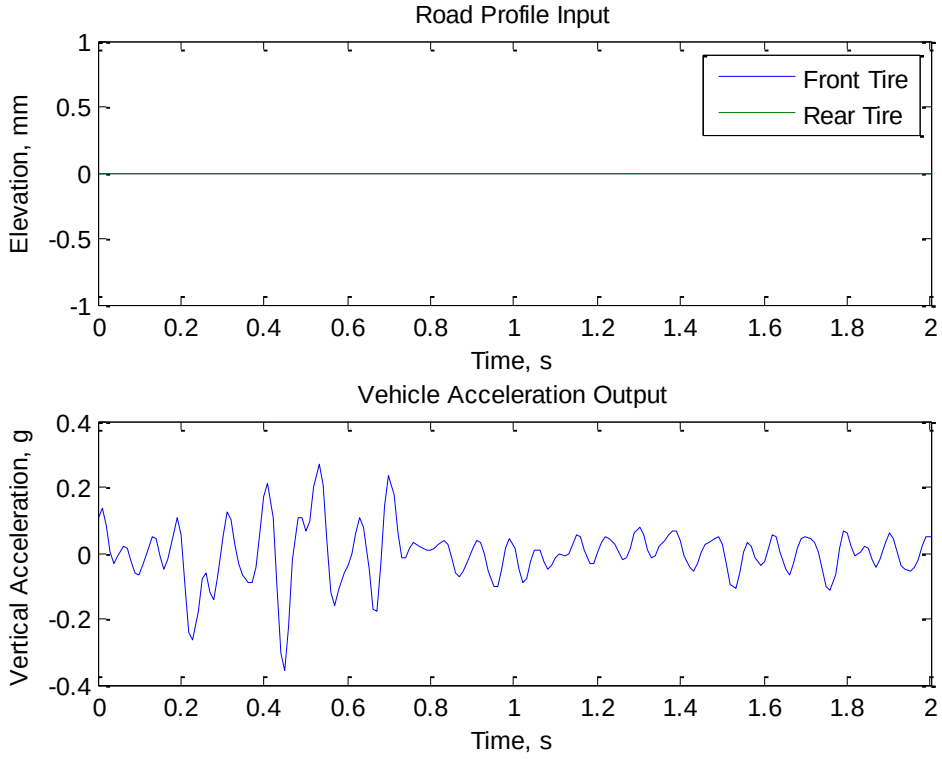

Figure C.2: Estimated Input / Recorded Response — Bridge Bump 1, Trial 2

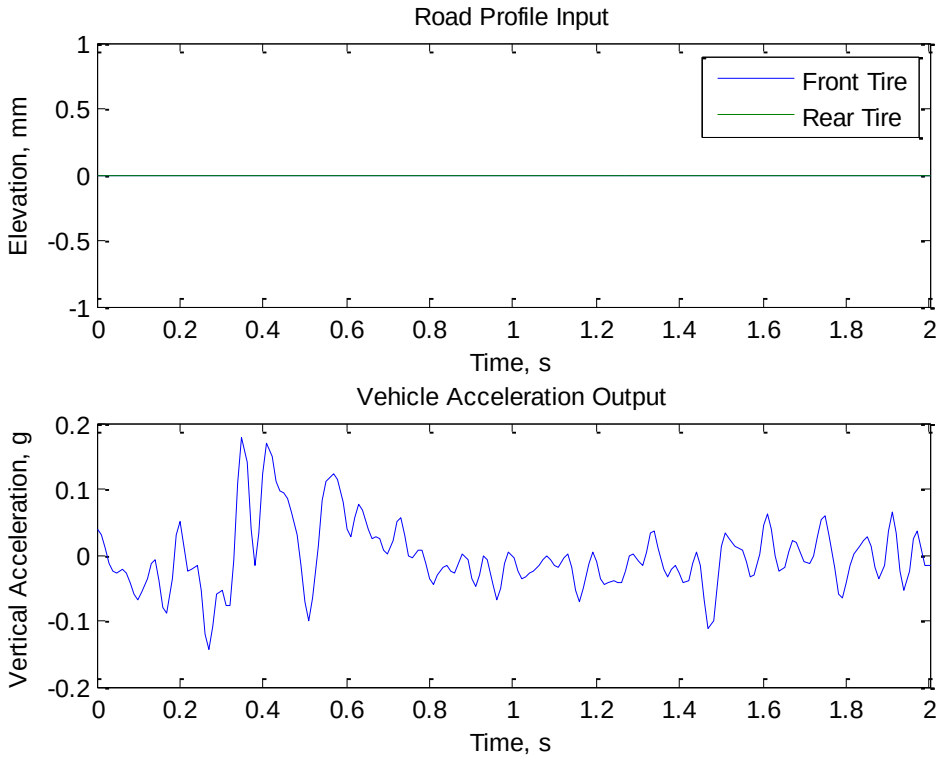

Figure C.3: Estimated Input / Recorded Response — Bridge Bump 2, Trial 1

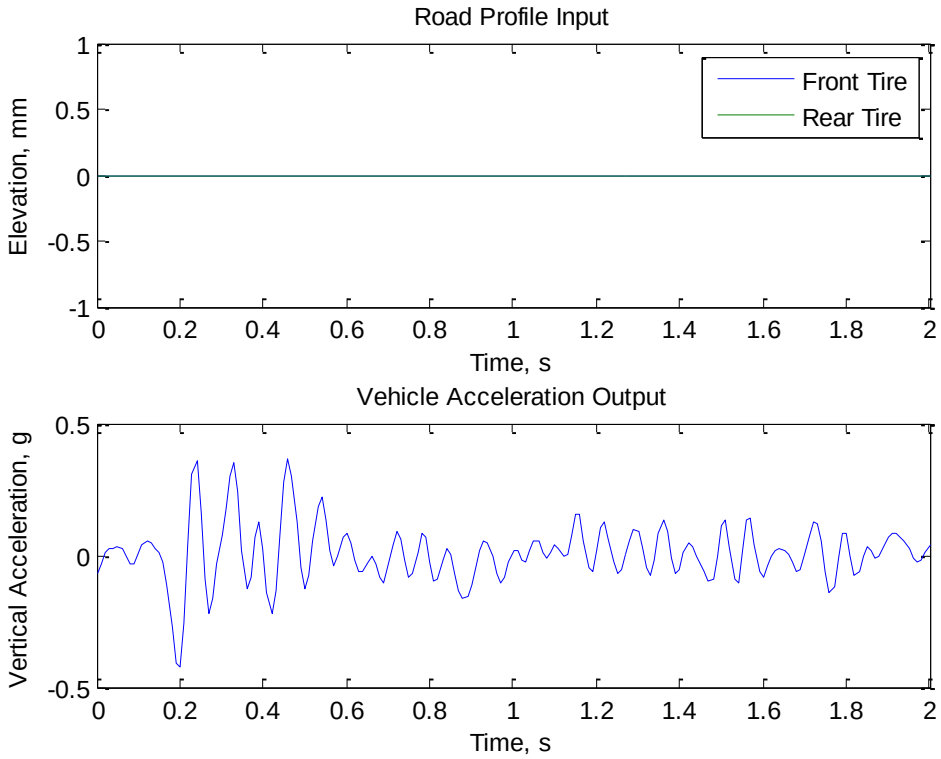

Figure C.4: Estimated Input / Recorded Response — Bridge Bump 2, Trial 2

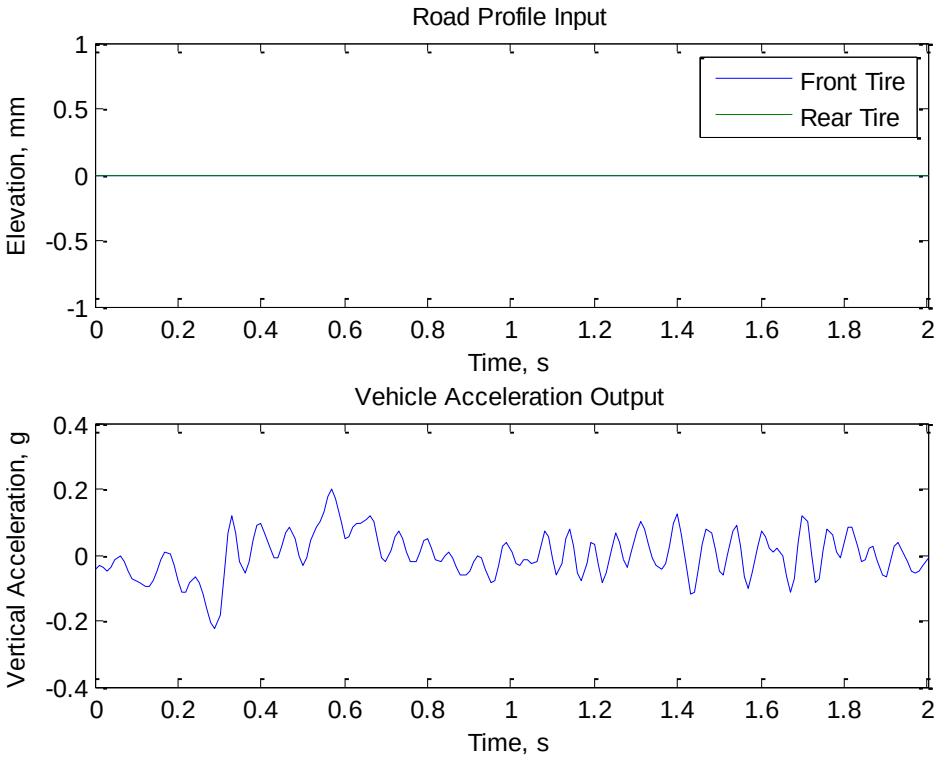

Figure C.5: Estimated Input / Recorded Response — Bridge Bump 3, Trial 1

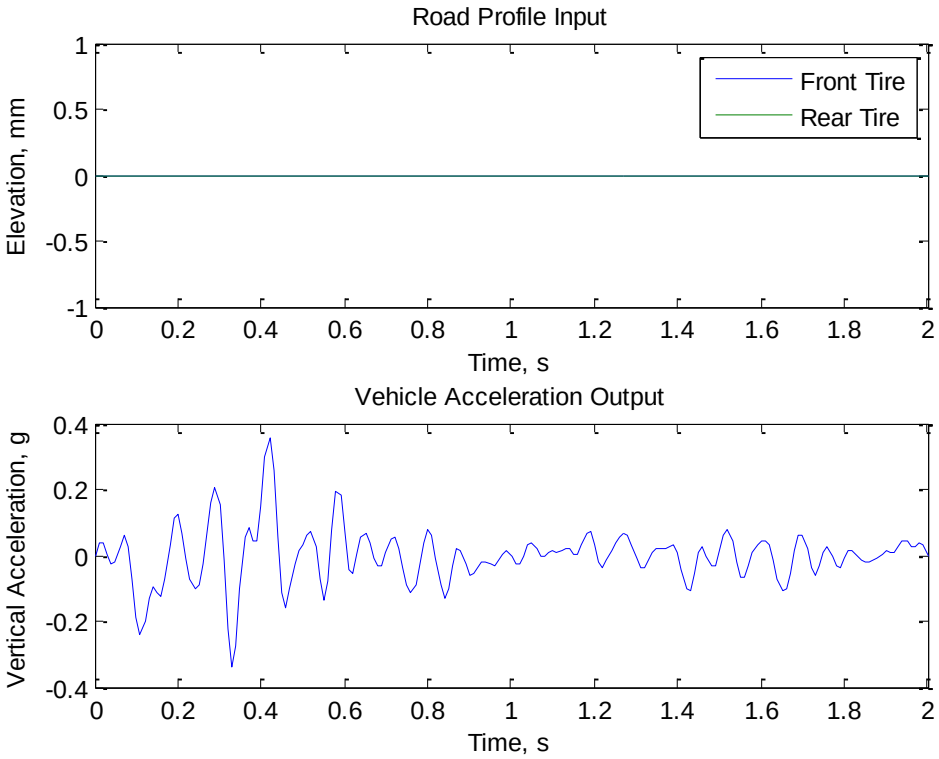

Figure C.6: Estimated Input / Recorded Response — Bridge Bump 3, Trial 2

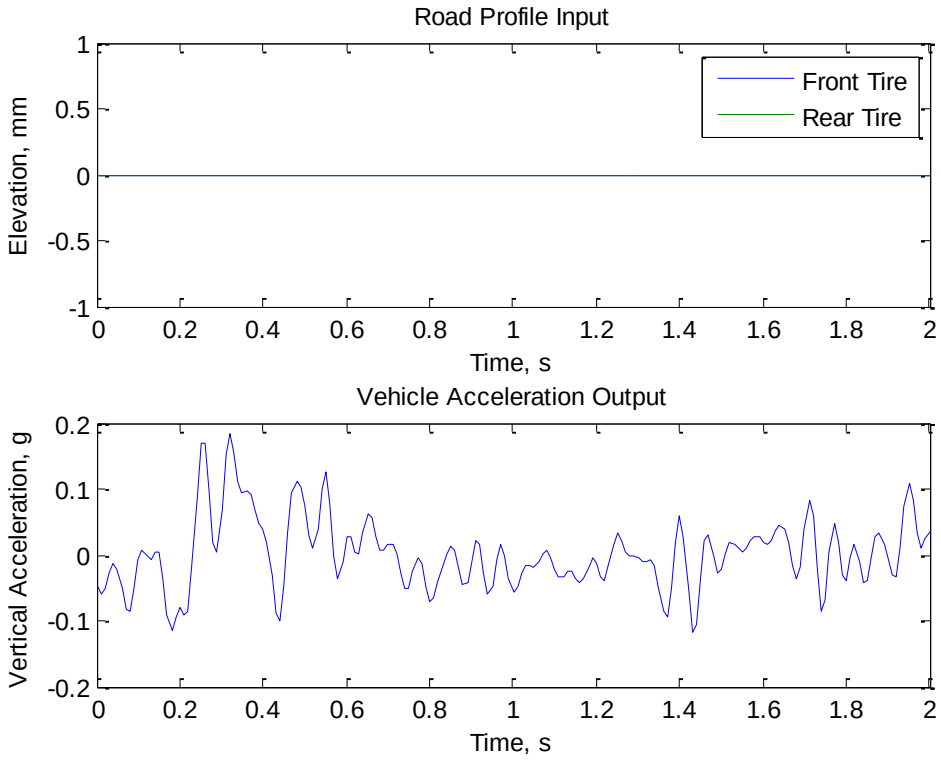

Figure C.7: Estimated Input / Recorded Response — Bridge Bump 4, Trial 1

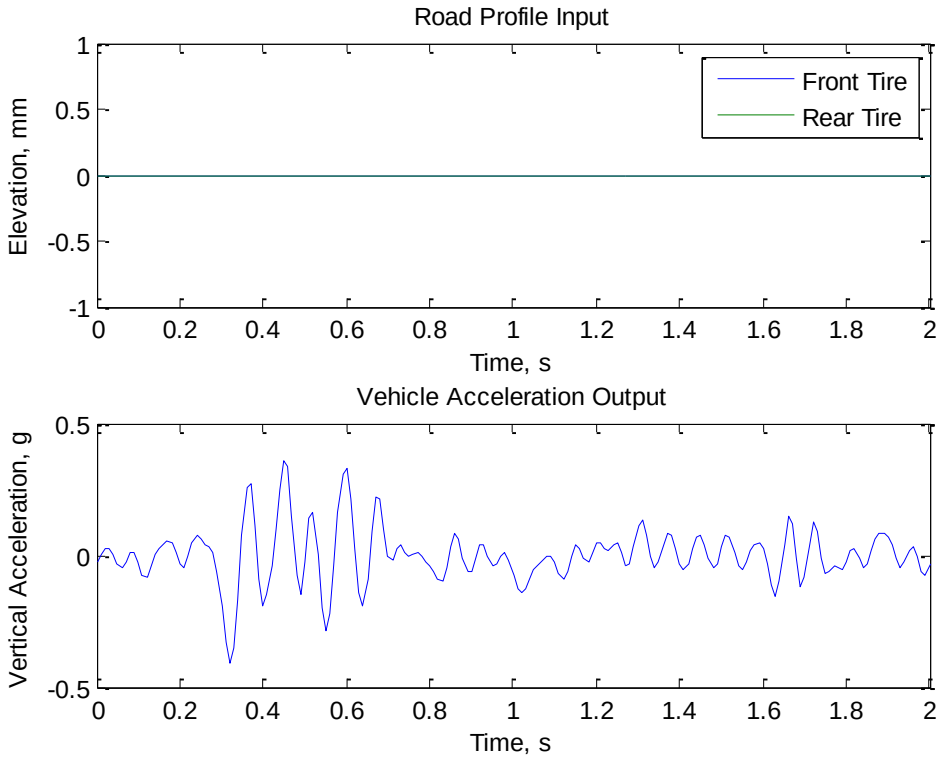

Figure C.8: Estimated Input / Recorded Response — Bridge Bump 4, Trial 2

Appendix D: Acceleration Response from Test Area

Acceleration responses from the 37 road segments tested in the University of Maryland, College Park area are provided in this section. Each road segment is analyzed for roughness and comfort level every 7.62 m (25 ft). The IRI is approximated using the correlation found in Figure 6.6. This correlation is dependent on the speed of the vehicle. The constant vehicle travel speeds for each road segment are shown in Table D.1. The comfort level is estimated by calculating the frequency weighted acceleration as described in ISO 2631-1. Each plot is colored according to the scale found in Figure 6.20.

Table D.1: Vehicle Travel Speeds

Road Segment	Vehicle Velocity	
	kph	mph
1	48.28	30
2	48.28	30
3	48.28	30
4	48.28	30
5	40.23	25
6	32.19	20
7	32.19	20
8	40.23	25
9	40.23	25
10	32.19	20
11	32.19	20
12	32.19	20
13	32.19	20
14	32.19	20
15	32.19	20
16	32.19	20
17	32.19	20
18	32.19	20
19	32.19	20
20	32.19	20
21	32.19	20
22	24.14	15
23	32.19	20
24	32.19	20
25	32.19	20
26	32.19	20
27	32.19	20
28	32.19	20
29	32.19	20
30	32.19	20
31	32.19	20
32	32.19	20
33	32.19	20
34	32.19	20
35	32.19	20
36	32.19	20
37	32.19	20

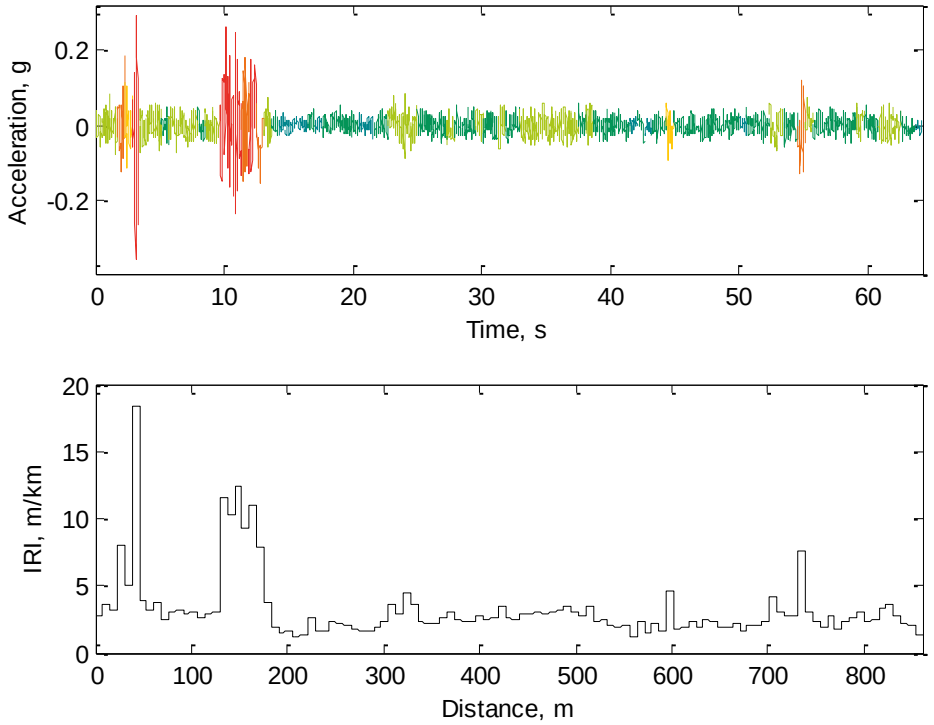

Figure D.1: IRI Approximation — Road Segment 1

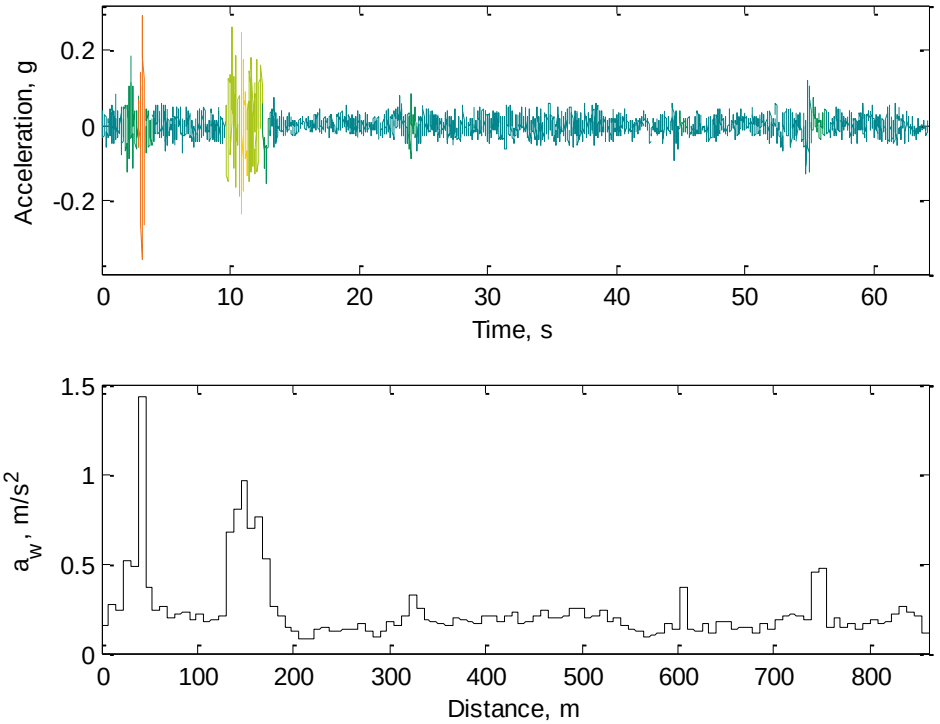

Figure D.2: Comfort Approximation — Road Segment 1

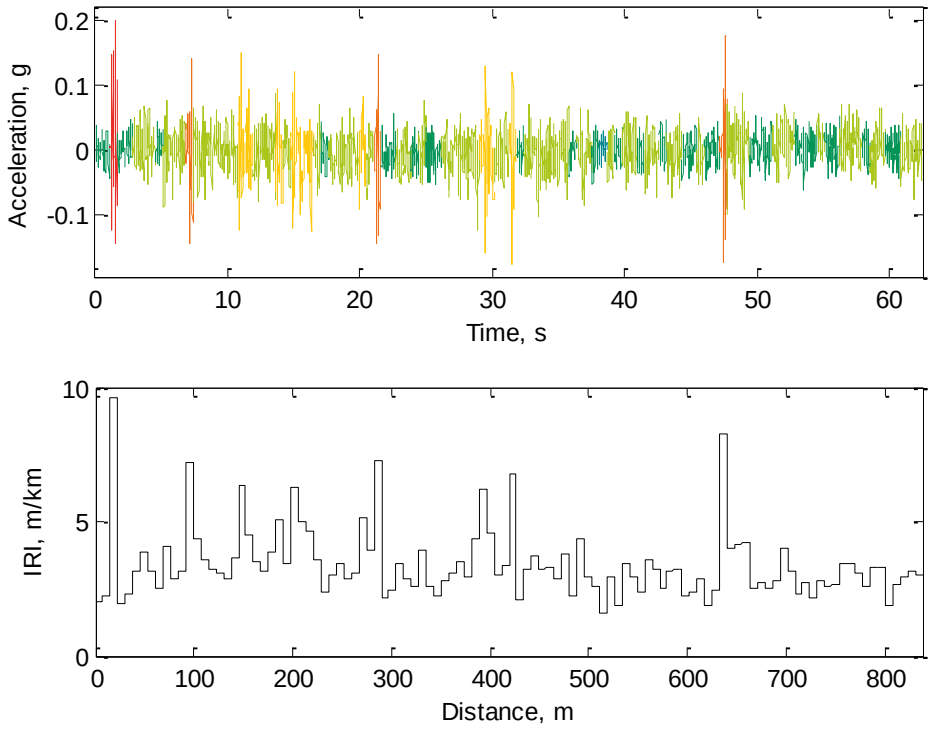

Figure D.3: IRI Approximation — Road Segment 2

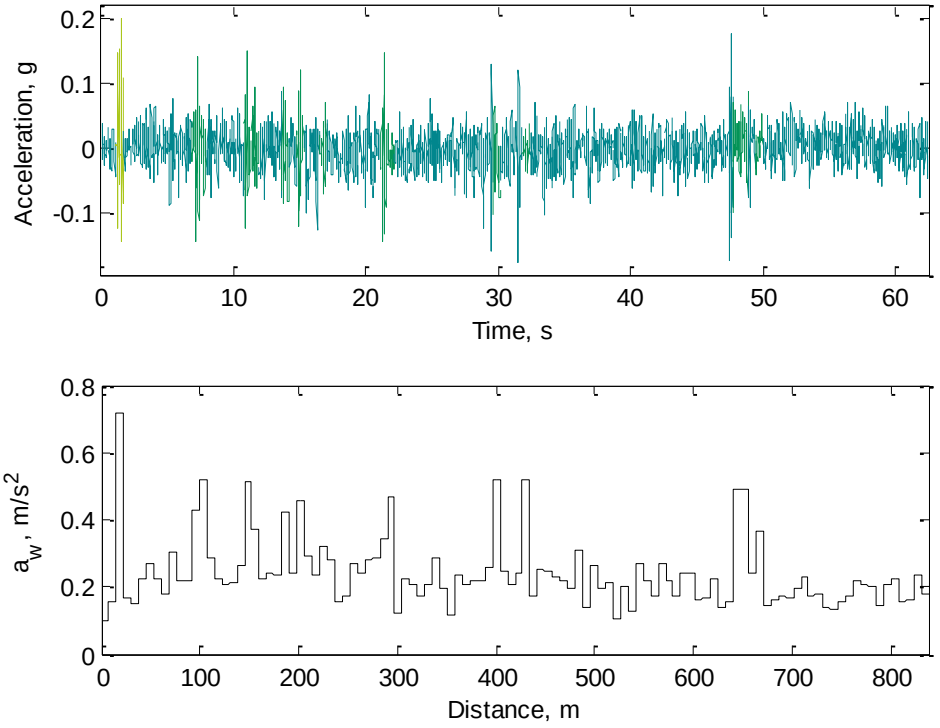

Figure D.4: Comfort Approximation — Road Segment 2

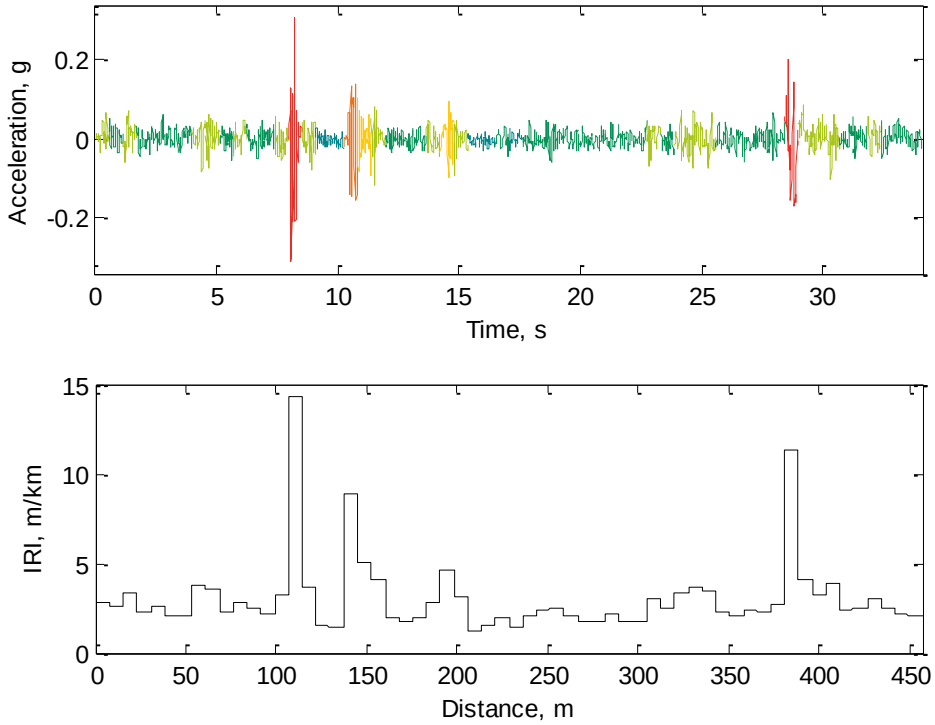

Figure D.5: IRI Approximation — Road Segment 3

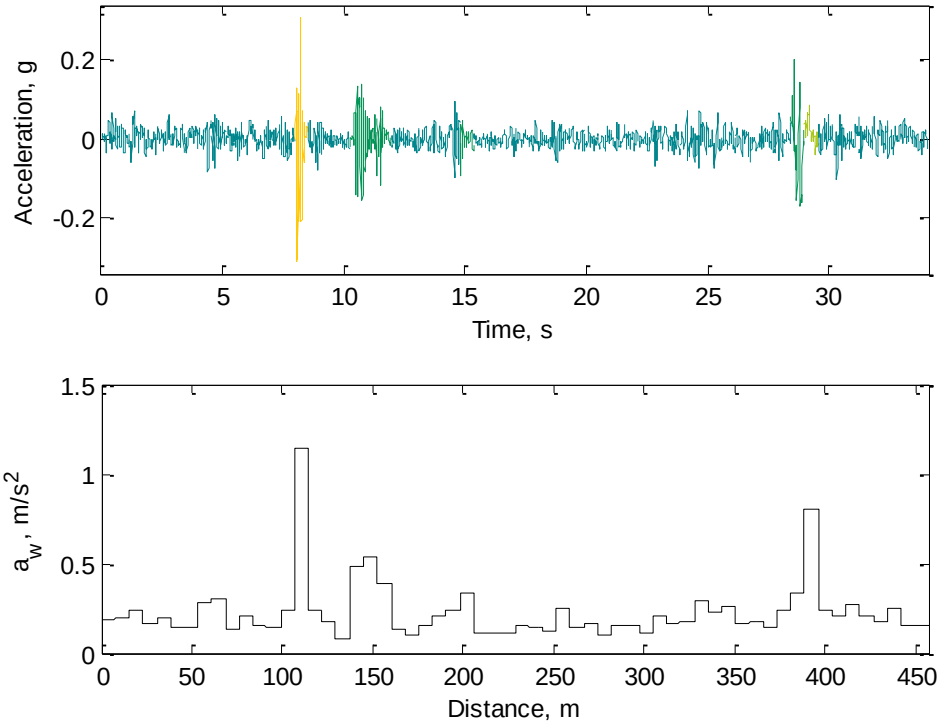

Figure D.6: Comfort Approximation — Road Segment 3

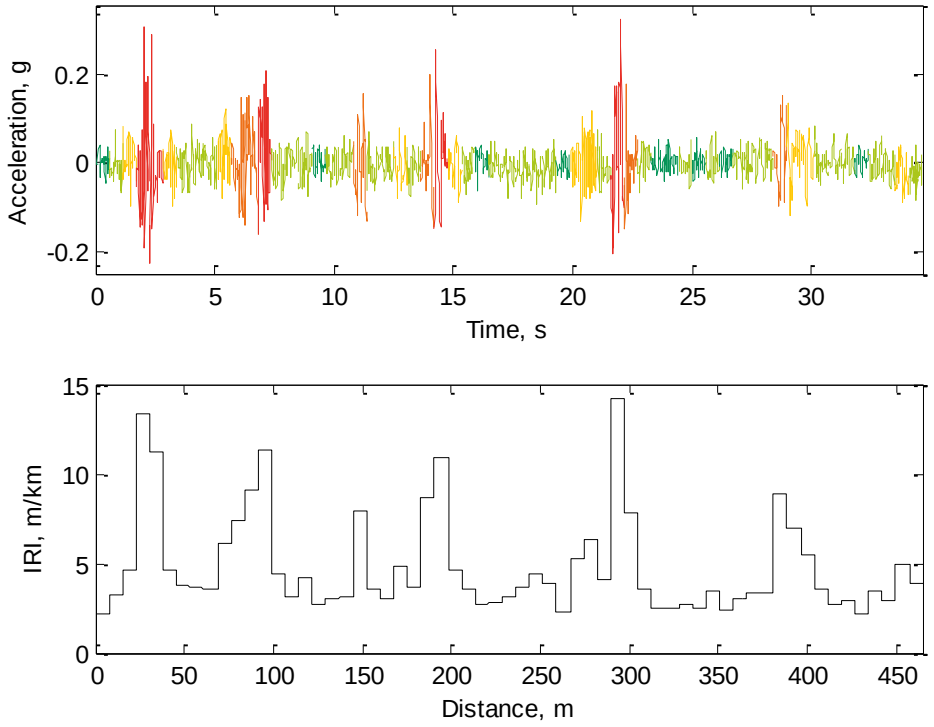

Figure D.7: IRI Approximation — Road Segment 4

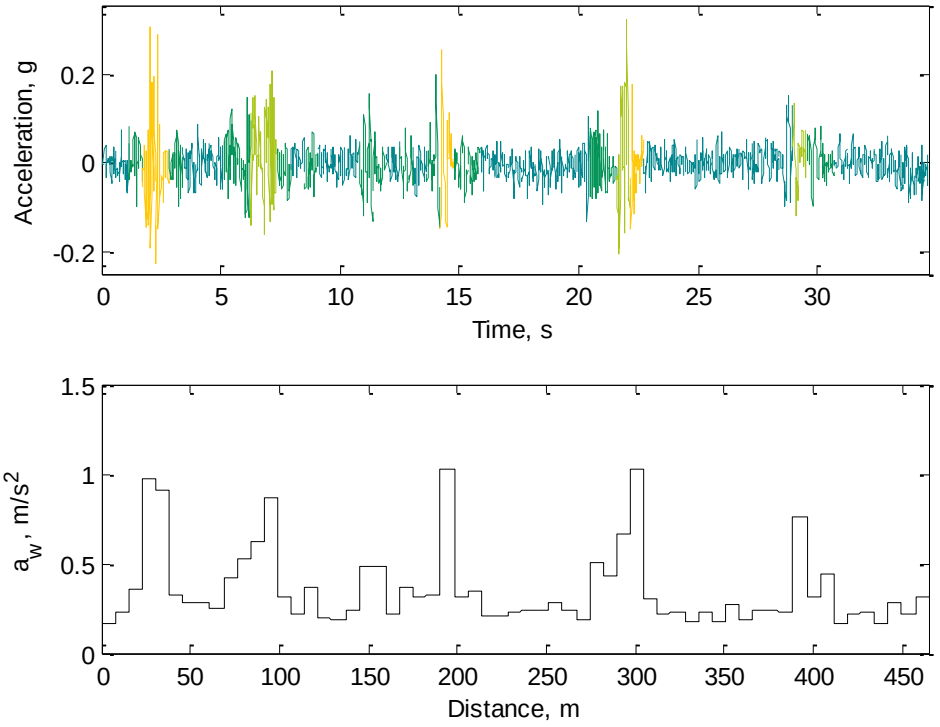

Figure D.8: Comfort Approximation — Road Segment 4

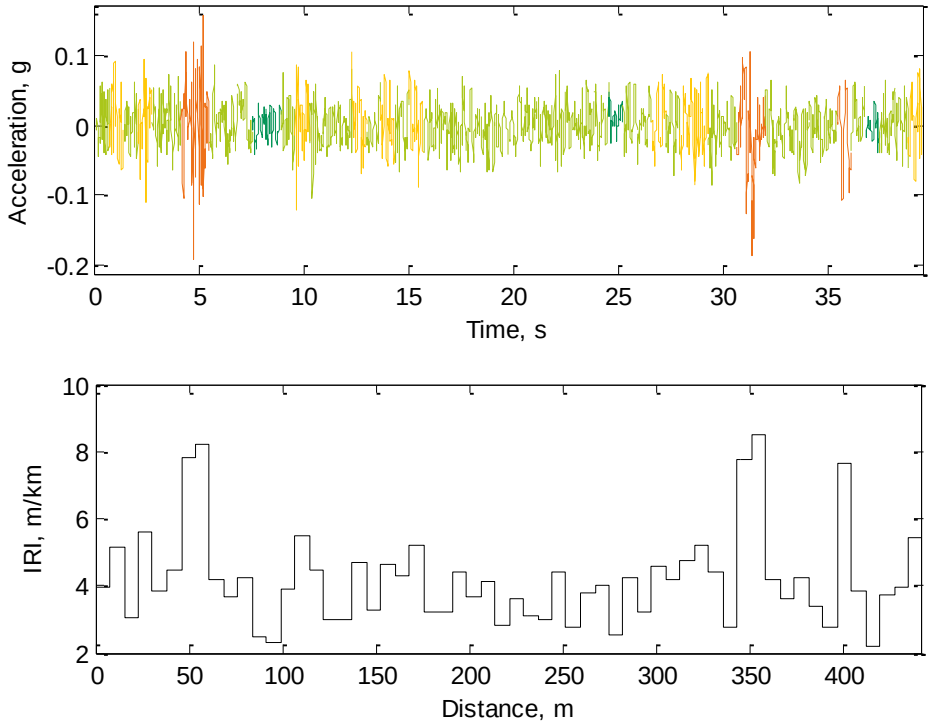

Figure D.9: IRI Approximation — Road Segment 5

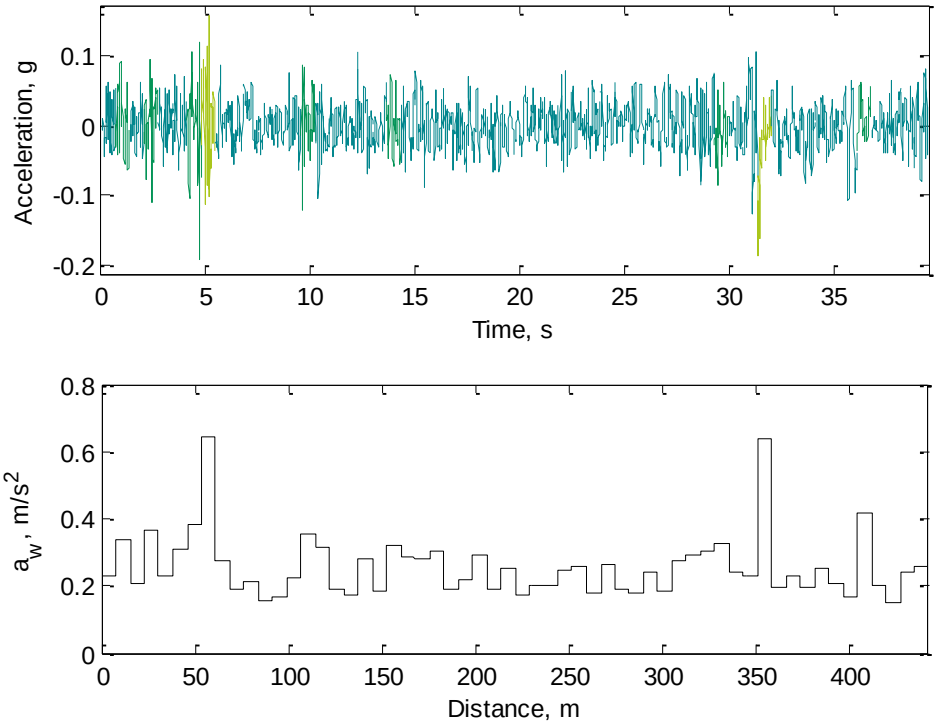

Figure D.10: Comfort Approximation — Road Segment 5

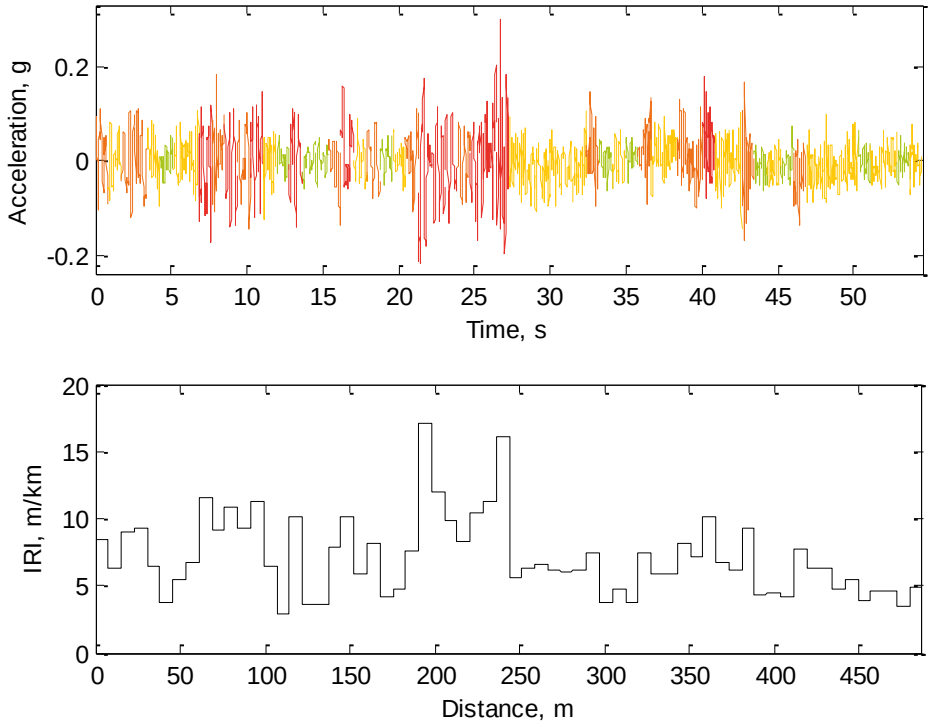

Figure D.11: IRI Approximation — Road Segment 6

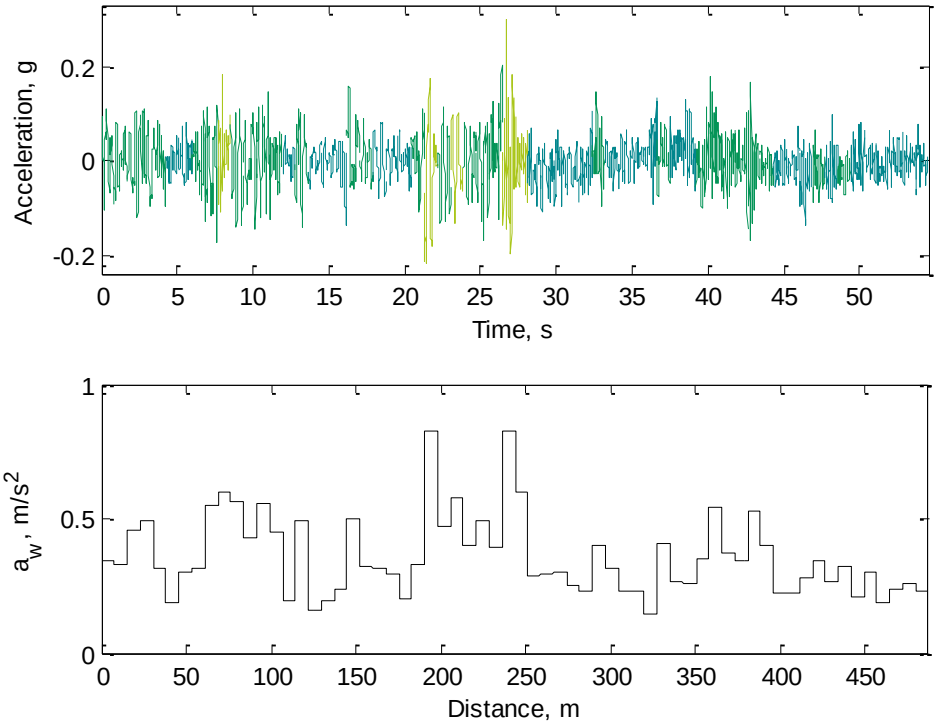

Figure D.12: Comfort Approximation — Road Segment 6

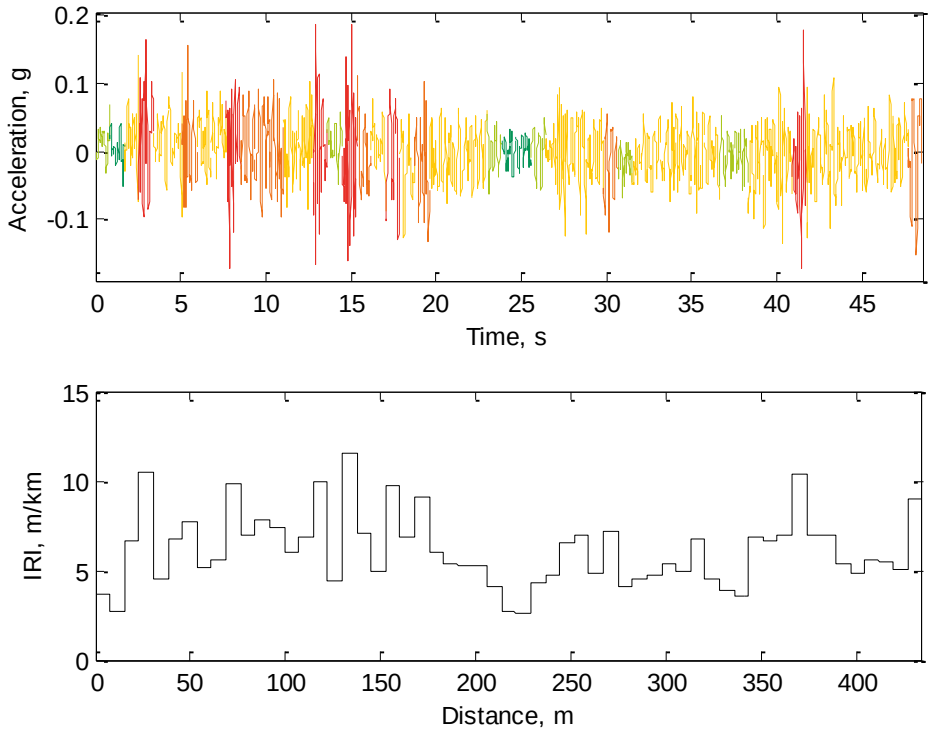

Figure D.13: IRI Approximation — Road Segment 7

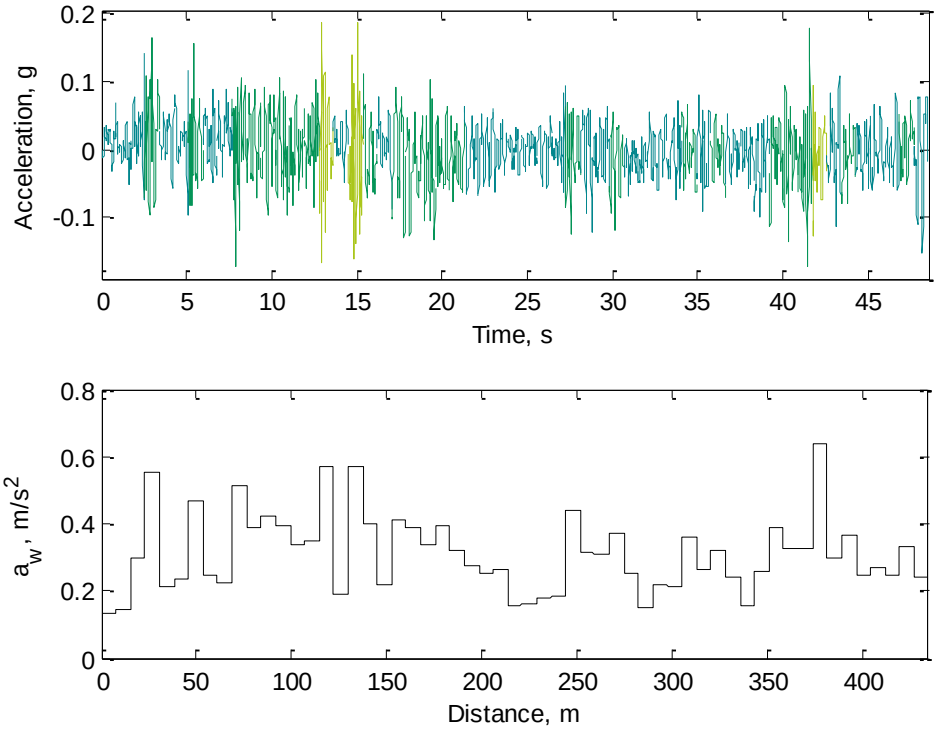

Figure D.14: Comfort Approximation — Road Segment 7

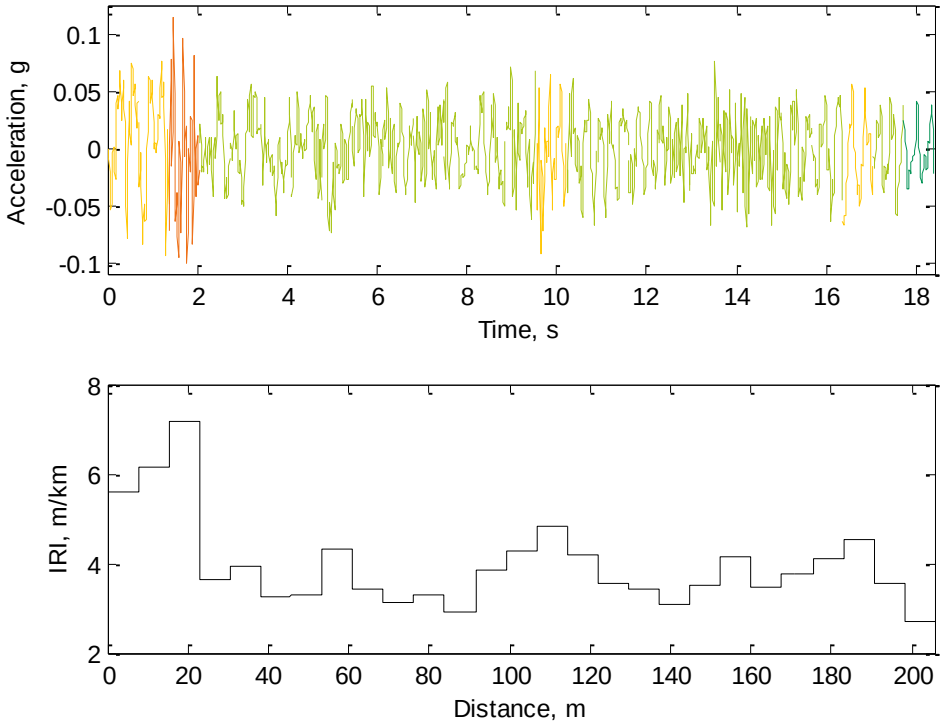

Figure D.15: IRI Approximation — Road Segment 8

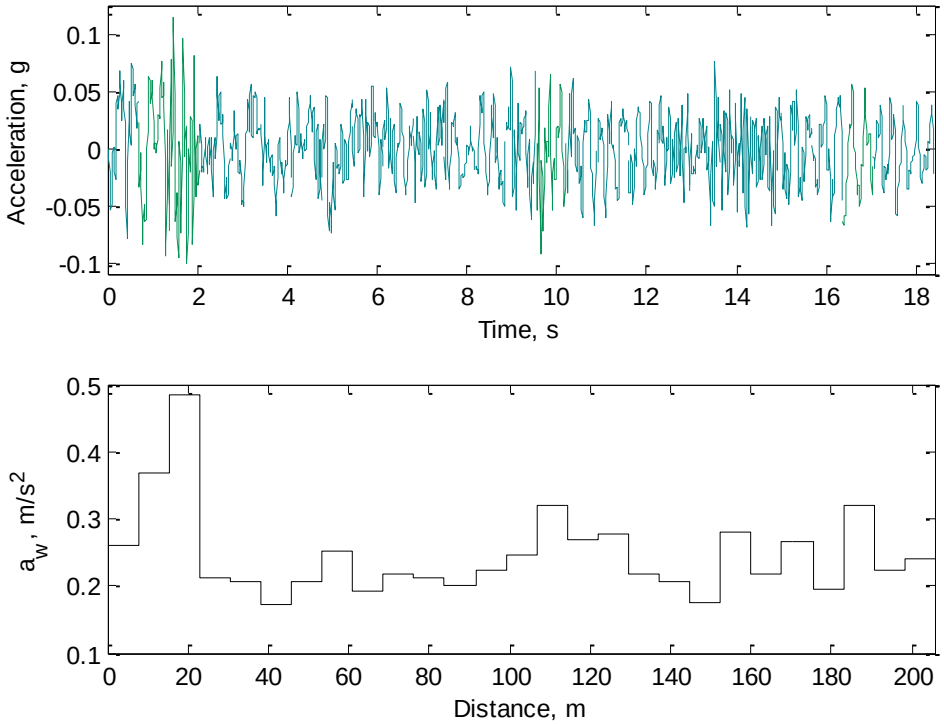

Figure D.16: Comfort Approximation — Road Segment 8

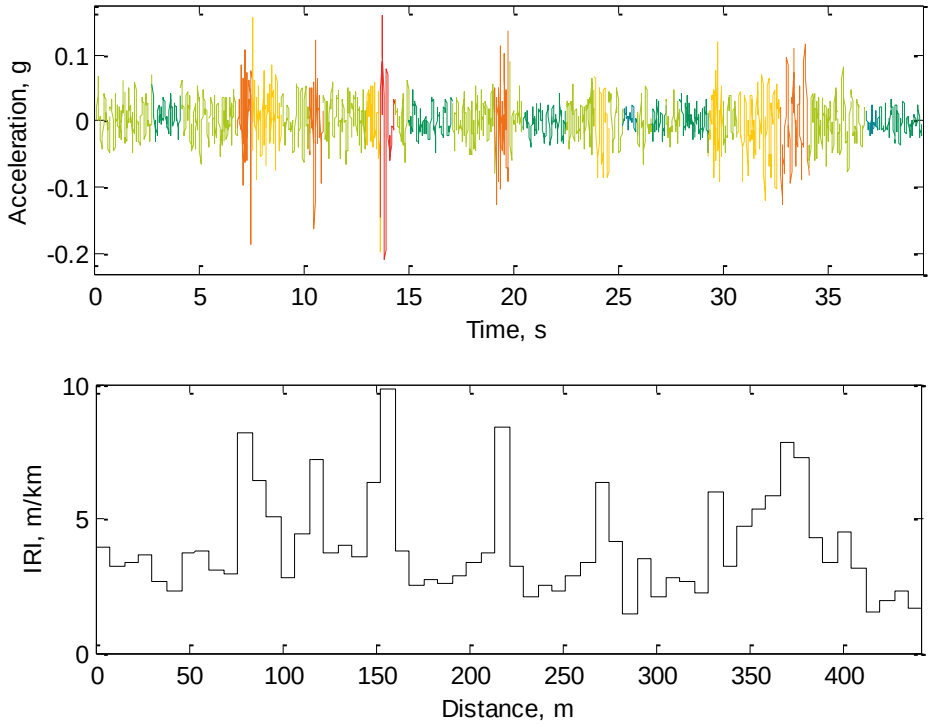

Figure D.17: IRI Approximation — Road Segment 9

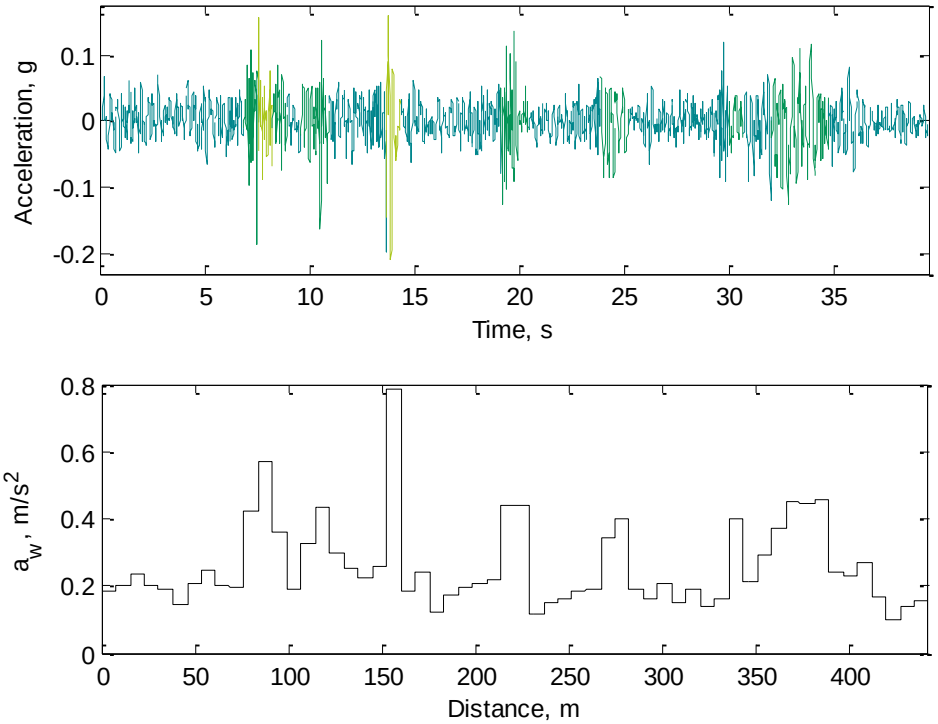

Figure D.18: Comfort Approximation — Road Segment 9

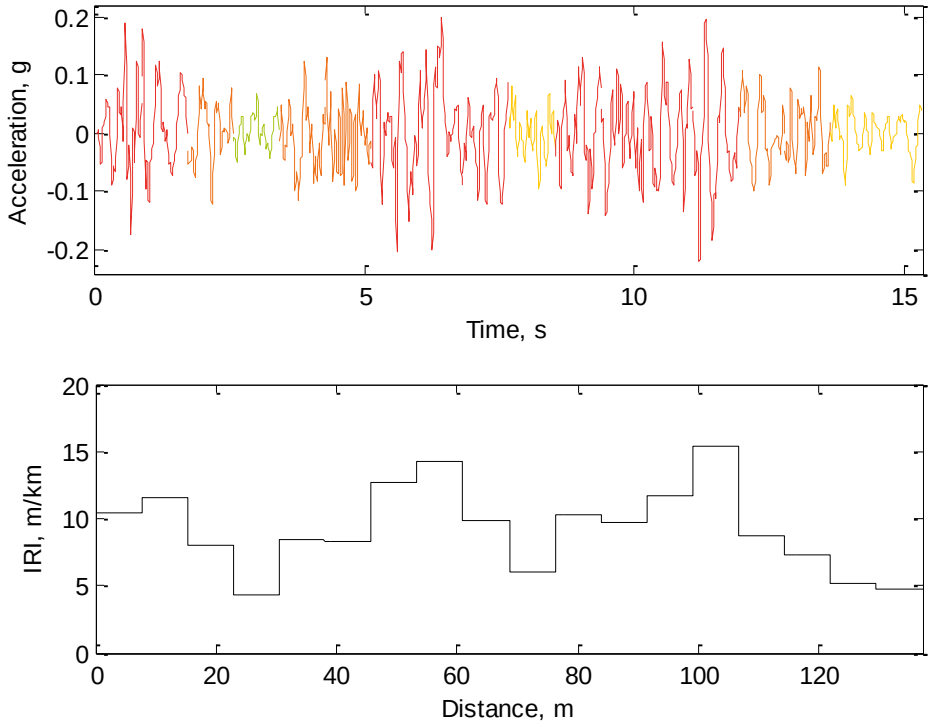

Figure D.19: IRI Approximation — Road Segment 10

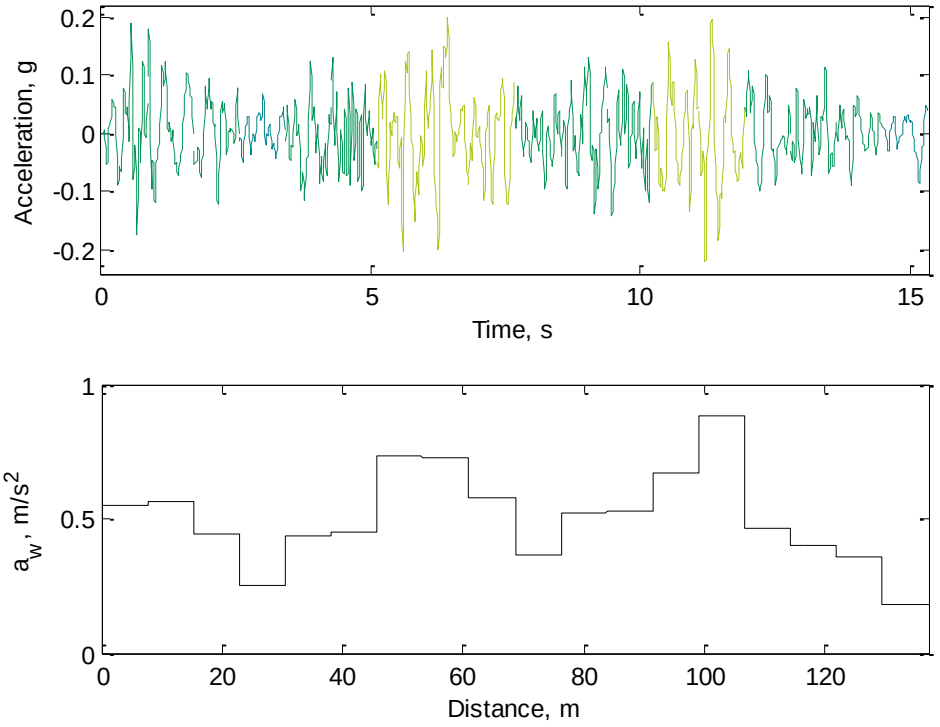

Figure D.20: Comfort Approximation — Road Segment 10

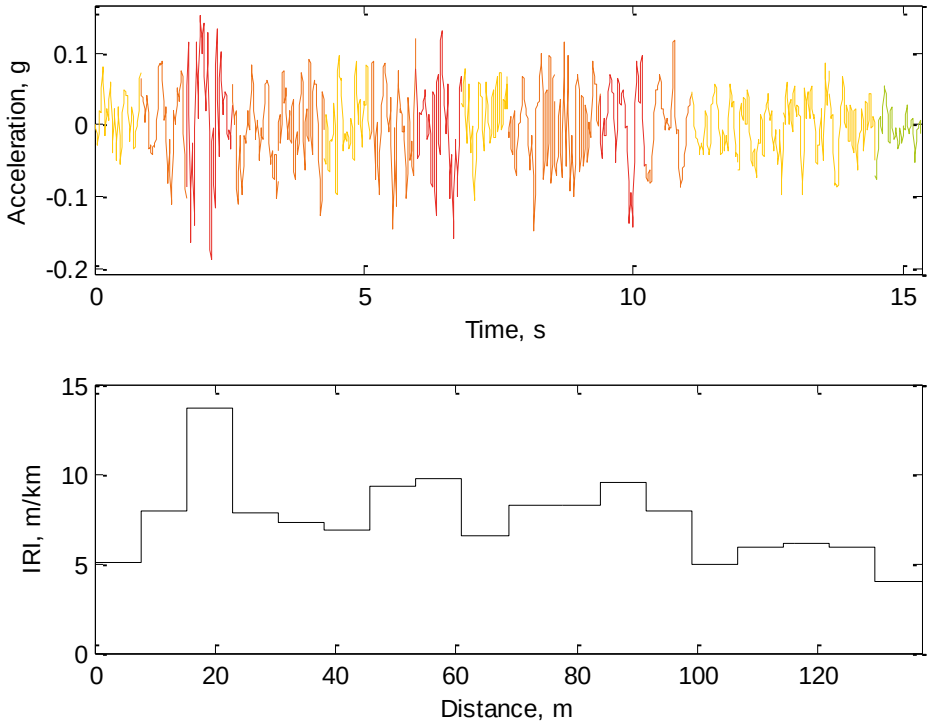

Figure D.21: IRI Approximation — Road Segment 11

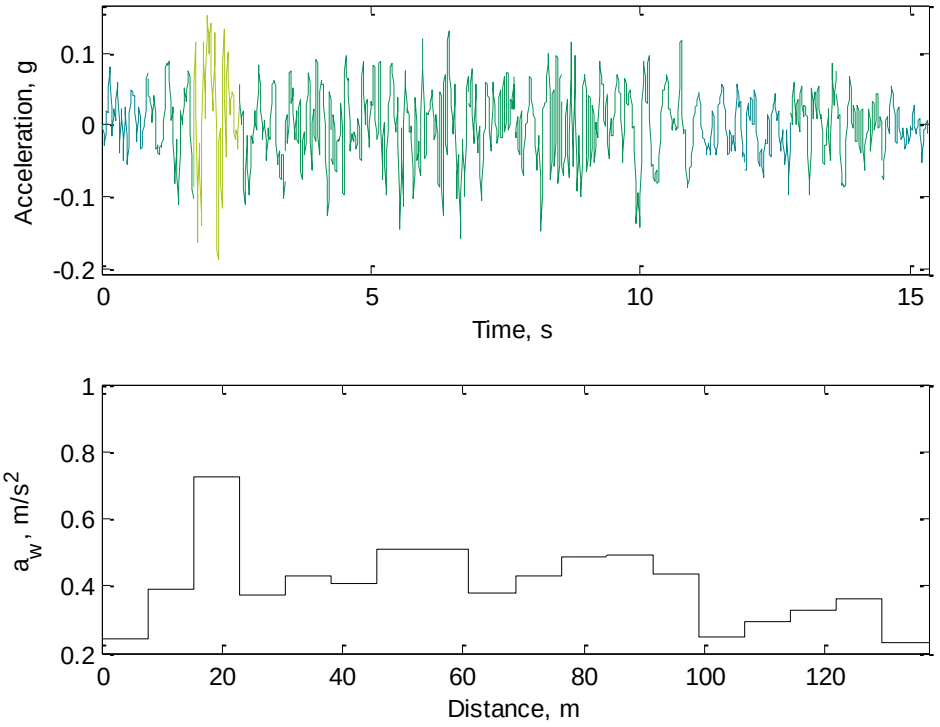

Figure D.22: Comfort Approximation — Road Segment 11

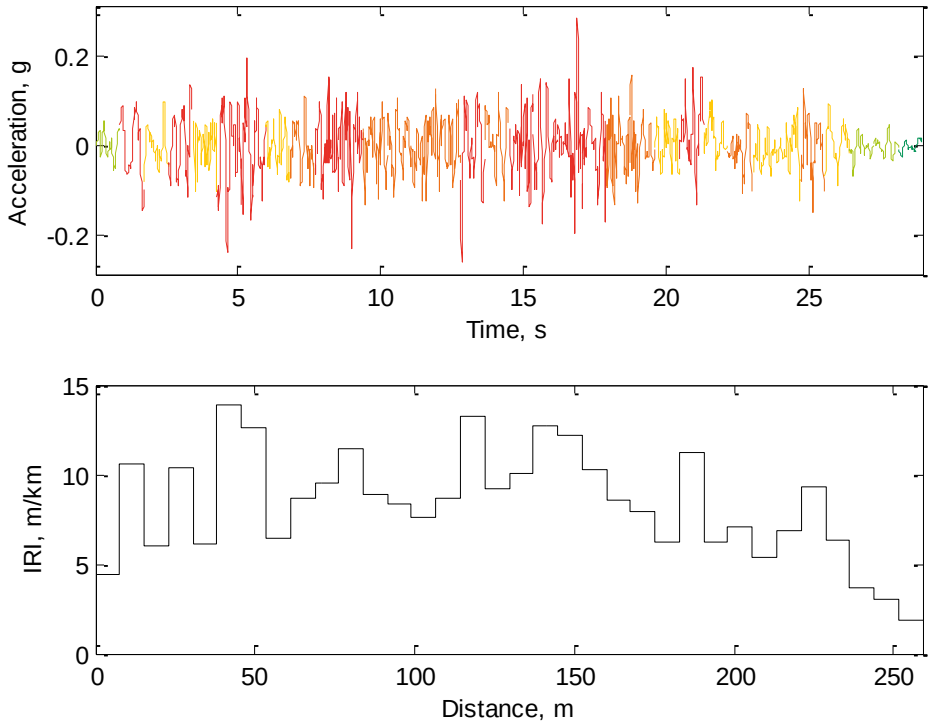

Figure D.23: IRI Approximation — Road Segment 12

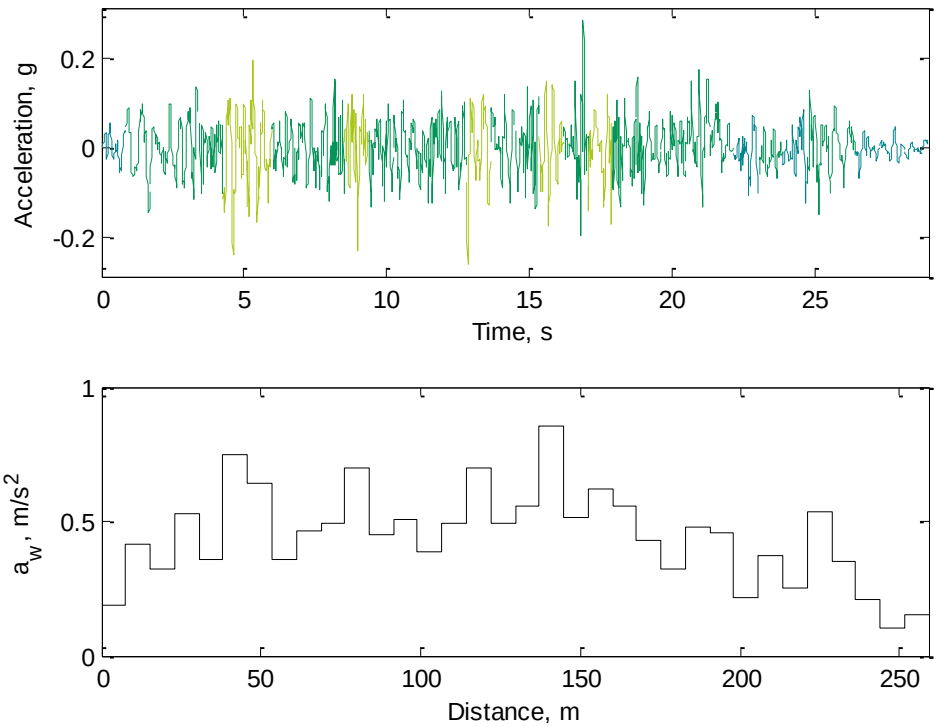

Figure D.24: Comfort Approximation — Road Segment 12

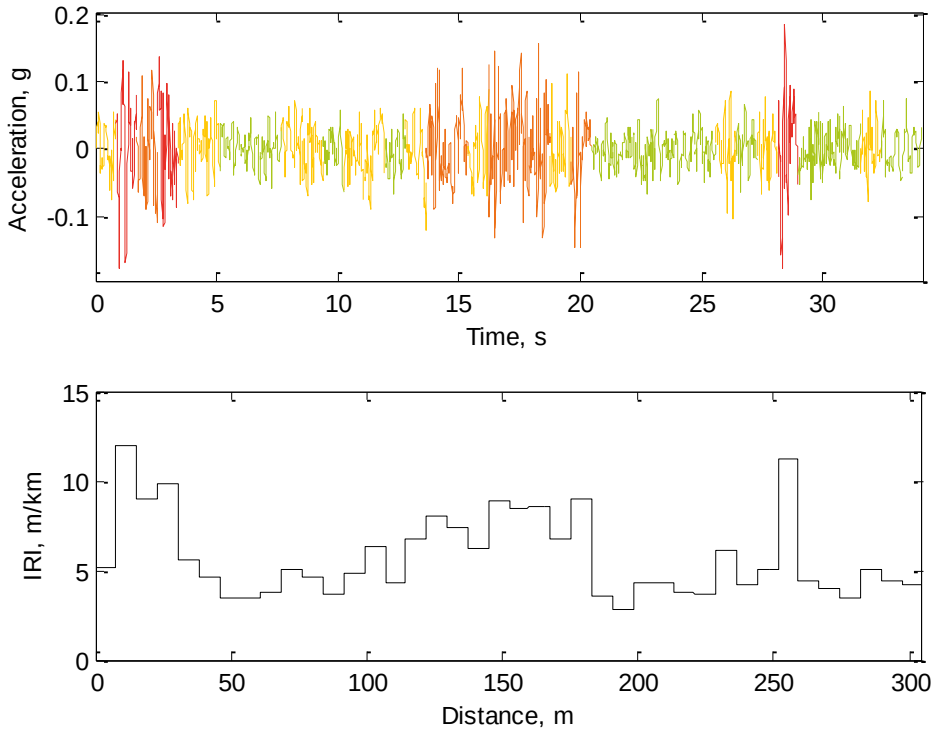

Figure D.25: IRI Approximation — Road Segment 13

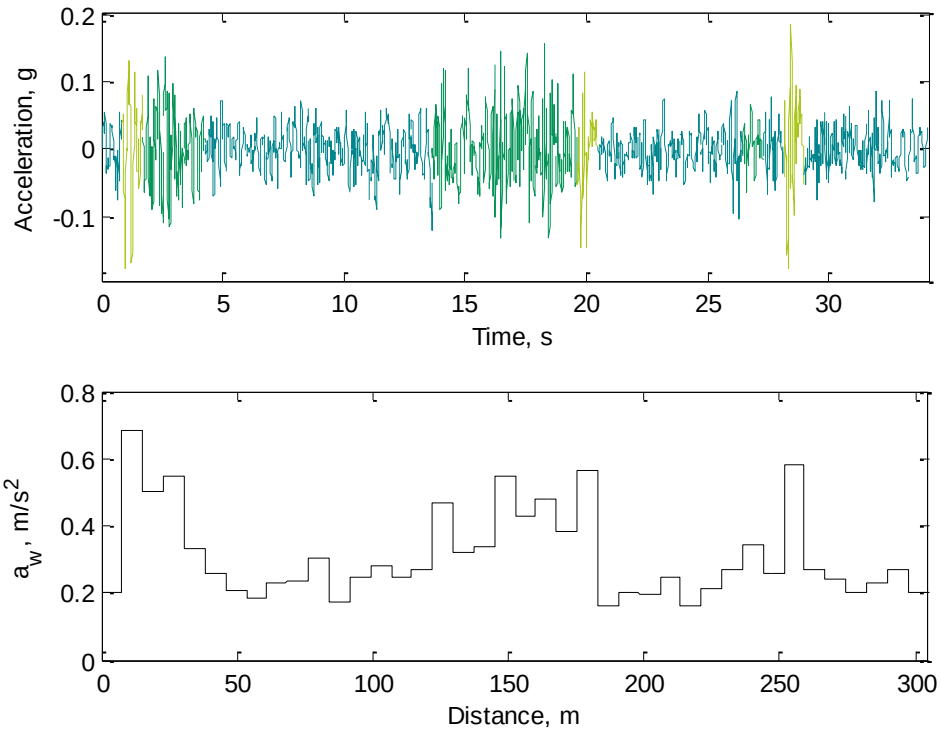

Figure D.26: Comfort Approximation — Road Segment 13

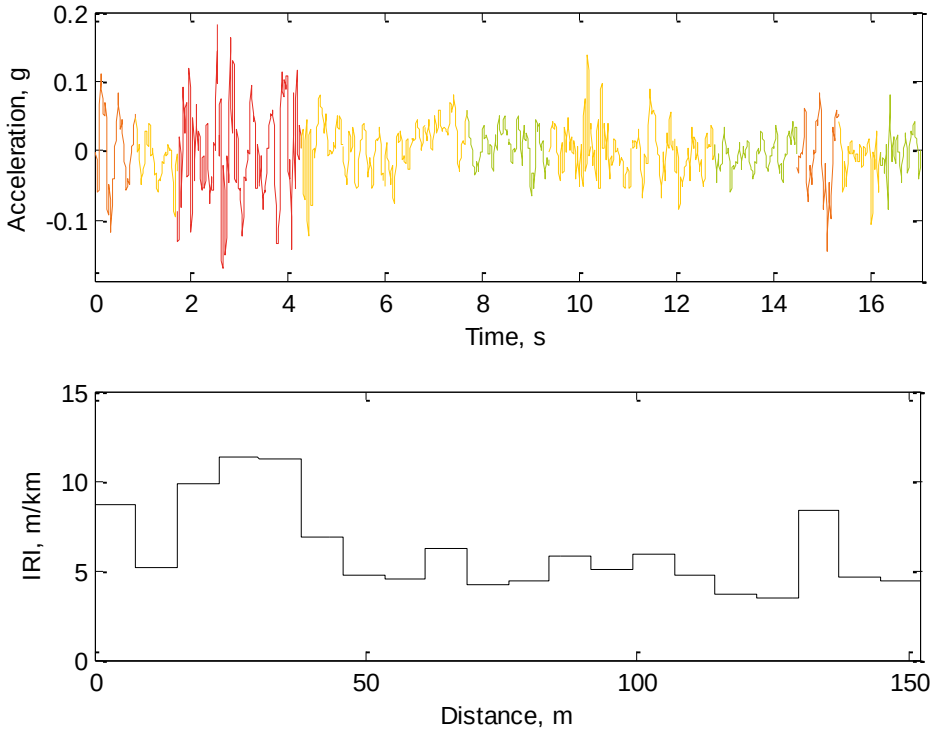

Figure D.27: IRI Approximation — Road Segment 14

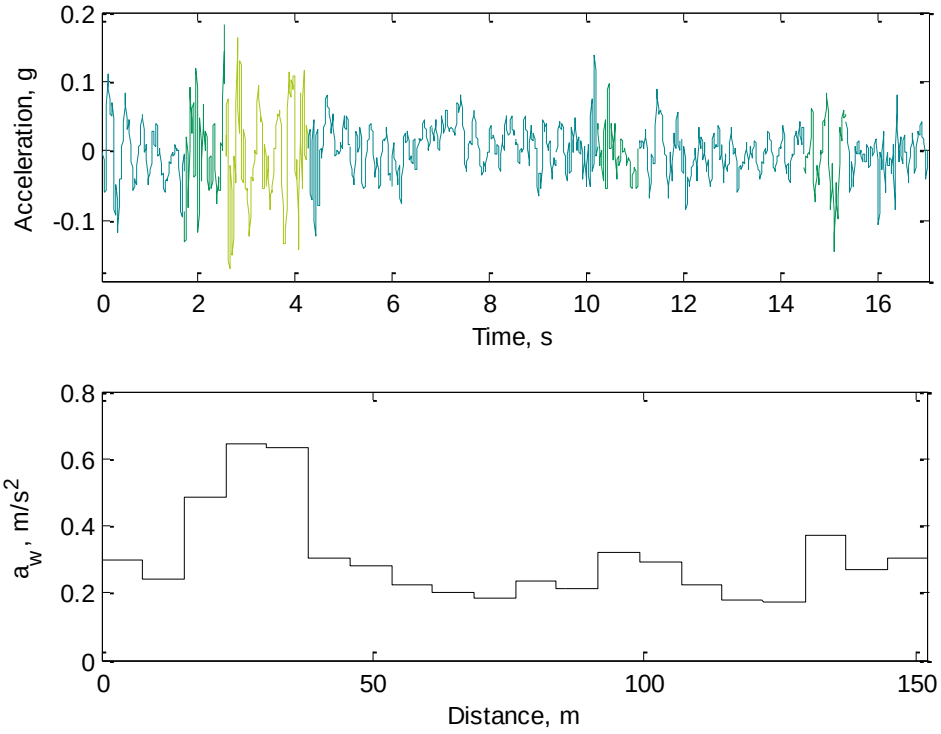

Figure D.28: Comfort Approximation — Road Segment 14

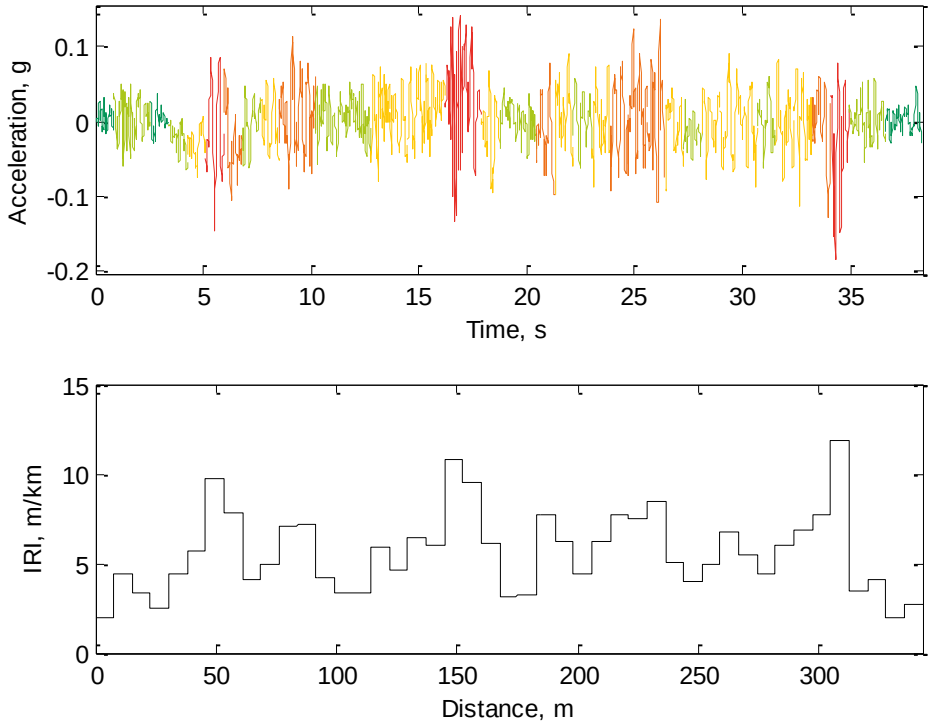

Figure D.29: IRI Approximation — Road Segment 15

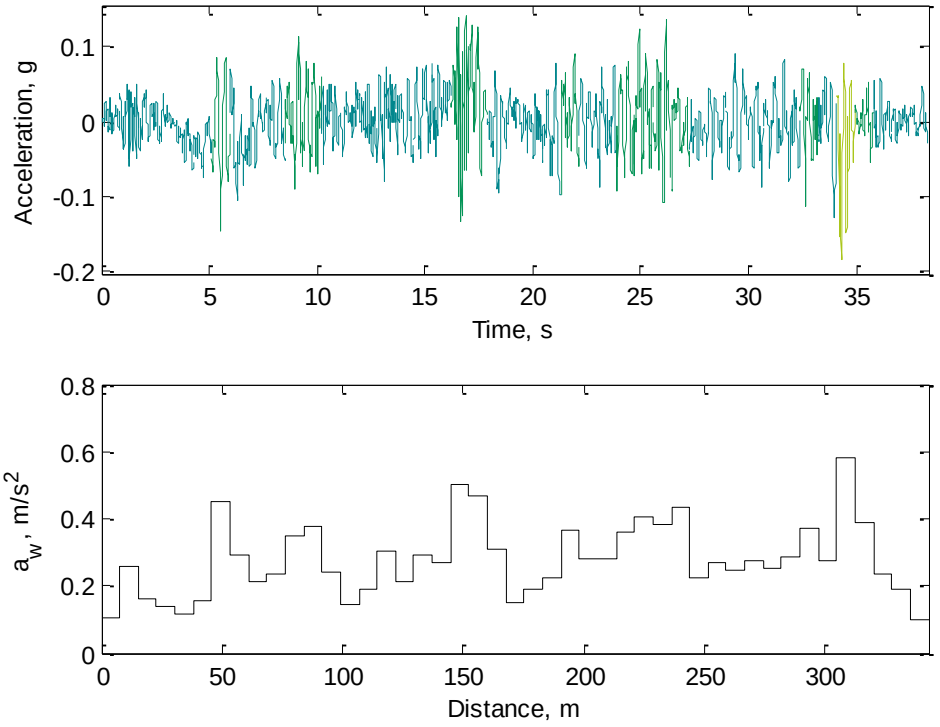

Figure D.30: Comfort Approximation — Road Segment 15

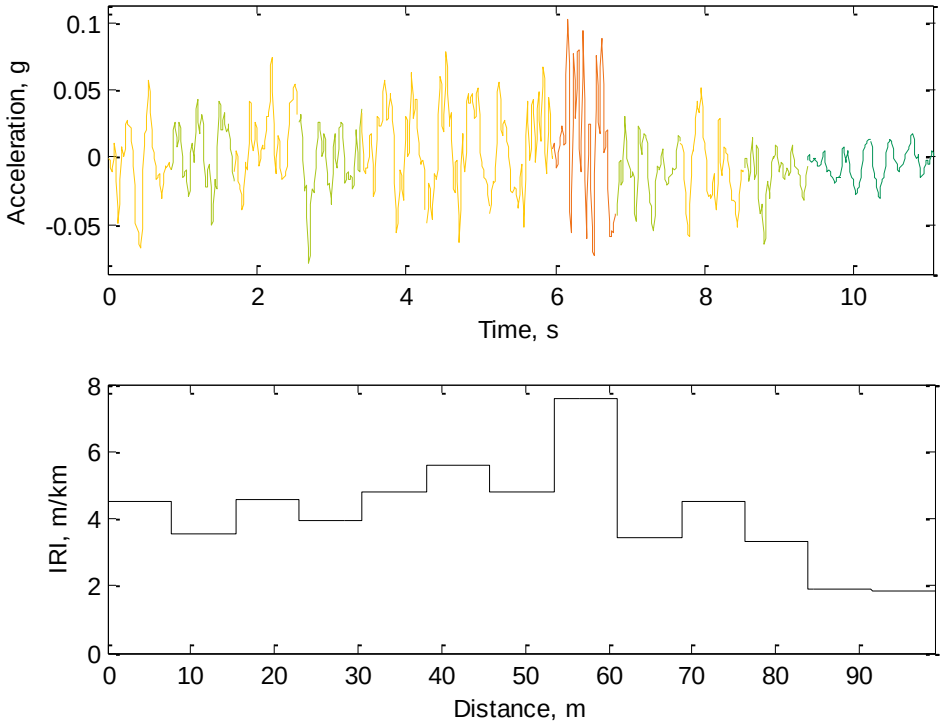

Figure D.31: IRI Approximation — Road Segment 16

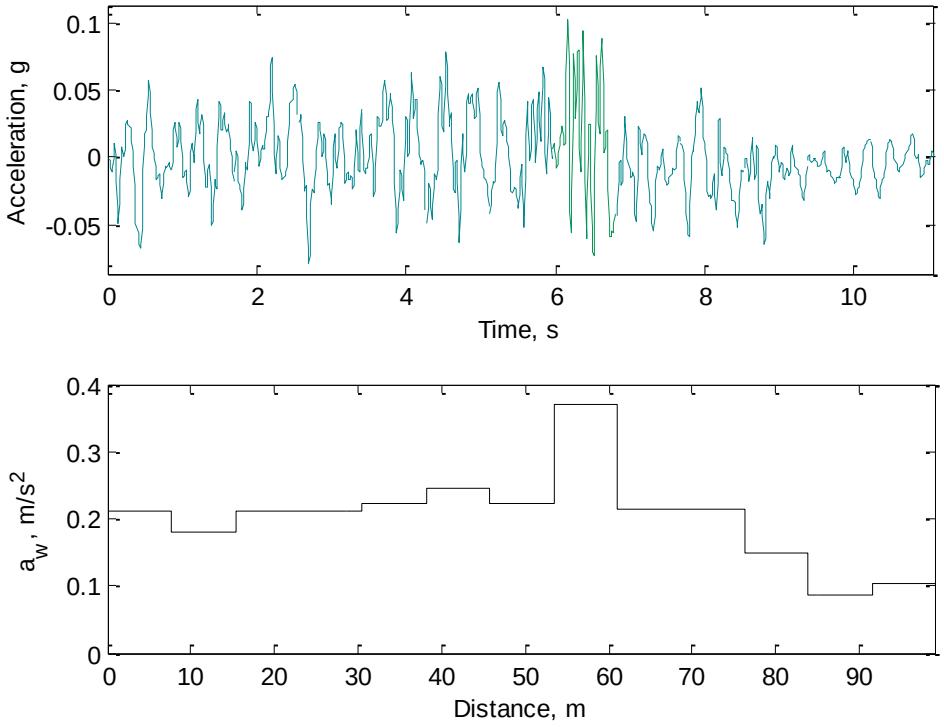

Figure D.32: Comfort Approximation — Road Segment 16

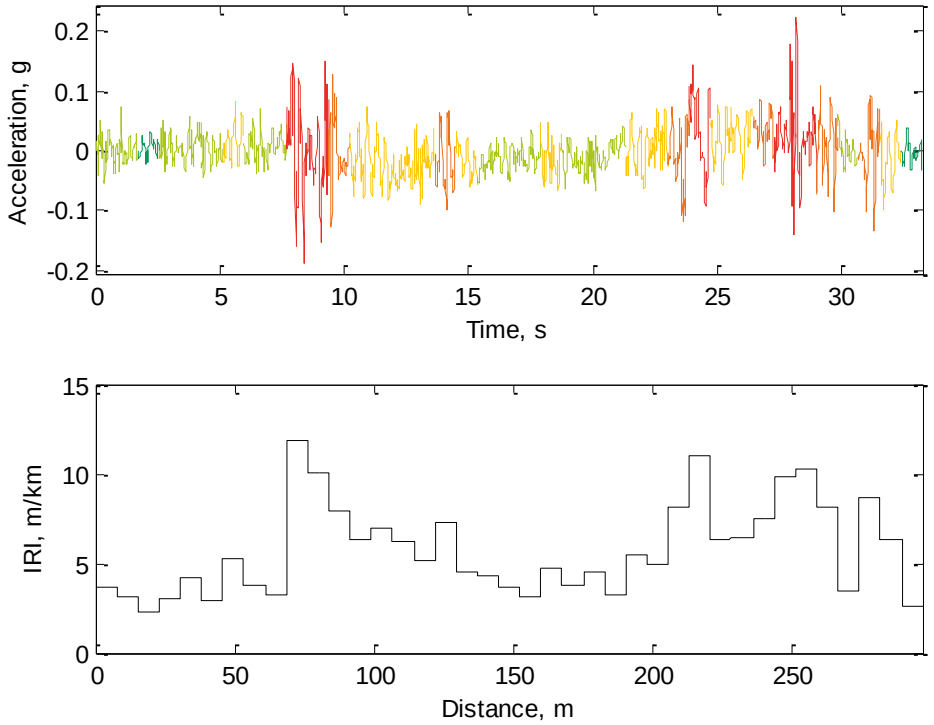

Figure D.33: IRI Approximation — Road Segment 17

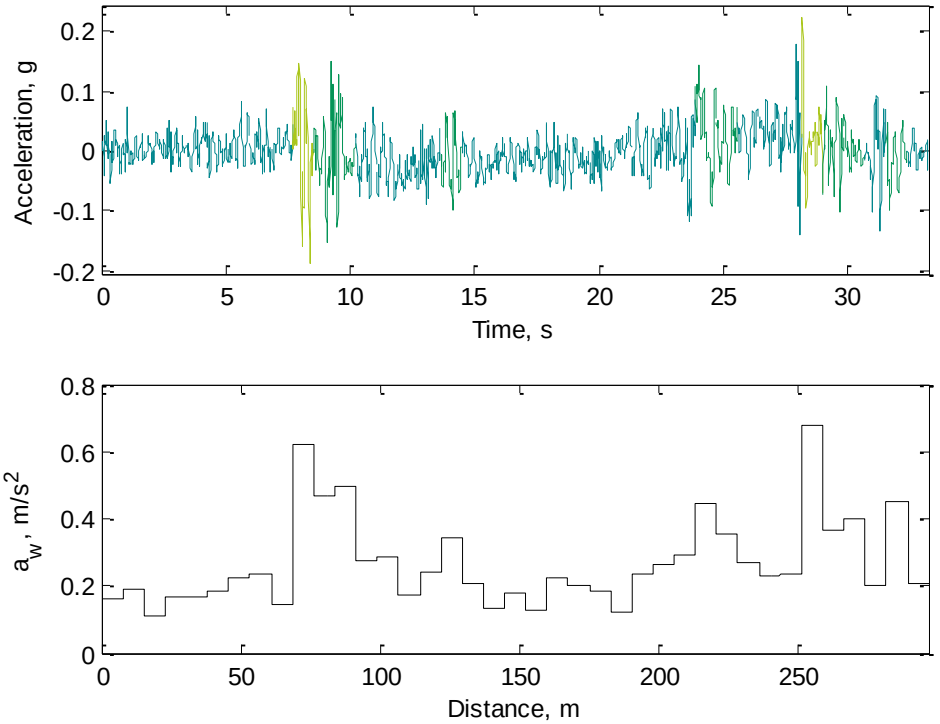

Figure D.34: Comfort Approximation — Road Segment 17

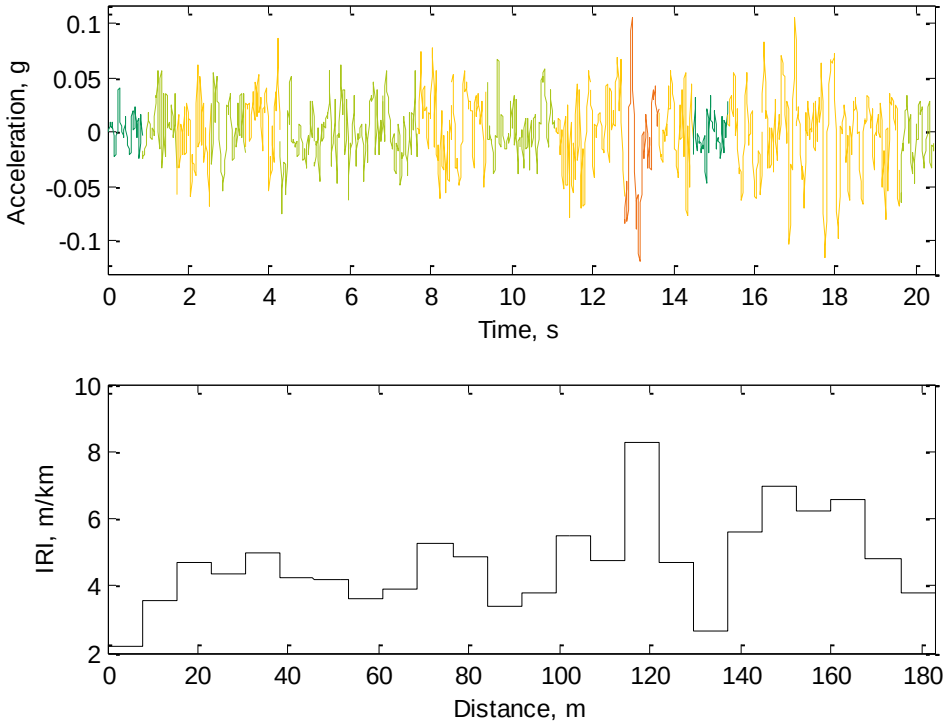

Figure D.35: IRI Approximation — Road Segment 18

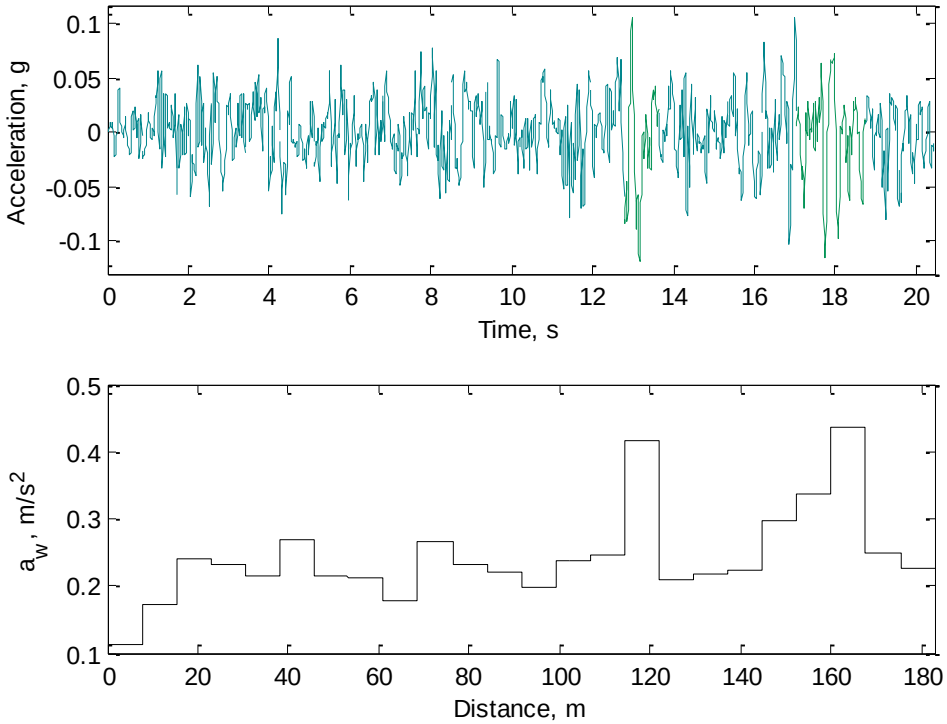

Figure D.36: Comfort Approximation — Road Segment 18

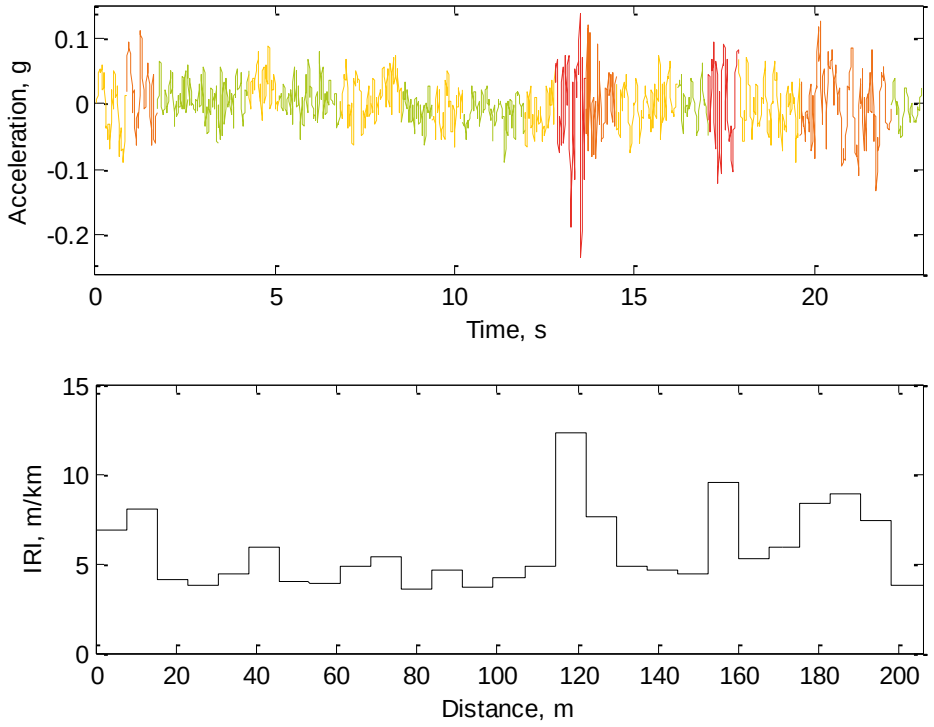

Figure D.37: IRI Approximation — Road Segment 19

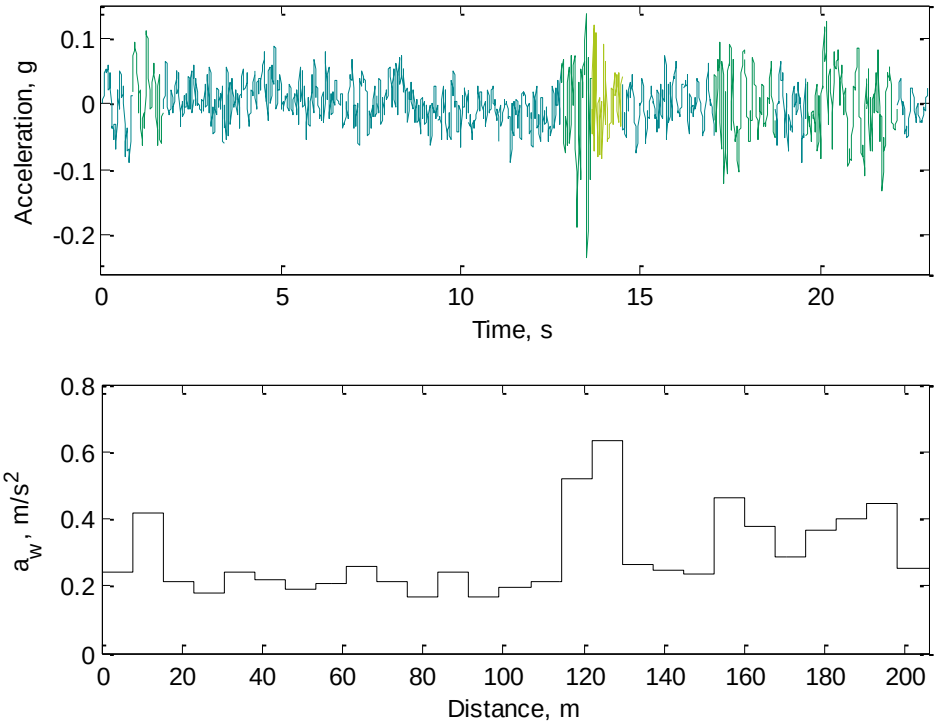

Figure D.38: Comfort Approximation — Road Segment 19

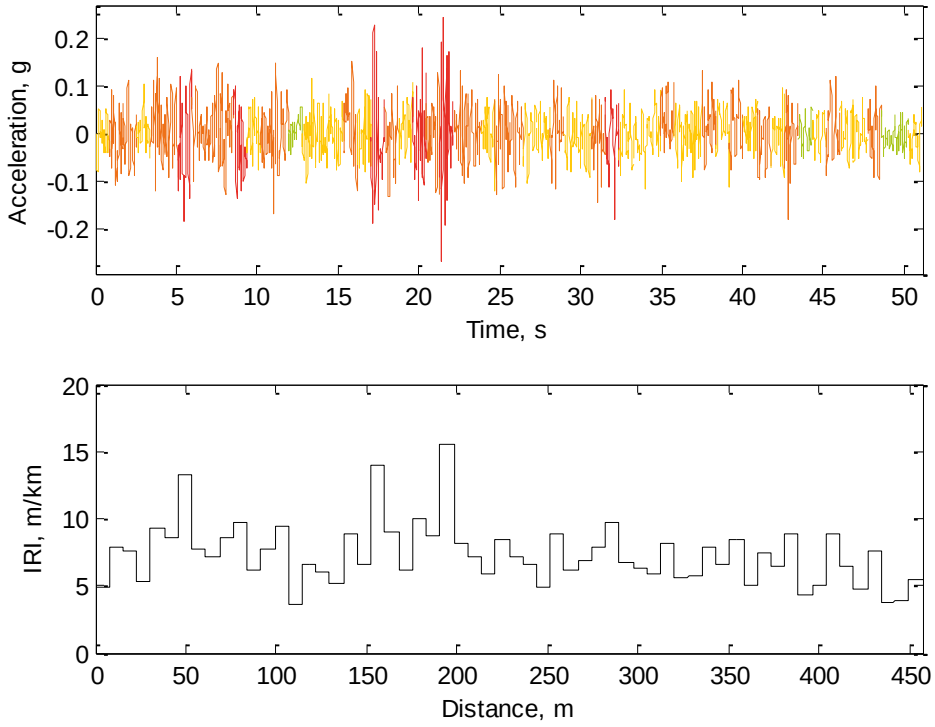

Figure D.39: IRI Approximation — Road Segment 20

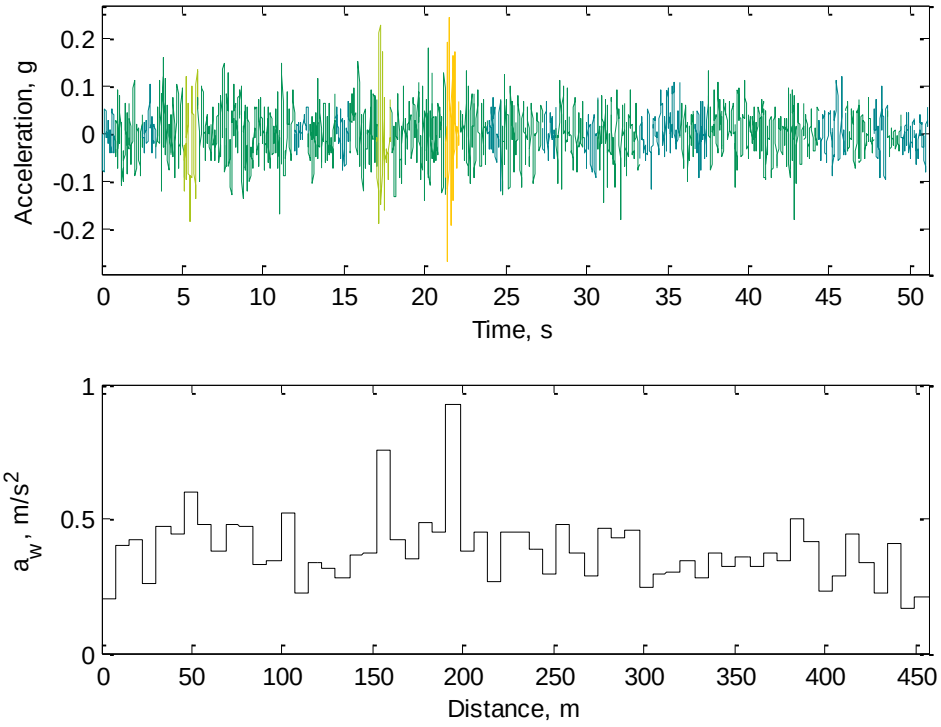

Figure D.40: Comfort Approximation — Road Segment 20

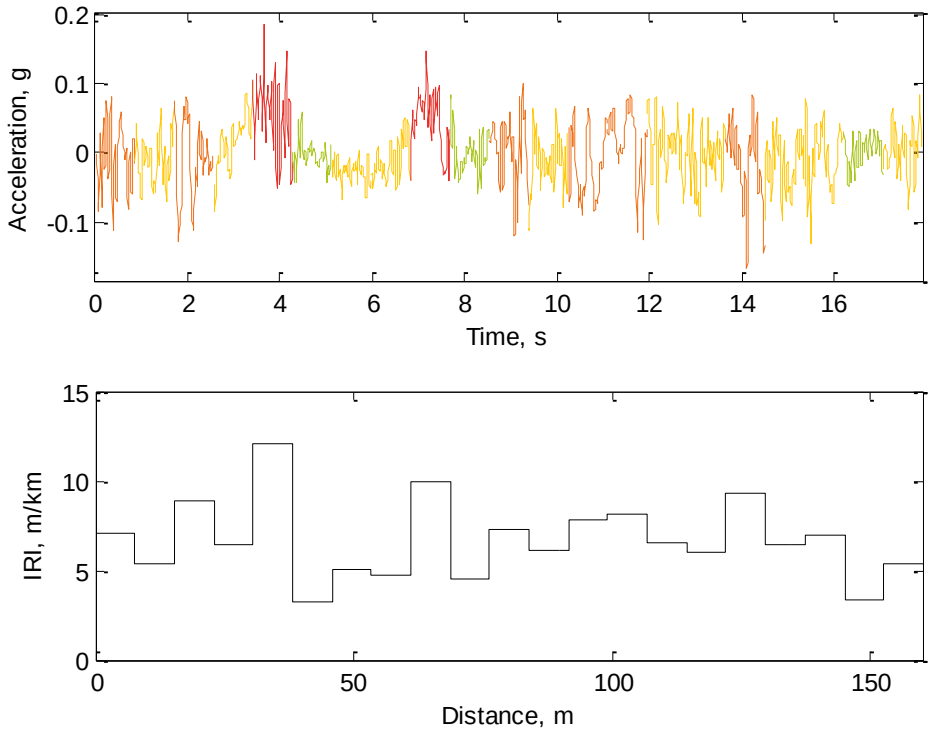

Figure D.41: IRI Approximation — Road Segment 21

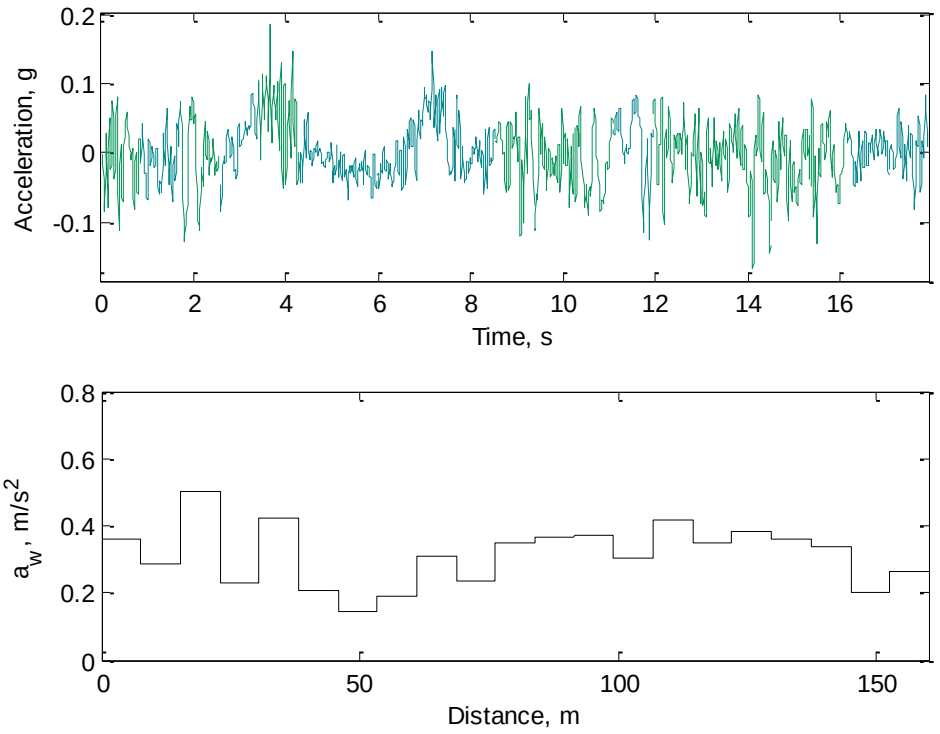

Figure D.42: Comfort Approximation — Road Segment 21

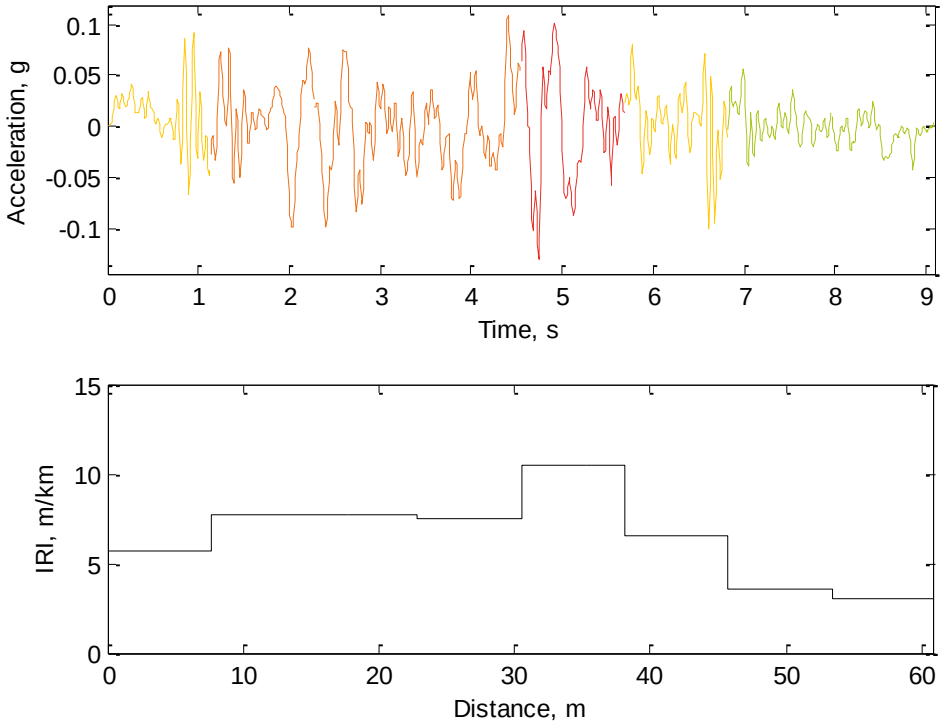

Figure D.43: IRI Approximation — Road Segment 22

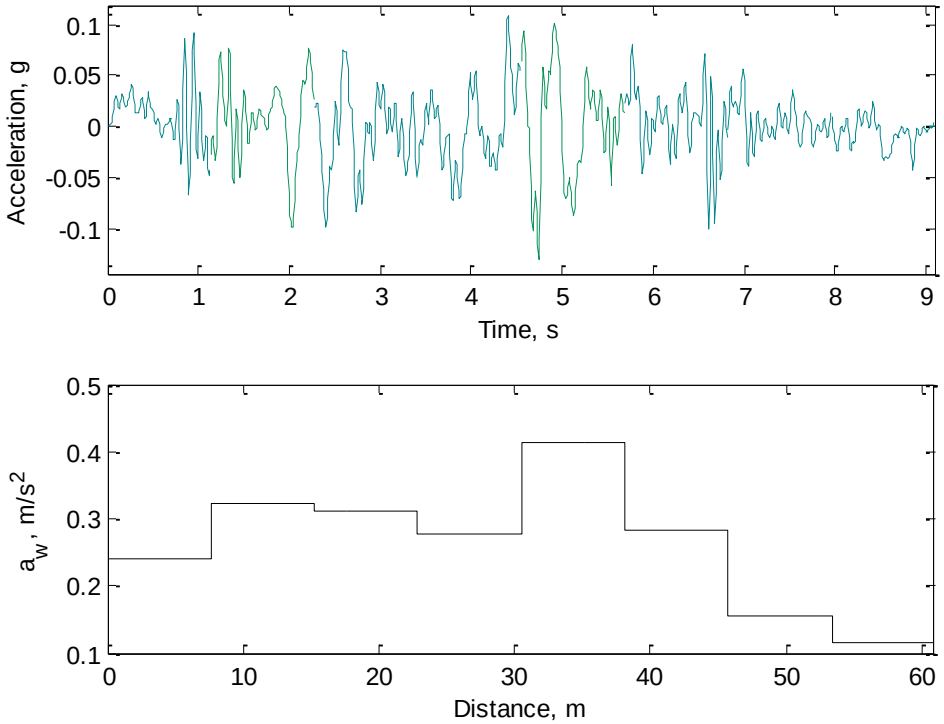

Figure D.44: Comfort Approximation — Road Segment 22

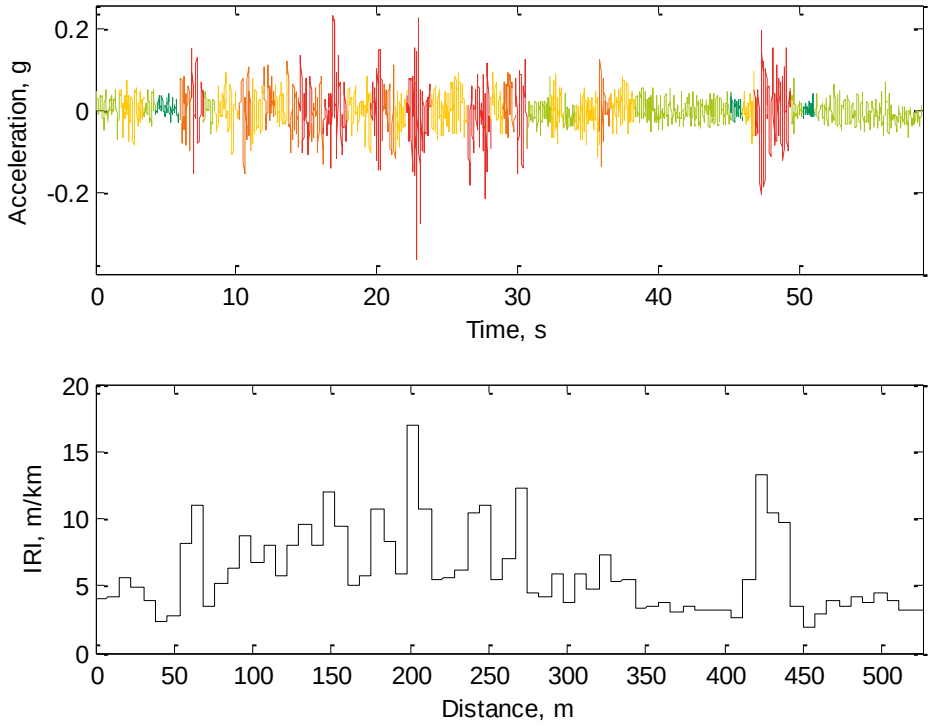

Figure D.45: IRI Approximation — Road Segment 23

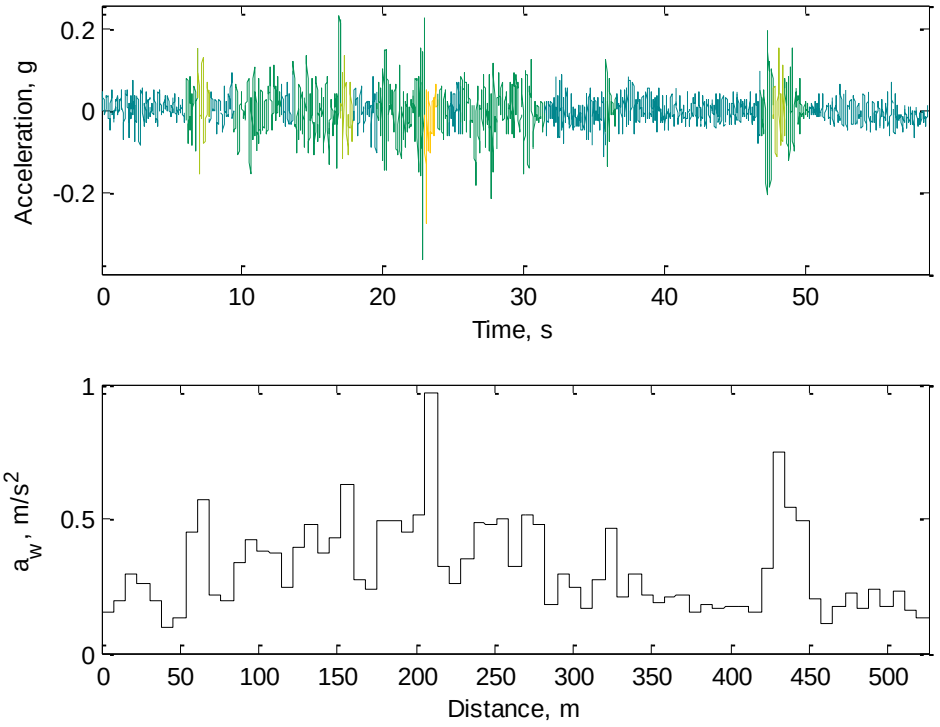

Figure D.46: Comfort Approximation — Road Segment 23

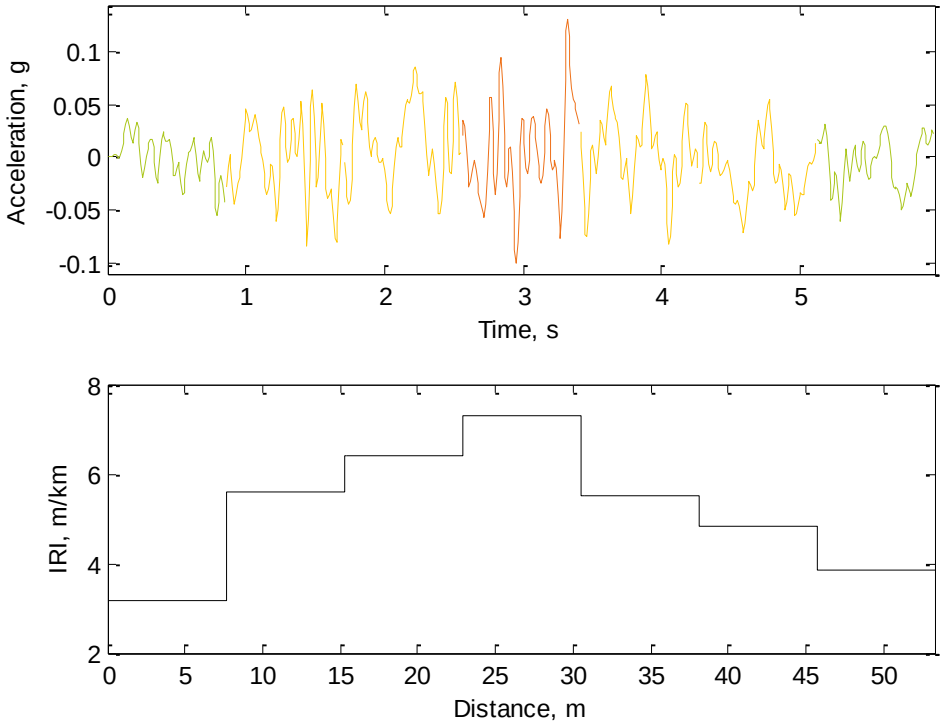

Figure D.47: IRI Approximation — Road Segment 24

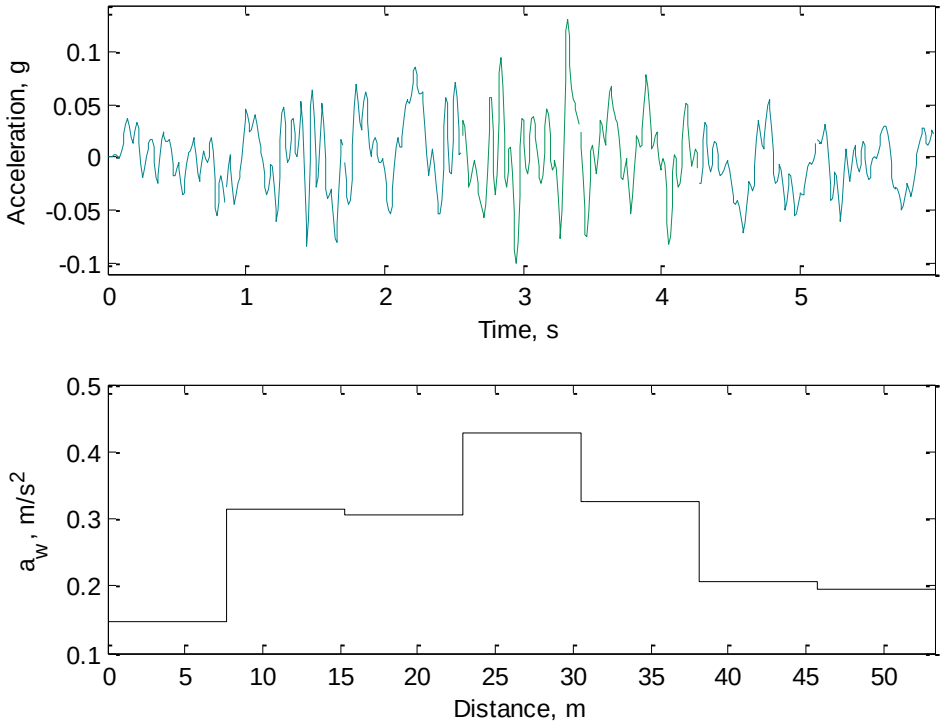

Figure D.48: Comfort Approximation — Road Segment 24

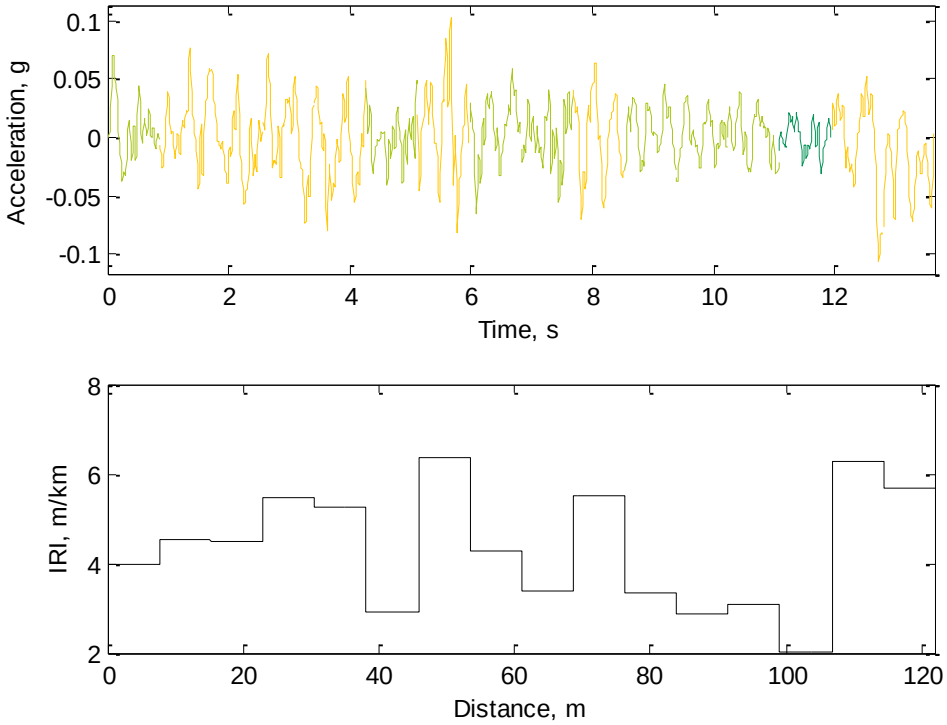

Figure D.49: IRI Approximation — Road Segment 25

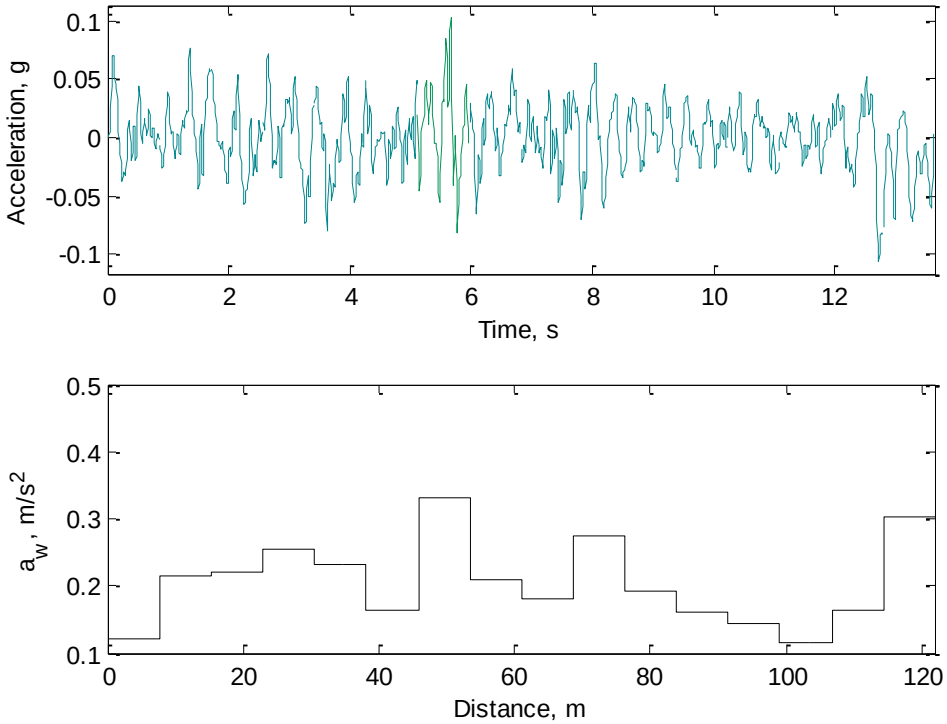

Figure D.50: Comfort Approximation — Road Segment 25

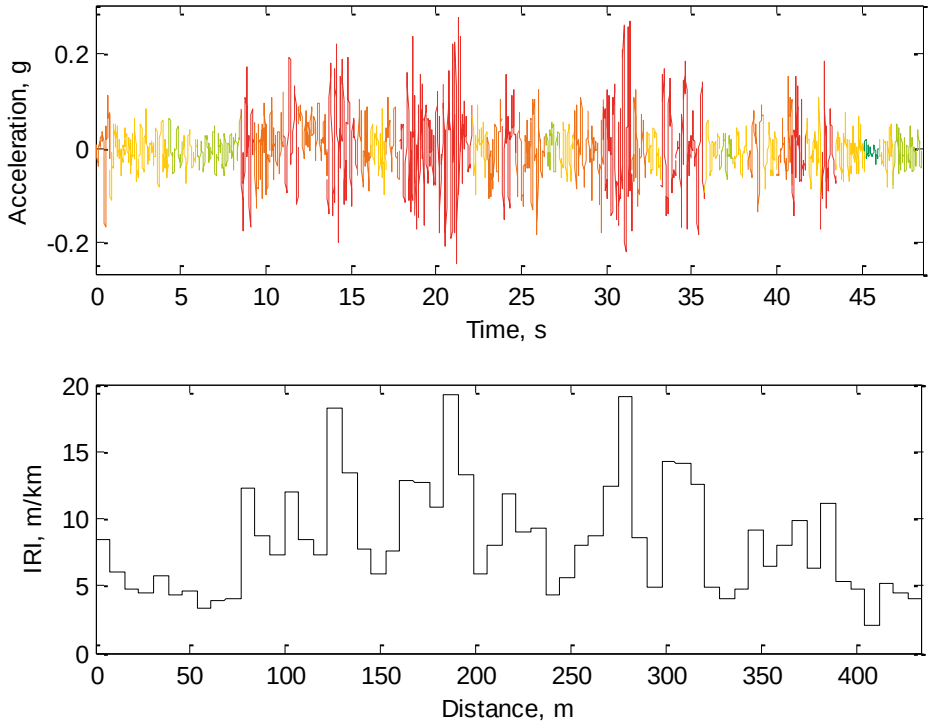

Figure D.51: IRI Approximation — Road Segment 26

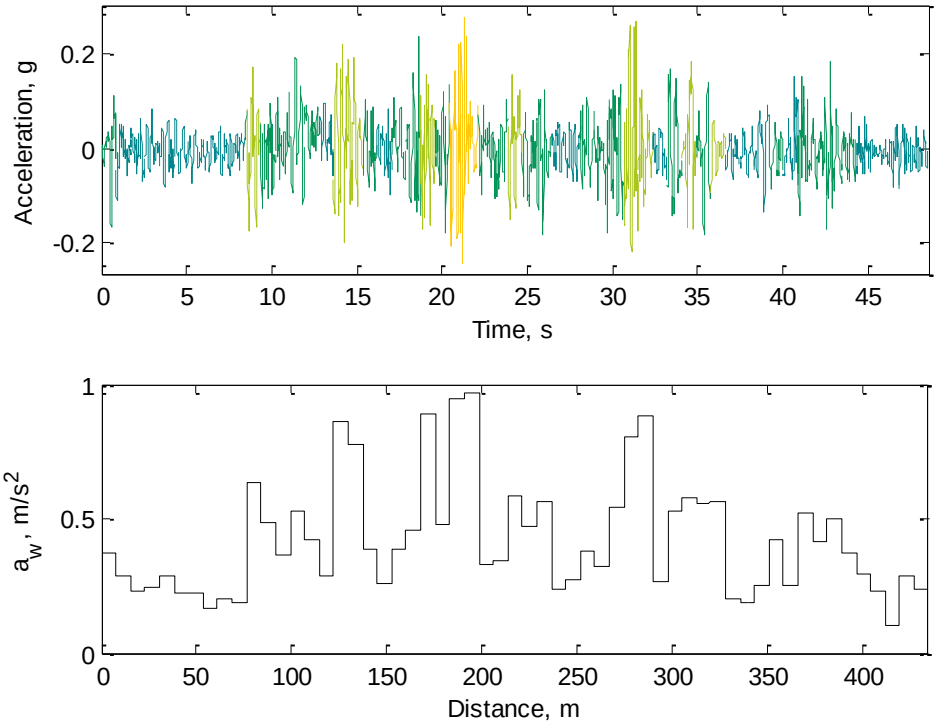

Figure D.52: Comfort Approximation — Road Segment 26

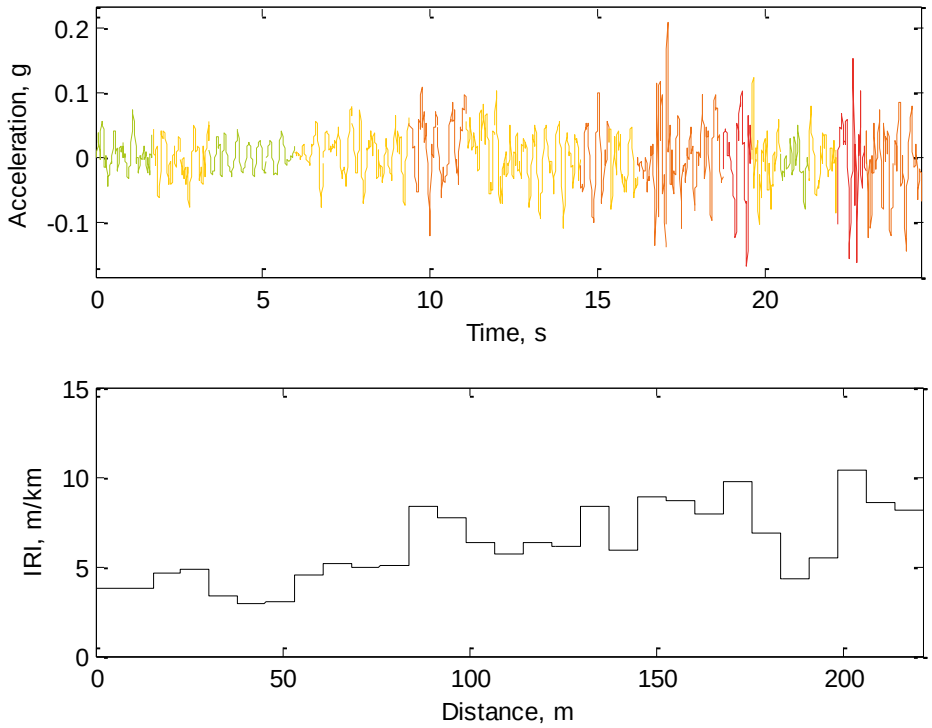

Figure D.53: IRI Approximation — Road Segment 27

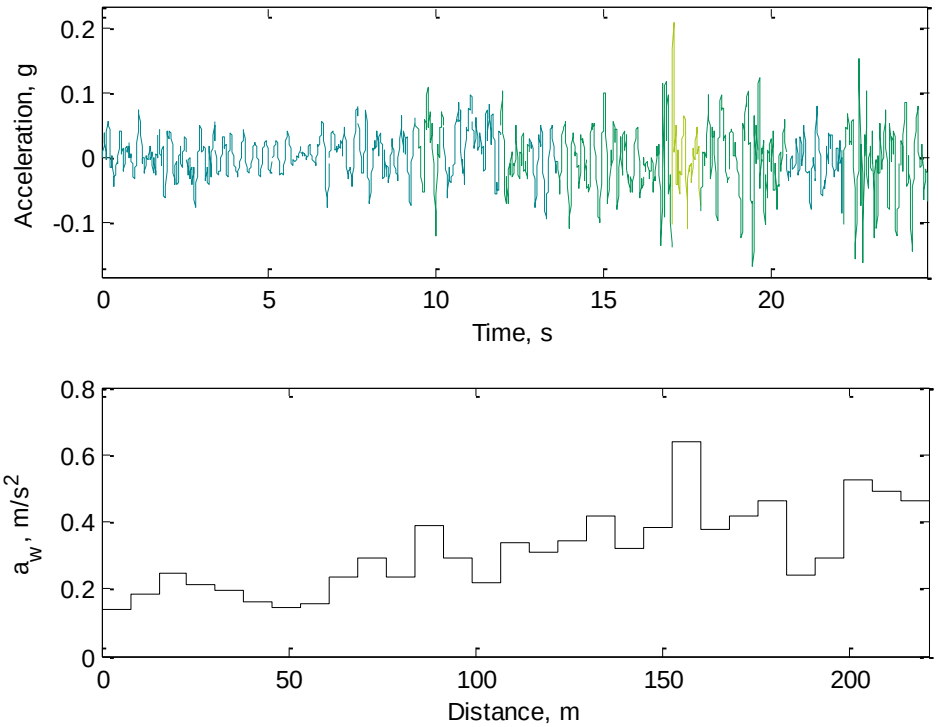

Figure D.54: Comfort Approximation — Road Segment 27

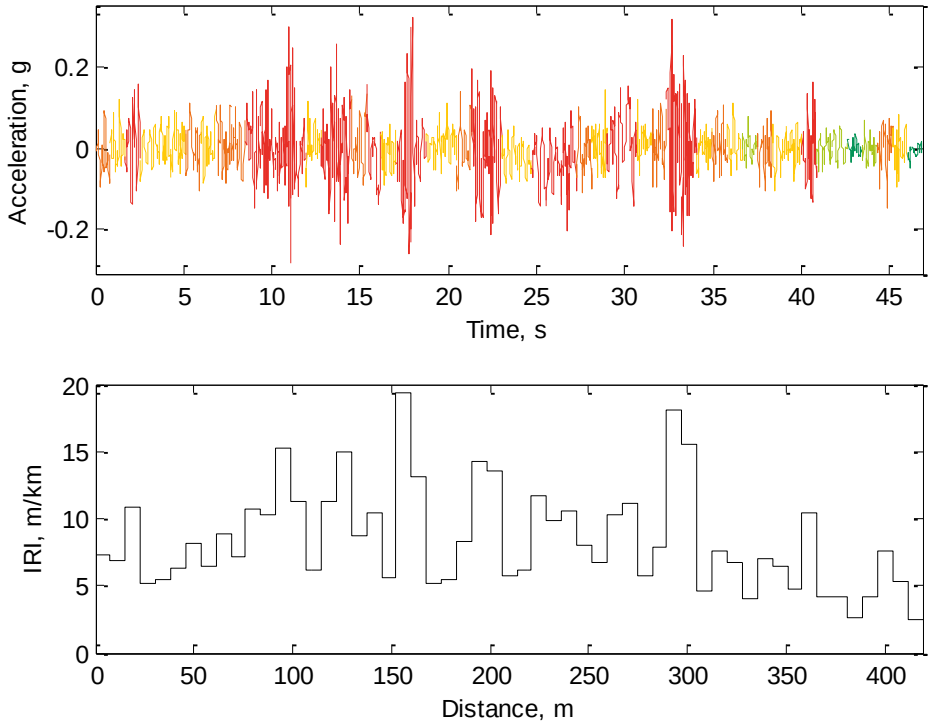

Figure D.55: IRI Approximation — Road Segment 28

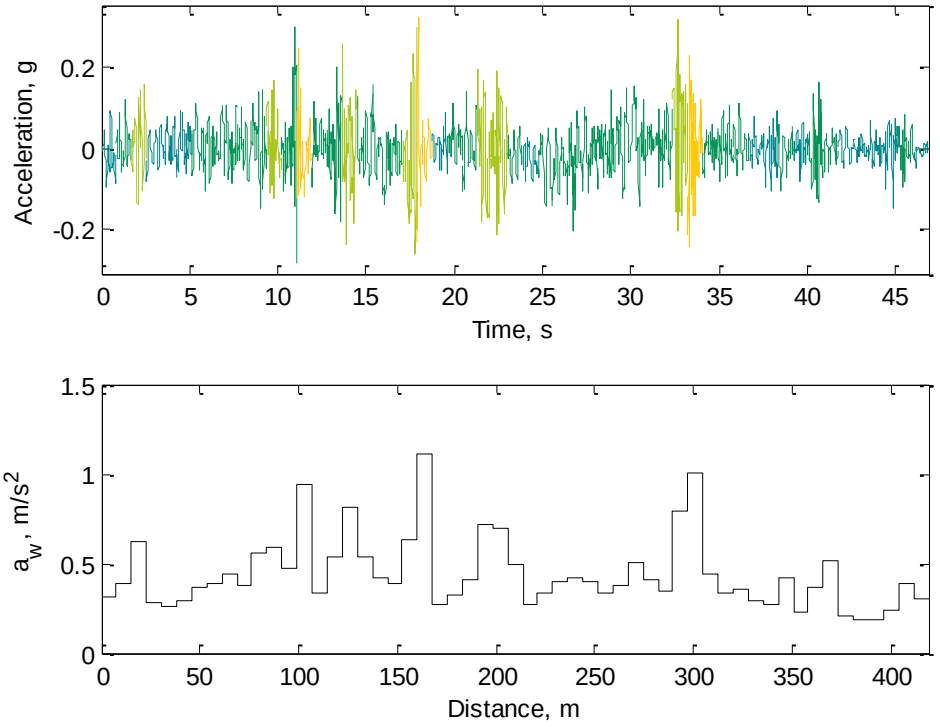

Figure D.56: Comfort Approximation — Road Segment 28

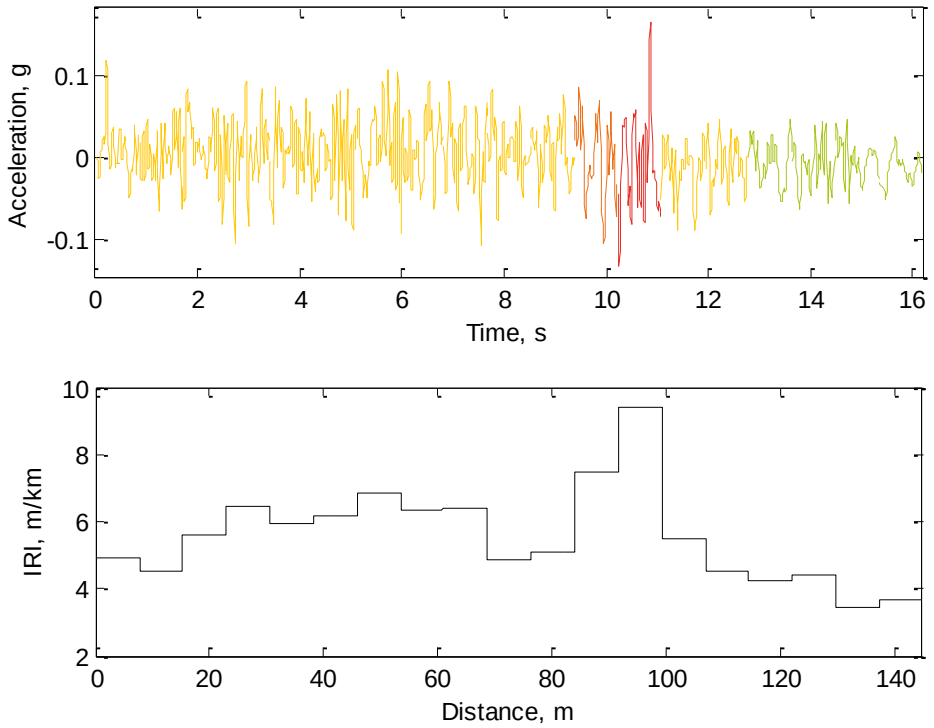

Figure D.57: IRI Approximation — Road Segment 29

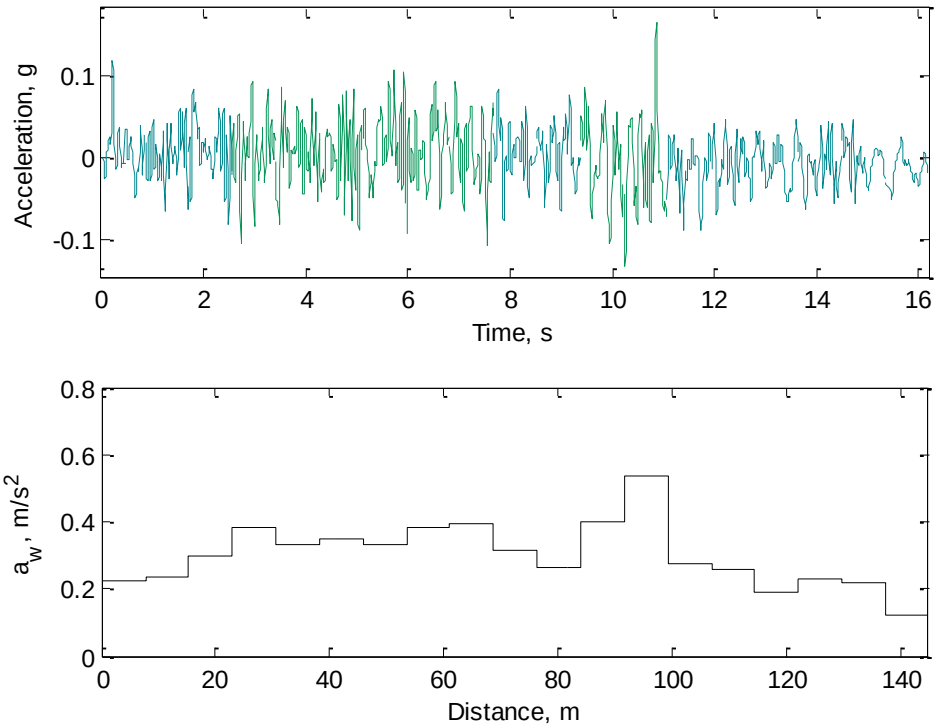

Figure D.58: Comfort Approximation — Road Segment 29

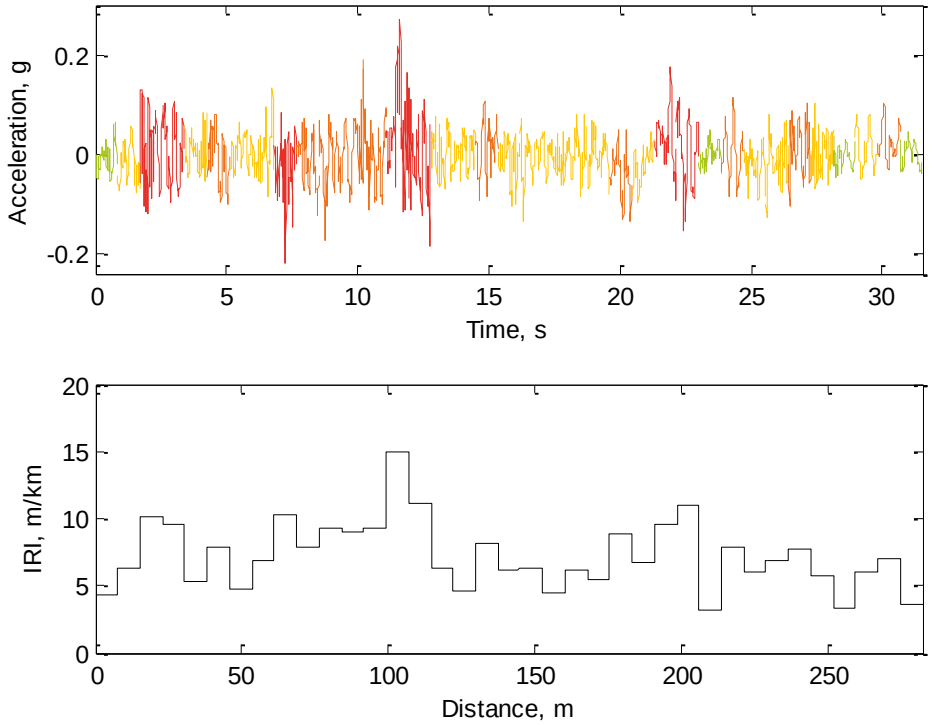

Figure D.59: IRI Approximation — Road Segment 30

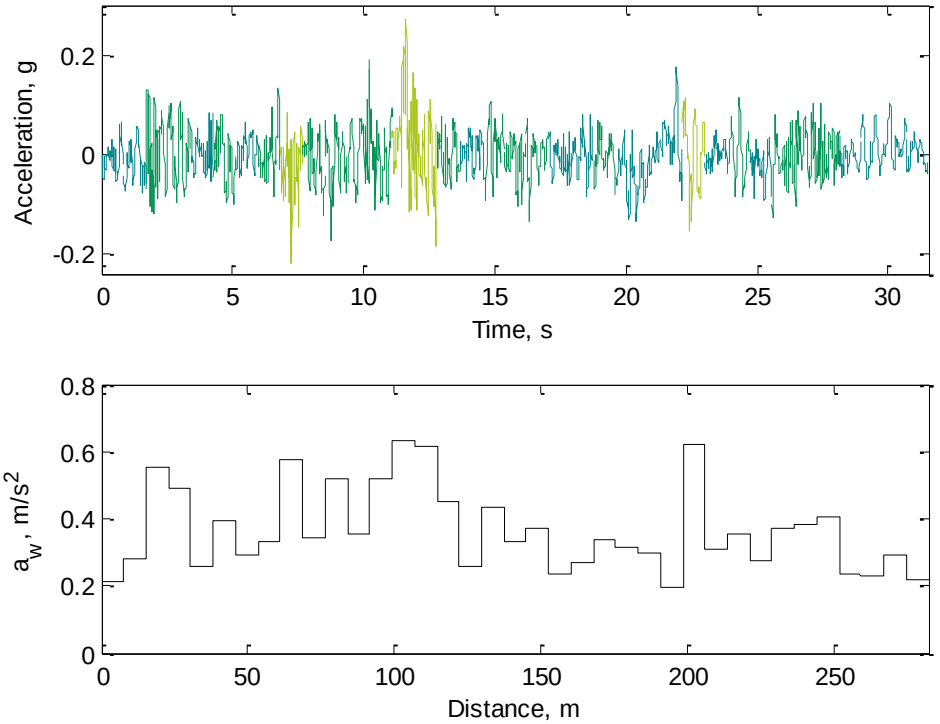

Figure D.60: Comfort Approximation — Road Segment 30

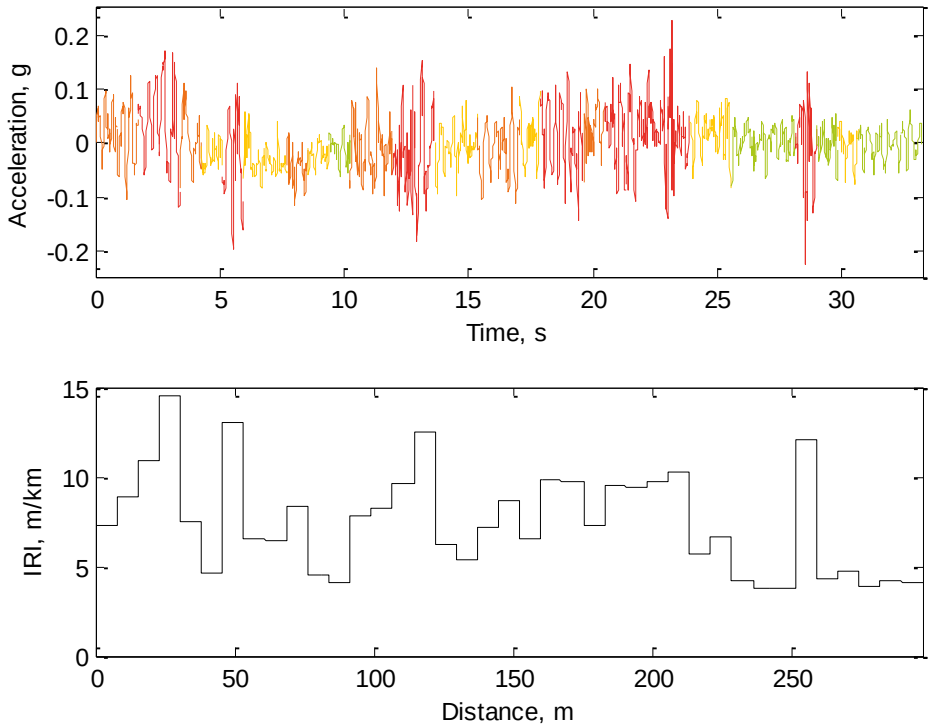

Figure D.61: IRI Approximation — Road Segment 31

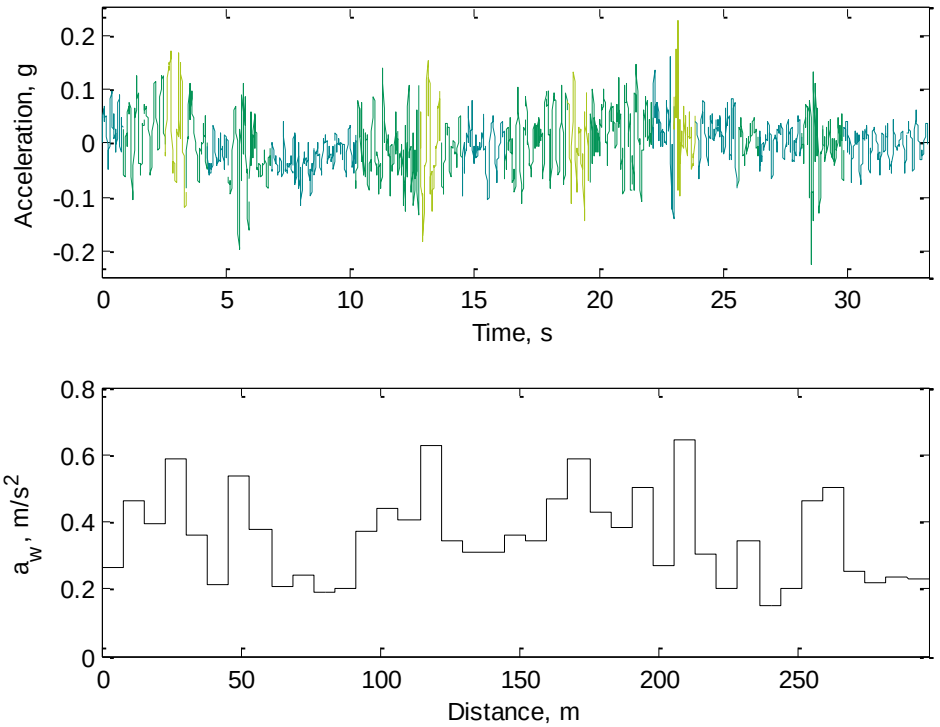

Figure D.62: Comfort Approximation — Road Segment 31

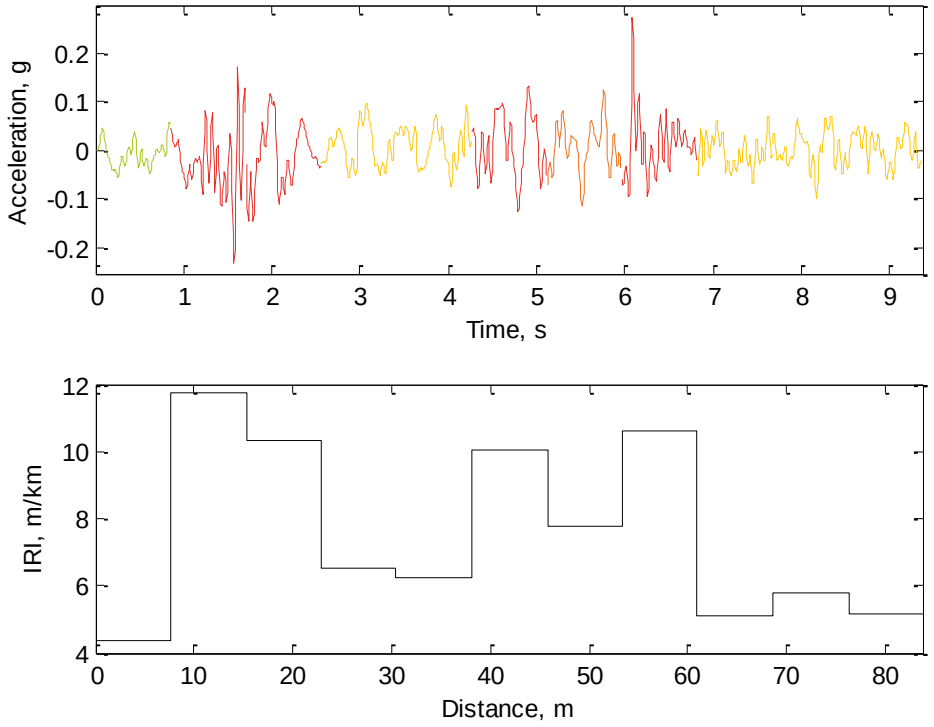

Figure D.63: IRI Approximation — Road Segment 32

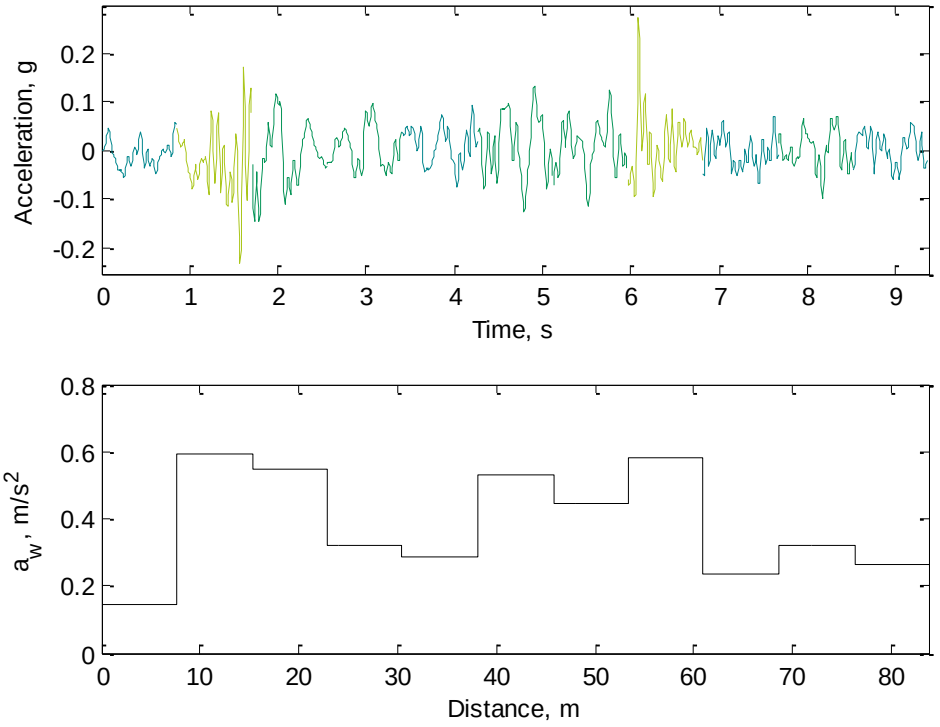

Figure D.64: Comfort Approximation — Road Segment 32

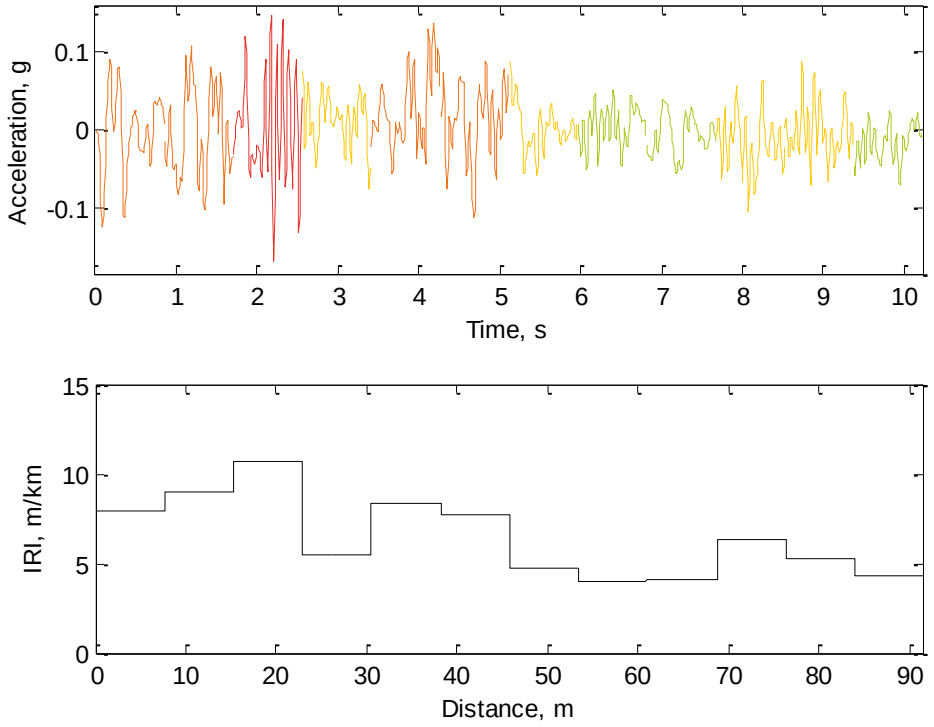

Figure D.65: IRI Approximation — Road Segment 33

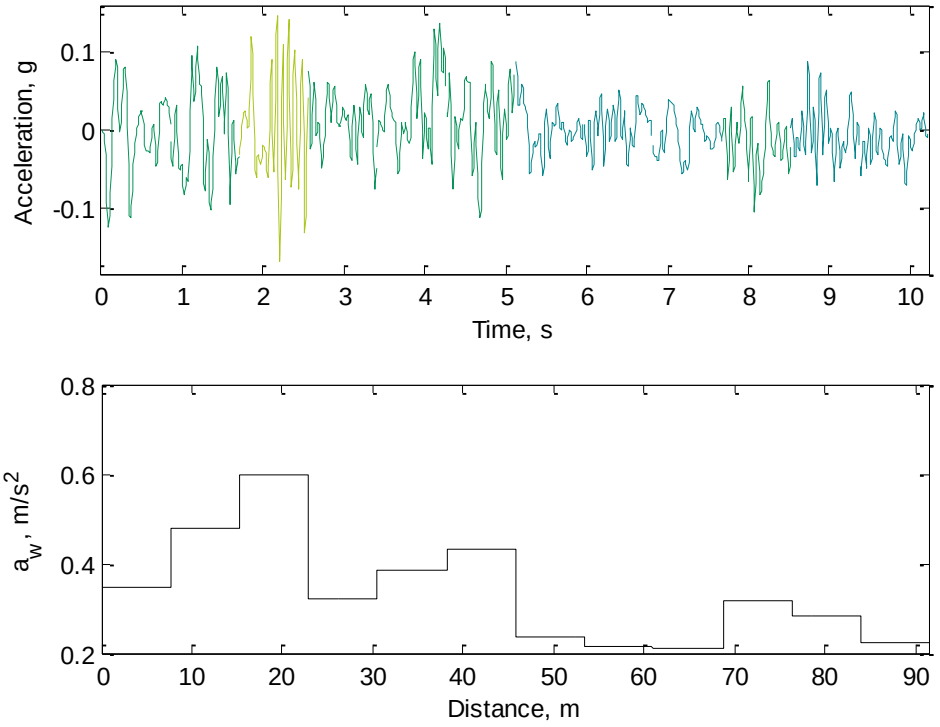

Figure D.66: Comfort Approximation — Road Segment 33

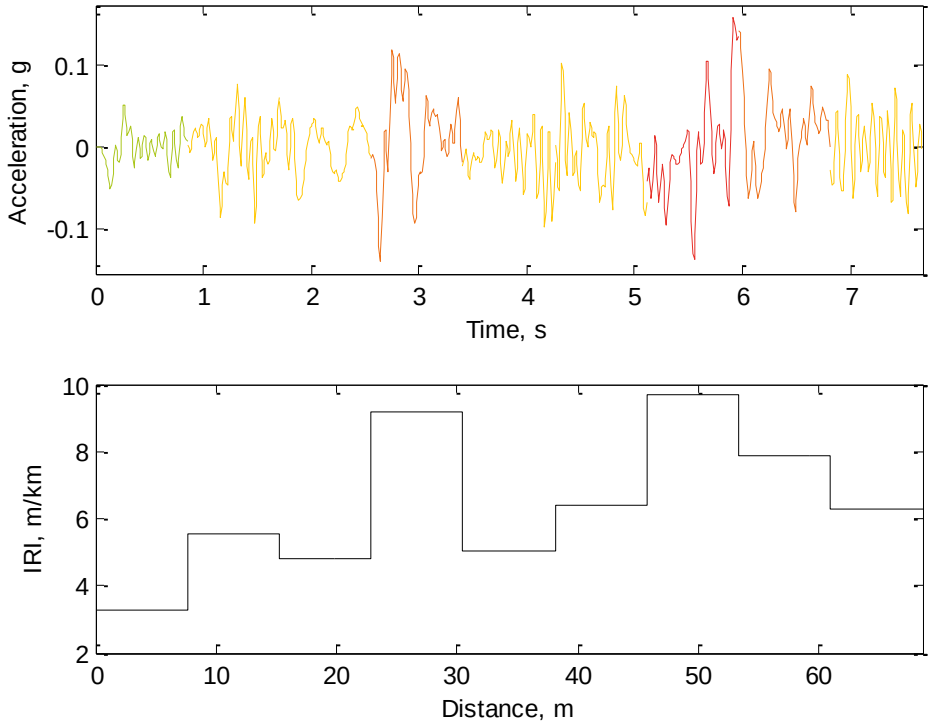

Figure D.67: IRI Approximation — Road Segment 34

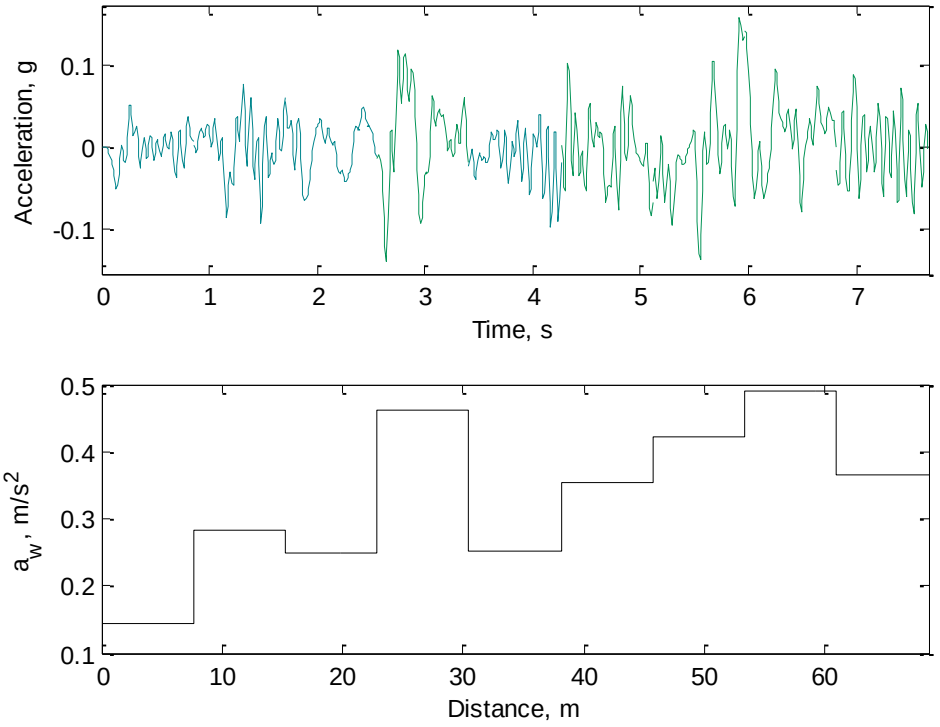

Figure D.68: Comfort Approximation — Road Segment 34

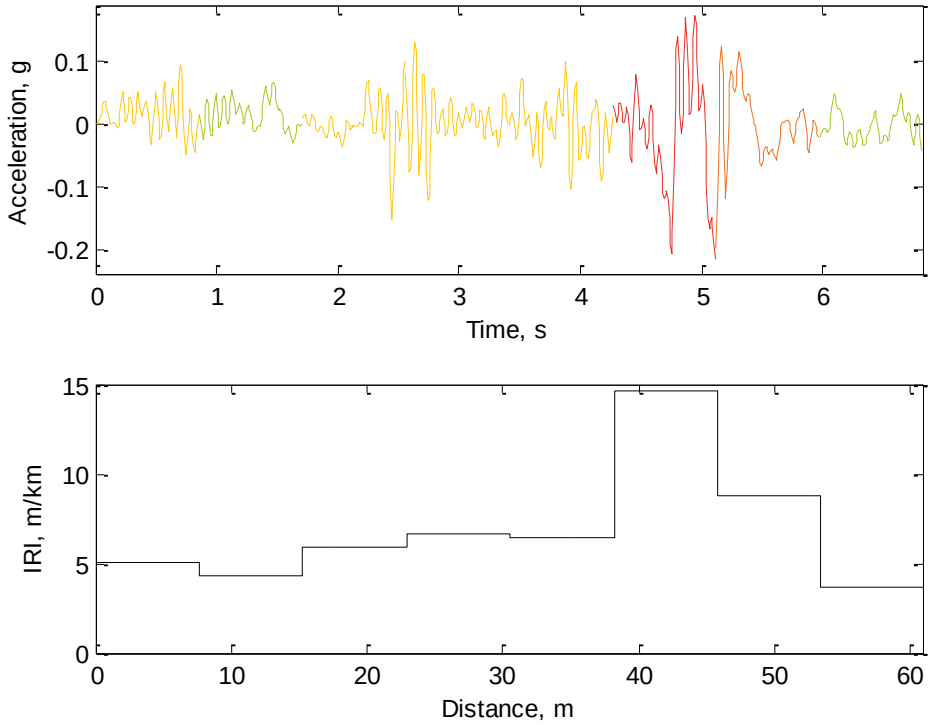

Figure D.69: IRI Approximation — Road Segment 35

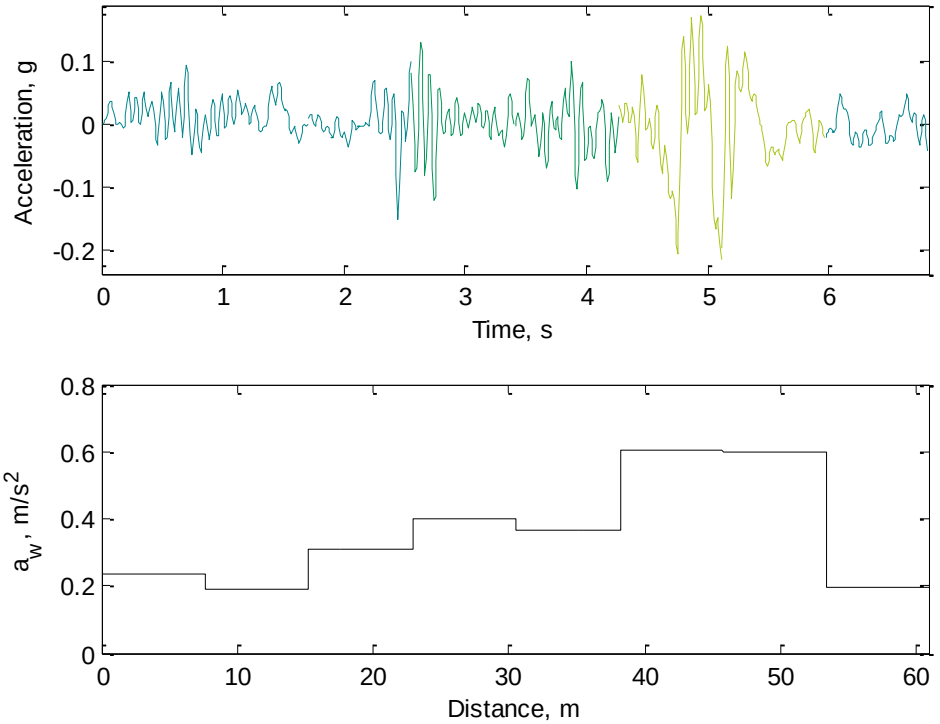

Figure D.70: Comfort Approximation — Road Segment 35

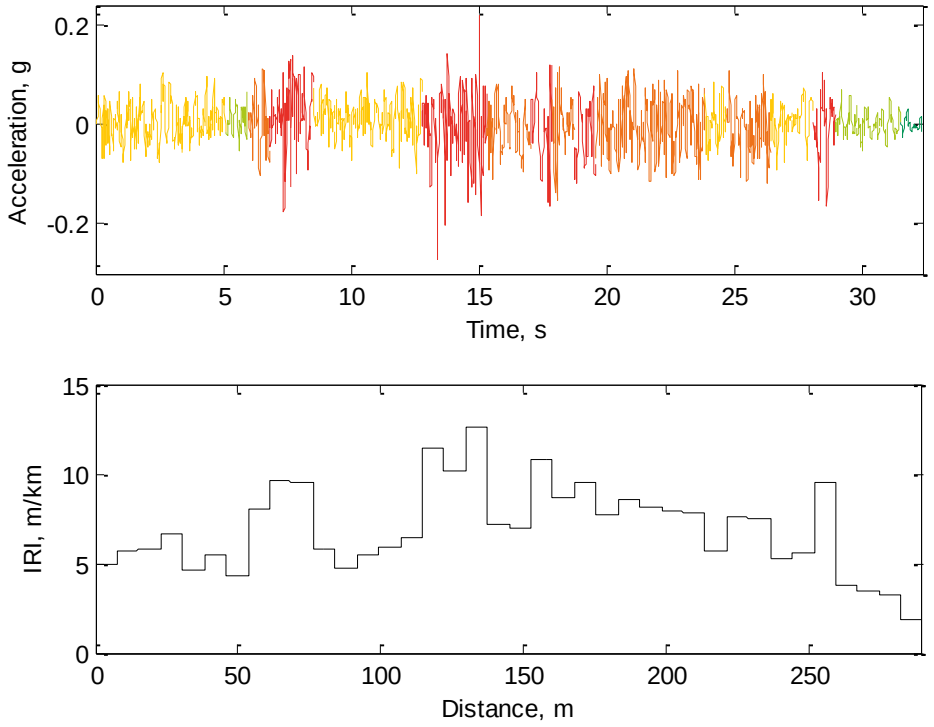

Figure D.71: IRI Approximation — Road Segment 36

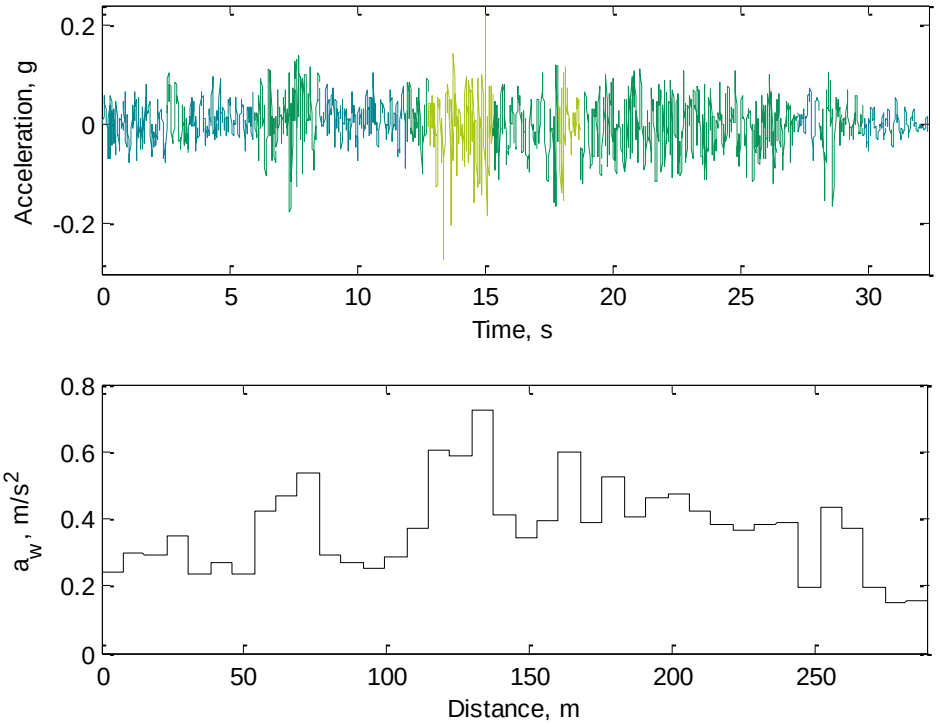

Figure D.72: Comfort Approximation — Road Segment 36

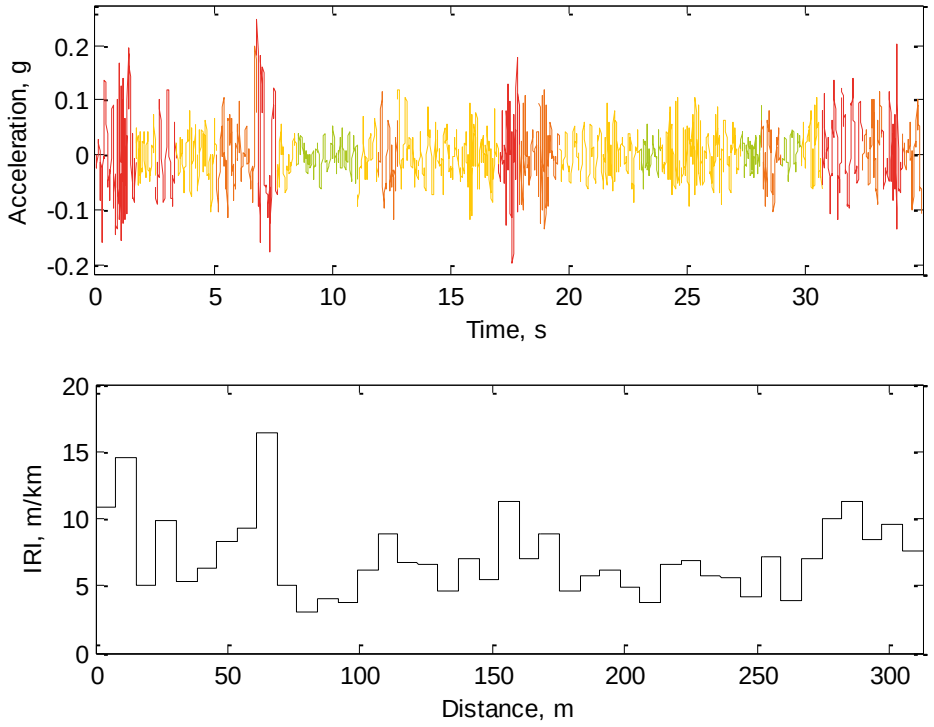

Figure D.73: IRI Approximation — Road Segment 37

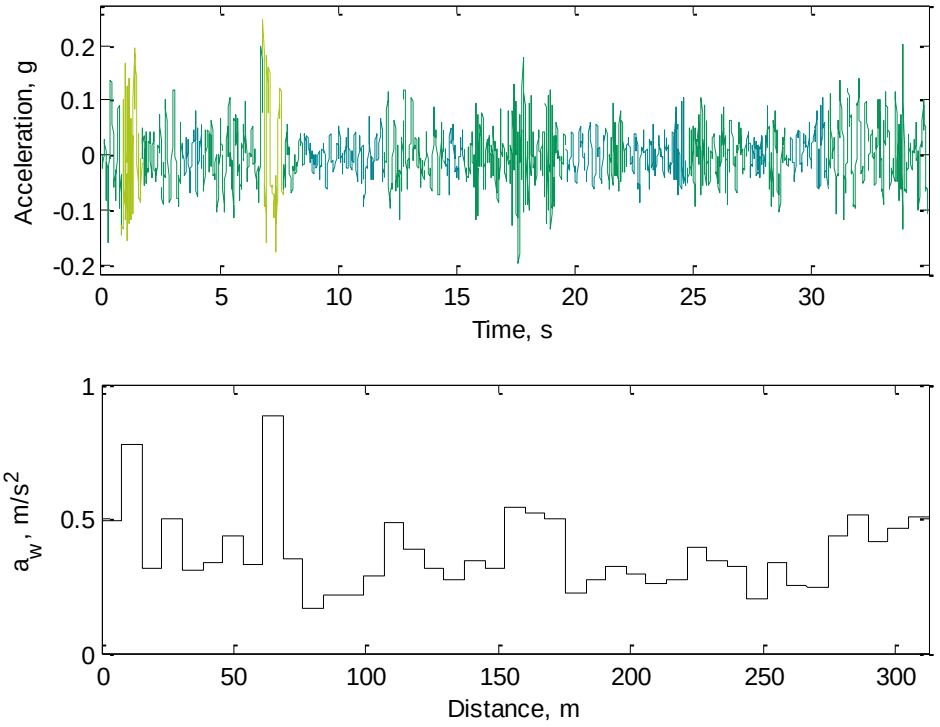

Figure D.74: Comfort Approximation — Road Segment 37

References

ASTM E1926 - 08. (2013). *Standard Practice for Computing International Roughness Index of Roads from Longitudinal Profile Measurements.* American Society for Testing and Materials.

Bighamian, R., & Mirdamadi, H. R. (2013). Input/Output System Identification of Simultaneous Mass/Stiffness Damage Assessment Using Discrete-Time Pulse, Differential Evolution Algorithm, and Equivalent Virtual Damped SDOF. *20*(4).

Bosch Sensortec. (2011). *BMA220 Datasheet.* Retrieved 2015, from Bosch Sensortec: http://ae-bst.resource.bosch.com/media/products/dokumente/bma220/BST-BMA220-DS003-08.pdf

Briaud, J. L., James, R. B., & Hoffman, S. B. (1997). *Settlement of Bridge Approaches (The Bump at the End of the Bridge).* Washington, D.C.: National Cooperative Highway Research Program.

Cebon, D. (2000). *Handbook of Vehicle-Road Interaction.* Lisse, Netherlands: Taylor & Francis.

Chang, M., Leonard, R. L., & Pakzad, S. N. (2012). *Structural Modal Identification Toolsuite (SMIT).* Retrieved from http://smit.atlss.lehigh.edu/wp-content/uploads/2012/07/SMIT-Users-Guide.pdf

Chopra, A. K. (2007). *Dynamics of Structures: Theory and Applications to Earthquake Engineering* (3rd ed.). Upper Saddle River, NJ: Pearson Prentice Hall.

Da Silva, J. (2004). Dynamical Performance of Highway Bridge Deck with Irregular Pavement Surface. *82*(11-12).

Dahlberg, T. (1978). Ride Comfort and Road Holding of a 2-DOF Vehicle Travelling on a Randomly Profiled Road. *58*(2).

De Angelis, M., Lus, H., Betti, R., & Longman, R. W. (2002). Extracting Physical Parameters of Mechanical Models from Identified State-Space Representations. *Journal of Applied Mechanics, 69*(5), 617-625.

Dixon, J. C. (2007). *The Shock Absorber Handbook* (2nd ed.). West Sussex, England: John Wiley and Sons.

Dodds, C. J., & Robson, J. D. (1973). The Description of Road Surface Roughness. *31*(2).

Douangphachanh, V., & Oneyama, H. (2013). Estimation of Road Roughness Condition from Smartphones under Realistic Settings. *International Conference on ITS Telecommunications.* Tampere: IEEE.

Dupont, B., & Allen, D. L. (2002). *Movements and Settlements of Highway Bridge Approaches.* Lexington, KY: Kentucky Transportation Center.

Dyer, S. A., & Dyer, J. S. (2008). Implementation Problems in Inertial Road-Profiling: An Overview. *IEEE International Instrumentation and Measurement Technology Conference.* Victoria, Vancouver Island, Canada.

Edmunds. (2015). *2009 Toyota RAV4 Base 4dr SUV 2.5L 4-cyl. 4-speed Automatic Features and Specs*. Retrieved 2015, from Edmunds: http://www.edmunds.com/toyota/rav4/2009/features-specs/

FHWA. (2003). *Product Brief: Pavement Profile Viewer and Analyzer.* FHWA-RD-03-070.

FHWA. (2011). *HPMS Field Manual*. (FHWA) Retrieved 2015, from U.S. Department of Transportation: Federal Highway Administration: http://www.fhwa.dot.gov/ohim/hpmsmanl/appe.cfm

FHWA. (2014). *Highway Performance Monitoring System Field Manual.* Retrieved 2015, from Federal Highway Administration: http://www.fhwa.dot.gov/policyinformation/hpms/fieldmanual/HPMS_2014.pdf

FHWA. (2014, 1 23). *Smoothness - Pavements*. Retrieved 2015, from Federal Highway Administration: http://www.fhwa.dot.gov/pavement/smoothness/

Gao, J., & Chen, K. (2011). Frequency-Domain Simulation and Analysis of Vehicle Ride Comfort based on Virtual Proving Ground. *4*(3).

Gao, W., Zhang, N., & Du, H. P. (2007). A Half-Car Model for Dynamic Analysis of Vehicles with Random Parameters. *5th Australasian Congress on Applied Mechanics.* Brisbane, Australia.

Gillespie, T. D. (1992). Everything You Always Wanted to Know about the IRI, but Were Afraid to Ask! *Road Profile Users Group Meeting.* Lincoln, Nebraska.

Gillespie, T. D., Sayers, M. W., & Segel, L. (1980). Calibration of Response-Type Road Roughness Measuring Systems. *National Coqmative Highway Research Program Transportation Research Board National Research Council.* Washington D.C.

González, A., O'Brien, E. J., Li, Y., & Cashell, K. (2008). The Use of Vehicle Acceleration Measurements to Estimate Road Roughness. *Vehicle System Dynamics, 46*(6), 483-499.

Google Maps. (2015). *College Park, MD.* (Google) Retrieved 2015, from Google Maps: https://www.google.com/maps/@38.9871181,-76.9410169,15z

Griffin, M. J. (1998). A Comparison of Stanardized Methods for Predicting the Hazards of Whole-Body Vibration and Repeated Shocks. *215*(4).

Hostens, I., Papaioannou, Y., Spaepen, A., & Ramon, H. (2003). A Study of Vibration Characteristics on a Luxury Wheelchair and a New Prototype Wheelchair. *266*(3).

Islam, A. A. (2010). *On Reducting Bumps at Pavement-Bridge Interface.* Youngstown, Ohio: Youngstown State University.

ISO 2631-1. (1997). *Mechanical Vibration and Shock - Evaluation of Human Exposure to Whole-Body Vibration - Part 1: General requirements.* International Organization for Standardization.

ISO 8608. (1995). *Mechanical Vibration - Road Surface Profiles - Reporting of Measured Data.* International Organization for Standardization.

Jazar, R. N. (2008). *Vehicle Dynamics: Theory and Application.* Riverdale, NY: Springer.

Johannesson, P., & Rychlik, I. (2012). *Modelling of Road Profiles Using Roughness Indicators.* Gothenborg, Sweden: Chalmers.

Kropac, O., & Mucka, P. (2008). Effect of Obstacles in the Road Profile on the Dynamic Response of a Vehicle. *222*(3).

Li, J., & Zhang, Y. (2006). Prediction error method-based second-order structural identification algorithm in stochastic state space formulation. *35*(6).

Liu, C., & Herman, R. (1999). Ride Profile, Vehicle Dynamics, and Ride Quality. *125*(2).

Ljung, L. (1987). *System Identification: Theory for the User.* Englewood Cliffs, New Jersey: Prentice Hall.

Ljung, L. (2002). Prediction Error Estimation Methods. *21*(1).

Londono, N. A., Desjardins, S. L., & Lau, D. T. (2004). Use of Stochastic Subspace Identification Methods for Post-Disaster Condition Assessment of Highway Bridges. *13th World Conference on Earthquake Engineering.* Vancouver, Canada.

Magalhaes, F., Cunha, A., & Caetano, E. (2009). Online Automatic Identification of the Modal Parameters of a Long Span Arch Bridge. *Mechanical Systems and Signal Processing, 23*(2), 316-329.

Maryland SHA. (2012). *Maryland Standard Method of Tests: Operation of the Inertial Profiler.* Retrieved 2015, from Department of Transportation State Highway Administration: http://sha.md.gov/OMT/msmt563.pdf

MATLAB. (2013). version 8.1.0.604 (R2013a). Natick, Massachusetts: The MathWorks Inc.

McGhee, K. H. (2004). *NCHRP Synthesis 334: Automated Pavement Distress Collection Techniques.* Washington, D.C.: Transportation Research Board.

McGowen, P., & Sanderson, M. (2011). Accuracy of Pneumatic Road Tube Counters. *Western District Annual Meeting.* Anchorage, AK: Institue of Transportation Engineers.

Mednis, A., Strazdins, G., Zviedris, R., Kanonirs, G., & Selavo, L. (2011). Real Time Pothole Detection using Android Smartphones with Accelerometers. *Distributed Computing in Sensor Systems and Workshops.* Barcelona: IEEE.

Nagarajaiah, S., & Basu, B. (2009). Output Only Modal Identification and Structural Damage Detection Using Time Frequency & Wavelet Techniques. *8*(4).

Nahvi, H., Fouladi, M. H., & Nor, M. J. (2009). Evaluation of Whole-Body Vibration and Ride Comfort in a Passenger Car. *14*(3).

PASCO. (2015). *PASPORT Airlink2 Manual (PS-2010).* Retrieved 2015, from PASPORT AirLink 2 - PS-2010 : PASCO: http://www.pasco.com/file_downloads/product_manuals/Airlink2-Manual-PS-2010.pdf

PASCO. (2015). *PASPORT-Acceleration-Sensor-3-axis-Manual-PS-2119.* Retrieved 2015, from PASPORT Acceleration Sensor (3-axis) - PS-2119 : PASCO: ttp://www.pasco.com/file_downloads/product_manuals/PASPORT-Acceleration-Sensor-3-axis-Manual-PS-2119.pdf

PASCO. (2015). SPARKvue. *version 2.1*. Roseville, CA: PASCO.

Peeters, B., & De Roeck, G. (1999). Reference-Based Stochastic Subspace Identification for Output-Only Modal Analysis. *13*(6).

Pence, B. L., Fathy, H. K., & Stein, J. L. (2009). Sprung Mass Estimation for Off-Road Vehicles via Base-Excitation Suspension Dynamics and Recursive Least Squares. *American Control Conference.* Riverfront, St. Louis.

Pence, B., Hays, J., Fathy, H., Sandu, C., & Stein, J. (2011). *Vehicle Sprung Mass Estimation for Rough Terrain.* Ann Arbor, Michigan: University of Michigan.

PennDOT. (2015). *High Speed Profiler*. Retrieved 2015, from Pennsylvania Department of Transportation:

http://www.dot.state.pa.us/Internet/Bureaus/pdBOMO.nsf/infoRMRIPROFILE

Petsounis, K. A., & Fassois, S. D. (2001). Parametric time-domain methods for the identification of vibrating structures – a critical comparison and assessment. *Mechanical Systems and Signal Processing, 15*(6), 1031-1060.

Piersol, A. G., & Paez, T. L. (2009). *Harris' Shock and Vibration Handbook* (Sixth Edition ed.). New York: McGraw-Hill Professional.

Prem, H., & Ayton, G. (2005). Improved Techniques for Assessing Ride Quality on Concrete Pavements. *8th International Conference on Concrete Pavements, 1*. Colorodo Springs, CO.

ProVAL. (2015). version 3.51.0339. Austin, Texas: The Transtec Group, Inc.

Ren, W.-X., & Zong, Z.-H. (2004). Output-Only Modal Parameter Identification of Civil Engineering Structures. *Structural Engineering and Mechanics, 17*(3-4), 1-16.

Sayers, M. W. (1995). On the Calculation of International Roughness Index from Longitudinal Road Profile. (1501).

Sayers, M. W., & Karamihas, S. M. (1996). *Interpretation of Road Roughness Profile Data.* Federal Highway Administration.

Sayers, M. W., & Karamihas, S. M. (1998). *The Little Book of Profiling.* University of Michigan Transportation Research Institute.

Sayers, M. W., Gillespie, T. D., & Queiroz, C. A. (1986). *The International Road Roughness Experiment: Establishing Correlation and a Calibration Standard for Measurements.* The World Bank.

Seber, G. A., & Wild, C. J. (2003). *Nonlinear Regression.* Hoboken, NJ: John Wiley & Sons.

Smith, C. C., McGehee, D. Y., & Healey, A. J. (1976). *The Prediction of Passenger Riding Comfort from Acceleration Data.* Washington, D.C.: Department of Transportation: Office of University Research.

Stark, T. D., Olson, S. M., & Long, J. H. (1995). *Differential Movement at the Embankment/Structure Interface: Mitigation and Rehabilitation.* Springfield, Illinois: University of Illinois, Dept. of Civil Engineering.

Sukhvarsh, J., & Gurav, S. (2008). Road Surface Roughness Generation by Power Spectral Density in Bridge Design. *Structures Congress 2008: Crossing Borders.* Vancouver, British Columbia, Canada: American Society of Civil Engineers.

Toyota. (2015). *2015 Toyota RAV4*. Retrieved 2015, from Toyota Official Site: http://www.toyota.com/rav4/

Turkay, S., & Akcay, H. (2005). A Study of Random Vibration Characteristics of the Quarter-Car Model. *Journal of Sound and Vibration, 282*(1-2), 111-124.

Tyan, F., Hong, Y.-F., Tu, S.-H., & Jeng, W. S. (2009). Generation of Random Road Profiles. 1373-1378.

Vahidi, A., Stefanopoulou, A., & Peng, H. (2005). Recursive Least Squares with Forgetting for Online Estimation of Vehicle Mass and Road Grade: Theory and Experiments. *43*(1).

Van Overschee, P., & De Moor, B. (1993). Subspace Algorithms for Stochastic Identification Problem. *29*(3).

Van Overschee, P., & De Moor, B. (1996). *Subspace Identification for Linear Systems: Theory - Implementation - Applications.* Boston/London/Dordrecht: Kluwer Academic Publishers.

Verros, G., Natsiavas, S., & Papadimitriou, C. (2005). Design Optimization of Quarter-Car Models with Passive and Semi-active Suspensions under Random Road Excitation. *Journal of Vibration and Control, 11*(5), 581-606.

Wakeham, K. J., & Rideout, D. G. (2011). Model Complexity Requirements in Design of Half Car Active Suspension Controllers. *ASME Dynamic Systems and Controls Conference.* Arlington, VA.

Wang, H., & Flintsch, G. W. (2009). Comparative Study of Road Profilers' Accuracy and Precision. *38*(2).

Xu, D. M., Mohamed, A. O., Yong, R. N., & Caporuscio, F. (1992). Development of a Criterion for Road Surface Roughness Based on Power Spectral Density Function. *29*(4-5).

Zambrano, A., Perez, I., Palau, C., & Esteve, M. (2014). Quake Detection System Using Smartphone-Based Wireless Sensor Network for Early Warning. *Pervasive Computing and Communications Workshops.* Budapest: IEEE.